THE UNIVERSITY OF SYDNEY

COPYRIGHT AND USE OF THIS THESIS

This thesis must be used in accordance with the provisions of the Copyright Act 1968.

Reproduction of material protected by copyright may be an infringement of copyright and copyright owners may be entitled to take legal action against persons who infringe their copyright.

Section 51 (2) of the Copyright Act permits an authorized officer of a university library or archives to provide a copy (by communication or otherwise) of an unpublished thesis kept in the library or archives, to a person who satisfies the authorized officer that he or she requires the reproduction for the purposes of research or study.

The Copyright Act grants the creator of a work a number of moral rights, specifically the right of attribution, the right against false attribution and the right of integrity.

You may infringe the author's moral rights if you:

- fail to acknowledge the author of this thesis if you quote sections from the work
- attribute this thesis to another author
- subject this thesis to derogatory treatment which may prejudice the author's reputation

For further information contact the University's Copyright Service.

sydney.edu.au/copyright

Centre-Triggered Pulsed Cathodic Arc Spacecraft Propulsion Systems

A thesis submitted in fulfilment of the requirements for the degree of

Doctor of Philosophy by Cotutelle

to be jointly awarded by the

Faculty of Science

at the

The University of Sydney

and the

Department of Applied Physics and Materials Science

at the

The City University of Hong Kong

written and submitted in 2015 by

Patrick Reinhard Christian Neumann, BE MSc

Declaration of Authorship

I, Patrick Reinhard Christian Neumann, certify that:

- I am the author of this work, being a Thesis for the Degree of Doctor of Philosophy;
- The work in this thesis has not previously been submitted for a degree nor has it been submitted as part of the requirements for a degree except as fully acknowledged within the text;
- Any assistance that I have received in my research work and the preparation of the thesis itself has been acknowledged;
- All literature used to prepare this work has been cited appropriately and the authors acknowledged.

Abstract

Satellites must carry some manner of propulsion system so that course correction or orbit stationkeeping manoeuvres can be carried out. Chemical thrusters have lower specific impulse than electric propulsion systems, and so focus has turned to using plasma and ion propulsion systems such as Hall Effect thrusters and gridded ion thrusters. Both of these systems use gaseous propellants and require a charge neutralisation system, both of which impose certain design compromises. This thesis explores the potential use of pulsed cathodic arcs as a spacecraft propulsion system, determining fuel specific impulse and jet power efficiency of a range of suitable materials over a range of arc currents and pulse durations. Comparisons between element classes are made, so as to identify candidate materials for various mission profiles. The results for magnesium in particular stand out as being comparable to several thruster technologies that are flight-rated.

Table of Figures

Table of Tables

1 Introduction to Rocket Propulsion

In recent years focus has turned to electric and plasma based propulsion systems for orbital station-keeping and long-duration spaceflight main engines. These propulsion systems are attractive for a number of reasons, namely their high specific impulse, controllability, deliverable mass fraction and technological maturity. However, every electrical propulsion system currently in use has flaws inherent to its design, flaws which a pulsed cathodic arc (PCA) system does not share. The aim of this thesis is to demonstrate that PCAs can be effective thrusters and to determine which cathode materials make the most efficient fuels. In this chapter the fundamentals of rocket propulsion will be discussed, as well as current electric propulsion technologies.

1.1 Theory

A rocket propelled vehicle generates acceleration by discharging propellant at high velocity, resulting in an exchange of momentum due to an unbalanced force. Neglecting gravitation and drag, the equation of motion describing the vehicle follows from the conservation of momentum that includes the vehicle and the propellant stream.

$$F_{thrust} = -\dot{m}v_e \tag{1.1}$$

Where $\dot{m}$ is the mass flow rate of the exhaust and v_e is the exhaust velocity of the propellant relative to the spacecraft. The right hand side of equation 1.1 is the thrust generated by the system, being the product of the exhaust velocity and the instantaneous rate of change of the mass of the spacecraft due to propellant expulsion. The negative sign in equation 1.1 is present so that the thrust calculated is positive. The thrust can be considered an external force applied to the spacecraft. The integral of the thrust over the time of application is the total change in momentum experienced by the spacecraft, referred to as impulse. The ratio of thrust to the propellant weight flow rate ($\dot{m}g$) is known as specific impulse. Weight is used to ease the conversion for users of imperial units, as pounds-force can be used rather than poundals or slugs. Specific impulse allows for simple comparisons to be made between thruster types, as it is a measure of the propulsion efficiency per unit weight of fuel consumed, often referred to as "bounce per ounce." Equation 1.2 shows the definition of specific impulse in seconds, also showing its dependence on propellant exhaust velocity [1].

$$F_{thrust} = I_{SP}\dot{m}g \qquad \therefore \qquad I_{SP} = \frac{F_{thrust}}{\dot{m}g} = \frac{v_e}{g} \tag{1.2}$$

Where I_{SP} denotes specific impulse, F_{thrust} is the thrust developed and g is the standard gravitational acceleration at sea-level. The units for specific impulse are seconds, as I_{SP} can be thought of as the length of time taken for a given thruster to burn 1 kilogram of fuel if the thruster is throttled so as to produce 1 Newton of thrust; therefore higher I_{SP} denotes higher mass efficiency. Literature values for the specific impulse of bipropellant liquid fuelled rockets, such as the hydrogen/oxygen fuelled Space Shuttle Orbital Manoeuvring System, have a maximum value of 450s, while solid fuelled chemical rocket engines have a limit of approximately 250s [1]. Various electric propulsion technologies have specific impulses from 1000 to 3500s [1-5]; thus the PCA thruster must have a specific impulse in this range to be considered an acceptable thruster technology.

However, as equation 1.2 shows, the mass efficiency of a thruster is dependent on exhaust velocity; higher exhaust velocities induce greater momentum transfers for given masses of propellant consumption, leading to higher thrust. In fact, integration of the equation of motion shows that if the exhaust velocity of the motor is constant during the thrust period, the spacecraft experiences a velocity increment proportional to the logarithm of the propellant mass expelled, but linearly dependent on exhaust velocity. This is shown in equation 1.3, which is the well-known Tsiolkovsky Rocket Equation [1] and indicates that higher exhaust velocities are preferable to higher mass flow rates.

$$\Delta v = v_e \ln \frac{m_0}{m_t} \tag{1.3}$$

Here Δv is the velocity increment experienced by the rocket, v_e is the velocity of the exhaust relative to the spacecraft, m_0 is the vehicle mass at the beginning of the thrust period and m_t is the vehicle mass at the end of the thrust period. A simple re-arrangement of the terms in equation 1.3 shows the deliverable mass fraction for a given operation, being the proportion of a spacecraft's initial mass that can be delivered to its destination.

$$\frac{m_t}{m_0} = \exp\left(\frac{-\Delta v}{v_e}\right) \tag{1.4}$$

With the terms having the same meaning as equation 1.3 , equation 1.4 shows that the deliverable mass fraction is a negative exponential of the ratio between the velocity increment produced by the thruster burn and the exhaust velocity [1, 6]. In the case where an electric field accelerates the ions in the plasma, the mean ion exhaust velocity is given by equation 1.5;

$$v_e = \sqrt{\frac{2\bar{q}V}{m}} \tag{1.5}$$

Where V is the potential difference used to accelerate the ions, $\bar{q}$ is the mean charge state of the ions and m is the atomic mass of the ions. The average momentum imparted to an ion p is:

$$p = mv = m\sqrt{\frac{2\bar{q}V}{m}} = \sqrt{2m\bar{q}V} \tag{1.6}$$

And in electrostatic thrusters p scales with the root of the atomic mass, mean ion charge state and accelerating voltage. Should the mission require the delivery of large payloads, either a prohibitively large propellant mass must be used, or the system must be multi-stage or the propulsion system exhaust velocity must be of the same order or greater than the required velocity change. Since interplanetary missions typically require velocity changes of tens of kilometres per second, it follows that the exhaust velocity of any thruster employed on such a mission must be comparable to this required change in velocity and sufficiently robust to operate for extended periods. The focus has therefore shifted from chemical fuelled rockets to electric propulsion technologies, due to their high propellant exhaust velocities and fewer mechanical parts.

Of course no solution is perfect, and one problem with electric propulsion systems as opposed to chemical propulsion systems is the need to have a power supply. While chemical thrusters carry the energy needed to effect momentum changes inside the chemical bonds of their fuel, electric propulsion systems need to have energy supplied to them in some manner. Since any power supply used for propulsion would add mass and volume, it is necessary to make the electrical propulsion system as energy efficient as possible. Quantifying the electrical power consumed by the system is simple; ammeters or Rogowski Coils can measure the current supplied while voltage probes determine the potential drop, and applying Ohm's Law will illustrate the power

consumption. The power that is transferred to the exhaust is known as the jet power and given by,

$$P_j = \frac{F_{thrust}^{\ 2}}{2\dot{m}} \tag{1.7}$$

Determining the ratio of jet power to power consumed allows for a simple determination of energy efficiency in a working rocket, with values of 50-80% quoted for flight rated systems [1-7]. This ratio is also termed "thrust efficiency," as it is the ratio of exhaust kinetic energy to available energy (in chemical thrusters) or input power (for electrical propulsion systems) [equation 17-12 in reference 1].

1.2 Existing Electric Propulsion Methods

Following the need for higher payload mass in orbit there has been a growing recognition of the benefits of electric propulsion systems. Since electric propulsion technologies have a higher specific impulse than chemically fuelled rockets, they can deliver the same change in impulse for much less propellant mass, leading to a higher deliverable mass fraction. The most effective manner in which to describe ion and plasma propulsion systems is to divide them into three main categories [chapter 17 of reference 1], being electrothermal, electrostatic and electromagnetic propulsion methods.

1.2.1 Electrothermal Propulsion Technologies

Resistojets and arcjets are examples of electrothermal propulsion systems, where the exhaust material is heated by electrical means then thermodynamically expanded and accelerated through an exhaust nozzle to produce thrust. Resistojets feed the propellant into the thruster chamber and heat it by contact with a heated surface, while arcjets heat the propellant by discharging an electrical arc through it. As the electrical current passes through the propellant material, it is heated, expands, and transits the rocket nozzle. Both of these methods have low efficiencies, as the exhaust spills out with thermal velocity and is often not heated uniformly. These devices have a typical I_{SP} of about 500-900s [table 17.4, reference 1], with low total thrust, problems with cryogenic propellant storage and a tendency to heat only a small fraction of the propellant.

1.2.2 Electrostatic Propulsion Technologies

These devices work by ionising the propellant and accelerating the exhaust ions by electrostatic means. This group includes electron bombardment, radiofrequency excitation, field emission electric propulsion (FEEP), cyclotron resonance, microwave discharge and gridded ion thrusters, each of which uses a different method to create and accelerate the ions [1, 8, and 14]. In order to limit space charge effects, the exhaust propellant ions are neutralised by electrons emitted by an external cathode. Electron bombardment thrusters generate their plasma by ionizing neutral propellant atoms with a low voltage electrical discharge, while radiofrequency ion thrusters generate the electron energies required for ionisation by subjecting the free "seed" electrons in the propellant to high frequency eddy fields generated by induction coils surrounding the discharge chamber. These systems tend to suffer from low ionisation fractions and wear on the electron gun.

FEEP ion thrusters do not generate plasma per se, but instead feed a liquid propellant to the tip of a needle-like emitter and create an intense local electric field on the tip of the needle [1]. This causes charged droplets to form spontaneously at the tip of the needle, which are then accelerated away from the needle by electrostatic forces. Certain newer FEEP designs utilise long, narrow needles of an easily ionisable metal such as caesium as their source material. When the intense electric field becomes concentrated on the tip of the electrode, a fraction of the metal atoms are able to be ionised and ejected from the electrode. The main drawbacks to this design are the high power requirements and the high reactivity of electrode materials suitable for this system; any metal of sufficiently low ionisation potential would be so highly reactive as to form an ionic oxide or nitride coating on the electrode surface within very short times, thus reducing thruster efficiency as a lower surface area is now available to generate thrust ions. In consequence, these thrusters are very hard to characterise from ground tests.

Electron resonance and microwave discharge ion thrusters energise the propellant in the discharge chamber with a circularly polarised microwave beam, which can then ionise sufficient propellant to generate thrust. These systems use electrostatic grids to accelerate the ions in the discharge plasma and are thus known as gridded ion thrusters; figure 1.1 illustrates such a system. Gridded ion thrusters have a common failure mode due to sputtering. Accelerated ions will frequently strike the grid, causing atoms in the grid to be sputtered off the surface of the grid. This not only

reduces the efficiency of the system by dissipating kinetic energy, it also slowly wears the grid away. Since the grids are an elaborate set of mesh so as to accelerate the ions without loss of efficiency due to sheath effects, sputtering over the duration of a typical mission (thousands of hours in some cases) will result in the creation of large holes in the mesh due to the breakage of strands [1, 4, 14, and 62]. As the mesh is eroded, the system becomes less efficient. Erosion of the electron gun used for charge neutralisation is another source of wear, which needs to be taken into account during the design process [1, 4, 14, and 62].

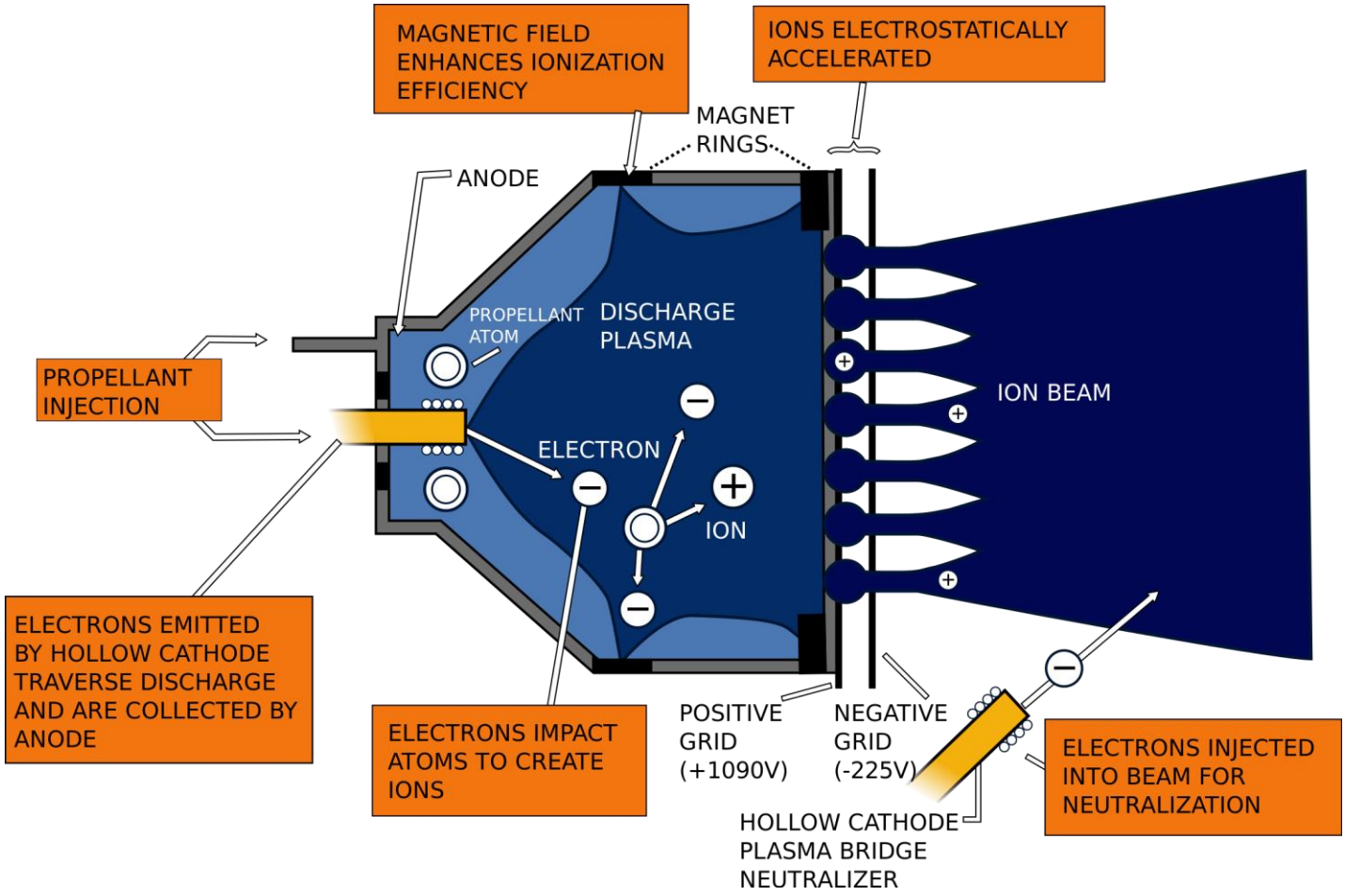

Figure 1.1: Diagram of the gridded ion thruster used on Deep Space 1.

This image was taken from NASA Glenn Research Centre's page on the development of NSTAR ion propulsion systems, at http://www.nasa.gov/centers/glenn/technology/Ion_Propulsion1.html and is thus public domain.

1.2.3 Electromagnetic Propulsion Technologies

This family of propulsion systems use the combined effects of electric and magnetic fields to ionise propellant and accelerate the resultant plasma, often achieving higher ionisation rates, plasma densities and thrust levels than electrothermal and electrostatic systems. This group includes Hall Effect, pulsed plasma and magnetoplasmadynamic thrusters.

Hall Effect Thrusters (HETs) operate by establishing an axial electrical field and a radial magnetic field across a cylindrical discharge chamber, one end of which is the open rocket nozzle as shown in figure 1.2 [1]. Electrons are injected from an external cathode and are trapped by the magnetic field. Neutral propellant gas, commonly xenon, is then injected into the discharge chamber. The gas atoms are then ionised by interaction with the trapped electrons, but since the ions are so much more massive than the electrons, they are essentially unaffected by the magnetic field and so escape by being accelerated down the length of the discharge chamber by the axial electric field. Since the entire system is maintained in a state of quasi-neutrality, there are no space charge effects present to hinder ion motion inside the discharge chamber. The electrons will gradually drift to the anode, but are hindered by the magnetic field, causing sufficient impedance to stop the circuit from shorting [1, 62]. Engines of this type have successfully operated for hundreds of hours of constant use, producing moderate thrusts, measurable in Newtons, with specific impulses of approximately 1200-1600s. However, since the exhaust plasma is primarily composed of ions, a charge-neutralisation device such as an electron gun is needed to maintain spacecraft charge balance.

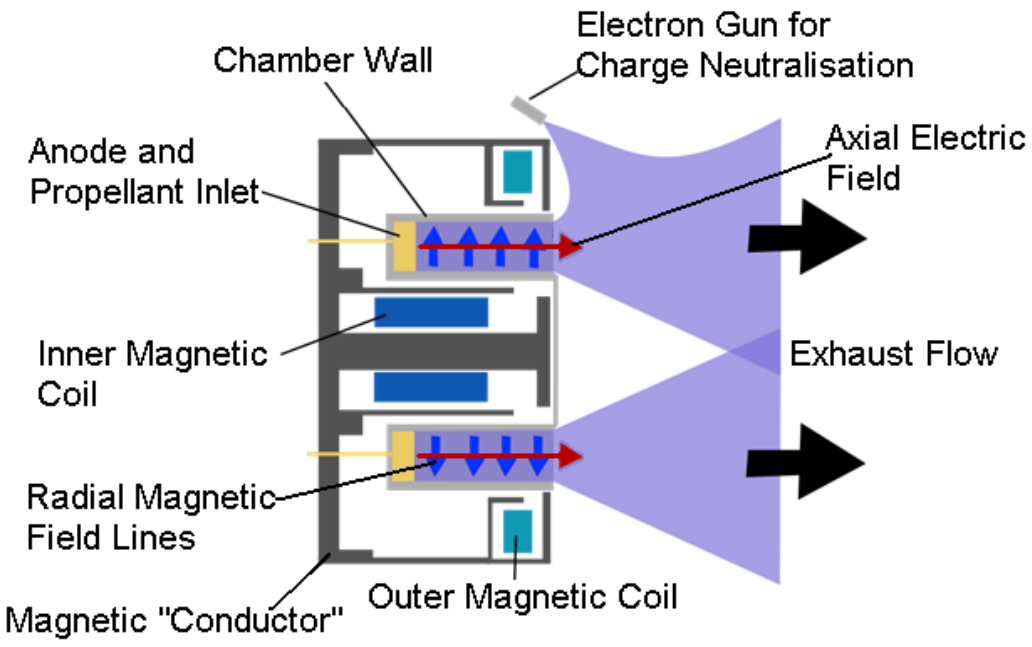

Figure 1.2: A Hall Effect Thruster in cross section along its thrust axis.

This diagram is modified for clarity from one in the public domain at https://commons.wikimedia.org/wiki/File:Wfm_hall_thruster.svg

Pulsed Plasma Thrusters (PPTs) ablate and ionise a proportion of the propellant feedstock, often a solid polymer such as Teflon, by creating an arc discharge sheet across the face of the propellant cylinder using a discharging capacitor [1]. The plasma that is created responds to the electric field of the arc and its own self-induced magnetic field, causing it to accelerate down the discharge chamber, resulting in moderate thrust. The propellant feedstock is generally a rod of solid material that is advanced by a spring, which is a simple and robust design that has seen use since the Zond 2 probe launched by the Soviet Union in 1964 [9]. This system is far more robust and reliable as it does not require the precision valves and pressure regulators required to admit the precise rate of cryogenic liquid propellant for Hall Effect thrusters and gridded ion thrusters. The main drawback of a PPT system is the low melting point of the polymer propellant; the heat generated during arcing causes evaporation of the propellant between arc pulses, which expends fuel with only marginal thrust produced.

Magnetoplasmadynamic thrusters (MPDTs) often use similar electrode geometries as arcjets, being long, concentric cylindrical anode-cathode pairs, and also use an electrical arc discharge to generate their plasma. The main differences here are that there is more gas present and that the

arc is of higher energy. Hence more of the propellant gas is ionised, creating a significant magnetic field by the motion of the plasma itself. The coupling of these various fields cause the plasma to be accelerated to high velocities as it streams down the discharge chamber, while the self-induced magnetic field constricts the plasma into a relatively narrow beam. The net result is very high exhaust velocities at low heat loss, resulting in specific impulses of 3000-4500s, at the cost of very high power usage – often measured in hundreds of kilowatts [2, 10, 14, and 62]. There exist some experimental devices in this family, such as the variable specific impulse magnetoplasmadynamic rocket (VASIMR) magnetic bottle technologies and more exotic plasmoid fusion devices, but these are far from commercial viability.

Electrodeless electromagnetic thrusters such as the helicon double layer thruster (HDLT) are also in the pre-commercial stage [11]. These systems utilise radio frequency resonance to ionise gaseous propellant inside a hollow cylindrical discharge chamber while accelerating the plasma using a divergent magnetic field. The field accelerates the electrons in the plasma, which causes the ions to flow with them, thereby maintaining quasineutrality. HDLTs therefore have a neutral exhaust without requiring an electron source for charge neutralisation, but have a low ionisation fraction in the exhaust and share the same drawbacks as other propulsion systems that also use a cryogenic gas as fuel.

Table 1.1 compares the various technologies used in flight rated thruster systems and MPDTs. Hollow cathode thrusters [12] and cathodic arc thrusters are not included in this table due to these technologies not yet having a testbed system rated for sustained use or data from flight testing.

Thruster type	I_{sp} (s)	Jet Power Efficiency (%)	Thrust to Power ratio (µN/W)	Typical Thrust Range (mN)	Benefits	Drawbacks
Arcjet	450-1500 [1]	30-35 [1]	100-140 [1]	50-5000 [1]	Simple, Flight-Rated, Robust	Inefficient
Resistojet	150-700 [1]	90-130 [1]	700-900 [1]	5-500 [1]	Simple, Flight-Rated, Robust, uses hypergolic reaction mass	Inefficient
FEEP	4000-6000 [13]	90 [13]	10-16 [13]	0.01-0.1 [13]	High $I_{sp,}$ Flight-Rated	Reactive propellant
Gridded Ion	2400-9000 [2, 4]	55-80 [2]	20-40 [2, 4, 5]	8-600 [2, 4]	High thrust, high efficiency, Flight-Rated	Gaseous propellant, needs charge neutralisation
Hall Effect	1100-1750 [2]	45-55 [2]	50-60 [2]	80-300 [2]	High thrust, high efficiency, Flight-Rated	Gaseous propellant, needs charge neutralisation
HDLT	2600-2900 [11]	12-15 [11]	10 [11]	10-20 [11]	Neutral exhaust	Low efficiency, gaseous propellant, not flight rated
PPT	300-5000 [14]	8-10 [1, 14]	12.3 [15]	.1-1 [15]	Simple, Flight-Rated, Robust,	Propellant prone to melting
MPDT	3000-5000 [10, 16]	40-80 [14, 16]	10-25 [1, 16]	100-5000 [1, 16]	High Thrust, High I_{sp}	High power needed to run (200kW)

Table 1.1: A comparison of various existing electric thruster technologies.

1.3 Pulsed Cathodic Arc Thrusters

All of the gas fuelled electric propulsion technologies suffer from the same design challenges, namely the added mass from propellant tanks and piping as well as the mechanical failure modes inherent in valves and pressure regulators. PPTs, being solid fuelled, do not face the same challenges but suffer from propellant evaporation due to waste heat produced during operation. PCA thrusters would not face any of these challenges; they are solid fuelled (no tanks, pipes,

valves or regulators) and they are fuelled by metals which typically have a much higher melting point than Teflon.

Some work has been done on the use of pulsed cathodic arcs as spacecraft thrusters, though as yet none are flight-rated [17-23]. Work by Polk et al [19] derived numerous theoretical performance metrics, though many of these can be shown to have flaws as their analysis relies on erosion rates measured in arcs operated with parameters outside the optimum range for a thruster [21]. This work also made the assumptions that the plasma is fully ionised and that the ion current comprises 10% of the total current; while these assumptions are good for most arc applications, they are not valid for all materials under all conditions [24-7]. The work done by Keidar et al [17, 23] has shown that the miniaturisation of PCA thrusters is achievable, and that they can indeed be used for microsatellite applications. Work by Schein et al [18] only investigated titanium and tungsten as potential fuels. Ti and W are common materials for PCA studies and are well characterised [28-31]. Tungsten is likely to be a good choice as it is known that the energy of W ions can reach 200eV and equation 1.6 suggests that massive ions with high mean charge states are most efficient [17]. The high ion velocity of magnesium cited by Yushkov et al [32] would suggest Mg also as an interesting fuel to test, given the dependence of rocket performance on exhaust velocity in equations 1.1 to 1.4. A thorough study of fuel types is therefore necessary in order to determine the best candidates for testing PCA thrusters for various mission types.

There has also been little exploration of the parameter space in terms of arc duration and arc current; the former is limited by the cathode spot motion dynamics of the edge-triggered systems that have been employed in all previous thruster studies [23, 32]. As for the latter, due to their convex erosion profile (see chapter 2.1.1 for more detail), cathodes in edge-triggered systems are typically small and the current is typically kept below a few hundred amps. Given that the designs used by Keidar, Schein and their collaborators are all edge-triggered, they were unable to explore the higher efficiencies in terms of cathode usage and plasma directionality possible with centre-triggered systems [30, 31]. It is therefore clear that testing a broad range of potential fuels in a centre-triggered PCA system across a range of arc durations and currents would add significantly to the existing knowledge base.

1.4 Motivation for This Study

There are disadvantages to all of the existing thruster systems that use a gaseous fuel. The pressurised tank, piping, valves and pressure regulator systems add mass to the spacecraft that could be given over to payload, as well as introducing manufacturing challenges and failure modes. These drawbacks could be eliminated if a reliable solid fuelled electromagnetic thruster were demonstrated. PPTs utilise a solid fuel and are reliable, but have problems with cathode evaporation between plasma pulses; this leads to much lower system efficiencies for PPTs when compared to other technologies, as well as lower total thrust. The solid fuel used by a pulsed cathodic arc thruster would not suffer from cathode evaporation between plasma pulses. While some work has been done on using edge-triggered arcs as microsatellite thrusters, these systems are far less efficient than an equivalent sized centre-triggered system. The work of this thesis investigates the potential of centre-triggered cathodic arc thrusters to revolutionise space travel by reducing the mass and time required for orbital manoeuvres. The next chapter contains a discussion of cathodic arc physics with reference to their use as a propulsion system, before the third chapter describes the apparatus and method used in this work. Chapter 4 describes the selection rubric for identifying cathode materials, while chapters 5 and 6 contain the results of the experiments undertaken; this data is then used to derive the efficiency metrics described earlier, the numerical values of which are shown in chapter 7. Chapter 8 discusses the various results with reference to current thruster technologies before addressing potential avenues for future work.

2 Cathodic Arc Physics Relevant to Thrusters

Many aspects of Pulsed cathodic arc (PCA) phenomena are still imperfectly understood after years of research. This section outlines the current understanding of pulsed cathodic arcs, including a short discussion on the workings of a typical PCA system.

2.1 Pulsed Cathodic Arc Description

PCA systems work on principles similar to those of arc-welding. When the arc discharge is struck, either by moving the cathode close to the anode (as in welding, where the welding rod acts as the cathode) or by triggering the arc by one of several methods, plasma flows along electric field lines in order to complete the circuit. The plasma consists of ions, electrons and neutral vapour ablated from the cathode. The main differences are that arc-welding is carried out at constant current, while PCA systems operate in pulses of very short duration, and that PCA devices are operated in vacuum.

2.1.1 Triggering methods

In order to create a conducting path between anode and cathode to sustain a discharge the arc must be triggered. As the background pressure in the chamber is below 10^{-5} mbar, there is insufficient gas present to ignite the discharge by the Paschen and Townsend processes. Therefore, ablation of the cathode is necessary to create the plasma to carry the current between cathode and anode. Triggering methods in addition to the high voltage trigger illustrated in Fig 2.1 include laser and mechanical triggering methods [33]. Laser triggers ablate and ionise a small amount of cathode material to create a conducting path between cathode and anode, which can carry the current needed to sustain the arc. A mechanical trigger uses a length of conducting material for this purpose. That is to say, a wire connected to the anode is moved to touch the cathode, then withdrawn, creating an arc. Electrical triggers utilise a short duration, high current surface flash-over across an insulating barrier between a trigger-wire and the face of the cathode. The trigger-wire and insulating spacer can be located anywhere on the face of the cathode, but the two main types are centre-triggering and edge-triggering.

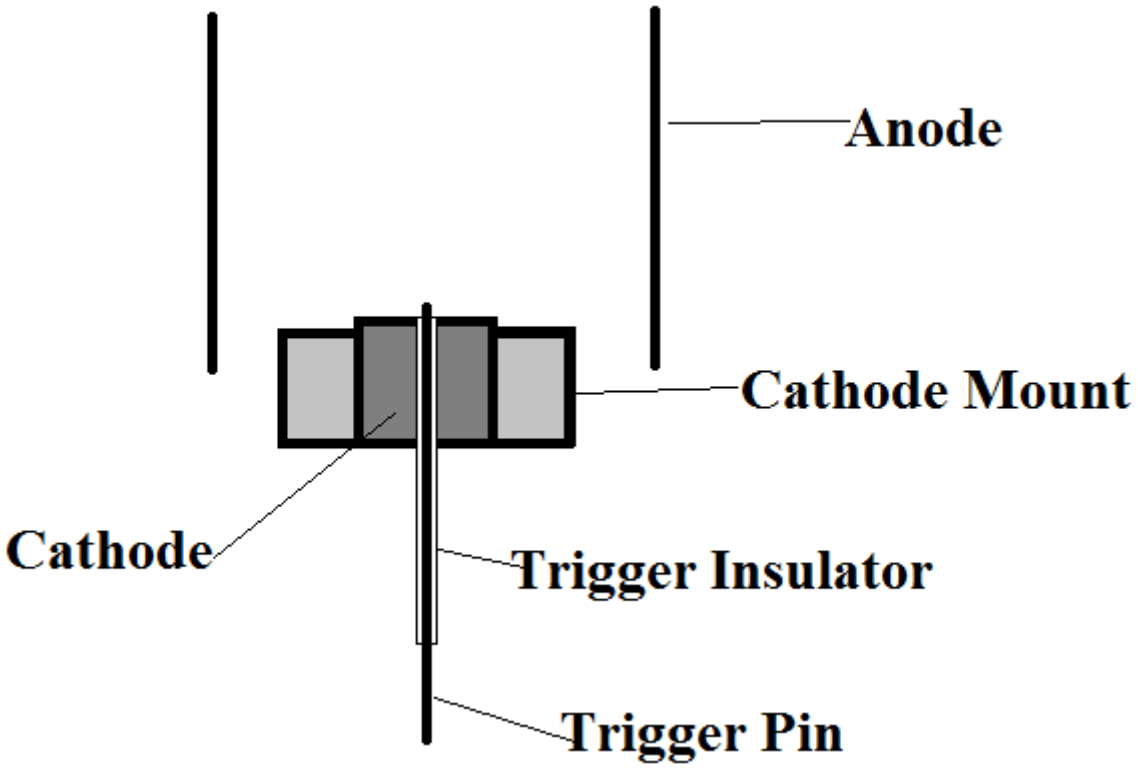

Figure 2.1: Schematic diagram of the centre-triggered high current pulsed cathodic system used in this work.

Laser triggering methods are attractive in that they can be used to start the arc at an arbitrary location on the cathode surface. However, the laser aperture must have a line of sight to the cathode surface and be within the vacuum chamber for maximum efficiency. Over time there will be deposition of cathode material on the laser aperture, eventually rendering it opaque. It is therefore necessary to either clean the aperture, or sacrifice some laser power by using mirrors to reflect the laser beam onto the cathode surface.

Mechanical methods use a sharp conductive element which is moved to touch the cathode. This system has a similar benefit to the laser triggering method, since the arc can be triggered at any point on the surface of the cathode. However, this system requires the use of moving mechanical components, which will wear out or be coated with deposited cathode material, leading to system failure over time.

Electrical triggering methods use a pulse of high voltage, typically kilovolts, over distances of millimetres to create electrical breakdown conditions over the face of an insulating material.

These arcs create the intense electric fields necessary for the creation of cathode spots, leading to the creation of plasma [34]. Plasma production is maintained by the potential difference between cathode and anode. The cathode spots move along the cathode surface, ejecting ionised material at high velocity in a narrow cone directed normal to the cathode surface [28, 29]. Electrical triggering methods are appealing in that there are no moving parts, they are robust and have a repetition rate limited only by the power supply used to drive them.

In centre-triggered electrical triggering systems the trigger is commonly a wire of tungsten sheathed in an insulating ceramic tube, with the end protruding as shown in figure 2.1, while edge-triggering systems use an annular (ring-shaped) trigger surrounding an annular insulator that contains the cylindrical cathode. The trigger element, whether a pin or ring, is rapidly charged and an electric field strong enough to cause breakdown across the surface of the insulator between the trigger and cathode is created. Dense electrical arcs travel down these breakdown paths to the cathode, causing localised plasma generation to occur. This plasma initiates a high current discharge on the cathode surface, which is driven by a low impedance power supply capable of delivering currents ranging from tens to thousands of amperes for short periods of time. The trigger pulse is commonly only a few microseconds long and is of very low current as it only exists to close the "switch" needed to fire the arc by creating a low impedance pathway from cathode to anode.

The plasma in the arc originates from several localised discharge sites known as cathode spots. Dense plasma is formed from the material ejected from the cathode spots. In a centre-triggered system, the spots travel radially outwards from the trigger site, following a dendritic pattern, that is, a semi-random walk with branches that resemble tree branches as they radiate from the trunk [35]. This radial motion is driven by repulsion arising from the phenomenon of retrograde JxB motion [35]. The repulsion of cathode spots is opposite to the expected attraction of two parallel currents. A similar repulsion effect is observed in edge-triggered systems, but since the cathode spots are created on the edge of the cathode the spots skitter around the edges of the cathode, only rarely moving towards the centre [30]. Though the spot motion appears macroscopically smooth, it is a result of individual spots extinguishing and new spots igniting at the edge of the crater created by the previous spot [28]. The motion is therefore subject to discontinuities and jumps [35], and the pattern as a whole is illustrated in figure 2.2.

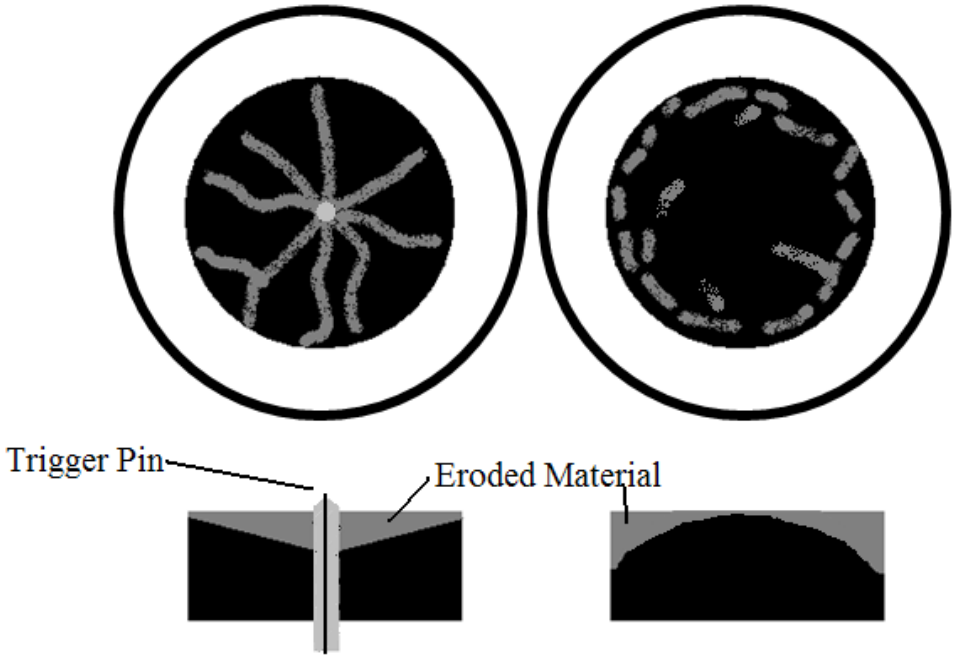

Figure 2.2: Cathode spot migration (upper diagrams) and erosion profiles (lower diagrams) for centre-triggered (left) and edge-triggered (right) arcs.

Since the plasma plume is directed normal to the local cathode surface [28], thrust is optimised by ensuring that the erosion profile is as flat as possible. A centre-triggered system has the advantage that the slope of the eroded zone can be adjusted by tuning the magnitude of the arc current as a function of the radial position of the spots during each pulse [36]. The retrograde motion of cathode spots causes the cathode spots in edge-triggered systems to remain at the edge of the cathode, leading to the undesirable convex erosion profile. This profile leads to a reduction of plasma transport parallel to the axis of the system and hence loss of thrust after extended use [30]. While the wear patterns created during the use of a centre-triggered cathodic arc would also result in lowered efficiency compared to a non-eroded cathode surface, the concave erosion would result in a smaller drop in performance which can be mitigated by appropriate pulse shaping [36]. Therefore, a centre-triggered pulsed cathodic arc using electrical flashover triggering techniques was used in this experiment.

2.1.2 The Properties of a Cathodic arc Plasma

The conditions to be found within each cathode spot are quite extreme, with very high localised electric field, small pits of boiling metal and dense plasma generation [28, 29, 34, 37-9]. The

plasma expands in a cone normal to the cathode surface from each cathode spot, with the spatial plasma distribution being conical, with an approximately cosinusoidal angular distribution [28]. That is, the plasma is primarily ejected normal to the plane of the cathode surface, with smaller quantities being ejected at angles further from the normal direction [38-9]. Magnetic fields can focus the plasma so that a higher proportion of the plasma plume is normally directed and this phenomenon can be used to further enhance the thrust [11, 23, and 40].

The plasma is a good conductor and it must form an electrical connection to the anode to allow the discharge to be sustained for the duration of the pulse. Under laboratory conditions, the bulk of the plasma current is carried by electrons since they are more mobile than ions. In order to satisfy the requirement that the plasma be quasineutral, there must also be ions in the plasma with a spatial density comparable to electrons; due to the higher mobility of electrons, there will be a current imbalance, however [17-19]. Literature indicates that ion current is in the range of 8-12% of total arc current [18], with many publications assuming an average of 10% [17-19, 23, 28]. Ions that impact the anode do not contribute to thrust, which is generated only by those ions that exit the anode mouth; electrons contribute negligibly to thrust, since they have approximately one twenty-four-thousandth of the mass of one carbon atom. Therefore, it is necessary to design the anode to maximise the escape of the ion stream while still ensuring a satisfactory electrical connection between anode and cathode; previous work has shown that a cylinder coaxial with the cathode is a good choice [22].

The difference between the current through the cathode and that collected at the anode is a measure of the plasma available to produce thrust. The difference between these two currents is termed the Net Ejected Current (NEC), and it is a measure of how much plasma is flowing out of the anode mouth and into the vacuum chamber. The salient point here is that a high NEC indicates that a large degree of material is escaping, and thus generating thrust, while a low NEC suggests that most of the material is travelling directly to the anode, impacting there and thus generating little net force. Integration of the NEC over the duration of the pulse determines the Net Ejected Charge (NEQ). Simply put, it is contended that NEQ should correlate strongly with the impulse delivered by a PCA thruster.

After the arc has been initiated, the cathode spots will migrate to the edge of the cathode face due to the repulsive force between cathode spots. If the arc is not stopped when the cathode spots reach the edge of the cathode face they will move onto the side of the cathode. Since the plasma would then be projected normal to the cathode sides, it would move straight to the anode wall, rather than exiting the anode mouth. This phenomenon is termed "side-arcing" and can result in major losses in efficiency. The evolution of the cathode spot locations and the transition to side arcing is shown in cross section in figure 2.3.

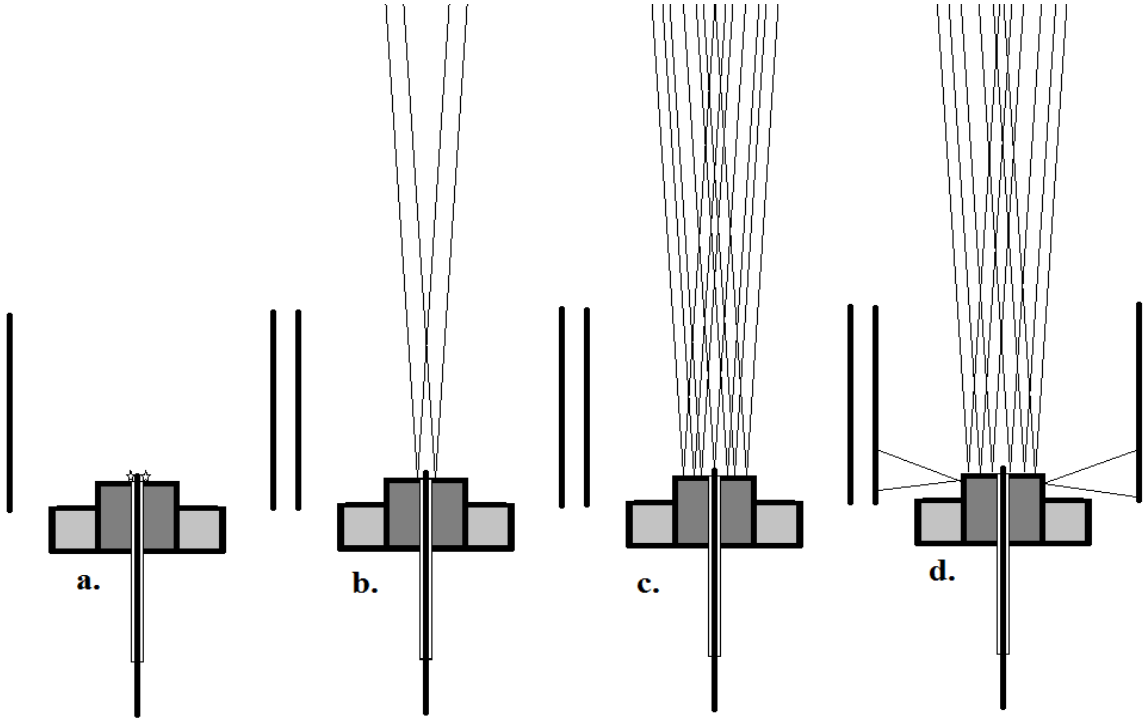

Figure 2.3: Cathode spot motion and arc evolution. Commencing with triggering (a), normal operation (b and c) and a transition to side-arcing (d).

Figure 2.3 shows the cathode spot motion and arc evolution from triggering to side-arcing. The arc has just been triggered in figure 2.3a; there is a potential difference of 50-400V between cathode and anode and a flashover between the cathode and trigger pin due to a potential difference of approximately 1200V, but no significant plasma production as yet. After the arc has been triggered and electron current between cathode and anode is sustained, the creation of cathode spots occurs close to the trigger location as shown in figure 2.3b [28-9]. These spots repel each other and are forced outwards as they erode cathode material to form the arc plasma as shown in figure 2.3c. Figure 2.3d shows side-arcing; if the arc is not halted by grounding the power supply at the correct time, then the cathode spots will continue to push each other

outwards, causing them to cross over the edge of the cathode's front face and commence eroding material from the side of the cathode directly to the anode.

While the plasma has a high degree of ionisation (often ~90% or higher) and a mean ion charge state often greater than +1, not all the material ejected is electrically charged [19, 24-7]. Neutral vapour evaporates from the cathode spots and their associated erosion sites, with low melting point metals such as bismuth being particularly prone. Micron scale droplets are also ejected during arc operation, with these macroparticles moving at tens of metres per second. The production of such neutral species is a source of inefficiency in any thruster application, as they take energy to produce and erode the cathode without producing thrust efficiently. It is therefore clear that production of neutral species ought to be minimised.

Any PCA thruster would need to operate for hours to affect any orbital transfer manoeuvre, and be able to commence operations after dormant periods of days to months in the case of orbital station-keeping or course correction manoeuvres. This would require that the arc be able to operate reliably for extended periods of time, with many thousands of pulses triggered reliably. While extended cathode lifetimes have not been a major facet of research in centre-triggered arcs, it is known that reliable triggering can occur over several hundred thousand pulses on the one cathode [36]. Methods of advancing the eroding cathode to ensure optimal cathode firings are not part of the work of this thesis, but other groups have used springs [23] and mechanical actuators [41, 42] to advance edge-triggered cathodes and it is believed that such systems could be generalised.

2.2 Modelling the Arc Using Kirchhoff's Law

Figure 2.4 shows a simplified circuit diagram of the thruster system with ion and electron flows indicated. A more complete schematic of the circuit used, including the trigger system, can be found in figure 3.9. This model of the arc uses Kirchhoff's Current Law, which states that the sum of the currents entering a circuit junction must be equal to the sum of the currents leaving that junction, to discuss current flow with reference to thruster applications [61].

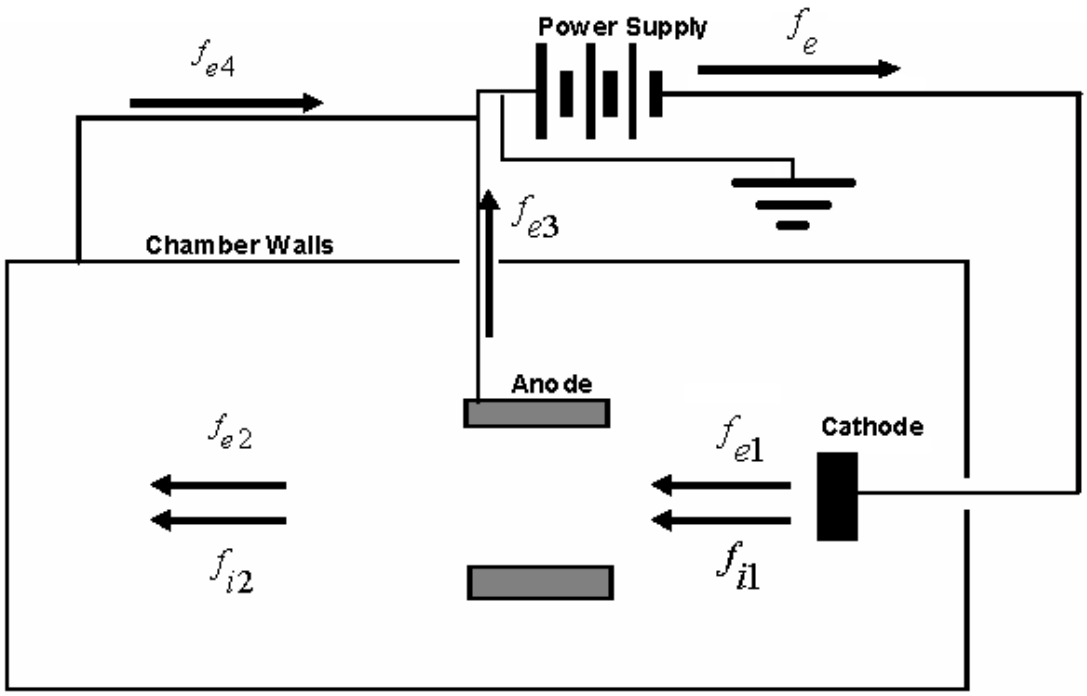

Figure 2.4: A circuit diagram of the arc system in operation, showing particle flows.

Where particle flows are given as *f*, the subscript *i* denotes ion flow and *e* denotes electron flow. Conversion to currents is achieved by multiplying the flows by the charge of the particles they represent, being $\bar{q}$for the average ion charge state and *e* for the electronic charge. An application of Kirchhoff's Current Law gives the following instantaneous equations at a given time;

$$ef_e + \bar{q}_1 f_{i1} = ef_{e1} \tag{2.1}$$

Equation 2.1 applies to the currents flowing through the cathode, namely the electron current from the power supply (ef_e), and the ion ($\bar{q}f_{i1}$) and electron (ef_{e1}) currents leaving the cathode in the plasma. Equation 2.2 applies to the anode, with terms defined as before. Equation 2.3 is the return node equation, as it shows that the sum of the return currents must equal the cathode current.

$$ef_{e1} + \bar{q}_2 f_{i2} = ef_{e3} + ef_{e2} + \bar{q}_1 f_{i1} \tag{2.2}$$

$$ef_e = ef_{e4} + ef_{e3} \tag{2.3}$$

$$ef_{e4} + \bar{q}_2 f_{i2} = ef_{e2} + I_{walls} \tag{2.4}$$

Equation 2.4 describes the collection of ejected plasma by the chamber walls, and its return to the main circuit. The circuit diagram is drawn to represent the laboratory system, but is equally applicable to a spacecraft by generalizing the chamber walls to include the spacecraft skin. I_{walls} represents the charging current that flows to modify the potential of the spacecraft skin. The potential of the spacecraft skin will eventually reach equilibrium, where I_{walls} integrates to zero over each cycle. I_{walls} is necessary to describe the current drawn from space plasma [43], as this can be large and depends on spacecraft orientation, velocity and orbital parameters.

To maximise thrust, the output ion flow f_{i2} must be maximised. Hence, f_{e2} must scale with f_{i2} to maintain quasi-neutrality. This is due to the higher mobility of the electrons, and previous work has found the electron current in laboratory plasmas to be approximately 10 times greater than the ion current [19]. However, for stable operation of the arc there must be a sufficiently large anode flow f_{e3}. Thus, the input electron flow, f_{e1} must be much larger than the output electron flow, f_{e2}, and in order to achieve this there must be a low impedance pathway from the cathode to the anode. If such a pathway does not exist, a high "burning voltage" between the anode and cathode combined with a low anode current should be observed.

Equation 2.2 is not complete as it does not contain any separate terms for ion recombination, ions captured by the anode or plasma deposition on the structures of the spacecraft. Plasma deposition is important for spacecraft applications because it reduces the thrust generated by the system. This problem is particularly prevalent when side-arcing is present [21].

Since the net ejected particle flow from a cathodic arc consists of more electrons than ions the craft will charge positive with respect to the local plasma potential and will attract more electrons from space [17]. The ejected ion flow f_{i2} will not be attracted back to the surface of the spacecraft, thus eliminating the need for electron guns. To clarify, this means that no charge neutralisation system is needed for this system, as a volumetrically quasineutral plasma stream is ejected, carrying net negative charge. This is in contrast to Hall Effect and gridded ion thrusters

which require an electron gun to prevent the attraction of the ions back onto the spacecraft, since these thrusters would expel net positive charge if the exhaust stream was left un-neutralised.

It is much easier to collect electrons from space plasma than ions [44]. A spacecraft in orbit will be moving subsonically with respect to the electrons, and so will collect negative charge over its entire surface, whereas the craft is supersonic with respect to the ions, and so only collects ions with its frontal area. That is, the only ions that are collected are those that the spacecraft collides with during its motion through space, which is termed the "ram current" [43, 44]. The higher electron current collected from the space plasma facilitates the rapid establishment of charge equilibrium, which can reduce the potential of destructive arcing.

2.3 Summary of Relevant Arc Physics

A centre-triggered pulsed cathodic arc has the potential to be an effective thruster system, due to its demonstrated reliability and high exhaust plasma drift velocity. It also generates an exhaust plume that is negatively charged. A pulsed arc will therefore not require charge neutralisation systems such as are needed for Hall Effect thrusters or gridded ion thrusters. The solid fuel eliminates the need for pressurised tanks, valves, regulators or other fluid transfer devices. Almost all of the materials that can be used in a PCA thruster have a higher melting point than Teflon, which overcomes the main drawback of PPT systems. It is therefore clear that a PCA system ought to be tested for efficiency and reliability, and the next section describes the apparatus and methodology used to test the system performance and efficiency.

3 Apparatus and Methodology

This chapter describes the equipment used, including the power supply, measurement devices and vacuum chamber, before describing the manner in which they were employed.

3.1 Ballistic Pendulum for Impulse Measurement

Since a pulsed cathodic arc generates dense and rapidly changing electromagnetic flux, a ballistic pendulum was used to measure momentum rather than an electronic load cell. The rapidly changing electromagnetic fields present in the plasma discharge would induce currents in electronic components, creating noise that could mask the signal of a load cell [45]. Instead, momentum transfer was determined by measuring the velocity and mass of a pendulum which is struck by the plasma. The pendulum mass was determined by weighing before and after the data run, while the velocity was measured using a laser beam being blocked by a periodic opacity grid. This grid was a series of lines of black ink, printed onto a small plate of thin overhead transparency film at regular intervals of 1.7mm. Laser light was shone onto the grid with transmitted light being imaged onto a photodiode by mirrors. The photodiode was part of the circuit shown in figure 3.6, with the light intensity being measured as a voltage by a Digital Storage Oscilloscope (DSO) triggered by the same signal as the arc trigger power supply. Variations in light intensity caused by the lines on the grid occluding the laser beam as the pendulum swung created repeating features in the photodiode signal, while the known separation in space of the gridlines allowed the determination of the displacement of the pendulum. Examining the DSO trace allowed the determination of the period between two intensity peaks, or troughs, giving the amount of time it took the pendulum to move a given distance. Using these two quantities, the velocity of the pendulum was deduced. Measuring the mass of the pendulum allowed its momentum to be calculated. Knowing the pulse duration allows the average net force experienced by the pendulum to be determined, and thus the metrics described in chapter 1 were derived. The following few sections describe the design of the pendulum, with a diagram and photograph of the final design shown in figure 3.5.

3.1.1 Calculations and Modelling Underpinning the Pendulum

The assumptions made in order to estimate the expected magnitudes of the impulse to be measured are taken from the work done by the author previously published [46]. Assumed values are; a typical Ti ion density n_i of 10^{20} ions.m^{-3} close to the cathode source [46] (it should be noted

that this is a guide value only - plasma density varies with plasma current and distance from the cathode spots); plasma pulse duration Δt of 300μs; and an average ion velocity v_i of 20000m.s^{-1} [18]; a uniform, cylindrical plasma flow from all parts of a cathode 25mm in diameter; composed of pure titanium (atomic mass 47.86).

Based on these assumptions the following order of magnitude estimates can be made about the plasma plume and the momentum it carries:

The length of the plasma plume is approximately

$$h = v_i.\Delta t = 20000 \times 300 \times 10^{-6} = 6.0m \qquad (3.1)$$

and its volume is approximately

$$V = h\pi r^2 = 2.945^{-3} m^3 \qquad (3.2)$$

The number of ions in the plume from a single shot is approximately

$$N_i = Vn_i = 2.209 \times 10^{-3} \times 10^{20} = 2.945 \times 10^{17} \ ions \qquad (3.3)$$

and their mass is

$$M_i = m_i N_i = 47.86 \times 1.67 \times 10^{-27} \times 2.209 \times 10^{17} = 2.354 \times 10^{-8} kg \qquad (3.4)$$

Thus the expected momentum transfer is therefore approximately

$$p_i = M_i v_i = 0.4708mN.s \qquad (3.5)$$

Since the impact happens over microseconds the impact can be treated as an instantaneous impulse, where the momentum is transferred to the pendulum at its rest position. Further, since the mass of plasma deposited during one pulse would be so small compared to the mass of any practical pendulum, it can be neglected for the purposes of these calculations. However, it should be noted that the estimate for n_i is uncertain to more than an order of magnitude due to the fitline used to calculate ion density being exponential in nature. This calculation also does not consider the momentum carried by any electrons, neutral vapour or macroparticles produced by the arc.

The mass of the pendulum determines the final speed attained from the plasma impact. Simple modelling in MatLab has shown that for reasonable mass ranges there is sufficient pendulum motion to measure pendulum velocity, as described previously. In this modelling all losses due to friction and drag are neglected. The curves shown as figures 3.1-3 are generated by the code included as Appendix A, using simple geometric and Newtonian assumptions about the behaviour of the pendulum, with the pendulum treated as a simple pendulum given momentum perpendicular to the support wire at the site of the concentrated mass. The momentum given was equal to that calculated above. Vertical displacement was determined by equating the kinetic energy of the pendulum to the potential energy to be gained by swinging upwards to the maximum height of the pendulum. This value of vertical displacement was used to determine the horizontal displacement of the pendulum and so gave a range for useful pendulum masses.

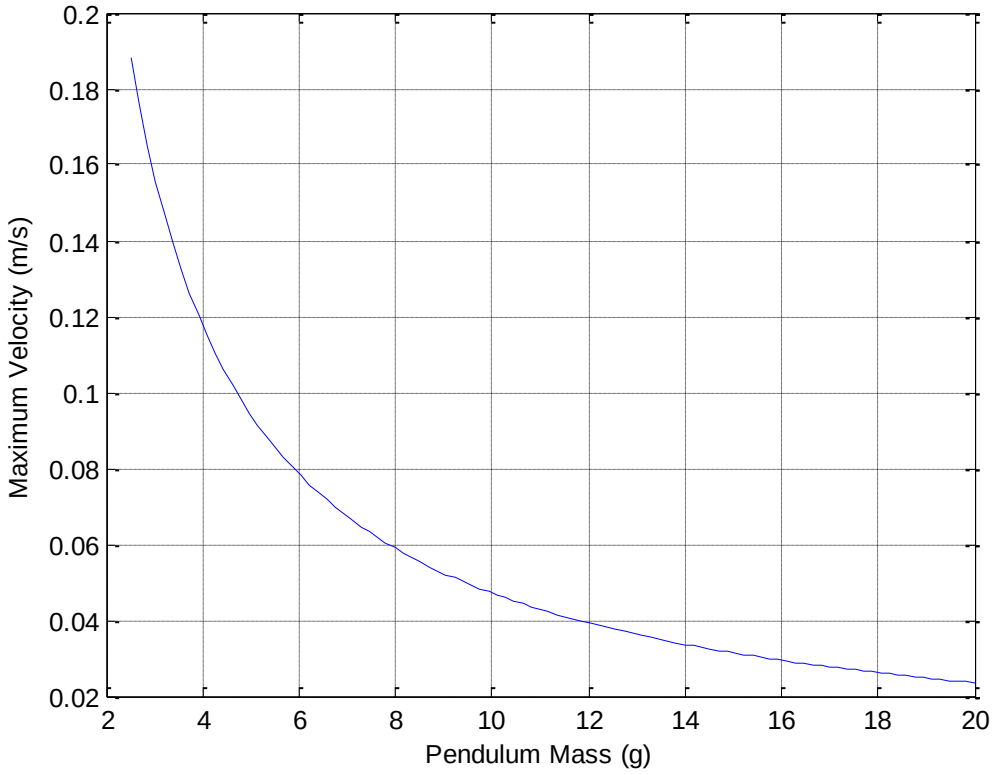

Figure 3.1: Maximum horizontal velocity of the pendulum as a function of pendulum mass.

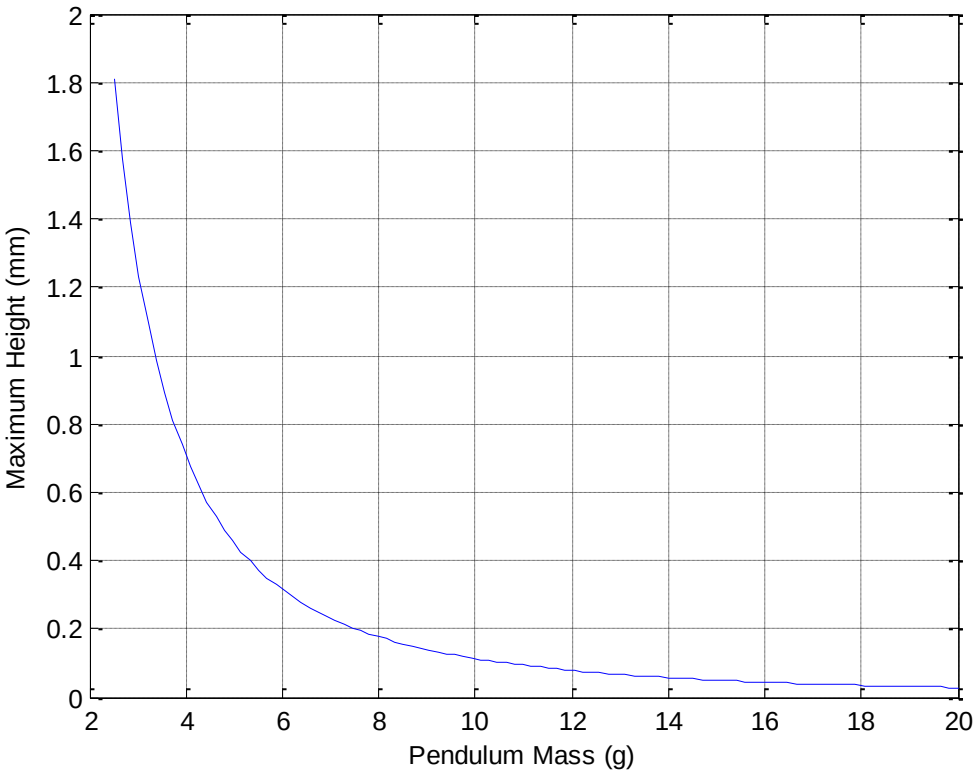

Figure 3.2: Maximum swing height of the pendulum as a function of pendulum mass.

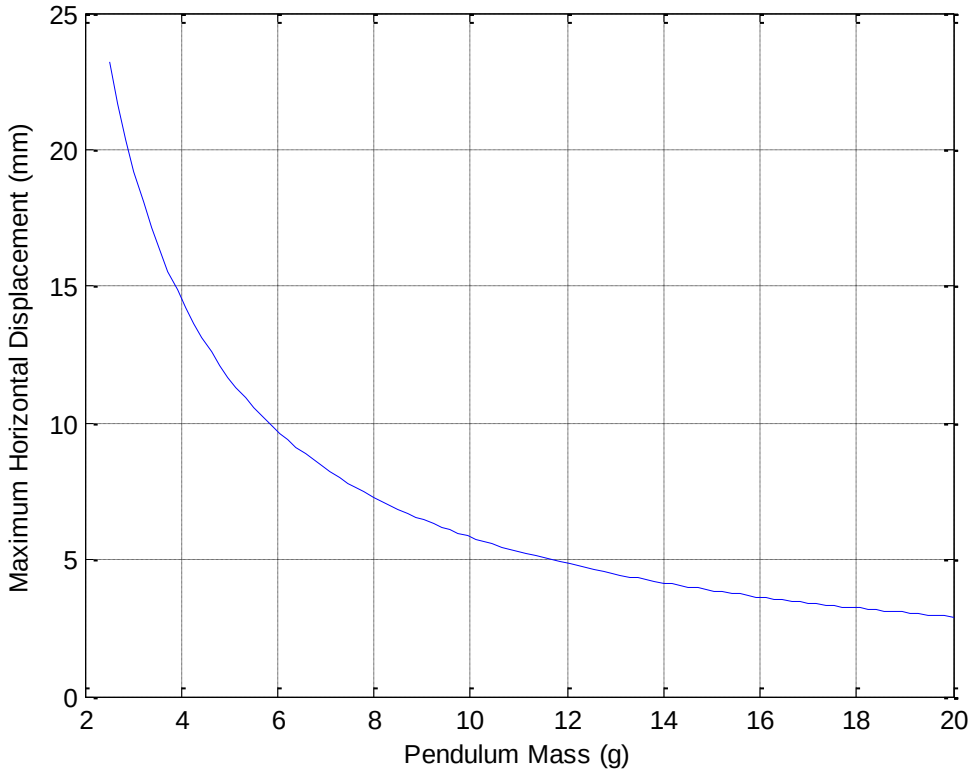

Figure 3.3: Maximum horizontal displacement of the pendulum as a function of pendulum mass.

A total pendulum mass of between 4 and 6g would permit pendulum swings of between 10 and 15mm while being massive enough to be durable and stiff. It was considered that this distance was sufficient for an accurate velocity measurement, though this was tested using proof of concept plates as described in section 3.1.4.

3.1.2 Pendulum Plate

Design criteria for the suspended pendulum place restrictions on mass, frontal area, stiffness, ion sticking coefficient and electrical conductivity. Of prime importance is pendulum mass, which should be as low as possible to maximise sensitivity. Suitable choices of pendulum plate material include polymers such as Mylar and lightweight metals such as aluminium or titanium. While each of these can be obtained in sizes and thicknesses that would minimise mass, plates thin enough to keep the mass low would be too flexible to swing as a rigid body. Flexibility can be overcome by the addition of stiffening ribs to the pendulum plate in a cross-wise manner, so as to restrict the flexural modes of the structure.

A pendulum mass of four to six grams is a good compromise between design and construction requirements, as it is sufficiently light to display significant movement under plasma impact, while being heavy enough to allow the addition of sufficient stiffeners to ensure rigid body motion and to have enough frontal area to collect all plasma generated by the system. A pendulum mass of approximately 5g was chosen as a good operating mass because of the convenient swing amplitude.

In order to measure the ion momentum accurately the frontal area of the pendulum plate ought to be as large as possible. Increasing this area will increase the mass, or decrease the rigidity of the structure if the mass is kept constant. As the plasma plume is narrow and cosinusoidal in angular distribution, the area can be kept to a square with side length about twice the diameter of the cathode, so long as the pendulum is kept close to the anode mouth. Thus mass can be saved without sacrificing too much collection area.

The pendulum plate must be stiff enough to resist torsion under plasma impact and be able to support the grid. Since the grid will weigh less than one gram, supporting it is not a major concern, but ensuring that the pendulum swings rather than twists is crucial. Thin sheets can be made stiffer by the addition of ribs or stringers, being rods of thicker material added to brace the thin sheet [figure 11-45 in reference 1]. These ribs can greatly increase the stiffness of the pendulum plate, allowing broad plates of thin material to behave as though they were thicker from a stiffness perspective, without adding much mass to the pendulum.

Ion sticking coefficients measure the ability of materials to adsorb incoming ions, rather than allowing them to bounce off. If the impacting ion is implanted into an object, then it transfers all of its momentum to that object. However, should the ion rebound elastically, then it would have transferred twice the momentum of the ion. Literature indicates that polymers retain deposited species well [47, 48], with some polymer surfaces retaining more than 95% of metal atoms deposited onto them [49].

Another process which needs to be addressed, and one related to ion sticking, is sputtering, which occurs when energetic ions impact a solid surface and cause some of the surface atoms to be ejected. As has been mentioned previously, reflection from the surface would cause an overestimation of thrust, as would sputtering. The degree of overestimation depends strongly on the exit angle of the sputtered atom and its velocity. In all cases however, the sputtered atoms leave the object from which they are ejected with low velocity relative to the incident ion velocity [50-52] and work done on the angular distribution of material ejected shows that a large amount of sputtered material is ejected at high angles to the incident ion path [53]. It is therefore expected that sputtering will have a negligible contribution to the measurement of thrust and so minimisation of sputtering yield is not considered an important design criterion.

Electrical conductivity is another design criterion, as the conductivity of any object placed in a plasma will affect how it is charged by the plasma. A conductive pendulum, with an uninterrupted ground connection, will draw current from the plasma to earth. This will create large amounts of heat in the pendulum, potentially damaging any fragile parts. If the pendulum is made from an insulating material then little current will flow via any pendulum coatings to

ground. An insulating pendulum would become charged by the plasma, and this charge would create a force between the pendulum and plasma, but this would not affect the measurements due to the pendulum and plasma forming an action reaction pair. Any momentum given to the plasma by the pendulum via electrostatic attraction would be countered by momentum given to the pendulum by the plasma, resulting in no net momentum exchange via pendulum charging. Thus the momentum given to the pendulum would be undisturbed by any insulating pendulum becoming charged. Significant charging would be evident in a shift in the pendulum's rest position due to attraction to other parts of the system. As all metals are conductive, the requirement that the pendulum be insulated removed metals from consideration for use as the pendulum plate.

3.1.3 Suspension Wires

If the pendulum were suspended by a single wire and struck by plasma, then the whole pendulum would twist about this support in addition to swinging unless the plasma impacted in precisely the right fashion. Thus, two wires must be used to support the pendulum. These wires must be thin enough so their beam flexure does not add appreciable damping to the pendulum swing over the short timescales being investigated, while being strong enough to hold the pendulum while swinging. These wires must also be light, so that their mass doesn't move the centroid of the entire pendulum or increase its mass too much, and thin, to minimise friction. Copper was chosen as it is readily available in fine, flexible wire.

3.1.4 Proof of Concept

Experimental tests were performed to ensure the feasibility of the measurement system. The test plates were made of overhead-projector film (cellulose acetate) and thick Mylar. They were suspended by two wires in front of the anode mouth and bombarded with plasma generated by a 31mm diameter Ti cathode. Both plates moved at considerable speed, often hitting the top of the chamber, giving motion through 90 degrees of swing. The mass of the heavier plate was 5.204g, showing that there is more momentum carried by the plasma than previously thought; a 31mm cathode ought to provide only 1.5 times as much momentum as a 25mm cathode, causing ~1.25 only times as much motion rather than having the plate hit the top of the chamber. This implies that the assumptions in 3.1.1 were overly conservative, possibly with respect to ion velocity. These example plates are shown in figure 3.4. Note that the deposition zones are quite narrow,

with the maximum diameter of the central deposition region being approximately 30mm. The central deposition region is more noticeable on the thicker plate (to the right of the ruler), while the thinner plate shows the total deposition range. This demonstrated the practicality of using ballistic pendula to measure the momentum generated by pulsed cathodic arc discharges, and so a final design was settled upon for conducting the experiments in this work.

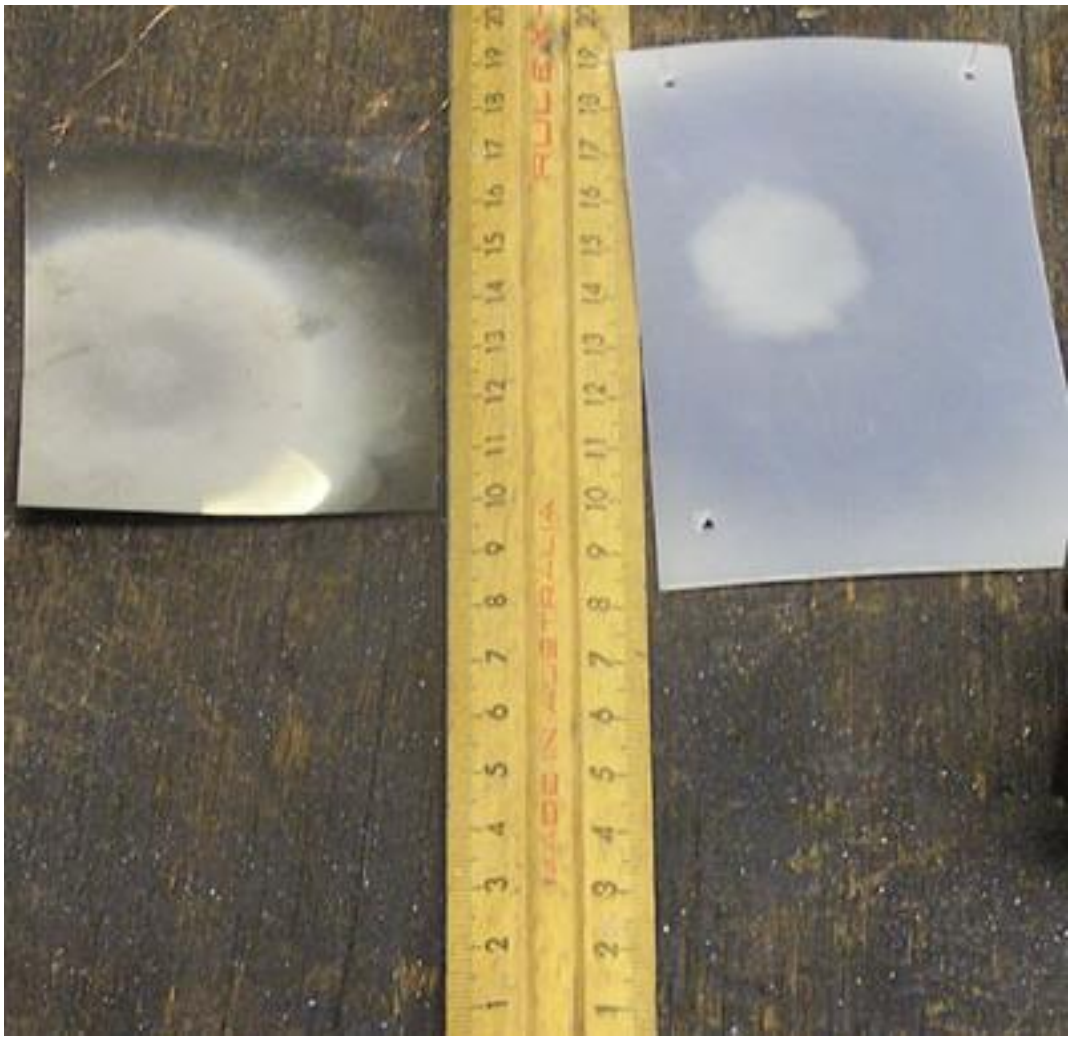

Figure 3.4: Polymer test plates, showing metal deposition.

3.1.5 Final Design

The final design of the pendulum plate was a rectangle of overhead projector film (cellulose acetate), stiffened with narrow bars of thicker Mylar placed crosswise to enhance stiffness. In order to induce a more rigid-body form of rotation, two bars of Mylar extend upward from the pendulum, and thin copper wires bent into loops secured the pendulum to the walls of the vessel. Adhesive cellophane tape was used to construct the pendulum, taking care to place the adhesive

in the correct locations. Care was taken not to place the tape in a location where there is likely to be extensive plasma deposition, as the liberated heat could cause the glue to dissociate and outgas, weakening the structure considerably. Thus, all tape used in constructing the pendulum was placed on the face of the pendulum away from the cathode-anode assembly. Testing has shown no significant change in performance over time, as well as very low friction present in the bearings. A diagram of the ballistic pendulum is shown in figure 3.5, as well as a photograph of one of the pendula constructed. In total two pendula were constructed for this project; the first was successful but had a hole melted through the pendulum plate by overly rapid shot repetition while the other worked and is pictured at the bottom of figure 3.5.

3.1.6 Sources of Uncertainty in Impulse Measurement

The pendulum method of thrust measurement has a number of intrinsic sources of error which will be discussed in the subsections below. The total uncertainty in thrust measurement was estimated to be 2% from these contributions.

3.1.6.1 Construction, Handling and Placement Errors

The pendulum was constructed by hand. While care was taken during manufacture and handling, tolerances will lead to the following potential errors: 1) pendulum geometry, 2) grid geometry, and 3) the contribution of a structure to stop the swinging of the pendulum called the momentum brake. Each of these sources of error will be analysed below to determine their contribution to the total error.

Firstly, the pendulum plate must intersect all the plasma and be perpendicular to the plasma flow. If not, then the plasma momentum will not be fully transferred as linear momentum to the pendulum. This would result in a misrepresentation of the total plasma momentum. Also, if the plasma impact site is located far from the support wires, the entire pendulum can twist. These effects were minimised by locating the pendulum close (~10mm) to the mouth of the anode so that the pendulum plate will intersect all the plasma flow, and so that the orientation of the plate with respect to the plasma flow can be measured. Twisting was minimised by using two support wires separated by a distance greater than the diameter of the plasma flux tube. By taking care to place the pendulum close to the anode mouth and perpendicular to the plasma flow to within 5 degrees, and measuring this with rule and protractor, the estimated uncertainty is 0.5% from positional sources.

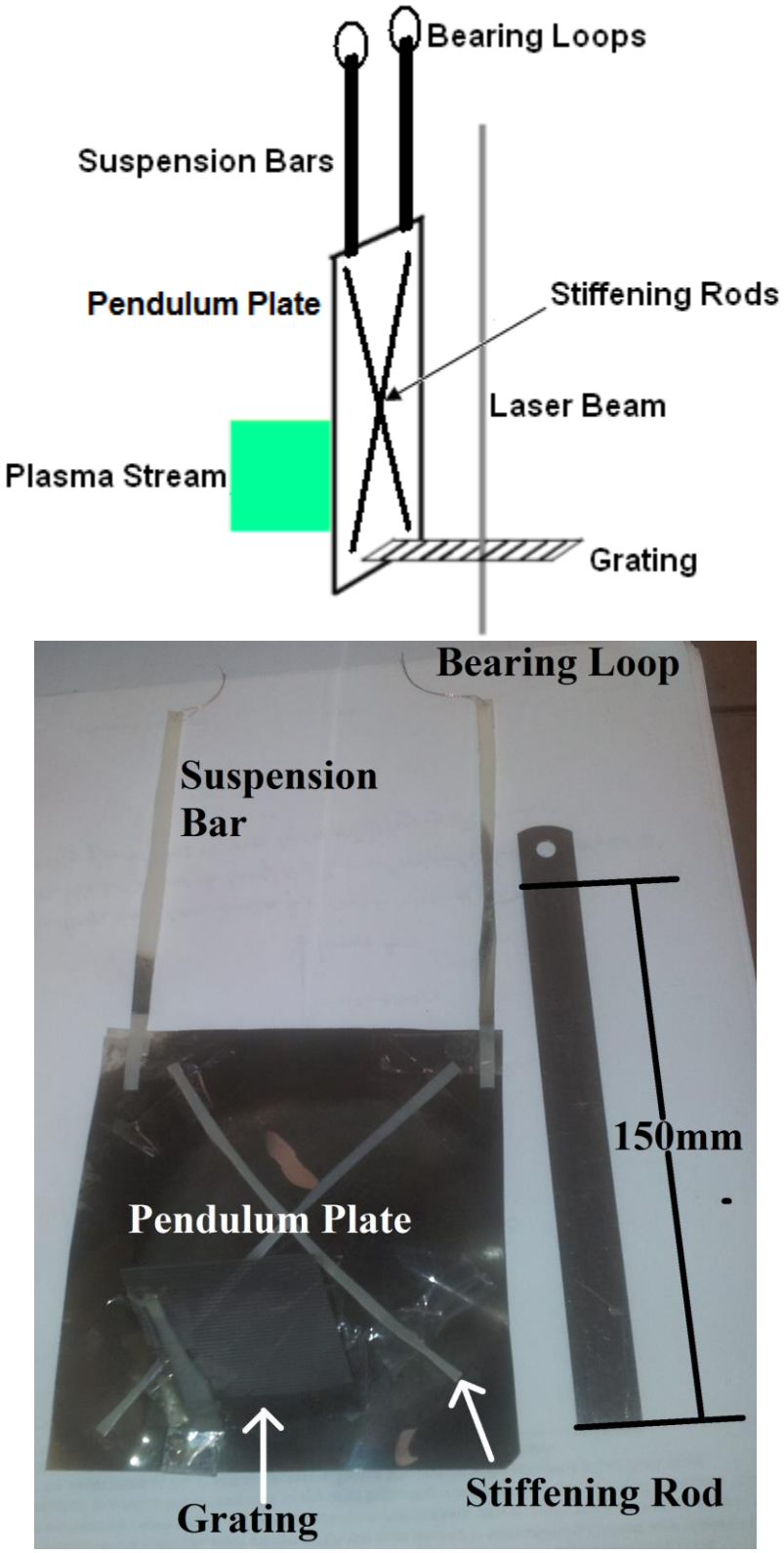

Figure 3.5: A schematic of the pendulum under impact of plasma (top) and a photograph of one of the pendula used (bottom).

The laser detection grid must be placed so that it is parallel to the direction of plasma travel and perpendicular to the laser beam. Thus the small angle approximation can be used, treating the grid as approximately level for short distances away from the "at-rest" vertical position, allowing the features on the DSO trace to be interpreted as representing features at a fixed distance. If the grid is bent or twisted in any fashion, then the apparent feature separation would be larger than the true separation by a factor of $sec(t)cos(d)$, where t is the angle of horizontal twist and d is the angle of grid plane dip. Twist angles result in greater apparent distance between features, while angles of dip (or rise) result in lower apparent distances between features. Typical construction and installation of the grid resulted in angles of dip and twist measured to be less than 10 degrees. Visual inspection with the aid of a protractor was carried out during construction of each pendulum, and revealed errors of no more than 5 degrees. Visual inspection of the pendulum before and after each thrust measurement run revealed no greater deviation than 5 degrees from horizontal for the grid. Thus the total deviation for the grid would be less than 10 degrees from horizontal, with twist angles being kept to below 5 degrees. The maximal error from these sources was estimated to be 1.1%.

A momentum brake had to be added to the system in order to force the system to slow between shots. Otherwise, the pendulum was observed to keep swinging for minutes after a pulse was fired at it. The brake was placed so that it pushed on the pendulum at the pendulum's rest position, disturbing it from rest by less than 5mm. The angle induced by this motion was taken into account when considering position errors, as discussed in the preceding paragraph.

3.1.6.2 Approximations in Data Processing

It is assumed that during the first instants of motion, the pendulum is moving linearly, and so the moment of inertia of the system can be neglected. This is a defensible assumption in that horizontal movement of a few millimetres for a pendulous body with the measurement grid approximately 210mm from the fulcrum results in angles of swing of only a few degrees. Typical placement of the laser beam on the grid would result in measurement being cut off after 20-25mm of pendulum swing, as the pendulum plate would swing into the beam path and scatter the beam. Thus the maximum angle of swing would be less than 8 degrees, making the uncertainty in using a small angle approximation less than 0.25%.

3.1.6.3 Acceleration of Ions in the Plasma Sheath

Another potential source of error is sheath formation. Due to the different velocities of ions and electrons in plasma, a sheath will form around any surface placed in contact with plasma. The sheath forms by having fast moving electrons impact on any object placed in the plasma stream. This causes the body, in this case the pendulum, to become negatively charged with respect to the plasma, causing ions to be accelerated towards the pendulum in order to balance this accumulation in charge. The end result is an equilibrium which is reached when the rate of ion diffusion is balanced by a small current of high energy electrons passing through this sheath. Sheath sizes are typically a few multiples of the Debye length, which is given by equation 3.6.

$$\lambda_D = \sqrt{\frac{\varepsilon_0 kT}{n_0 e^2}} \tag{3.6}$$

Where λ_D is the Debye length, ε_0 is the permittivity of free space, k is Boltzmann's constant, T is the electron temperature, e is the charge on an electron and n_0 is the density of the species present in the bulk plasma, assuming that the plasma is quasi-neutral and that the plasma is singly ionised. The plasma is multiply ionised in this case, but equation 3.6 can be generalised easily. Since the ions are accelerated across this sheath towards the plate, this would lead to an over-estimation of the plasma impulse if the pendulum were fixed, as the ions impact with greater momentum. However, as the plate is able to swing, it is accelerated towards the ions in order to conserve momentum. That is, the ions and the pendulum form an action-reaction pair and no net momentum is added to the system, thus adding no errors to measurement.

3.1.6.4 Summary of Impulse Measurement Uncertainties

The sum of the various uncertainties quantified in sections 3.1.6.1-3 is 1.85%. These uncertainties are random uncertainties, and would contribute to the sampling error as evaluated by the Standard Error of the Mean (SEM). There is agreement between the uncertainties estimated in this section and the SEMs found from experimental data (chapter 6) which were below 2% in almost all data sets.

3.2 Instruments

This section details specifications of the various technical instruments and software packages used in the measurement of the pendulum motion. The laser used was a Spectra Physics 156 He-

Ne laser, with a .95mW maximum output at 632.8nm and a measured beam diameter at the grating of approximately 1mm. Pendulum and cathode masses were measured using a Kern AEJ 220-4M digital micro-balance, with resolution in the hundreds of micrograms up to a limit of 220g. The mirrors and windows employed are all standard items constructed by Newport, and when kept clear of deposition have negligible absorbance over optical wavelengths. The photodiode was constructed for a previous optical interferometry experiment by the departmental electronics technician, Mr Phillip Deniss. The photodiode was placed so that the return signal from the laser grid would illuminate the photodiode. The circuit diagram of the photodiode is shown as figure 3.6.

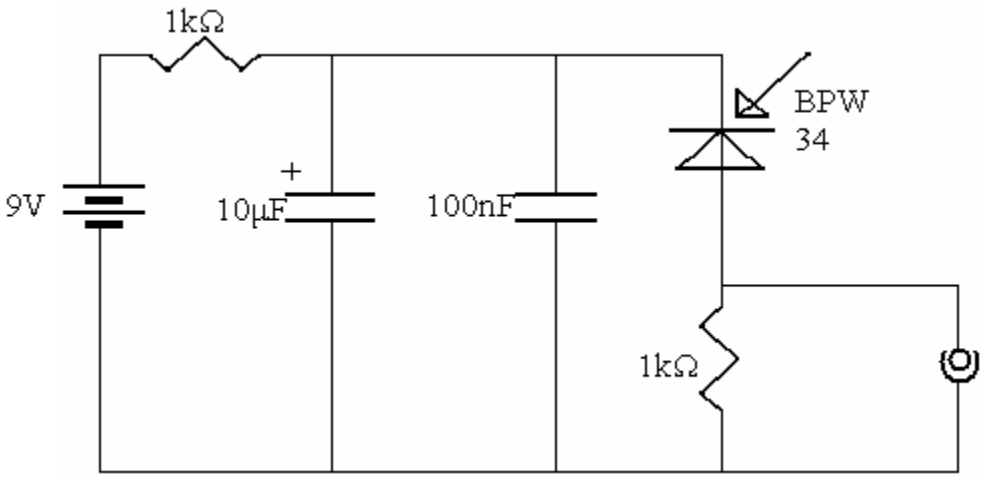

Figure 3.6: Photodiode circuit diagram, using BPW 34 PIN photodiode component.

The currents through the cathode and anode were measured using Rogowski coils made within the School of Physics and calibrated against an Ion Physics Corporation CM-1-H Rogowski coil current monitor, which could not be used for the measurements as on some occasions they were outside of its range. System voltages were measured using 100:1 voltage probes, to step down the large voltages used to charge the cathodes to levels that would not damage the oscilloscopes.

The experimental data was captured by banks of digital storage oscilloscopes (DSOs), specifically by Tektronix TDS2014 DSOs. Each was triggered by the same signal used to trigger the arc discharge, and separate oscilloscopes were used due to the difference in timescales. The

plasma is generated, impacts and then dissipates over lengths of time measurable in hundreds of microseconds, while the pendulum moves at speeds requiring measurements over hundreds of milliseconds. The data taken by the DSOs were then transferred to a desktop PC via GPIB cables and interface boards, so that a programme written in LabView® could display the data for inspection. This programme was also configured as the command software for the arc system. The data is stored in an MDSPlus database on the laboratory computer.

3.3 Vacuum Chamber

Figure 3.7 shows an isometric view of the vessel, being an evacuated stainless steel semi-torus of rectangular cross section, with major radius 440mm, minor radius 120mm, internal height 360mm and 12mm wall thickness. The vacuum is established with two pumps, the first being a rotary roughing pump and the second a turbomolecular pump (also known as a turbopump). Pressure was measured with a Pirani vacuum gauge contained as part of the turbopump. The system can achieve pressures on the order of 10^{-6} mbar, with all experiments conducted after the chamber had been pumped to below 50nbar.

Figures 3.7-8 show the ports on the walls of the vessel used. Only one port was used in this experiment, being the top vertical aperture as indicated on both figures 3.7 and 3.8, which was used to transmit the probing laser beam into the chamber.

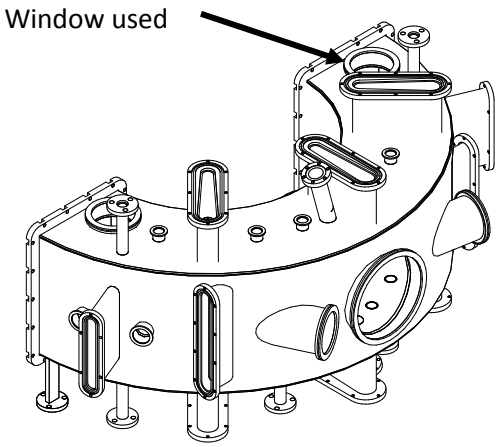

Figure 3.7: Isometric View of Vacuum Chamber.

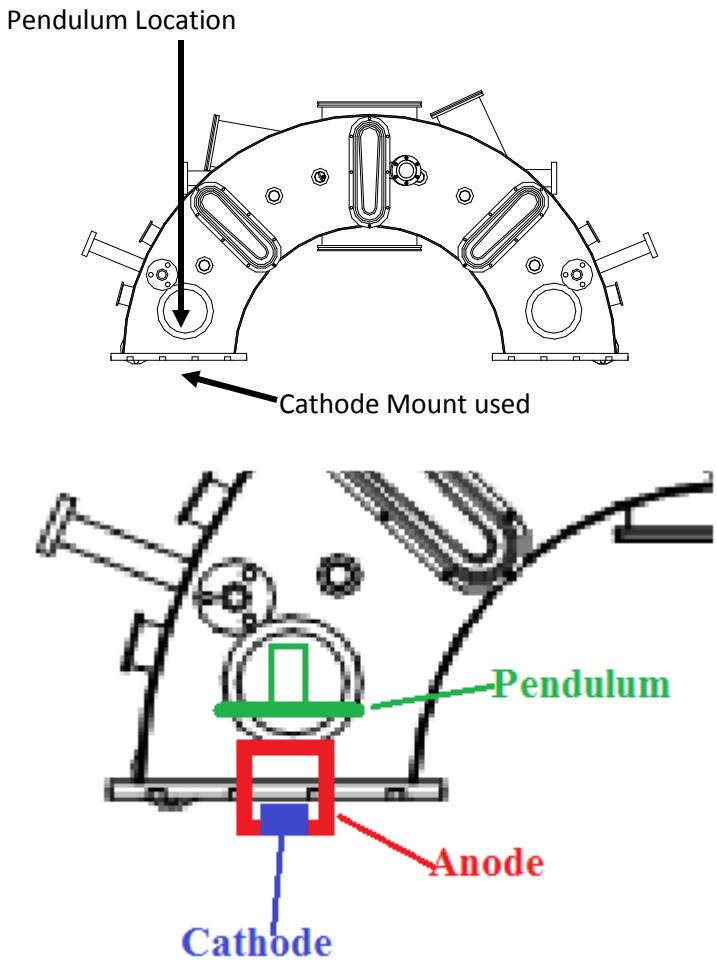

Figure 3.8: Top View of Vacuum Chamber; detail at bottom showing cathode, anode and pendulum.

The pendulum was suspended from the side of the access port flange closest to the mouth of the anode. Care was taken to ensure that the pendulum plate was perpendicular to the anticipated plasma thrust vector, that the pendulum could swing freely and that the momentum brake was correctly positioned to stop the pendulum from swinging after the measurement. Attachment of the bearing loops and momentum brake to the correct parts of the inner chamber walls was accomplished satisfactorily with adhesive tape.

3.4 Power Source

The 3-phase power supply used to charge the capacitor banks and the capacitor banks themselves were designed and built within the School of Physics at the University of Sydney. A schematic

diagram of the electrical connections of these to the cathode, anode and trigger is shown as figure 3.9. The main bank (21mF) can dissipate its stored energy through the cathode over a period of less than 1 millisecond, thus supplying the apparatus with the high power required. Once the arc has been triggered it creates a low-impedance short between cathode and anode, through which the main capacitor bank discharges. This means that the trigger circuit acts as the switch for the main bank, allowing current to flow through the cathode, then through the plasma to the anode and the grounded walls before being earthed. The trigger circuit itself was activated by computer control using software written by Dr. Michael Proschek, and extensively modified by former PhD student Luke Ryves and programmer Paul Leopardi. The chamber walls are connected to ground to assist with earthing, and not included in figure 3.9.

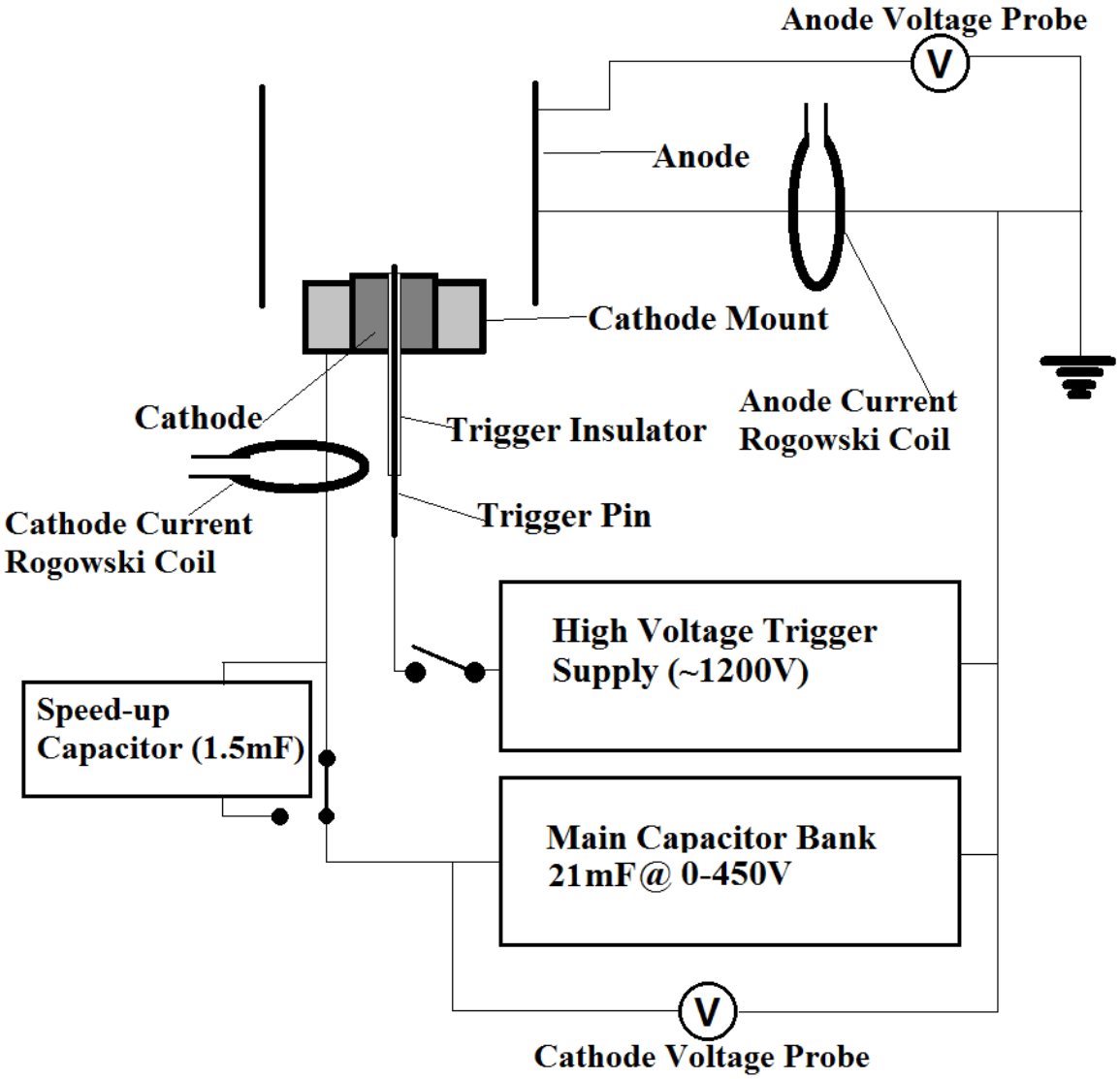

Figure 3.9: Schematic Diagram of the Power Supply

Various configurations of the capacitors can supply current to the cathode as a pulse with either a square or a sawtooth profile. It has been shown that the erosion profile of the cathode is different depending on the current profile [36]. The main bank will ordinarily deliver a sawtooth pulse, but this can be altered to a square pulse with the addition of fast-rising "speed-up" capacitors mounted close to the cathode. These pulses are illustrated in figure 3.10. The speed-up capacitors supply an extra 1.5mF to the total capacitance of the power supply.

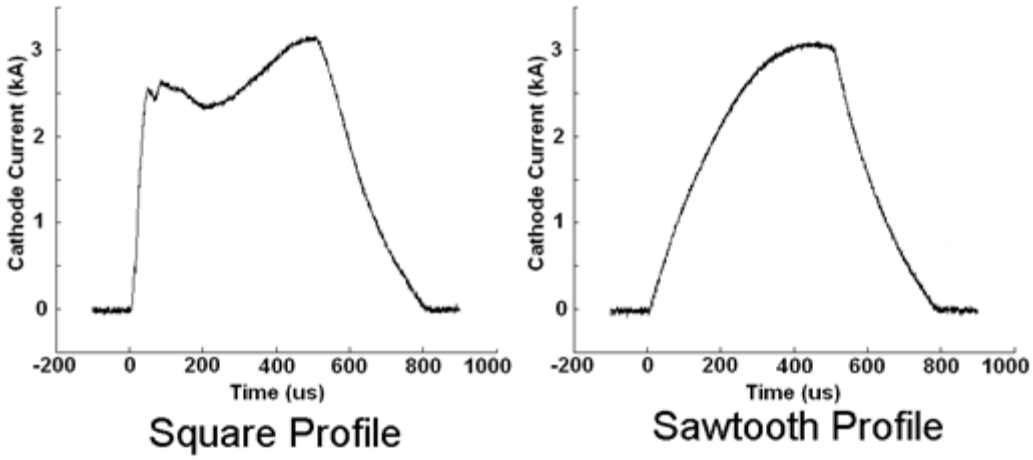

Figure 3.10: Pulse current profiles. Used with permission from L Ryves.

3.5 Data Collection

All of the signals from the various current and voltage probes were taken to a bank of DSOs, where they could be viewed in real time and then stored for later use. Once the measurements were taken, they were uploaded to the computer by the collection software (written by a past research fellow, Dr. Michael Proschek, and extensively modified by former PhD student Luke Ryves and programmer Paul Leopardi). The collection software was run in a Windows™ environment, and written in LabView VI. The data was saved to an MDSPlus database for further processing. Data processing was performed in MatLab by code written by the author and included in the appendices to this thesis.

3.6 Method

There were three distinct phases to the experiments undertaken for this thesis, being instrument construction & calibration; experimental parameter selection & investigation and lastly data

acquisition & processing. Each of these phases will be addressed within the following subsections.

3.6.1 Instrument Construction and Calibration

Construction of the ballistic pendulum and placement of it in the chamber was done as described in sections 3.1 and 3.3. During pump-down, which took approximately 1 hour, the optics were fine-tuned so that the signal could be captured. The physical set-up of the optics is shown in figure 3.11. The plasma parameters chosen for recording were anode current, cathode current, anode-to-ground voltage and cathode-to-ground voltage.

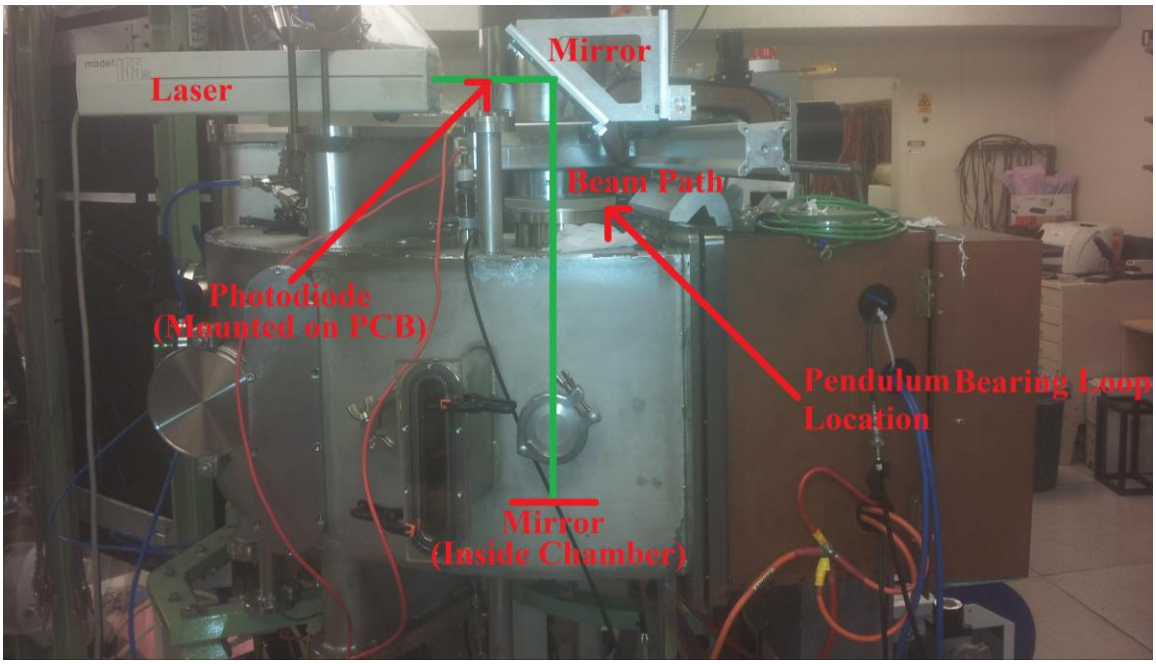

Figure 3.11: Optical bench used to hold mirrors, lens and photodiode for measurement.

3.6.2 Experimental Parameter Selection and Investigation

Work exploring erosion rates in both square- and sawtooth-shaped current pulses in Sn and Ti was done to determine which pulse shape to focus on in further investigations. The results from this work (shown in section 5.1.1 and section 5.2.1) [20], coupled with the work on thrusts measured for the two pulse shapes [22], led to the selection of square-shaped current pulses for this work. A concentric cylindrical anode was used, as previous work showed that this geometry was best [22]. Cathode cleaning to remove the contaminating oxide layer was undertaken after each return to atmosphere. Cathode charging voltages (V_{ch}) used were 100, 120, 140, 160 and 180V; the pulse durations explored were 100, 150, 200, 250 and 300 microseconds. At least six

datapoints were taken for impulse measurements for all materials at all combinations of settings within this parameter space, and an erosion rate datapoint was taken at each point.

3.6.3 Data Acquisition and Processing

Figure 3.12 illustrates the data acquisition and processing procedure schematically. Calibrated Rogowski coils and voltage probes, located as shown in figure 3.9, were used to measure the plasma parameters, with their signals collected by Tektronix TDS 2014 DSOs and then exported to the MDSPlus database as discussed in section 3.5. The database exported experimental results as sequentially numbered "shots" in plain text files. These were processed into .mat data files by code included as Appendix B; this code also used Riemannian integration and arithmetic averaging to convert measured currents and voltages into total charges and total energy for that pulse. These integrated parameters were all exported to an Excel spreadsheet for further processing.

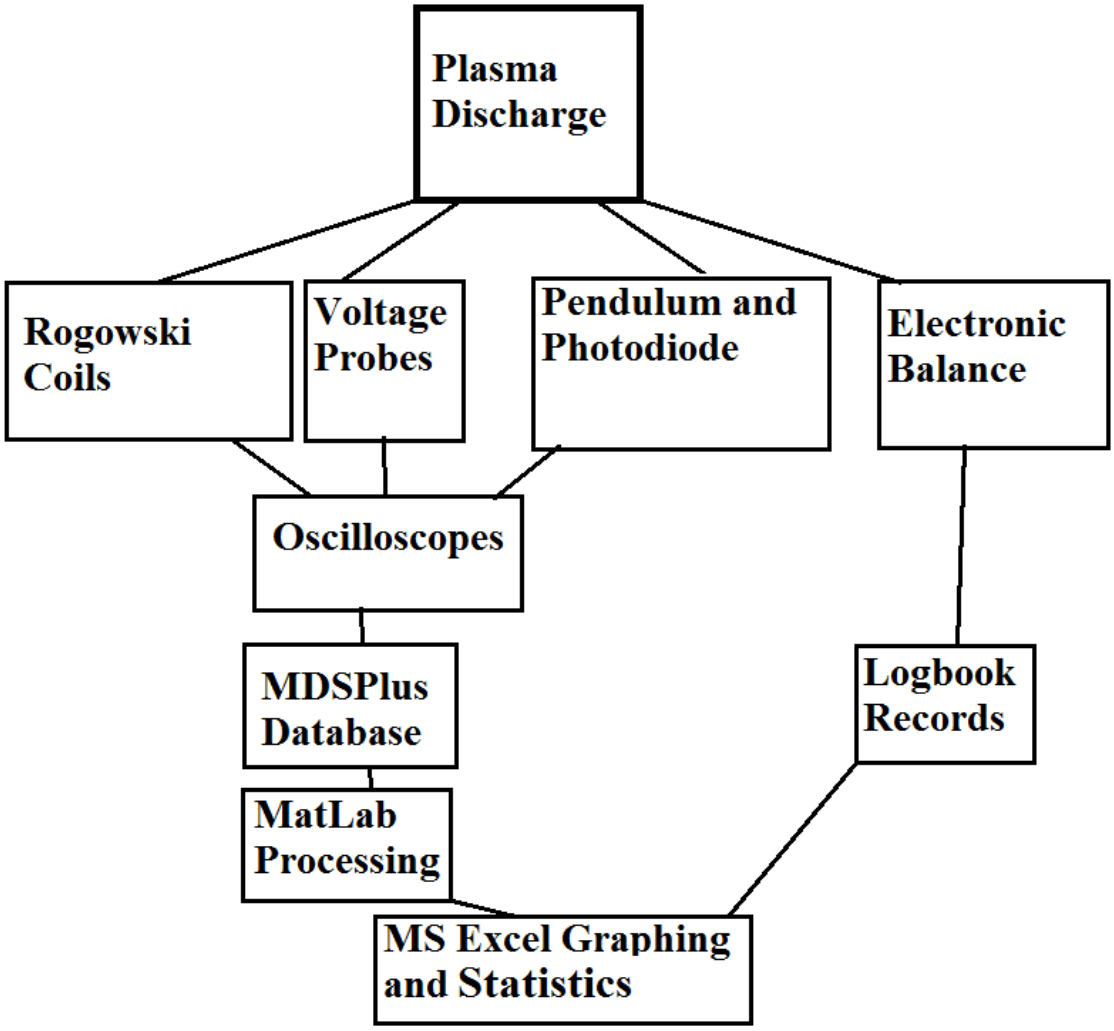

Figure 3.12: Block Diagram of Data Acquisition and Processing System.

Whenever a cathode is removed from the system an oxide layer is formed on the surface, and this oxide must be removed in order to take reliable thrust and erosion measurements. Removal of this oxide is done by firing approximately 100 pulses of plasma, which will clean the surface by eroding the oxide. The plasma currents and discharge voltages showed when the surface had been cleaned, as the currents were significantly lower and the discharge voltage significantly higher when produced by a clean surface. Plots of plasma measurements from uncleaned and cleaned surfaces are shown in figures 3.13-5. The mass of eroded oxide material was determined to ensure accurate erosion measurements.

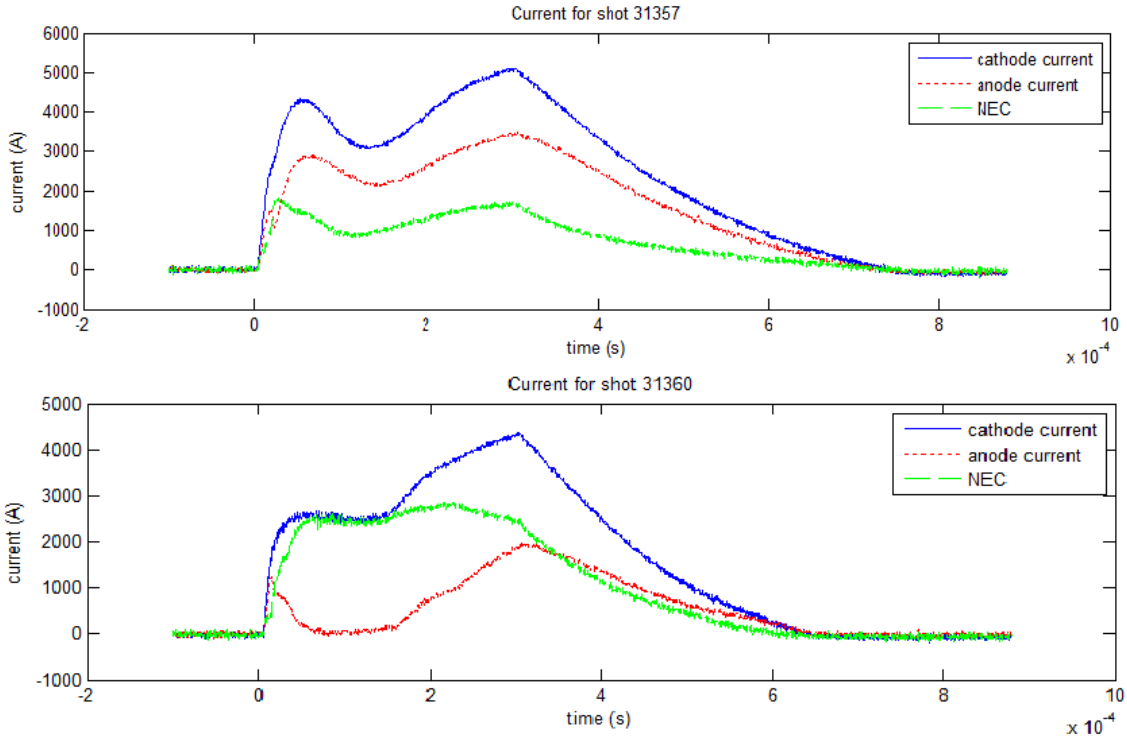

Figure 3.13: Comparison of plasma currents in plasma produced from uncleaned (top) and cleaned (bottom) surfaces.

Shots 31357 and 31360 were vanadium cleaning shots with 130 pulses fired between the two saved shots; V_{ch} 180V and 300μs duration

Figure 3.13 shows the change in currents while the cathode is being cleaned. Shot 31357 at top was fired when the vanadium cathode was still oxidised, and so has a higher anode current due to the oxide vapour interfering with plasma transport through the anode mouth, as shown by the lower NEC. The cleaned surface of shot 31360 did not have this oxide problem, and so shows lower anode and cathode currents as well as an elevated and more uniform NEC.

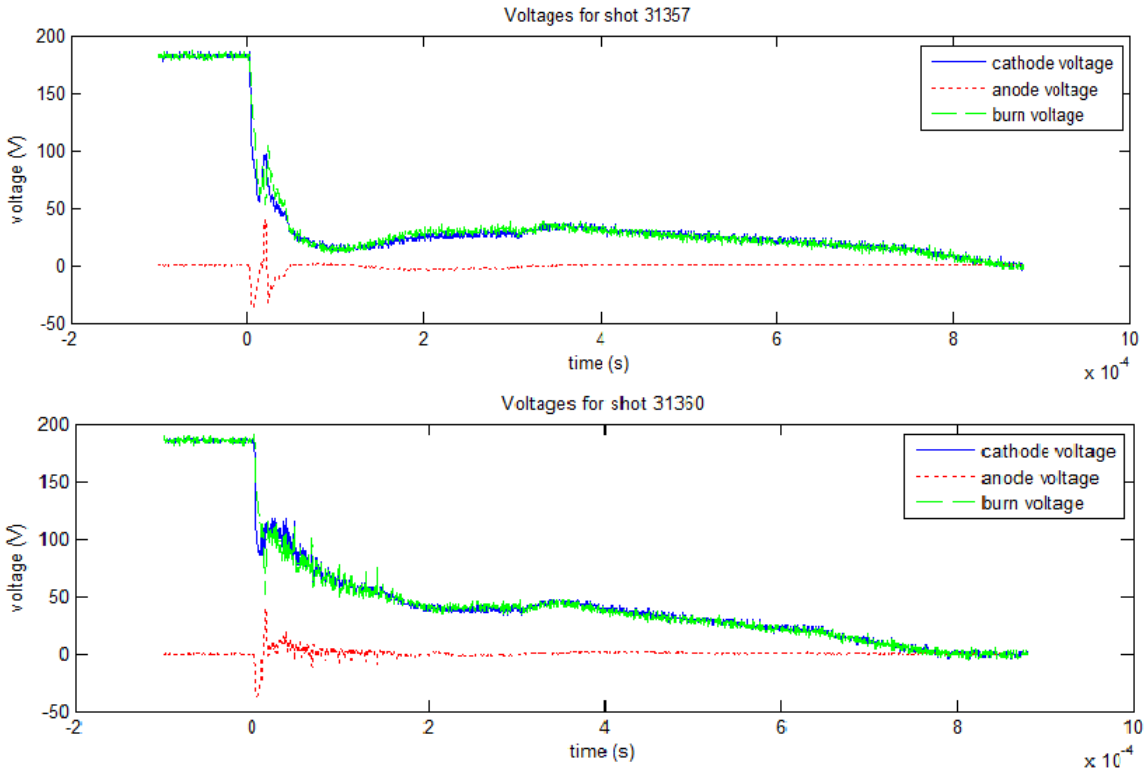

Figure 3.14: Comparison of plasma voltages in plasma produced from uncleaned (top) and cleaned (bottom) surfaces.

Shots 31357 and 31360 were vanadium cleaning shots with 130 pulses fired between the two saved shots; V_{ch} 180V and 300μs duration

Figure 3.14 shows the change in voltages between uncleaned and cleaned surfaces. The oxide surface is easier to erode, and so a lower burning voltage is measured; often dipping to only 10V between cathode and anode. In clean pulses this dip is not observed; the steady-state burning voltage for this V arc was approximately 50V. It is necessary to clean the cathode surface before firing pulses to ensure reliable comparison between pulses, and to increase the efficiency of the system; figure 3.15 shows the difference in photodiode traces.

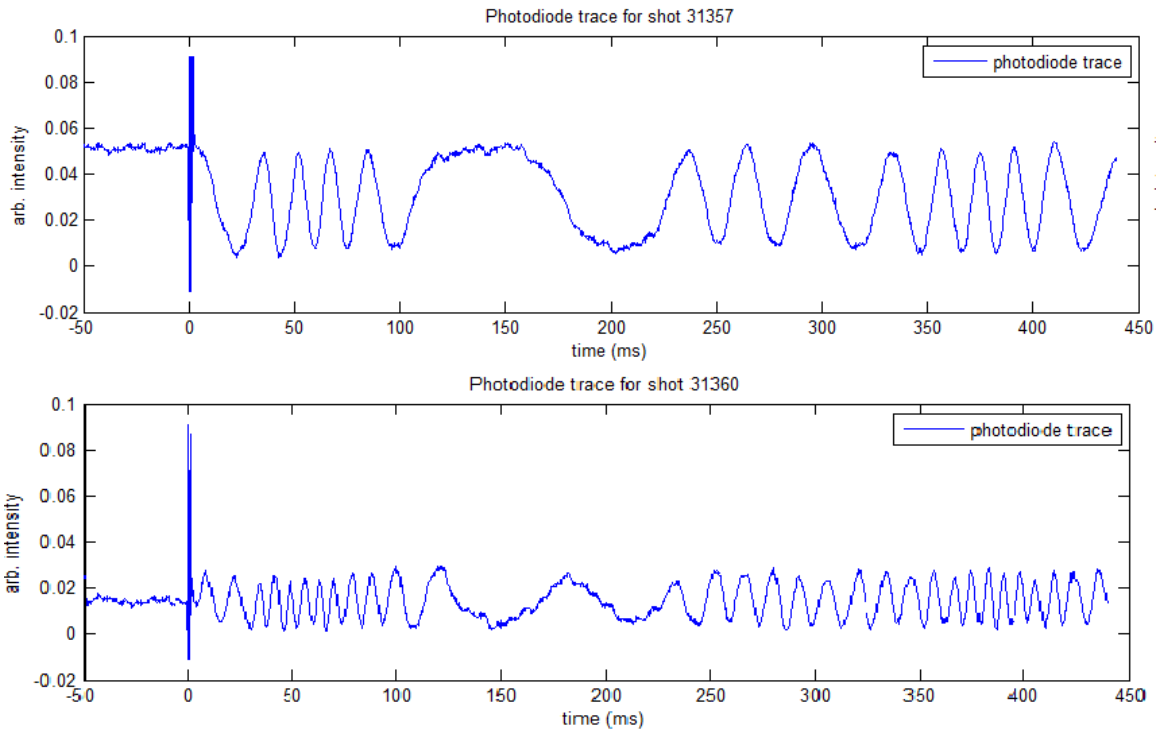

Figure 3.15: Comparison of photodiode traces created by pendulum motion caused by plasma from uncleaned (top) and cleaned (bottom) surfaces.

Shots 31357 and 31360 were vanadium cleaning shots with 130 pulses fired between the two saved shots; V_{ch} 180V and 300μs duration

Faster pendulum motion is indicated by more features being present in the photodiode trace while the pendulum is swinging. The lower plot in figure 3.15 shows more peaks and troughs in the photodiode trace measuring pendulum motion caused by plasma produced by a clean cathode. This indicates that clean cathodes produce more thrust than uncleaned, thus requiring that all cathodes be adequately cleaned before thrust measurements are taken.

Raw photodiode data was plotted using the code included as Appendix C, with the times of the peaks and troughs shown in the photodiode trace (bottom, fig 3.16) determined by visual inspection. The times of these peaks and troughs were entered into the Excel spreadsheet to determine the mean swing velocity of the pendulum during the period in which it was moving most quickly. Weighing the pendulum before and after the collection of data quantified the average pendulum mass, allowing the determination of the impulse delivered to the pendulum. The average force exerted on the pendulum quantified by dividing impulse by pulse duration, giving the thrust measurement. The measurements of thrust and impulse are presented in chapter

6. Impulse measurements were taken for plasma produced by both non-eroded and eroded cathode surfaces to determine the effect cathode wear has on thruster performance. Thus there are two sets of impulse data for each material tested.

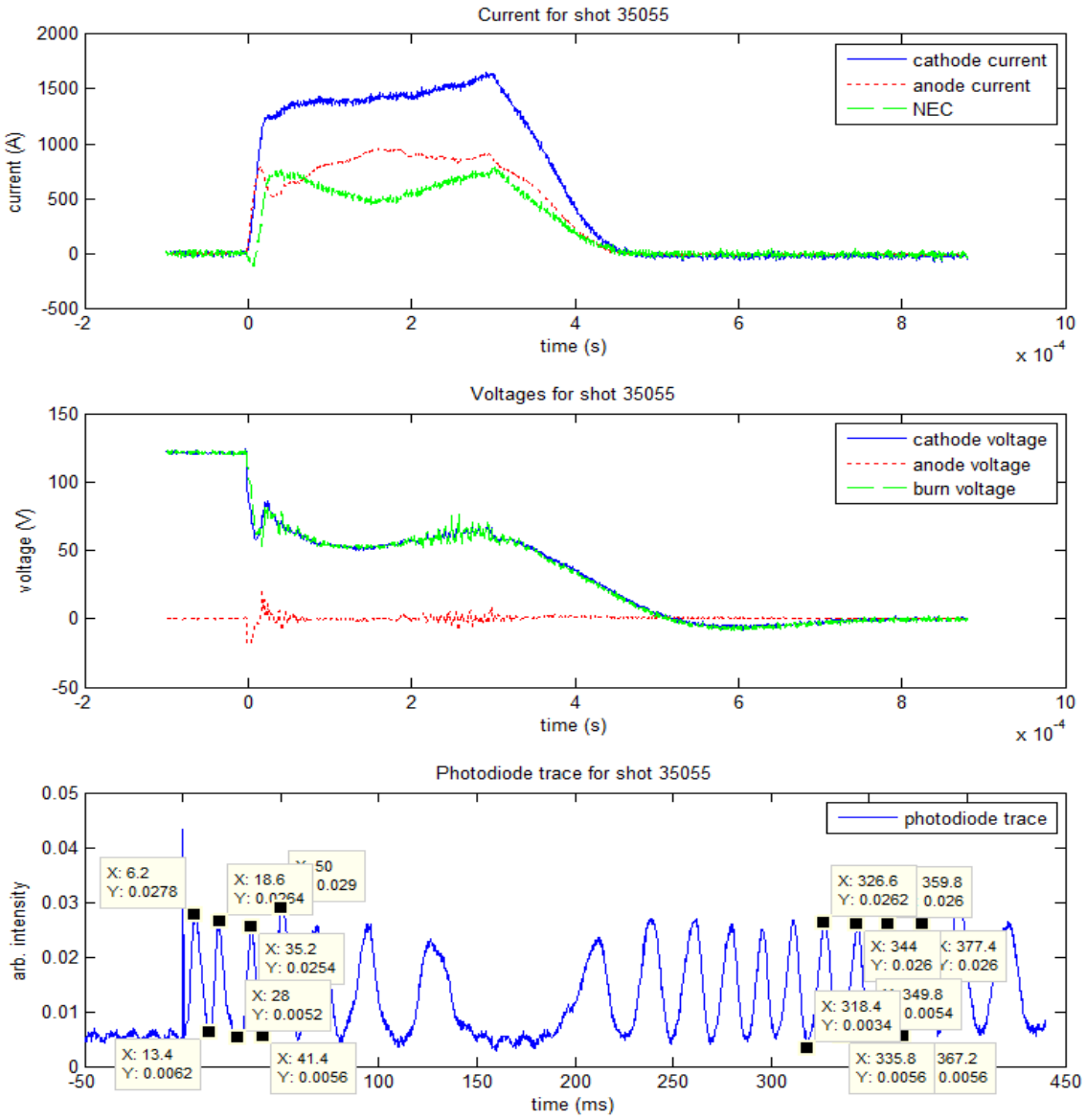

Figure 3.16: Typical data collected to determine velocity.

These plots show the time dependency of the (from top) currents, voltages and photodiode traces. Data markers to show the times of the photodiode peaks and troughs have been included on the photodiode trace as part of the data processing method. Shot 35055 was a carbon eroded cathode surface impulse measurement; V_{ch} 120V and 300µs duration.

Cathode erosion rates were determined by measuring the cathode mass before and after firing a large number of pulses at the same experimental settings as those for which thrust was measured. Measuring the same plasma parameters described in section 3.6.1 allows the determination of the

cathode erosion rate per unit charge transiting the cathode at each point in the parameter space described in section 3.6.2. Erosion rates per unit charge were determined by measuring the loss in cathode mass over a large number of pulses using a Kern AEJ 220-4M electronic balance, subtracting the mass eroded during cleaning, and then comparing the mass loss to the measured parameters of the plasma pulse. The DSO traces used were averages of the last 128 pulses of the thousands fired during to determine that measurement, to reduce uncertainty; care was taken to sample the traces in the middle of each measurement to ensure that the voltage settings had not drifted from their nominal values. The integrated parameters were exported to the Excel spreadsheet as before, while cathode mass values were entered into the experimental log book as well as the spreadsheet. The mass loss data was plotted against integrated cathode current, NEQ and the energy expended in the plasma. Linear regression fits were applied to determine the erosion rate for the different pulse durations. The results of the cathode erosion rate experiments are presented in chapter 5.

The order of experiments for most cathodes was to clean the non-eroded cathode surface of the cathode before taking impulse data across the parameter space, to measure the impulse produced by pulses fired from a non-eroded cathode surface. Ti and Sn erosion data were taken much earlier to show the feasibility of the experiments, and so eroded and non-eroded Ti and Sn impulse measurements were performed back-to-back. After this was done for one cathode, another was installed, and the same process repeated. When all the non-eroded cathode surface data was taken, the pendulum was removed from the chamber and a cathode selected for erosion rate measurement. This cathode was weighed before the same non-eroded cathode surface was placed facing forwards in the chamber and cleaned by firing a number of pulses. The cathode was then extracted, weighed and replaced with the same face forwards, cleaned, and then a larger number of pulses would be fired to determine the erosion rate for that material for those conditions. Cleaning conditions, such as the number, length and charging voltage of the pulses used to clean a particular cathode, were kept constant so that the same mass loss during cleaning could be applied across the parameter space. Once erosion rate data was obtained across all of the parameter space for one cathode, it was replaced with another and the process repeated. After the erosion data for all cathodes was taken, the pendulum was replaced in the chamber and a cathode was selected to have the thrust generated by plasma ejected from its eroded surface measured. The cleaning and measuring process for eroded cathode surfaces was the same as for non-eroded cathode surfaces.

Once the thrust and cathode erosion rate had been measured, the efficiency metrics described in chapter 1.1 were derived. The product of the erosion rate (in mass per unit charge, frequently given in units of $\mu g.C^{-1}$) and integrated cathode current (C) gave the mass eroded from the cathode surface. Assuming that erosion only happened while the pulse is active lets us calculate the average mass flow rate of the arc. This assumption is justifiable, as measurements of the light emitted by the plasma show that plasma generation ceases very soon after the power supply is shorted to ground by closing the "crow bar" switch. This is shown in figure 3.17, where the photodiode trace drops within 10μs to a value substantially below that which is measured during steady arc operation, while the current flows and voltages take over 100μs to decay.

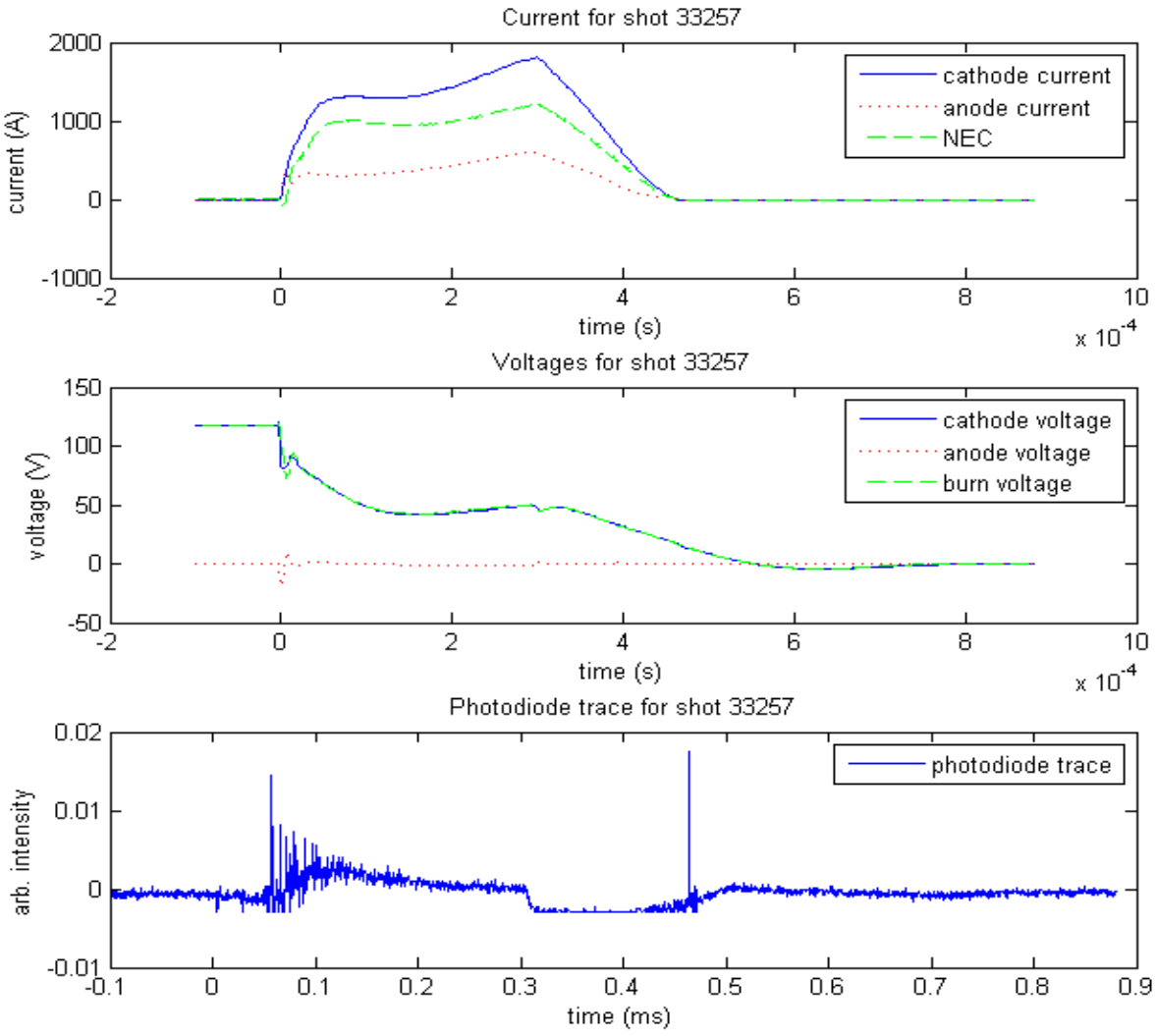

Figure 3.17: Plot (bottom) showing the rapid cessation of plasma generation as shown by the photodiode trace, compared to the more gradual decay of the current (top) and voltage (middle) signals after crow bar switching.

Mass flow rates were derived in Excel by multiplying the cathode erosion rate by the integrated cathode current and dividing by the pulse duration. Fuel specific impulse and jet power efficiency values were derived for each thrust measurement using the cathode erosion rate derived from the trendline for cathode erosion per unit integrated cathode current for each pulse duration. This was done in Excel and results for these two derived quantities are shown in chapter 7, together with the uncertainties in their derivation.

3.7 Summary of Experimental Apparatus and Method

A thrust measurement system with an optical occultation method of determining ballistic pendulum displacement and velocity was developed. The system has no electronic parts within the vacuum chamber to minimise noise. The experimental method included impulse measurements from eroded as well as non-eroded cathode surfaces, to investigate the effects of cathode wear on performance. Care was taken to ensure that all measurements were taken from surfaces cleaned of oxide contamination, to ensure an accurate representation of in-orbit performance. Experiments were constructed so as to explore a range of pulse durations and currents to assess the effects of these parameters on performance.

4 Cathode Material Selection

The choice of fuel for pulsed cathodic arc thrusters is subject to various design parameters. Whilst any conductive material could be used as a cathode, identification of efficient fuels from literature would allow for more efficient experimental design and the determination of the most efficient fuel. The measurements of the system thrust and mass flow rate required to quantify the standard efficiency metrics described in chapter 1 are not available in the literature. In this chapter estimates are derived from other quantities available in the literature so that potential fuels can be evaluated. These estimated performance metrics were the subject of a published paper [21].

4.1 Derivation of Non-Standard Efficiency Metrics

Four metrics by which a material's thruster performance can be estimated are: the impulse delivered per mole of cathode material; the impulse delivered per unit volume; the impulse delivered per kilogram; and the impulse delivered per Joule of energy expended. Comparing across all four of these metrics allows evaluation of fuels for different mission requirements, though it is expected that the impulse delivered per kilogram of cathode material eroded would be the most important due to the high cost of launching mass into orbit.

The impulse per mole of ions is derived in equation 4.1 for ions of atomic mass m, with velocity v_e and with N_A being Avogadro's number.

$$p_{mol} = m v_e N_A \tag{4.1}$$

Using the erosion rate and ion fraction data from Polk et al [19], it is possible to evaluate the impulse delivered per unit volume and unit mass of cathode material. As not all the material ejected from the cathode is ionised [24-7], not all the exhaust will contribute the same momentum to the spacecraft. Although it is important to know how much impulse is delivered by a given quantity of eroded cathode material, material erosion rates depend on the mode of arc operation, as exemplified by the reported erosion rates for DC and pulsed operation [54-6]. It is clear that erosion rates will be highly sensitive to the pulse duration in pulsed mode [24]. Hence, we examine metrics based on the quantity of material eroded from the cathode surface and metrics based on the flow of ions ejected from the system. The limited erosion rate data in the literature was applied where available to provide estimates of material performance. Ion momentum data is presented to allow comparison across all materials. Since cathodic arcs operate by ejecting material from a solid metallic cathode, knowledge of how much impulse can be gained from the

finite volume of cathode material available is a key selection criterion for the fuel of an arc thruster. The impulse delivered per cubic centimetre of solid cathode material of specific gravity ρ and erosion rate ε_r (in mass per charge) is

$$p_{Cccm} = \frac{\rho m v f_i}{\varepsilon_r e \bar{q}} \tag{4.2}$$

Where e is the electronic charge, $\bar{q}$ the mean ion charge state and f_i is the ion current fraction, assumed here to be 0.1. The plasma flow is quasi-neutral, but the electron current is higher due to the greater mobility of the electrons. The ion current percentage is assumed to be ~10% of the total current in all cases, as is found as a rule of thumb in many papers on the subject [17, 19, 23].

Energy efficiency is approximated by the impulse delivered per Joule of energy expended by the arc. The impulse delivered per Joule of energy expended by an arc with burning voltage V_B is estimated to be

$$p_J = \frac{mv}{e\bar{q}V_B} \tag{4.3}$$

In an actual PCA system, the energy use per pulse can be determined by integrating the product of the instantaneous current and voltages. For a given energy input, a low burn voltage and high current is desirable, as it would maximise the quantity of ions flowing through the system. Therefore impulse delivered per unit energy would be maximised by using a material with a low burn voltage and a low mean charge state.

The mass efficiency of the system is approximated by the impulse delivered per kilogram of ions expelled and is determined by equation 4.4,

$$p_m = \frac{p_{mol}}{M} \tag{4.4}$$

Where M is the molar mass of the material. Equation 4.4 assumes that all the material expelled is ionised, but this is not the case. The impulse per kilogram of cathode material is given by

$$p_{Cm} = \frac{mvf_i}{\varepsilon_r e \bar{q}} \tag{4.5}$$

Cathode erosion rates are not available in the literature for all materials or all operating conditions. The information used to evaluate equations 4.1 to 4.5 were taken from sources cited in the relevant columns of table 4.1. The mean charge state data available in the literature is averaged over the length of the pulse, and therefore is only accurate for the pulse length used. The burning voltage will change with the system used, including any changes to anode-cathode geometry [22]. Therefore the numerical results presented can not be considered definitive, but rather they are estimates to allow comparison between elements.

Information could not be found for all conducting and semi-conducting elements. This may be due to cathode melting (Hg, Ge), chemical reactivity (most of the elements in groups 1 and 2), radioactivity (most of the actinides, Tc and Pm), toxicity (e.g. Be) or cost (e.g. Re, Os, Ir). Elements for which this information would have been interesting include Be, B, Na, K, Sc, Re, Os, Ir and the remaining actinide series. The estimates for elements for which data was available in the literature are incorporated in the survey shown in table 4.1.

Element	Burn voltage [57] (V) (pulsed, 300A arc current)	Mean charge state [32]	Temp. at which SVP is 1 Pa (K) [58]	Time of flight velocity [32] (10^4m/s)	Ion kinetic energy [32] (eV)	Impulse per mole of ions (N.s)	Impulse per Joule of energy expended (mN.s/J)	Impulse per kg of ions (N.s/kg)	Cathode erosion rate (µg/C) [19]	Impulse per cubic cm of cathode material (N.s/cm^3)	Impulse per kg of cathode material (N.s/kg)
Li	23.5	1	797	2.38	20	164	0.0724	23792			
C	29.6	1	2800	2.97	54	356	0.1248	29690	17	22.71	10015.77
Mg	18.8	1.5	701	3.06	117	743	0.2732	30589	31	20.72	11920.19
Al	23.6	1.7	1482	2.76	106	745	0.1925	27590	28	49.56	18356.32
Si	27.5	1.4	1908	2.58	97	722	0.1951	25791			
Ca	23.5	1.9	864	2.59	140	1036	0.2410	25891			
Ti	21.3	2.1	1982	2.22	122	1065	0.2463	22192	30	85.01	18891.93
V	22.5	2.1	2101	1.93	97	984	0.2154	19293			
Cr	22.9	2.1	1656	1.94	101	1008	0.2174	19393	20	174.37	24251.18
Mn	22	1.5	1228	1.08	33	594	0.1862	10796			
Fe	22.7	1.8	1728	1.18	40	659	0.1670	11796	48	67.23	8538.29
Co	22.8	1.7	1790	1.18	43	696	0.1858	11796	44	76.72	8619.82
Ni	20.5	1.8	1783	1.09	36	640	0.1797	10896	47	80.34	9018.98
Cu	23.1	2	1509	1.28	45	813	0.1823	12796	35	94.14	10530.07
Zn	15.5	1.4	610	1.04	94	680	0.3248	10396	320	9.40	1316.77
Ge	17.5	2	1644	1.1	45	798	0.2364	10996			
Y	18.1	2.3	1883	1.43	94	1271	0.3164	14295	45	41.14	9200.13
Zr	23.4	2.6	2639	1.57	116	1431	0.2439	15695	53	70.50	10812.88
Nb	27	3	2942	1.55	116	1439	0.1842	15495			
Mo	29.3	3.1	2742	1.74	151	1670	0.1904	17394	36	142.11	13823.91
Rh	24.8	3	2288	1.57	131	1615	0.2250	15695			
Ag	23	2.1	1283	1.04	61	1122	0.2407	10396	140	41.84	3988.16
Cd	16	1.3	530	0.68	27	764	0.3808	6798	620	7.73	893.62
In	17.5	1.4	1196	0.55	18	631	0.2670	5498			

Sn	17.5	1.5	1497	0.75	34	890	0.3514	7497	295	11.67	1585.12
Sb	15.8	1	807	0.52	17	633	0.4154	5198			
Ba	18.3	2	911	0.67	32	920	0.2604	6698			
La	17.2	2.2	2005	0.7	35	972	0.2663	6998			
Ce	17.9	2.1	1992	0.7	36	980	0.2703	6998			
Pr	20	2.2	1771	0.87	55	1225	0.2887	8697			
Sm	14.6	2.1	1001	0.74	43	1113	0.3761	7397			
Eu	21.3	2.1	863	0.78	48	1185	0.2747	7797			
Gd	21.6	2.2	1836	0.74	45	1164	0.2538	7397	55	84.08	10642.98
Tb	18.1	2.2	1789	0.74	45	1175	0.3060	7397			
Dy	19.8	2.3	1378	0.74	46	1202	0.2736	7397			
Ho	20	2.3	1432	0.83	58	1368	0.3083	8297			
Er	19	2.4	1504	0.82	59	1371	0.3117	8197			
Tm	21.7	2	1117	0.83	61	1401	0.3347	8297			
Hf	24.3	2.9	2689	0.92	79	1642	0.2415	9197			
Ta	28.7	2.9	3297	1.14	121	2062	0.2567	11396	56	174.99	10484.49
W	31.9	3.1	3477	1.05	106	1929	0.2022	10496	55	258.06	13405.71
Pt	22.5	2.1	2330	0.68	47	1326	0.2909	6798			
Au	19.7	2	1646	0.58	34	1142	0.3005	5798			
Pb	15.5	1.6	978	0.54	31	1118	0.4675	5398	510	13.17	1161.45
Bi	15.6	1.2	941	0.42	19	877	0.4859	4199			
Th	23.3	2.9	2633	0.99	118	2296	0.3522	9897			
U	23.5	3.2	2325	1.14	160	2712	0.3739	11396			

Table 4.1: Literature values and derived data for cathode material selection

The columns in table 4.1 that detail the metrics are highlighted in grey. These are the impulse delivered per mole, per cubic centimetre, per Joule and per kilogram. There are two metrics given for impulse per kilogram eroded, one which is derived from ion velocity data (which assumes that the plasma is fully ionised), and one which is derived from the small amount of

cathode erosion data found in the literature. The latter is more reliable as it utilises experimental measurements of cathode erosion rates and takes into account the mass eroded to form neutral species. The best performing elements according to these criteria can be placed in groups on the periodic table, being the refractory metals, heavy non-refractory metals, actinide elements and lighter elements. This grouping is illustrated on the periodic table in figure 4.1, with the various groups being shaded in the same shade of grey.

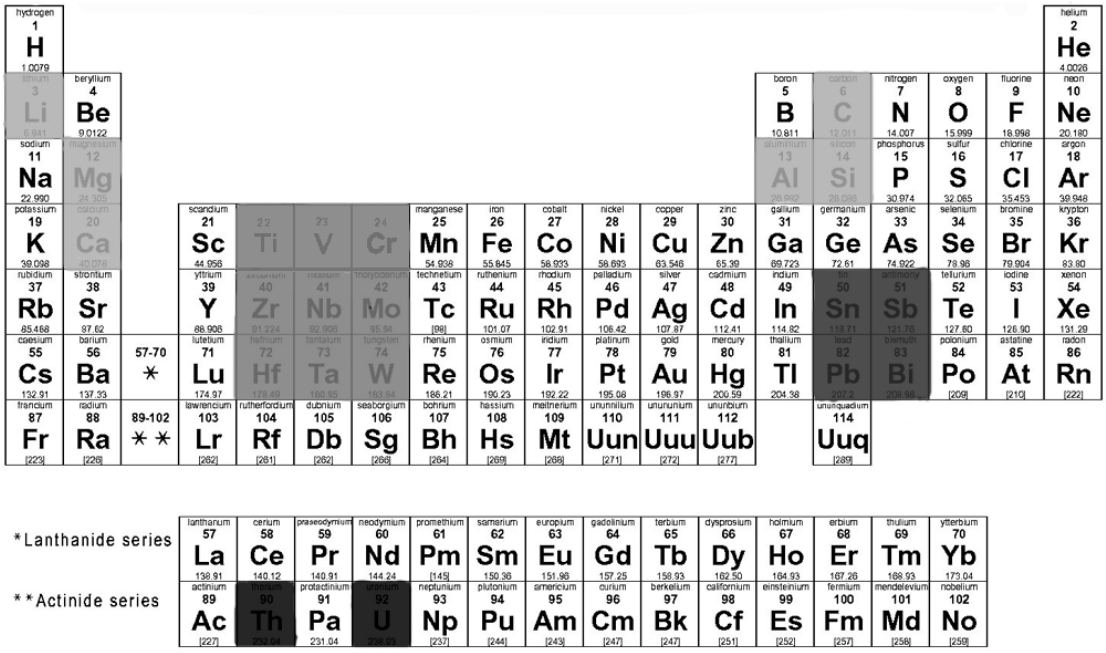

Figure 4.1: Periodic table with the four element classes highlighted.
The classes are light elements (lightest grey), refractory metals (medium grey), heavy non-refractory metals (dark grey) and actinides (darkest grey).

The four plots in figure 4.2 show the results of this survey. Note the peaks in 4.2a, which correspond with the refractory and actinide elements. The hollow symbols denote data derived from the cathode erosion rates, and so should lie below the data derived from ion momentum data (solid symbols), as not all the material ejected is ionised. This is not the case for three elements (Cr, Gd, W) because the erosion rate data and ionisation fraction data were from different sources and refer to arcs operating in different modes and hence are not self-consistent [19, 54-56].

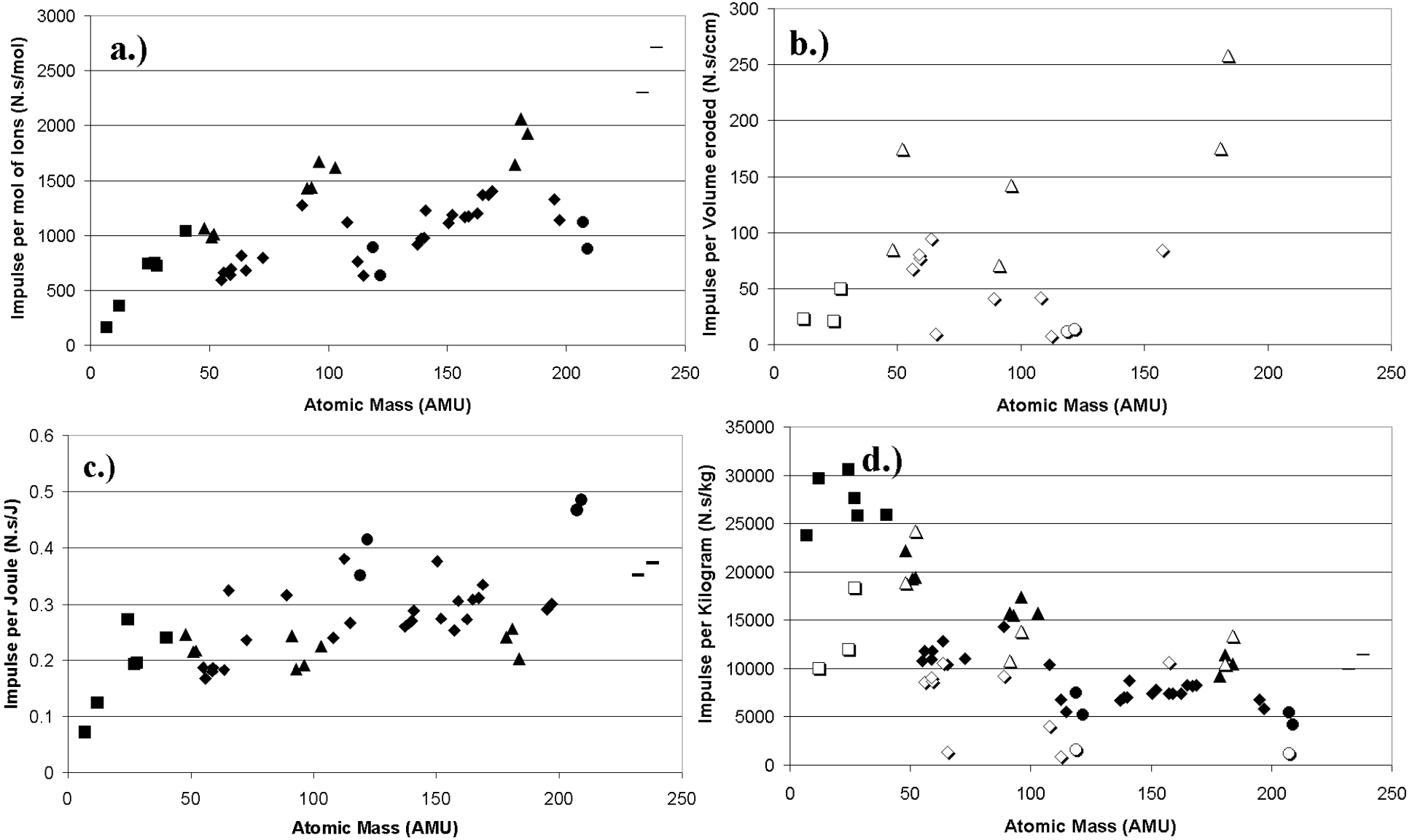

Figure 4.2: Results for the four metrics (equations 4.1-5) plotted against atomic mass.

Subplot a.) shows impulse per mole of ions, b.) shows impulse per cm^3 of cathode material, c.) shows impulse per Joule expended and d.) shows impulse per kilogram of ions. In all plots squares denote light elements, triangles denote refractory metals, circles denote heavy non-refractory metals, dashes denote actinide metals and diamonds denote other elements. Hollow symbols denote data derived from the erosion rates.

All of these plots are strongly non-linear, especially that for the predicted impulse per mol of ions. This serves to indicate that processes other than electrostatic acceleration are occurring in the arc discharge, but a full discussion of this is beyond the scope of this work. What is clear from these plots is that there are strong elemental groupings present, which is to be expected from the periodic table's grouping of elements based on similar physical characteristics.

The refractory elements perform well on the metric of impulse delivered per mole of ions, due to the relatively high mean charge states of these elements; their high densities also lead to them scoring well on the metric of impulse per unit volume. This performance makes the refractory metals attractive fuels for applications where cathode longevity is a key mission parameter. When ranked by impulse per unit energy, the refractory elements perform poorly, reflecting the large energy cost of breaking the lattice. The refractory elements give an impulse delivered per unit mass of ions that is close to the median value of the distribution of the elements except molybdenum, which is decidedly above average due to its high charge state distribution, moderate mass and high ion velocity.

The actinide elements uranium and thorium were the best performing on the metric of impulse per mole of ions, due to their high atomic mass and high mean charge state. These elements also performed well on the metric of impulse delivered per joule expended, although the impulse delivered per unit mass is moderate. All the actinide series are radioactive, with uranium 238 and thorium 232 being the most stable isotopes, with half-lives of billions of years [58]. As these isotopes present a dust inhalation hazard and pulsed cathodic arcs produce quantities of micrometre scale dust, ground tests with these elements are difficult to do safely. It was therefore impossible to find cathode erosion rate data for these elements, and so their scoring on the metric of impulse per unit volume of cathode cannot be determined. It would be expected that they would score at least as well as the heavy refractory metals, given their other physical characteristics.

The heavy non-refractory elements perform poorly on the metrics of impulse per mole and per kilogram of ions. This is due to their relatively high mass and low mean ion charge states. Conversely, they are the best group when measured against the criterion of impulse delivered per Joule of energy expended. This is due to their low lattice cohesive energies and ionisation energies, which reduce the energy required to remove an ion from the lattice. Their low

cohesive energies lead to high vapour pressures, and work by Anders and others has shown that elements with high vapour pressures tend to produce large quantities of neutral species [24-6]. These neutrals travel at velocities much lower than the plasma itself and tend to lower the mean charge state of the plasma plume through collisional processes. Thus, high vapour pressure metals are not desirable because they waste cathode material by producing neutral species and reduce the energy of the ejected ions. Elements that mimic heavy non-refractory elements but do not fall into the same groups in the periodic table are cadmium and samarium. These elements are attractive for missions where the power budget is especially tight, such as for cubesats and other microsatellites.

The light elements perform badly in the categories of impulse per mole of ions and impulse per Joule, but all show high impulse delivered per kilogram of ions due to their low atomic mass. However, due to the high vapour pressures of some of these elements, some of the light elements were outperformed by some lighter refractory elements on the metric of impulse per kilogram eroded from the cathode surface [24-6]. Should this vapour production problem be solved, the light elements would be the most efficient fuels per unit mass.

Recent work shows that the mean charge state is highest at the beginning of the cathode current pulse [24-6]. This observation is consistent with there being fewer neutral particles present to collide with the ions and redistribute their charge at the beginning of the pulse. The observation may also be attributed to the coupling between cathode spots when they are close together at the ignition site [27]. Materials with low boiling points also tend to have the lowest mean charge states, and an argument based on collisional processes with evaporated neutrals would explain this. This suggests a benefit to thruster operation in using very short pulse durations, as less neutral material will be ejected and the ions will have a higher mean charge state. Mean charge state is an important property of the plasma plume of a thruster and requires further study.

4.2 Material Selection Summary

Analysing the cathodic arc literature in order to assess the theoretical performance of pulsed cathodic arcs as thrusters was necessary to identify potential fuels. The analysis shows that there are four distinct classes of elements when measured against the four performance metrics. If a mission is mass-constrained, a designer should choose a light element (Mg, Ca, Al) or one of the lighter refractory elements (Cr, Ti, Mo). Missions with a tight power budget would benefit from

a heavy nonrefractory cathode (Bi, Pb). Volume or component longevity constrained missions should employ a heavy refractory (Ta, W) or actinide element (U, Th) as the cathode material. Good all-round performing elements are Mg, Cr, Mo, Ta, W, Th and U.

Cost and safety considerations constrained the selection of cathodes for testing, as this project had neither the budget for iridium nor the safety equipment required for uranium. Therefore the selected heavy non-refractory metals were tin and bismuth; the refractory metals chosen were titanium, vanadium, chromium, molybdenum, tantalum and tungsten; and the light elements chosen were carbon, magnesium and aluminium. Cylindrical cathodes 25mm in diameter and 12.5mm tall were purchased from the Kurt J Lesker Company for this work, with all cathodes at least 99.5% pure.

5 Cathode Erosion Rates

Determining the mass flow rate from a PCA thruster will allow the derivation of the standard efficiency metrics described in chapter one. This chapter contains the results of experiments performed to determine the cathode erosion rates of the materials identified in chapter four across the parameter space described in chapter 3.6. Table 5.1 contains a short summary of the data sets used to determine the erosion rate data. A well behaved data set showed erosion rates scaling with pulse duration and pulse current, clear transition to type 2 arcs and was reliably triggered throughout the data set.

Cathode material	Shots Used to Determine Cathode Erosion Rates	General remarks on the data.
Sn	30497-30560	Well behaved.
Bi	33208-33235	Very high mass flow rate with no transition to type 2 arcs observed.
Ti	30117-30215	Well behaved.
V	33303-33353	Well behaved.
Cr	33354-33409	Well behaved.
Mo	33249-33302	Well behaved.
Ta	33039-33101	Well behaved.
W	32986-33165	Well behaved.
C	33166-33248 35528-35557	Two series of shots used as discussed in 5.3.1 due to behaviour of C cathode.
Mg	33105-33153	Fast cathode spots caused anomalous wear on cathode surface at long pulse durations, so the cathode was flipped after shot 33119, otherwise well behaved.
Al	33410-33462	Well behaved.

Table 5.1: Summary with comments of Erosion Data Sets. A well-behaved data set shows erosion scaling linearly with the number of pulses and was reliably triggered throughout.

Linear regression trendlines have been fitted to the data in each plot in this chapter, with the equations for each fit and the square of the correlation factor for each fit placed next to the relevant data series. The numerical legend for the plots in this chapter and those in the following two chapters refer to the duration of the pulses as described in chapter 3.6.2.

5.1 Non-Refractory metals

Data for Sn was taken in late 2011 at the University of Sydney, and is published in part as part of a paper presented at the 12th Asia Pacific Physics Conference [20]. Bi Data were taken in mid-2014 at the University of Sydney and has not been previously published.

5.1.1 Tin

Figure 5.1 shows the data for Sn erosion, plotted against the energy expended in the arc per pulse, the integrated cathode current and the net ejected charge. These are shown as subplots a, b and c respectively.

5.1.2 Bismuth

Figure 5.2 shows the data for Bi erosion, plotted against the energy expended in the arc per pulse, the integrated cathode current and the net ejected charge. These are shown as subplots a, b and c respectively. The anomalously low erosion rate for the 200 microsecond pulses led to the use of the trendline for the whole data set being used to determine the efficiency metrics shown in chapter 7.1.2. This rate is 1176.5 µg of Bi eroded per Coulomb of integrated cathode current.

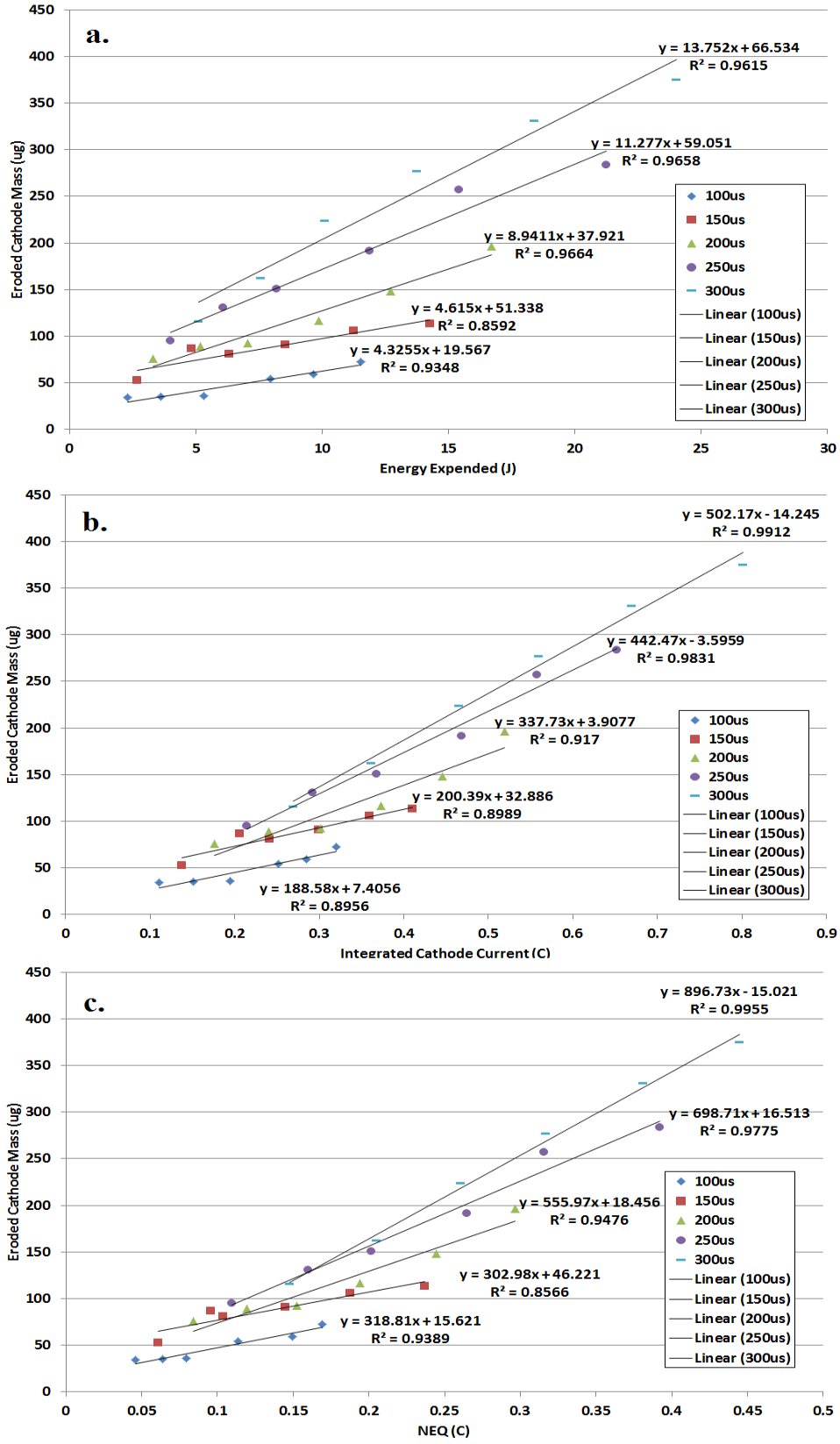

Figure 5.1: Sn erosion rate data.

The vertical axis in each plot is the average mass eroded from the cathode surface per pulse, while the horizontal axes are (from top) the energy expended per pulse, the integrated cathode current per pulse and the net ejected charge (NEQ) per pulse.

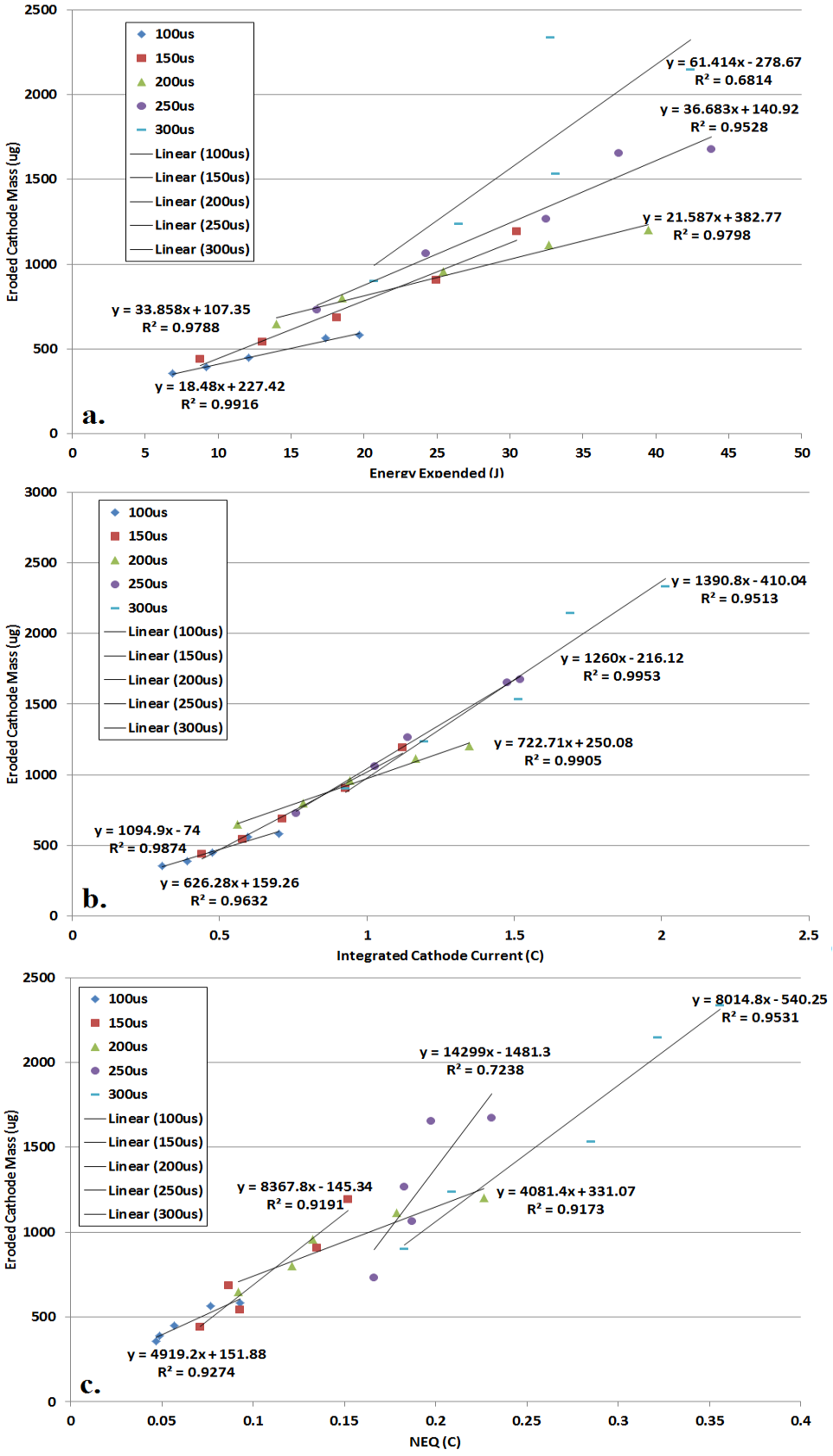

Figure 5.2: Bi erosion rate data.

The vertical axis in each plot is the average mass eroded from the cathode surface per pulse, while the horizontal axes are (from top) the energy expended per pulse, the integrated cathode current per pulse and the net ejected charge (NEQ) per pulse.

5.2 Refractory Metals

Data for Ti were taken in late 2011 at the University of Sydney, and is published in part as part of a paper presented at the 12th Asia Pacific Physics Conference [20]. Data for V, Cr, Mo, Ta, and W were taken in mid-2014 at the University of Sydney and have not been previously published. Ti, V and Cr are referred to as light refractory elements, Mo is the only medium refractory investigated (Zr and Nb were prohibitively expensive) and Ta and W are referred to as heavy refractory elements.

5.2.1 Titanium

Figure 5.3 shows the data for Ti erosion, plotted against the energy expended in the arc per pulse, the integrated cathode current and the net ejected charge. These are shown as subplots a, b and c respectively. Titanium showed moderate erosion in the pattern of behaviour that is described in detail in chapter 8.1.

5.2.2 Vanadium

Figure 5.4 shows the data for V erosion, plotted against the energy expended in the arc per pulse, the integrated cathode current and the net ejected charge. These are shown as subplots a, b and c respectively. The erosion rate of V was moderate, though slightly lower than that of Ti, also following the pattern of erosion rate behaviour described in chapter 8.1.

5.2.3 Chromium

Figure 5.5 shows the data for Cr erosion, plotted against the energy expended in the arc per pulse, the integrated cathode current and the net ejected charge. These are shown as subplots a, b and c respectively. Due to anomalously low mass erosion measurement for the 150µs long, 180 V_{ch} pulses, the slope of the trendline for the other four points was used to derive the quantities presented in chapter 7.2.3; this slope is 20.24µg/C, as opposed to the 17.01µg/C slope of the full data set; the amended slope is much closer to that of the complete dataset, at 23.25µg/C and is within the uncertainty bounds of the other trend slopes.

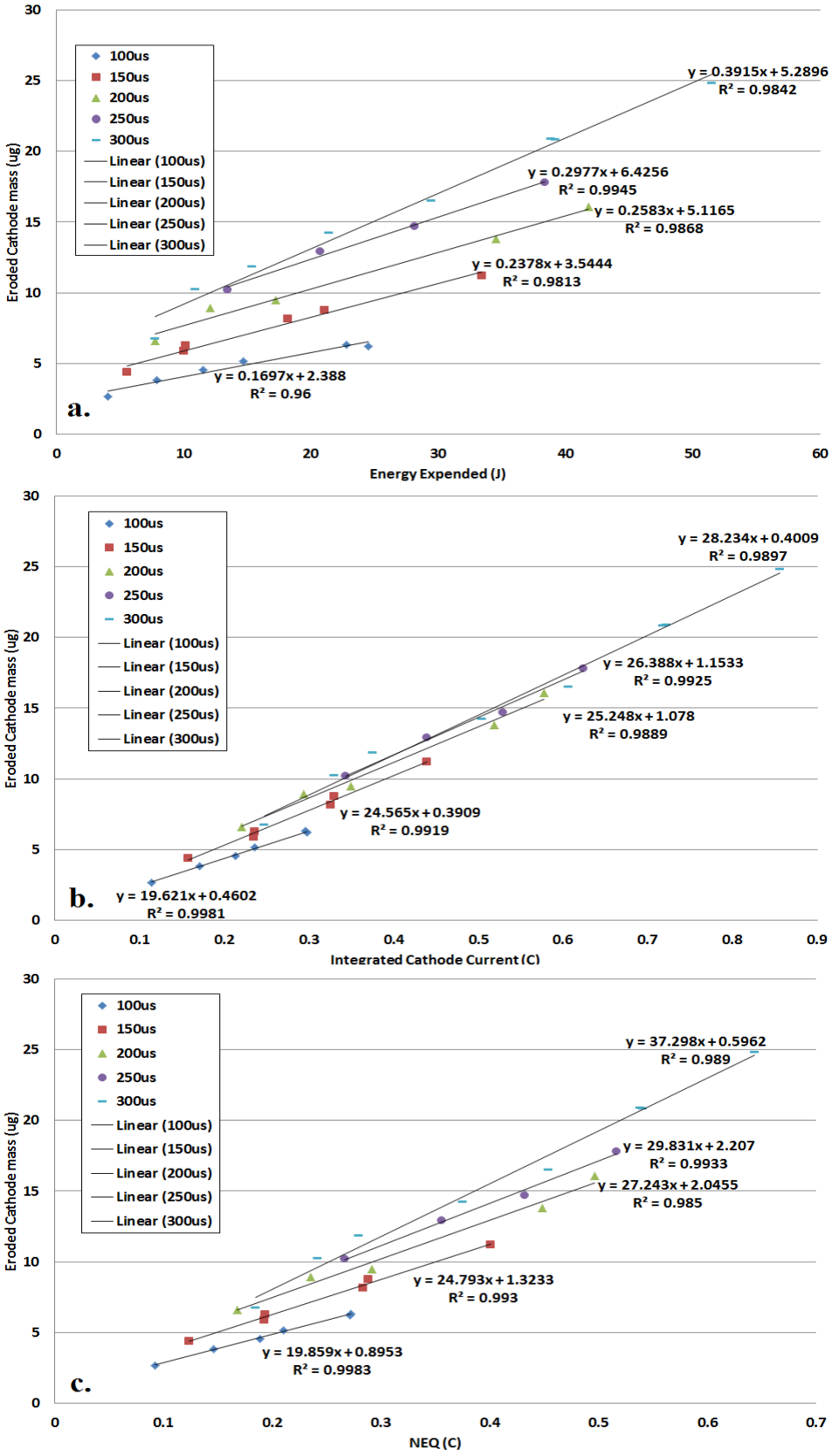

Figure 5.3: Ti erosion rate data.

The vertical axis in each plot is the average mass eroded from the cathode surface per pulse, while the horizontal axes are (from top) the energy expended per pulse, the integrated cathode current per pulse and the net ejected charge (NEQ) per pulse.

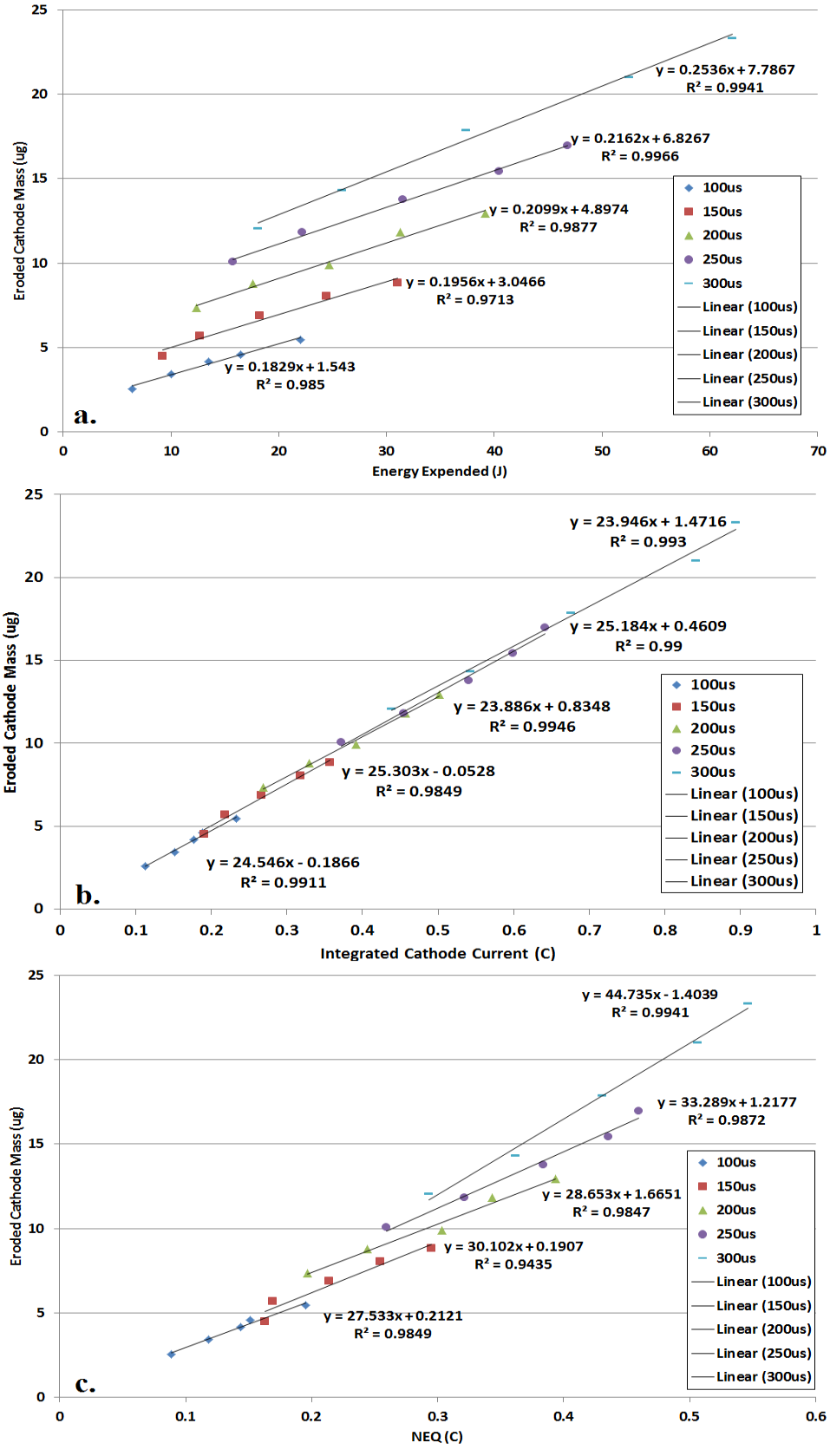

Figure 5.4: V erosion rate data.

The vertical axis in each plot is the average mass eroded from the cathode surface per pulse, while the horizontal axes are (from top) the energy expended per pulse, the integrated cathode current per pulse and the net ejected charge (NEQ) per pulse.

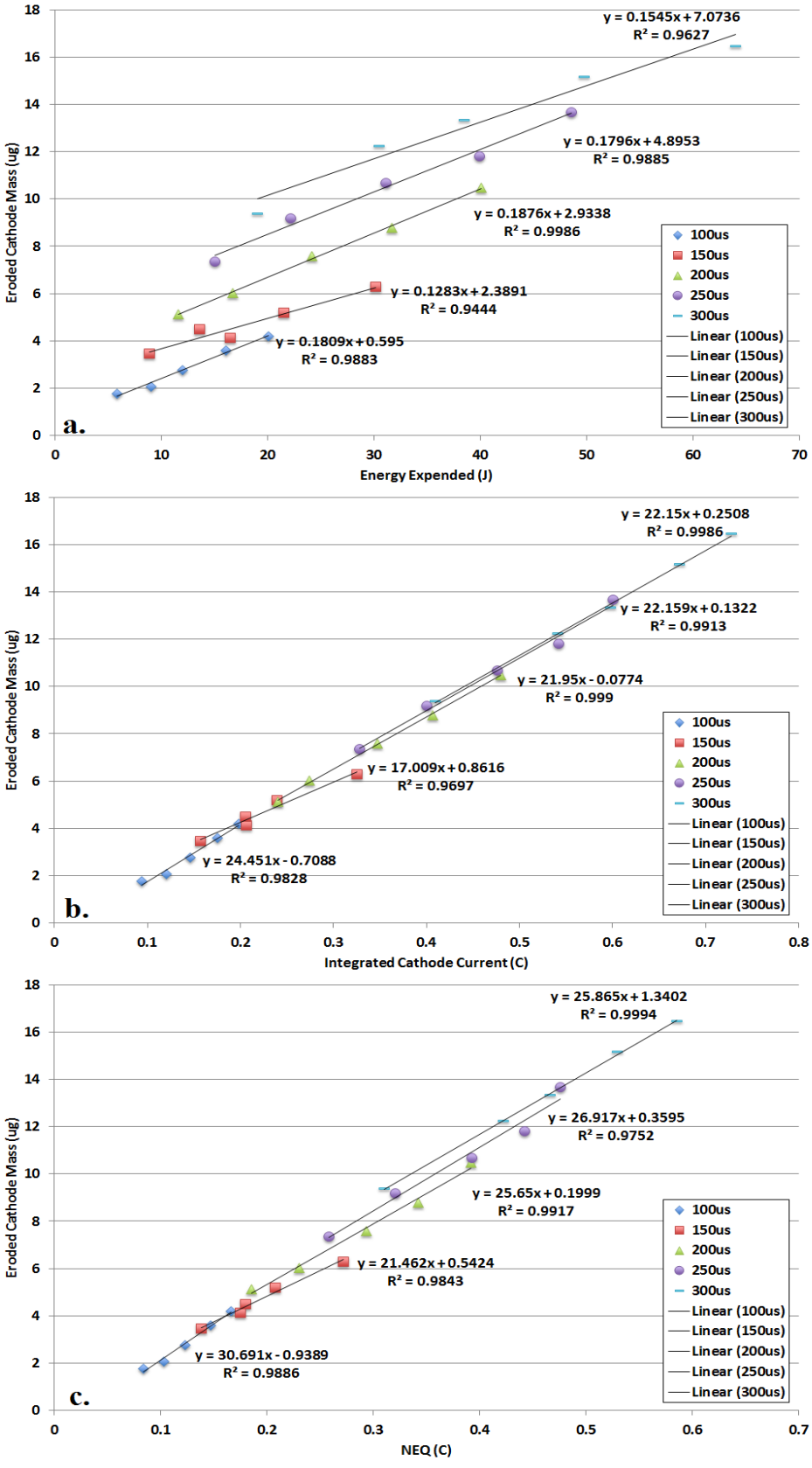

Figure 5.5: Cr erosion rate data.

The vertical axis in each plot is the average mass eroded from the cathode surface per pulse, while the horizontal axes are (from top) the energy expended per pulse, the integrated cathode current per pulse and the net ejected charge (NEQ) per pulse.

5.2.4 Molybdenum

Figure 5.6 shows the data for Mo erosion, plotted against the energy expended in the arc per pulse, the integrated cathode current and the net ejected charge. These are shown as subplots a, b and c respectively. As befits a heavier metal, Mo eroded more mass per charge that V or Ti, while still displaying the same pattern of results described in section 8.1.

5.2.5 Tantalum

Figure 5.7 shows the data for Ta erosion, plotted against the energy expended in the arc per pulse, the integrated cathode current and the net ejected charge. These are shown as subplots a, b and c respectively. Ta erosion rates were at the higher end of moderate, and they followed the same pattern described in section 8.1.

5.2.6 Tungsten

Figure 5.8 shows the data for W erosion, plotted against the energy expended in the arc per pulse, the integrated cathode current and the net ejected charge. These are shown as subplots a, b and c respectively. W erosion rates were at the higher end of moderate, and they followed the same pattern described in section 8.1.

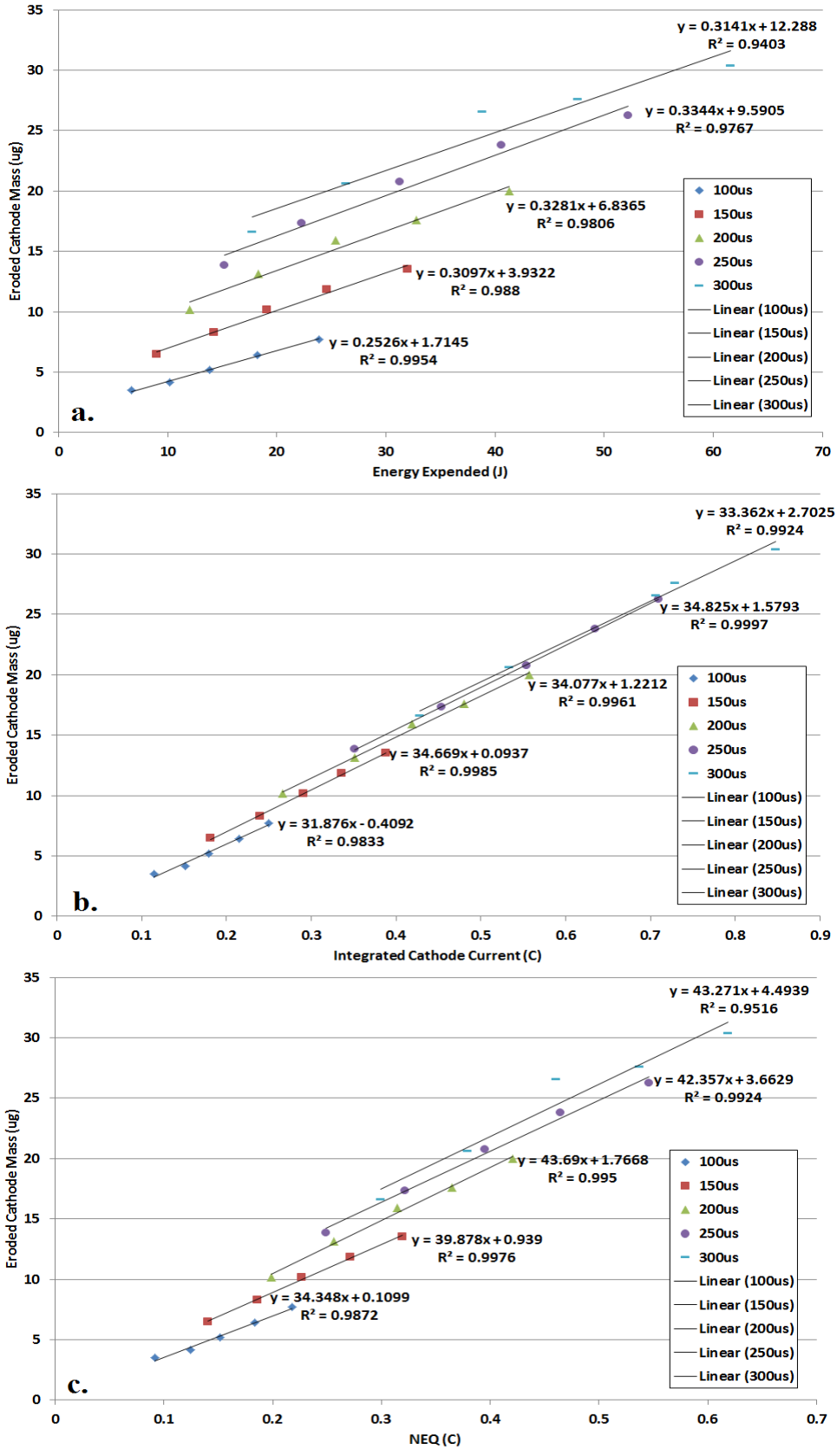

Figure 5.6: Mo erosion rate data.

The vertical axis in each plot is the average mass eroded from the cathode surface per pulse, while the horizontal axes are (from top) the energy expended per pulse, the integrated cathode current per pulse and the net ejected charge (NEQ) per pulse.

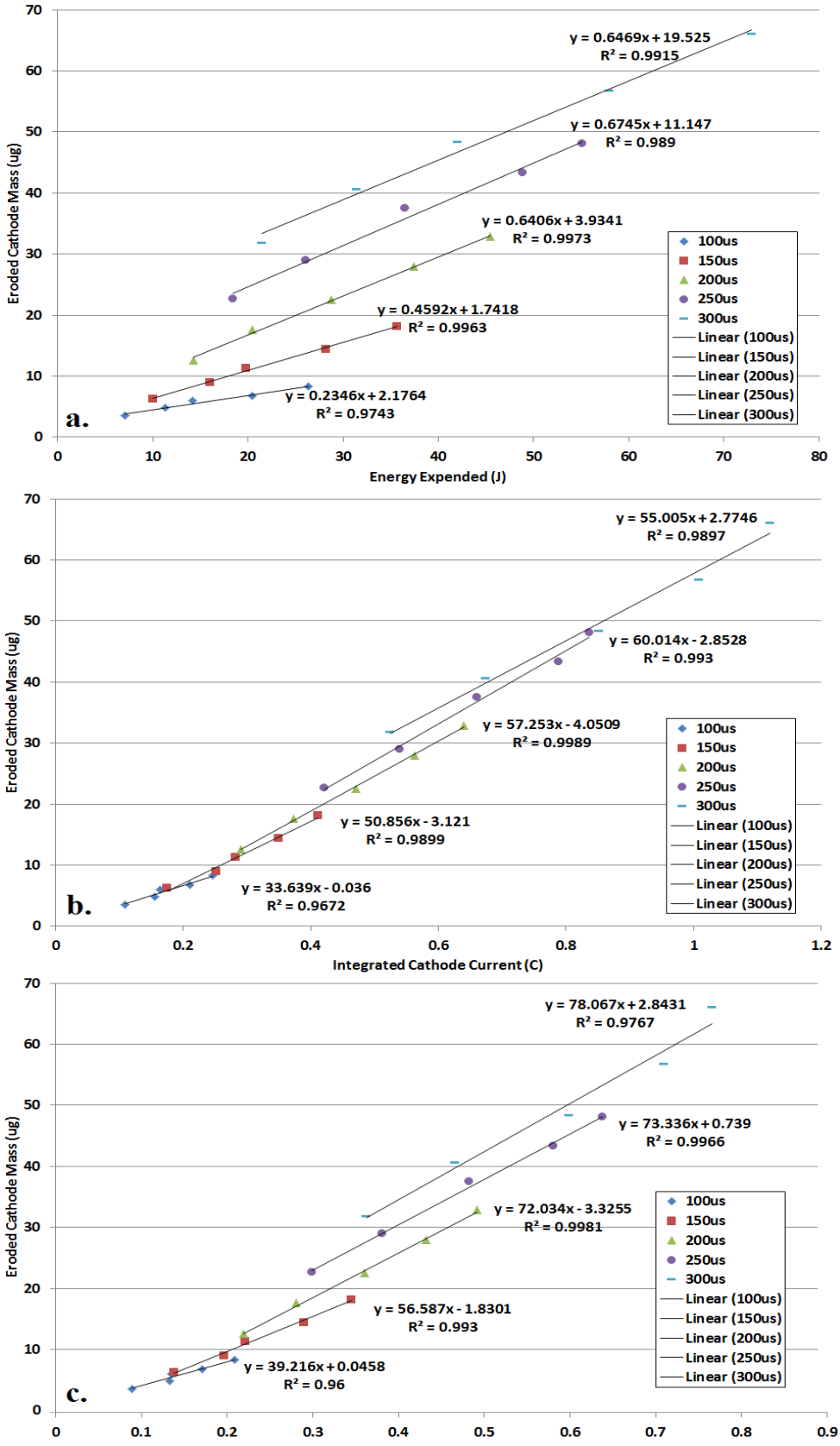

Figure 5.7: Ta erosion rate data.

The vertical axis in each plot is the average mass eroded from the cathode surface per pulse, while the horizontal axes are (from top) the energy expended per pulse, the integrated cathode current per pulse and the net ejected charge (NEQ) per pulse.

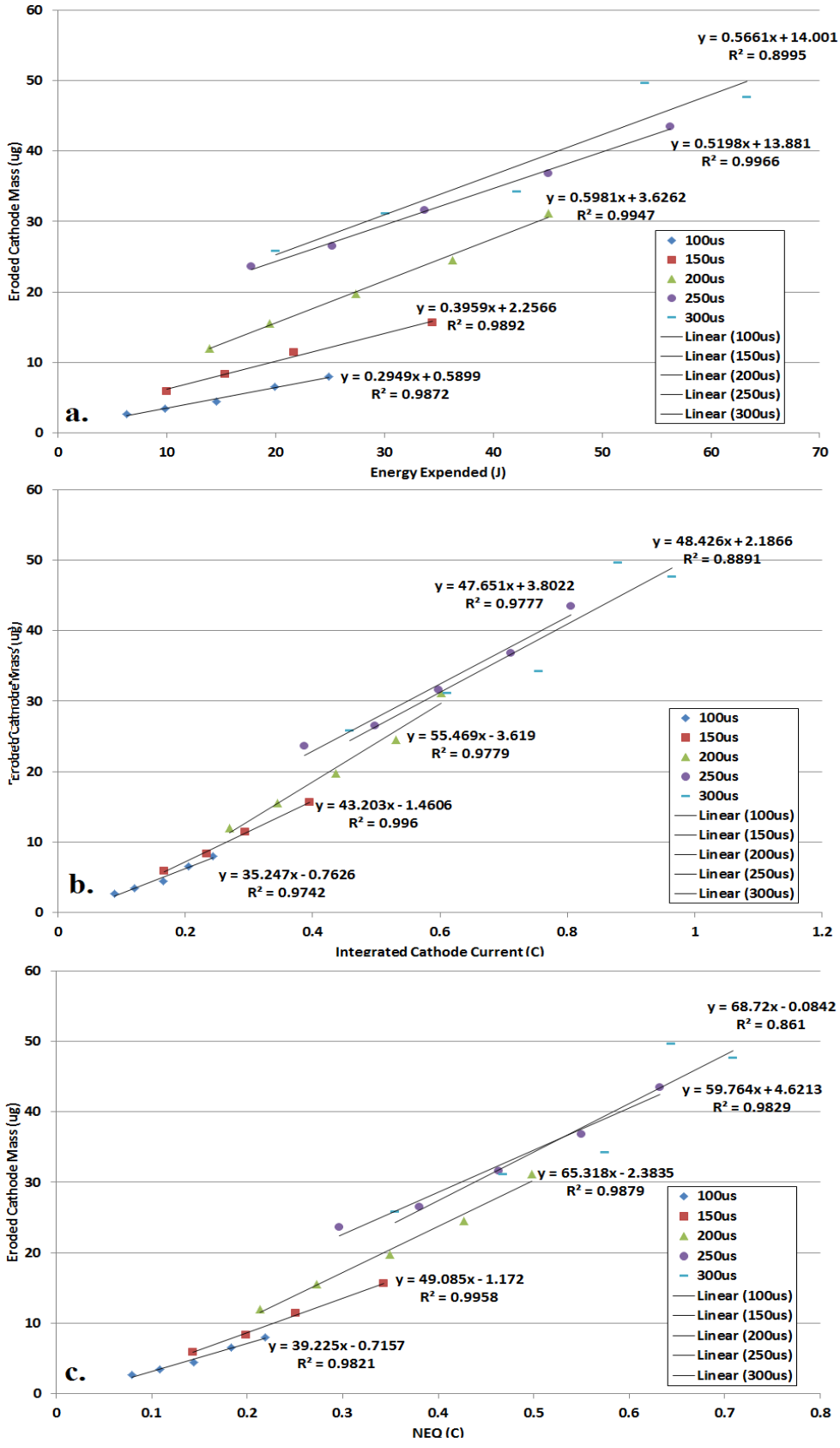

Figure 5.8: W erosion rate data.

The vertical axis in each plot is the average mass eroded from the cathode surface per pulse, while the horizontal axes are (from top) the energy expended per pulse, the integrated cathode current per pulse and the net ejected charge (NEQ) per pulse.

5.3 Light Elements

Data for all light elements investigated, being C, Mg and Al, were taken in mid-2014 at the University of Sydney and has not been previously published.

5.3.1 Carbon

Figure 5.9 shows the data for C erosion, plotted against the energy expended in the arc per pulse, the integrated cathode current and the net ejected charge. These are shown as subplots a, b and c respectively. The deep pits eroded in C cathodes necessitated using several C cathodes to derive the erosion rate data. It was also found that the heat generated by the arc firing seemed to bake out volatiles and increase thrust; see chapter 6.3.1 for more information. Due to the variability in packing density and granular size between carbon cathodes the trendline slope for all C data taken was used to determine the carbon erosion rate. The C cathode erosion rate used in chapter 7.3.1 is 33.46µg/C.

5.3.2 Magnesium

Figure 5.10 shows the data for Mg erosion, plotted against the energy expended in the arc per pulse, the integrated cathode current and the net ejected charge. These are shown as subplots a, b and c respectively. The data for 300µs long pulses fired at a charging voltage of 180V have been omitted from the plot due to the large amount of side-arcing observed; this led to a significantly increased amount of erosion and thus a large departure from linearity. The full plot can be found in figure 11.1. Magnesium erosion rates were the lowest of any material tested in this thesis.

5.3.3 Aluminium

Figure 5.11 shows the data for Al erosion, plotted against the energy expended in the arc per pulse, the integrated cathode current and the net ejected charge. These are shown as subplots a, b and c respectively. Al erosion rate behaviour was similar to that of V; moderate erosion rates, following the pattern described in section 8.1.

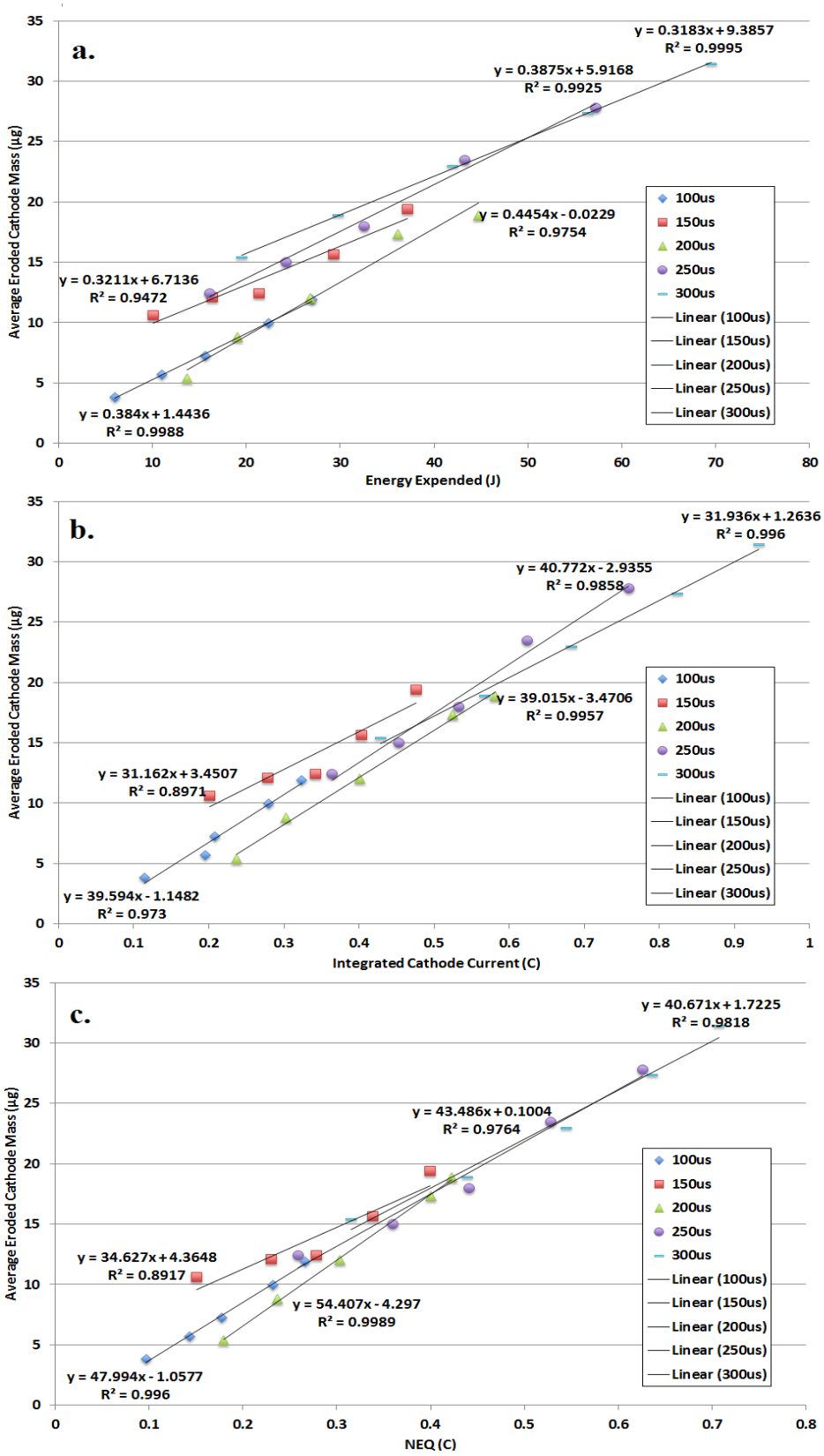

Figure 5.9: C erosion rate data.

The vertical axis in each plot is the average mass eroded from the cathode surface per pulse, while the horizontal axes are (from top) the energy expended per pulse, the integrated cathode current per pulse and the net ejected charge (NEQ) per pulse.

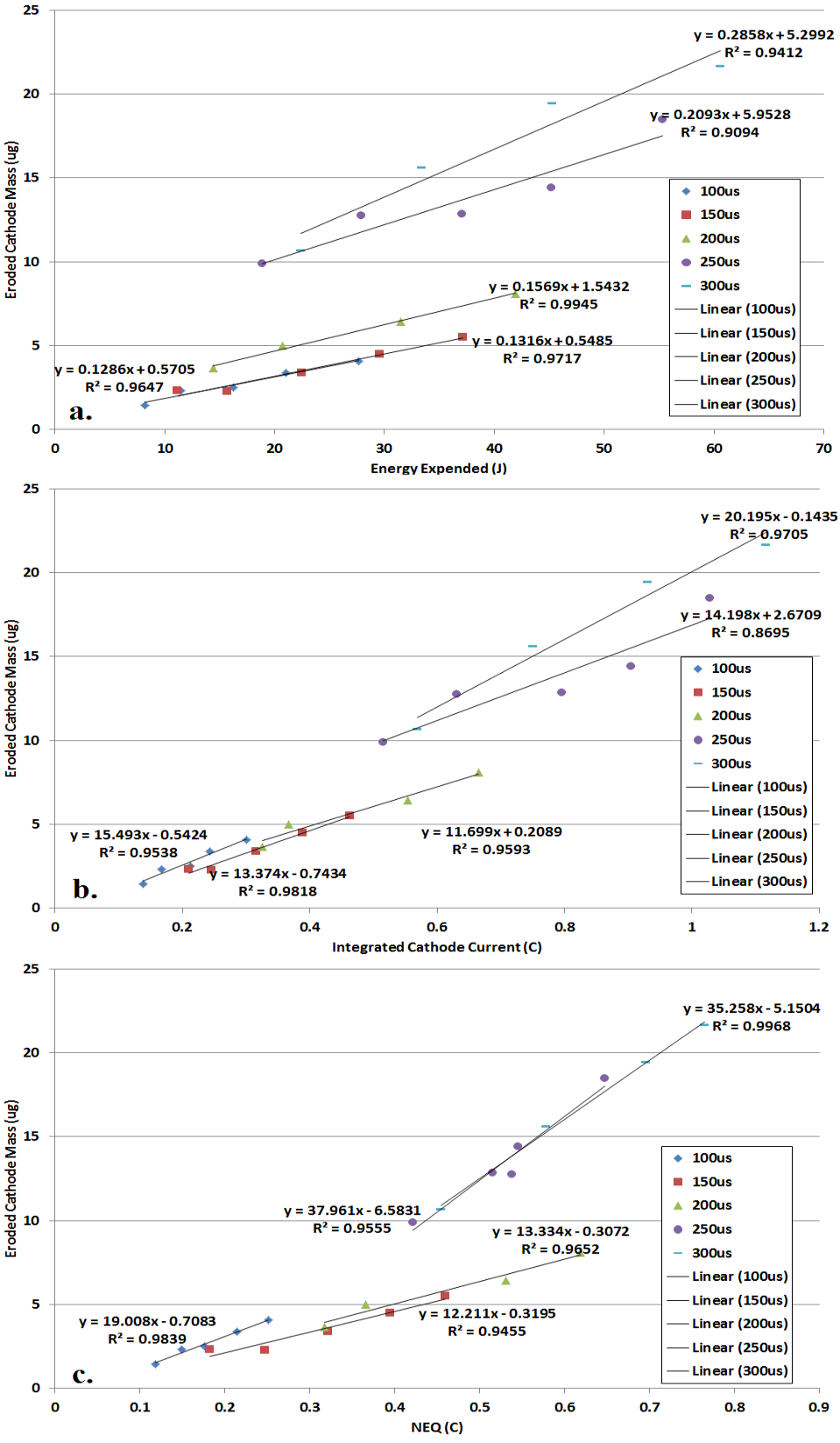

Figure 5.10: Mg erosion rate data.

The vertical axis in each plot is the average mass eroded from the cathode surface per pulse, while the horizontal axes are (from top) the energy expended per pulse, the integrated cathode current per pulse and the net ejected charge (NEQ) per pulse.

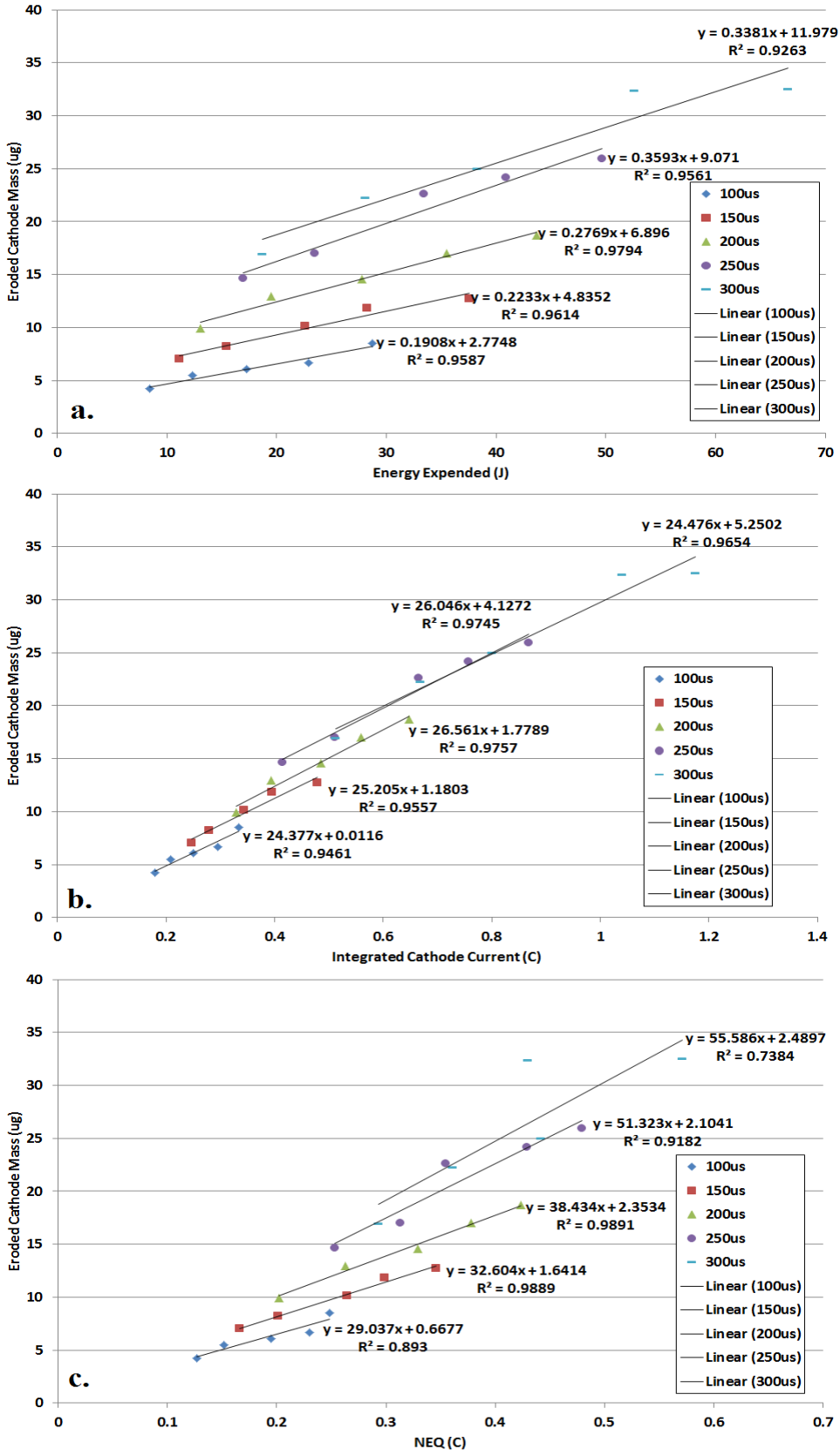

Figure 5.11: Al erosion rate data.

The vertical axis in each plot is the average mass eroded from the cathode surface per pulse, while the horizontal axes are (from top) the energy expended per pulse, the integrated cathode current per pulse and the net ejected charge (NEQ) per pulse.

5.4 Summary of Cathode Erosion Rates

The data shows that elements with high vapour pressures tend to have much higher cathode erosion rates, though the low erosion rate of Mg comes as a surprise given its high vapour pressure at low temperatures (elemental SVP of 1Pa at: 701K for Mg, 941K for Bi, 1497K for Sn, 1656K for Cr [58]). Magnesium and chromium are the most efficient materials in terms of material eroded per unit charge transiting the cathode, while bismuth is by far the most eroded material under any metric.

The trendline gradients of the various "b" subplots, those for average cathode mass eroded per pulse vs integrated cathode current were used to determine the cathode mass flow rate needed to determine specific impulse and jet power efficiency. These derived quantities are shown in chapter 7, while chapter 6 shows the raw impulse and thrust data for non-eroded and eroded cathode surfaces. The slopes of each trendline fitted to each dataset plotted in a "b" subplot, which is the cathode erosion rate, is shown in table 5.2.

Element	Figure	100 μs Erosion Rate (μg/C)	150 μs Erosion Rate (μg/C)	200 μs Erosion Rate (μg/C)	250 μs Erosion Rate (μg/C)	300 μs Erosion Rate (μg/C)
Sn	5.1	189±32	200±34	377±51	442±29	502±24
Bi	5.2	626±71	1090±71	723±41	1260±50	1390±182
Ti	5.3	19.6±0.4	24.6±1.1	25.2±1.5	26.4±1.6	28.2±1.2
V	5.4	24.5±1.3	25.3±1.8	23.9±1.0	25.1±1.5	23.9±1.2
Cr	5.5	24.5±1.9	20.2±3.7	21.9±0.4	22.2±1.2	22.2±0.5
Mo	5.6	31.8±2.4	34.7±0.8	34.1±1.2	34.8±0.3	33.4±1.7
Ta	5.7	33.6±3.6	50.9±3.0	57.3±1.1	60.0±2.9	55.0±3.2
W	5.8	35.2±3.3	43.2±1.9	47.7±0.7	47.7±4.2	48.4±9.9
C	5.9	39.6±3.8	31.2±6.1	39.0±1.5	40.8±2.8	31.9±1.2
Mg	5.10	15.5±2.0	13.4±1.1	11.7±1.7	14.2±3.2	20.2±2.5
Al	5.11	24.4±3.4	25.2±3.1	26.7±2.4	26.0±2.4	24.5±2.7

Table 5.2: Cathode erosion rates for all elements examined. Erosion rates are calculated from the gradients of the trendline fits, which were not constrained to pass through the origin. Erosion rate values are to three significant figures.

Comparison between the slopes of the plots of erosion vs integrated cathode current and erosion vs NEQ lends itself to a discussion on the prevalence of side-arcing from cathode to anode, which appears in chapter 8. The relative rate of production of neutral species can be inferred from analysis of the slopes of the various plots, which is also discussed in chapter 8.

6 Impulse and Thrust Measurements

This chapter contains measurements of the impulse delivered to the pendulum described in chapter 3 by arcs struck from the surface of cathodes made from the materials selected in chapter 4. The experiments explore the same parameter space as chapter 5. Table 6.1 summarises the data sets used to produce these results. All measurements have 2% uncertainty as discussed in section 3.1.6.

Cathode material	Shot Numbers for Impulse Measurement from a Non-eroded Cathode Surface	Average Pendulum Mass for Non-eroded Measurements (g)	Shot Numbers for Impulse Measurement from an Eroded Cathode Surface	Average Pendulum Mass for Eroded Measurements (g)	General Notes on the data set.
Bi	35719-35884	4.7070	35166-35323	4.6384	Bi non-eroded retaken to attempt to find trends wrt NEQ, with no change in result.
Sn	32688-32808	4.7655	32496-32650	4.7655	Well behaved.
Ti	36134-36304	4.7070	32155-32311	4.7655	Ti Non-eroded re-taken due to an inadequately cleaned cathode, otherwise well behaved.
V	31361-31518	4.6245	35337-35527	4.6384	Well behaved.
Cr	33946-34123	4.6384	33783-33934	4.6384	Well behaved.
Mo	35968-36132	4.7070	34289-34456	4.6384	Mo Non-eroded re-taken due to an inadequately cleaned cathode, otherwise well behaved.
Ta	31979-32143	4.7655	34460-34626	4.6384	Well behaved.
W	32833-32913 35887-35941	4.7655 4.7070	34629-34807	4.6384	Part of W Non-eroded re-taken due to poor photodiode readings due to material deposition on the window, otherwise well behaved.
C	35560-35717	4.7070	34989-35164	4.6384	C Non-eroded data taken after 3000 pulses had been fired to remove all volatiles from the cathode, otherwise well behaved.
Mg	31807-31973	4.7655	34810-34987	4.6384	Well behaved.
Al	33625-33781	4.8851	33464-33623	4.8851	Well behaved.

Table 6.1: Summary of impulse and thrust data sets with comments. A well-behaved data set shows impulse scaling with pulse current and duration while being reliably triggered throughout.

In all odd numbered figures in this chapter (ie 6.1, 6.3, 6.5 etc) the first row of panels (showing subplots a, c and e) plot the impulse measurements for a non-eroded cathode surface while the second row of plots (b, d and f) show the impulse measurements for an eroded cathode surface. Subplots a and b show the impulse delivered plotted against energy expended in the arc per pulse; c and d against integrated cathode current; and e and f against NEQ.

Dividing the impulse delivered by the pulse duration gives the average net force exerted on the pendulum. This force is plotted in the even numbered figures in this chapter (ie 6.2, 6.4, 6.6 etc) and is used to calculate the standard efficiency metrics discussed in chapter 7. The first row of sub-plots (showing subplots a, c and e) plot the force produced by plasma from a non-eroded cathode surface while the second row of plots (b, d and f) show the force produced by plasma from eroded cathode surfaces. Subplots a and b show the force exerted plotted against energy expended in the arc per pulse; c and d against integrated cathode current; and e and f against NEQ.

6.1 Non-Refractory metals

Data for both Sn and Bi were taken in mid-2014 at the University of Sydney and have not been previously published.

6.1.1 Tin

Figures 6.1 and 6.2 show the data for Sn impulse measurements. Approximately 20,000 pulses were fired, which eroded approximately 7.3g of cathode material. Linear trendlines have been fitted to both figures, with regression coefficients greater than 0.9 in all cases. Data were linear within each duration data set, with trends discussed in chapter 8.

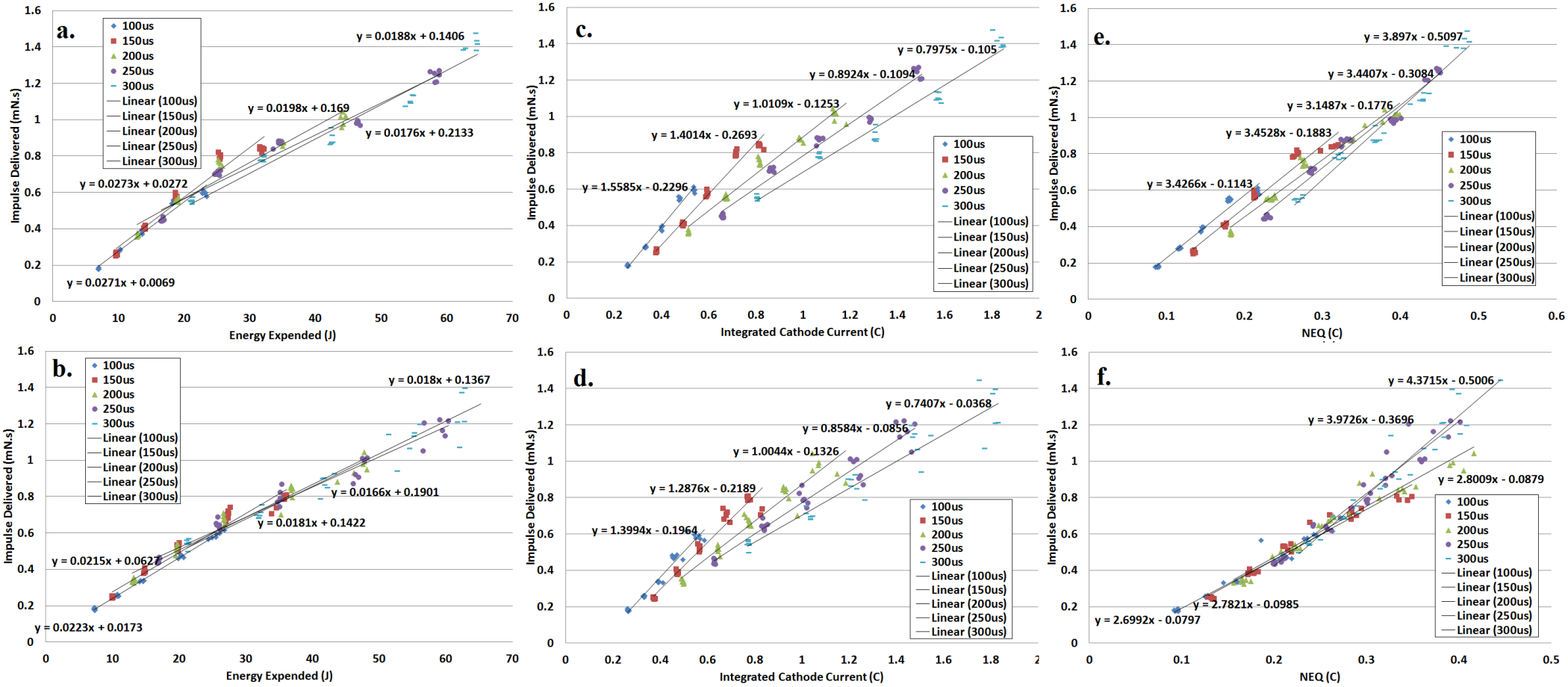

Figure 6.1: Sn impulse data.

Vertical axis in each plot is the measured impulse delivered to the pendulum by each pulse of plasma, while horizontal axes are (from left) the energy expended in the arc by that pulse, the integrated cathode current for that pulse and the net ejected charge (NEQ) for that pulse. Each trendline has R greater than 0.9. Top row of plots shows data for a non-eroded cathode, bottom row shows eroded cathode data.

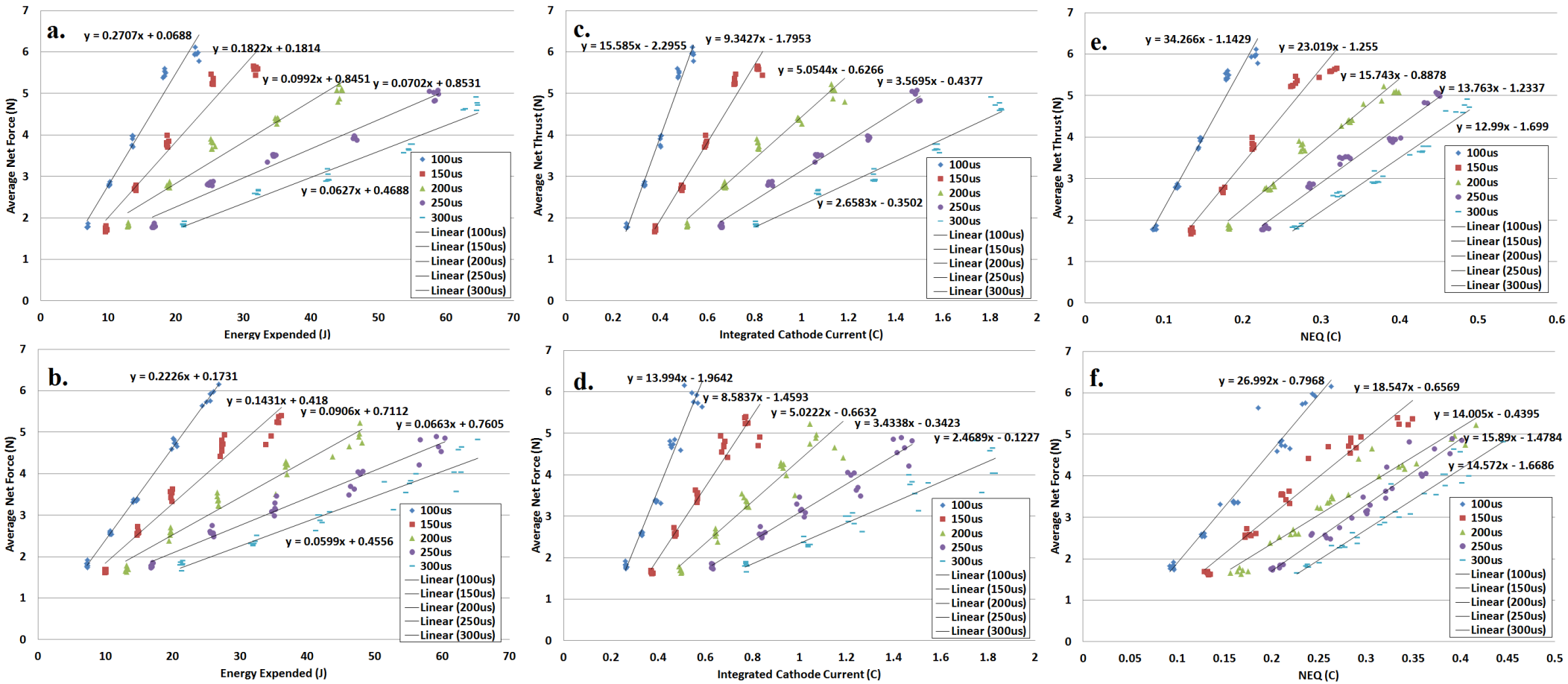

Figure 6.2: Sn Thrust data.

Vertical axis in each plot is the average net force exerted on the pendulum by each pulse of plasma, while horizontal axes are (from left) the energy expended in the arc by that pulse, the integrated cathode current for that pulse and the net ejected charge (NEQ) for that pulse. Each trendline has R greater than 0.9. Top row of plots shows data for a non-eroded cathode, bottom row shows eroded cathode data.

6.1.2 Bismuth

Figures 6.3 and 6.4 show the data for Bi impulse measurements. Approximately 15,000 pulses were fired, which eroded approximately 14.9g of cathode material. Linear trendlines have been fitted to all data sets to allow easy comparison, except for the data plotted against NEQ. The regression coefficients of the plotted trendlines are greater than 0.9 in all cases, whereas no good fit could be found for the NEQ data.

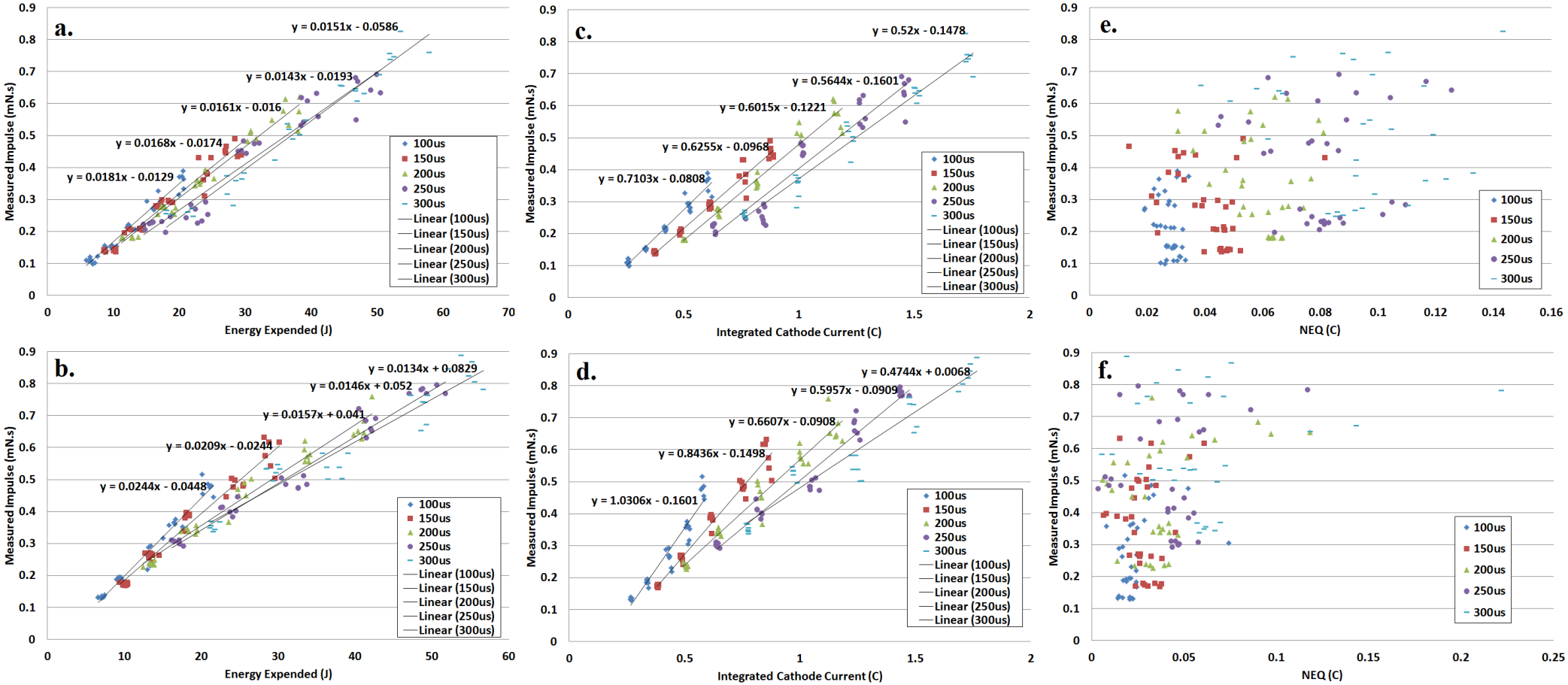

Figure 6.3: Bi impulse data.

Vertical axis in each plot is the measured impulse delivered to the pendulum by each pulse of plasma, while horizontal axes are (from left) the energy expended in the arc by that pulse, the integrated cathode current for that pulse and the net ejected charge (NEQ) for that pulse. Each trendline has R greater than 0.9. Top row of plots shows data for a non-eroded cathode, bottom row shows eroded cathode data.

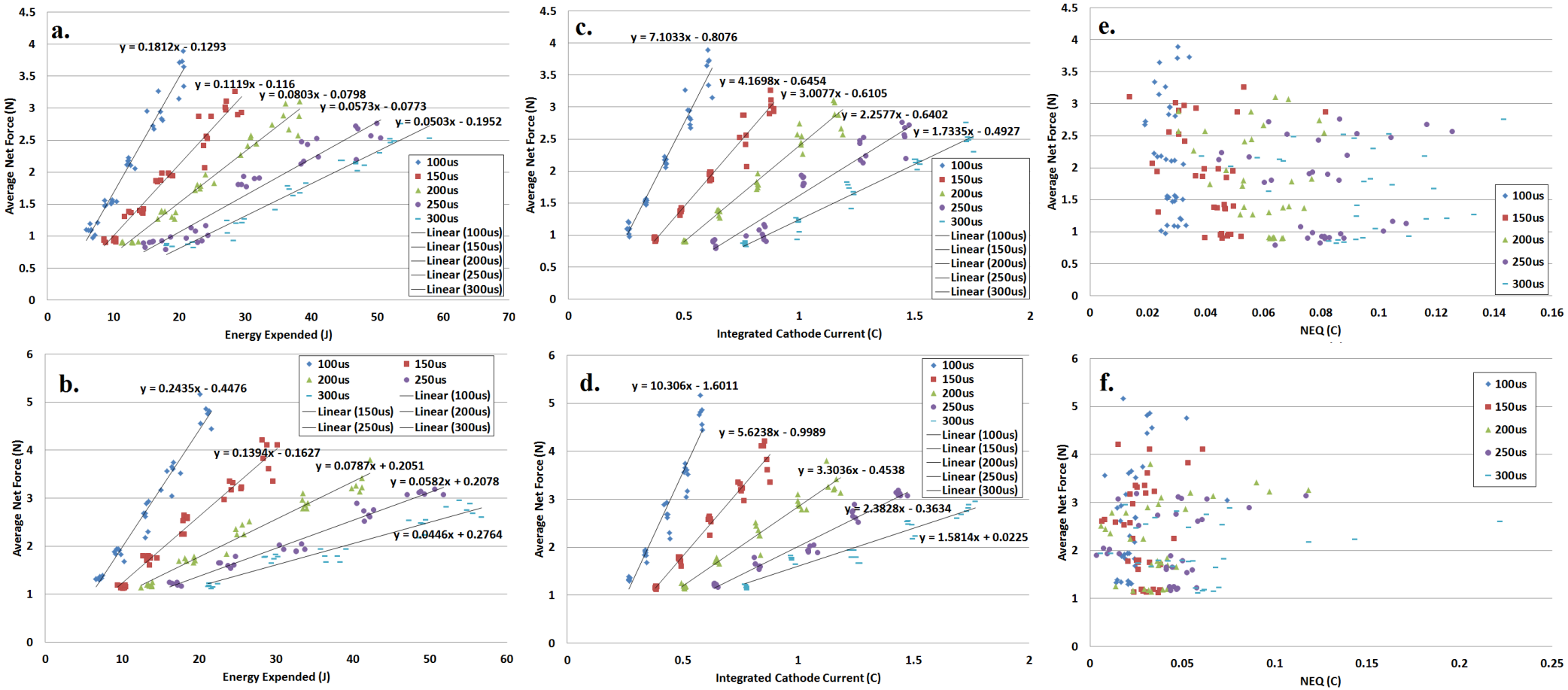

Figure 6.4: Bi thrust data.

Vertical axis in each plot is the average net force exerted on the pendulum by each pulse of plasma, while horizontal axes are (from left) the energy expended in the arc by that pulse, the integrated cathode current for that pulse and the net ejected charge (NEQ) for that pulse. Each trendline has R greater than 0.9. Top row of plots shows data for a non-eroded cathode, bottom row shows eroded cathode data.

6.2 Refractory Metals

Data for Ti, V, Cr, Mo, Ta, and W were taken in mid-2014 at the University of Sydney and have not been previously published. Ti, V and Cr are referred to as light refractory elements, Mo is the only medium refractory investigated (Zr and Nb were prohibitively expensive) and Ta and W are referred to as heavy refractory elements.

6.2.1 Titanium

Figures 6.5 and 6.6 show the data for Ti impulse measurements. Approximately 460,000 pulses were fired, which eroded approximately 3.8g of cathode material. Linear trendlines have been fitted, with regression coefficients greater than 0.95 in all cases. Titanium was well-behaved and highly linear in its behaviour.

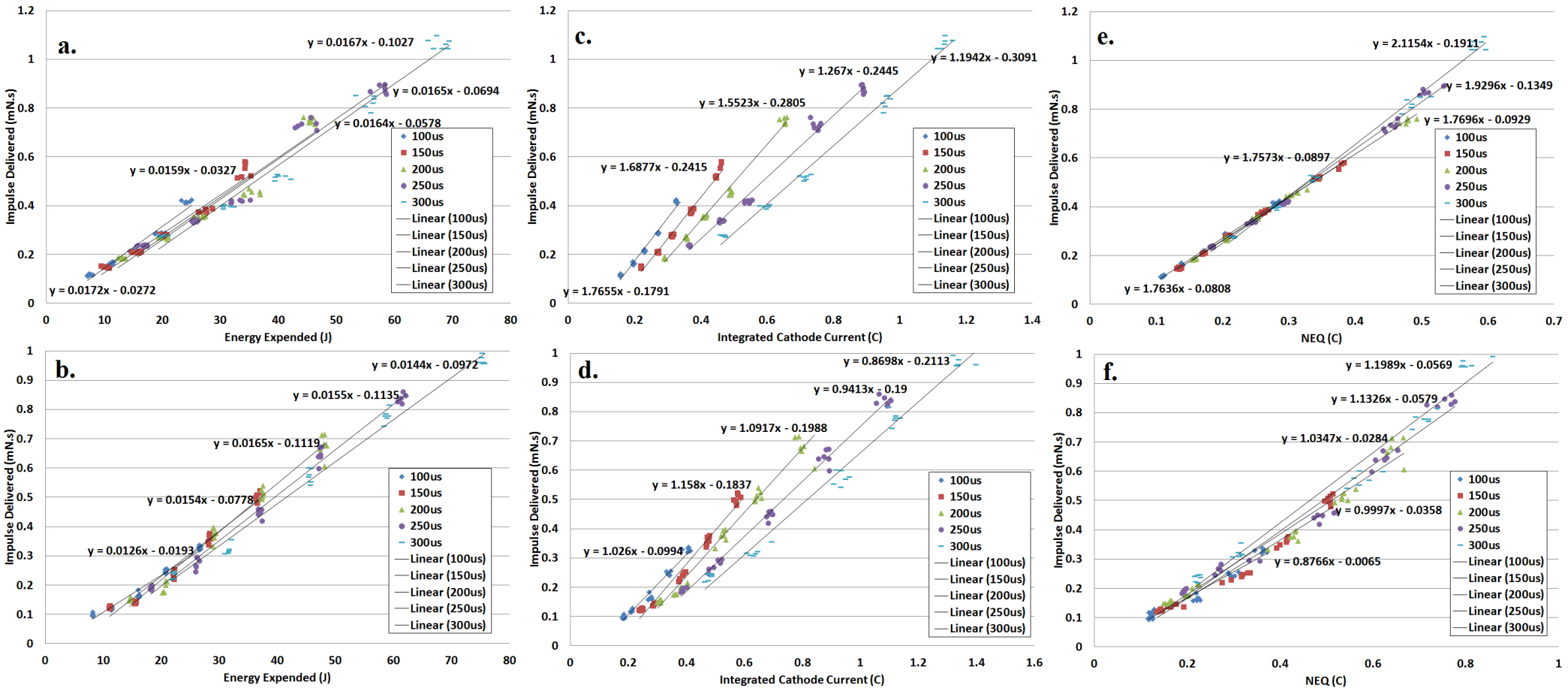

Figure 6.5: Ti impulse data.

Vertical axis in each plot is the measured impulse delivered to the pendulum by each pulse of plasma, while horizontal axes are (from left) the energy expended in the arc by that pulse, the integrated cathode current for that pulse and the net ejected charge (NEQ) for that pulse. Each trendline has R greater than 0.95. Top row of plots shows data for a non-eroded cathode, bottom row shows eroded cathode data.

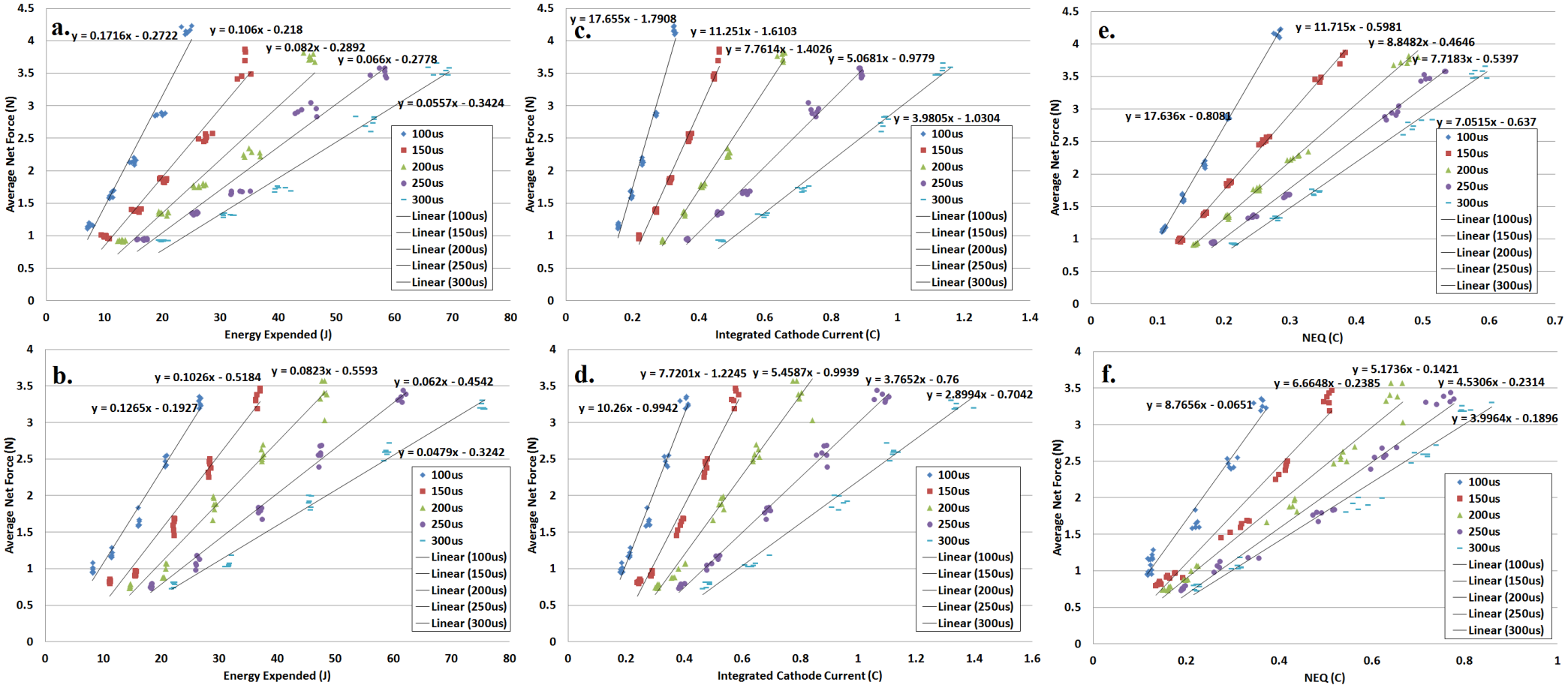

Figure 6.6: Ti thrust data.

Vertical axis in each plot is the average net force exerted on the pendulum by each pulse of plasma, while horizontal axes are (from left) the energy expended in the arc by that pulse, the integrated cathode current for that pulse and the net ejected charge (NEQ) for that pulse. Each trendline has R greater than 0.95. Top row of plots shows data for a non-eroded cathode, bottom row shows eroded cathode data.

6.2.2 Vanadium

Figure 6.7 and 6.8 show the data for V impulse measurements. Approximately 333,000 pulses were fired, which eroded approximately 3.0g of cathode material. Linear trendlines have been fitted, with regression coefficients greater than 0.95 in all cases. Vanadium was well-behaved and highly linear in its behaviour.

. .

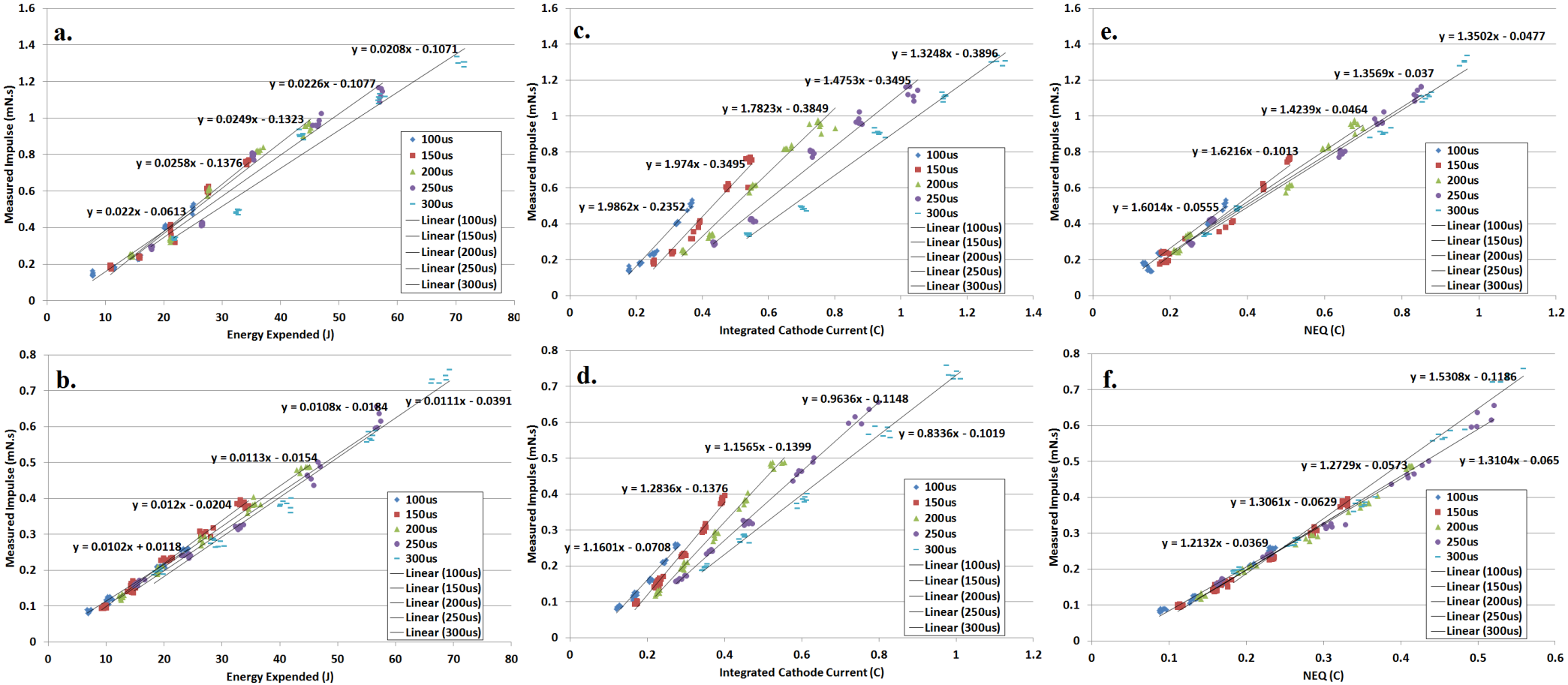

Figure 6.7: V impulse data.

Vertical axis in each plot is the measured impulse delivered to the pendulum by each pulse of plasma, while horizontal axes are (from left) the energy expended in the arc by that pulse, the integrated cathode current for that pulse and the net ejected charge (NEQ) for that pulse. Each trendline has R greater than 0.95. Top row of plots shows data for a non-eroded cathode, bottom row shows eroded cathode data.

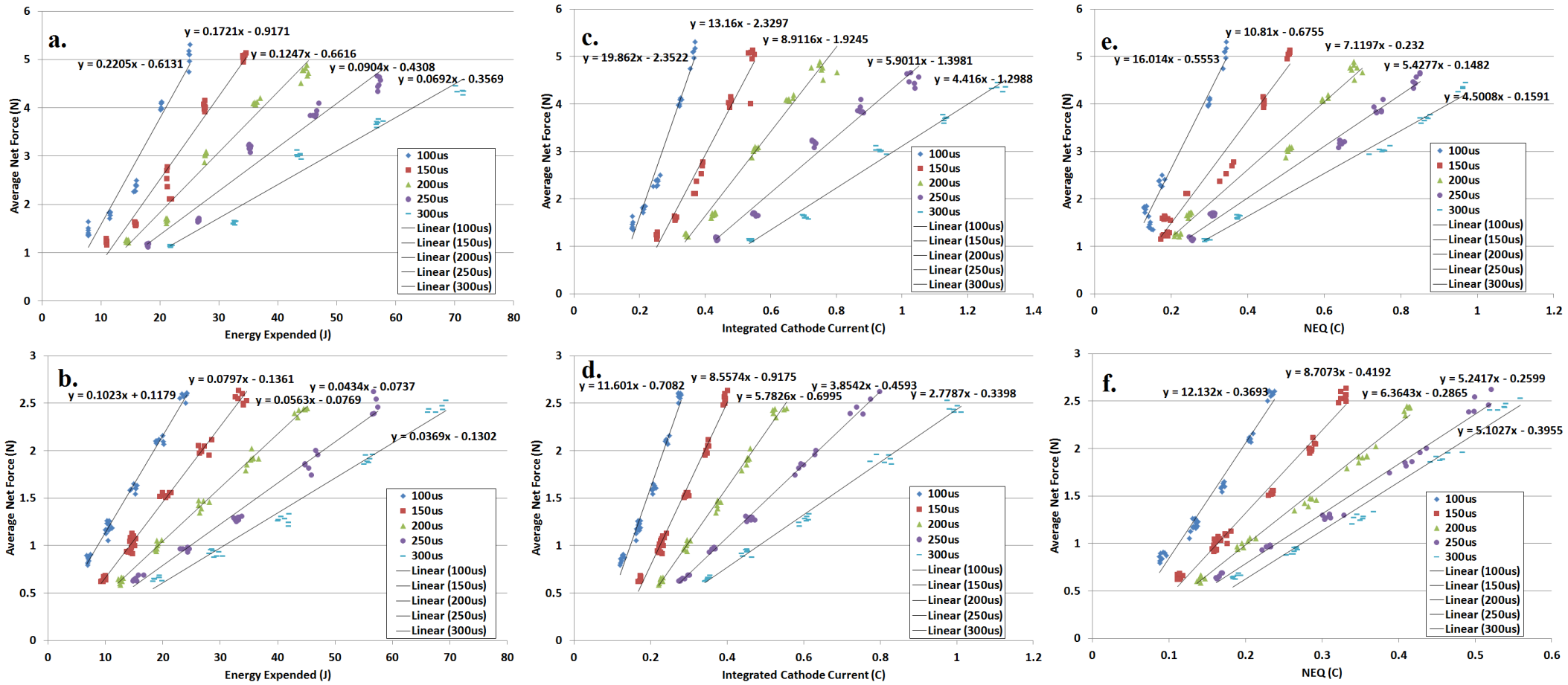

Figure 6.8: V thrust data.

Vertical axis in each plot is the average net force exerted on the pendulum by each pulse of plasma, while horizontal axes are (from left) the energy expended in the arc by that pulse, the integrated cathode current for that pulse and the net ejected charge (NEQ) for that pulse. Each trendline has R greater than 0.95. Top row of plots shows data for a non-eroded cathode, bottom row shows eroded cathode data.

6.2.3 Chromium

Figures 6.9 and 6.10 show the data for Cr impulse measurements. Approximately 406,000 pulses were fired, which eroded approximately 3.1g of cathode material. Linear trendlines have been fitted, with regression coefficients greater than 0.9 in all cases. Chromium was well-behaved and highly linear in its behaviour, though producing less thrust than Ti or V.

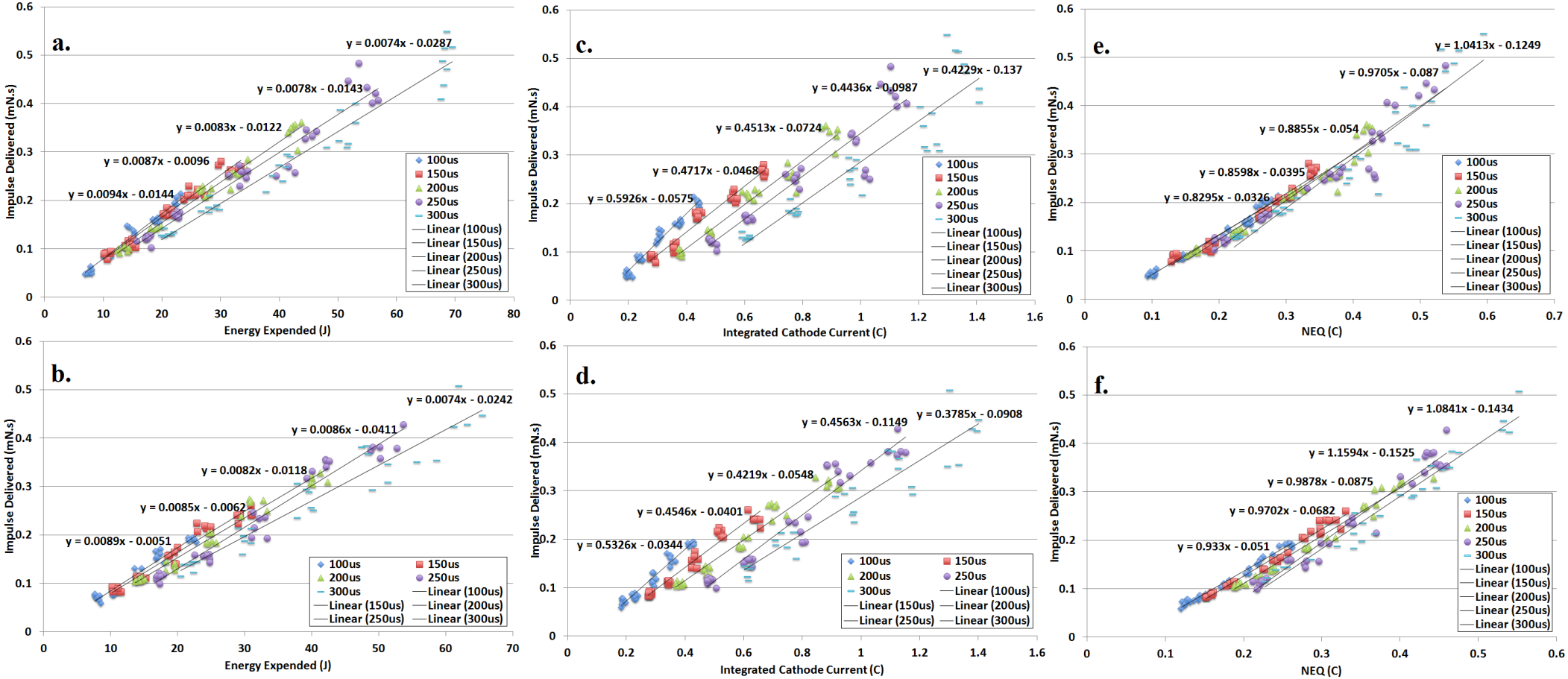

Figure 6.9: Cr impulse data.

Vertical axis in each plot is the measured impulse delivered to the pendulum by each pulse of plasma, while horizontal axes are (from left) the energy expended in the arc by that pulse, the integrated cathode current for that pulse and the net ejected charge (NEQ) for that pulse. Each trendline has R greater than 0.95. Top row of plots shows data for a non-eroded cathode, bottom row shows eroded cathode data.

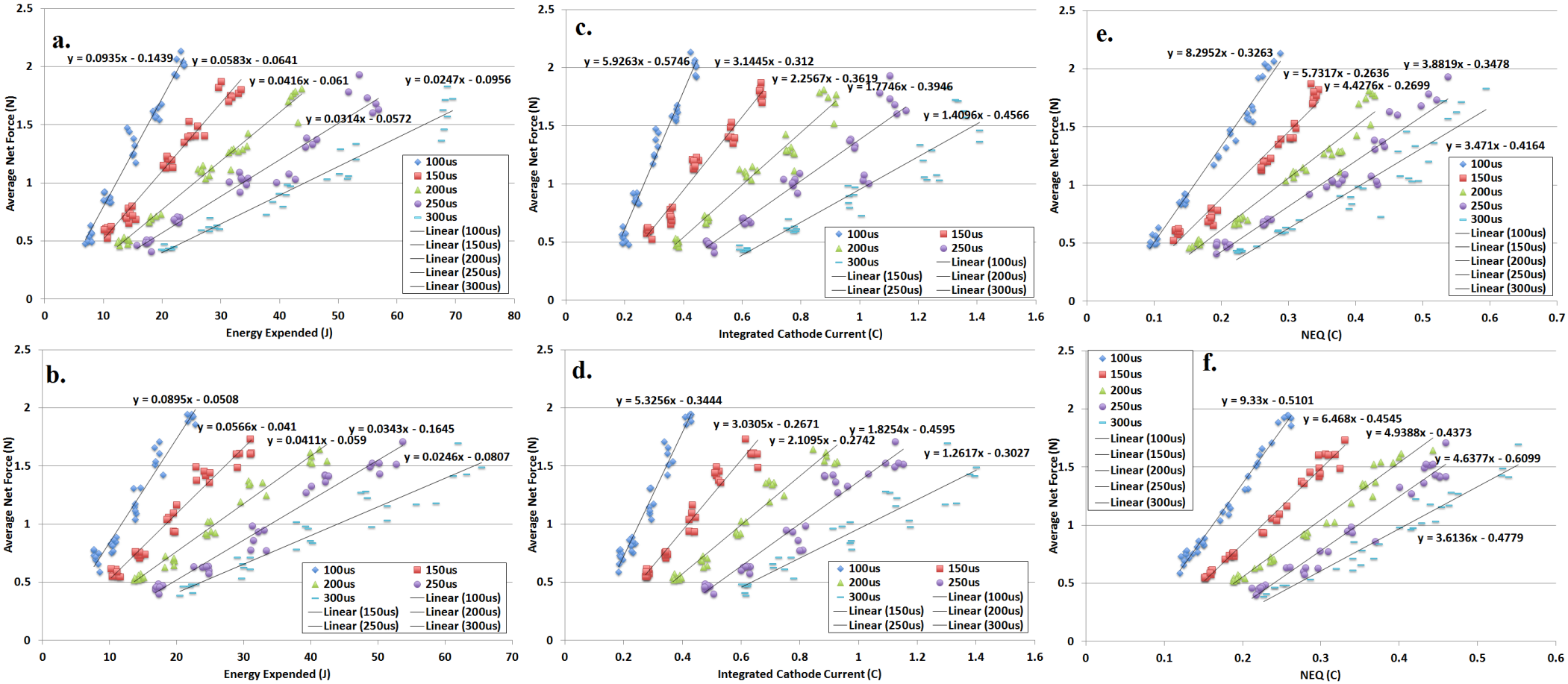

Figure 6.10: Cr thrust data.

Vertical axis in each plot is the average net force exerted on the pendulum by each pulse of plasma, while horizontal axes are (from left) the energy expended in the arc by that pulse, the integrated cathode current for that pulse and the net ejected charge (NEQ) for that pulse. Each trendline has R greater than 0.95. Top row of plots shows data for a non-eroded cathode, bottom row shows eroded cathode data.

6.2.4 Molybdenum

Figures 6.11 and 6.12 show the data for Mo impulse measurements. Approximately 333,000 pulses were fired, which eroded approximately 3.0g of cathode material. Linear trendlines have been fitted, with regression coefficients greater than 0.95 in most cases; the exception being the 250 and 300μs thrust data, with coefficients above 0.9. Molybdenum was well-behaved and highly linear in its behaviour.

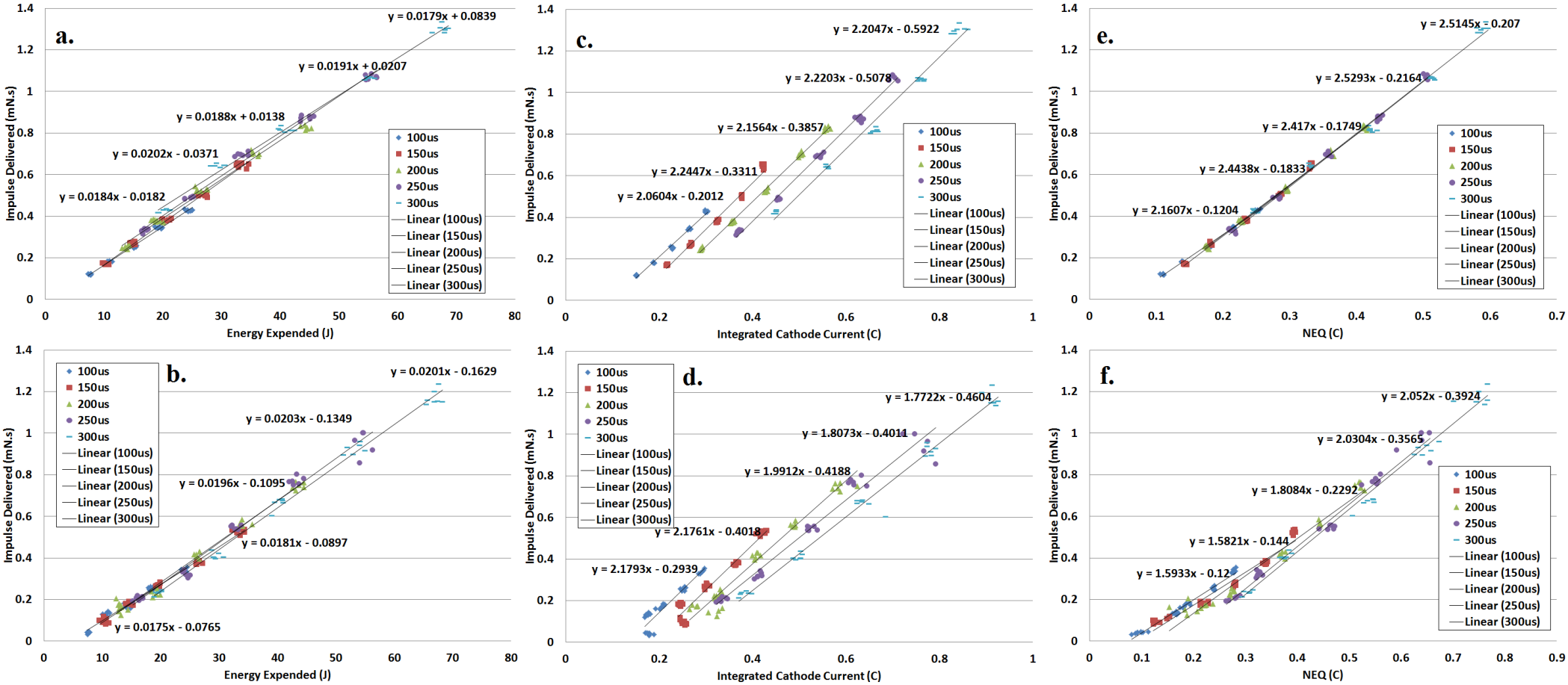

Figure 6.11: Mo impulse data.

Vertical axis in each plot is the measured impulse delivered to the pendulum by each pulse of plasma, while horizontal axes are (from left) the energy expended in the arc by that pulse, the integrated cathode current for that pulse and the net ejected charge (NEQ) for that pulse. Each trendline has R greater than 0.95. Top row of plots shows data for a non-eroded cathode, bottom row shows eroded cathode data.

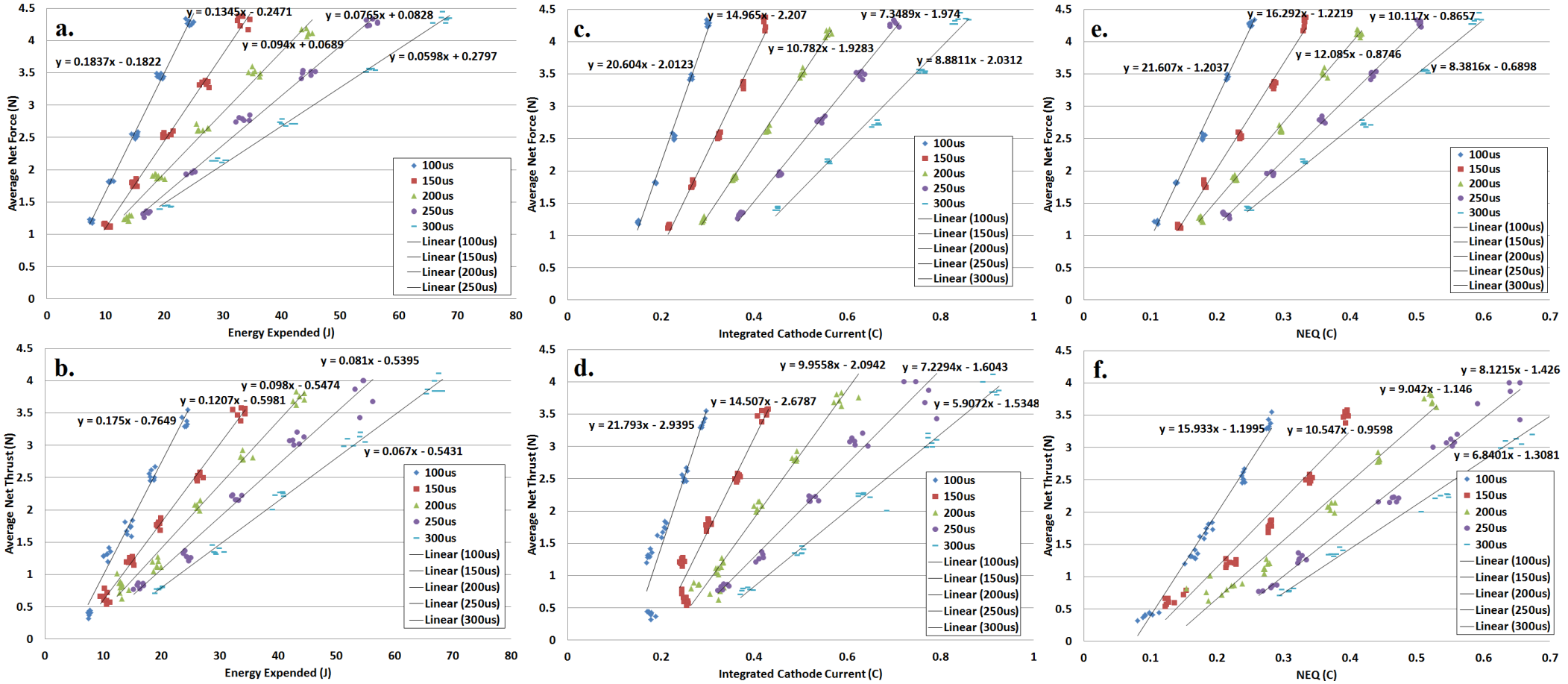

Figure 6.12: Mo thrust data.

Vertical axis in each plot is the average net force exerted on the pendulum by each pulse of plasma, while horizontal axes are (from left) the energy expended in the arc by that pulse, the integrated cathode current for that pulse and the net ejected charge (NEQ) for that pulse. Each trendline has R greater than 0.95. Top row of plots shows data for a non-eroded cathode, bottom row shows eroded cathode data.

6.2.5 Tantalum

Figures 6.13 and 6.14 show the data for Ta impulse measurements. Approximately 342,000 pulses were fired, which eroded approximately 8.6g of cathode material. Linear trendlines have been fitted, with regression coefficients greater than 0.9 in all cases. Tantalum was well-behaved and highly linear in its behaviour.

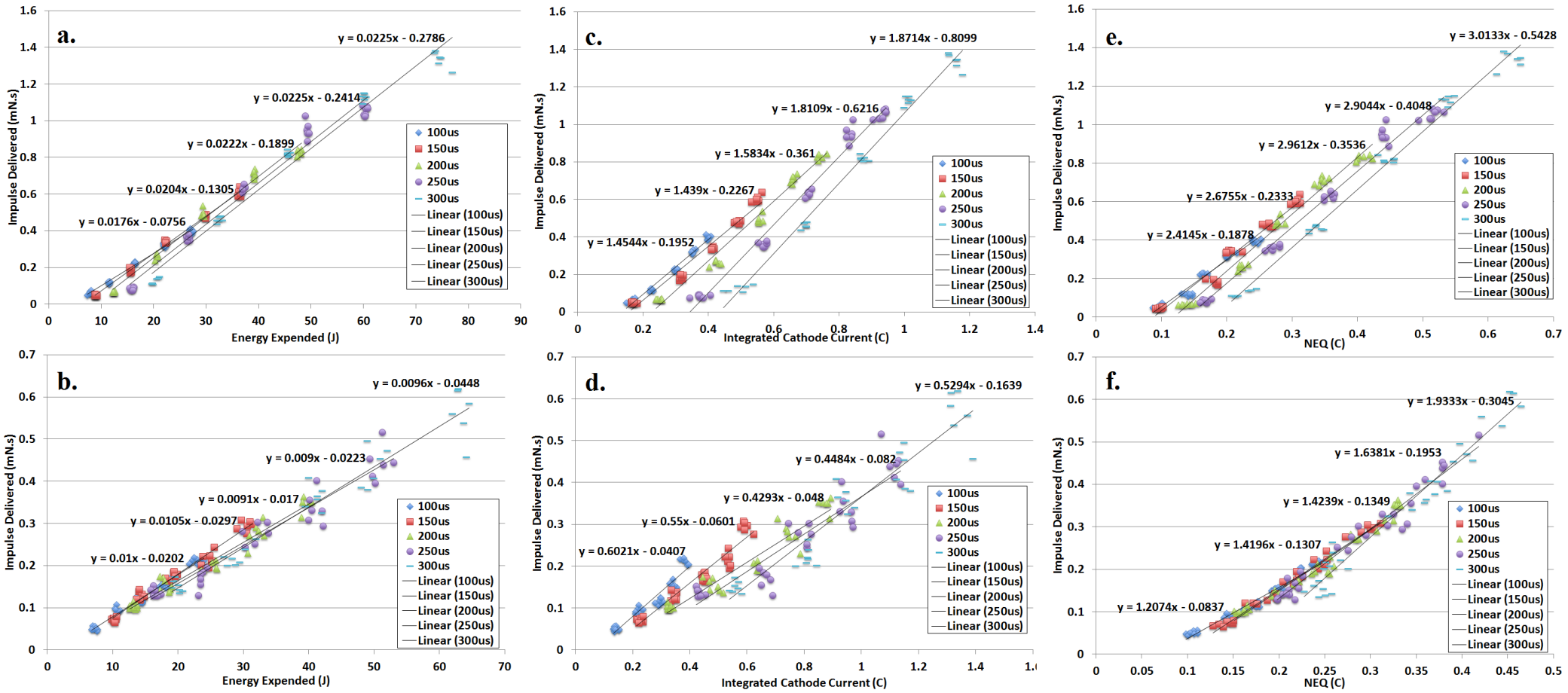

Figure 6.13: Ta impulse data.

Vertical axis in each plot is the measured impulse delivered to the pendulum by each pulse of plasma, while horizontal axes are (from left) the energy expended in the arc by that pulse, the integrated cathode current for that pulse and the net ejected charge (NEQ) for that pulse. Each trendline has R greater than 0.95. Top row of plots shows data for a non-eroded cathode, bottom row shows eroded cathode data.

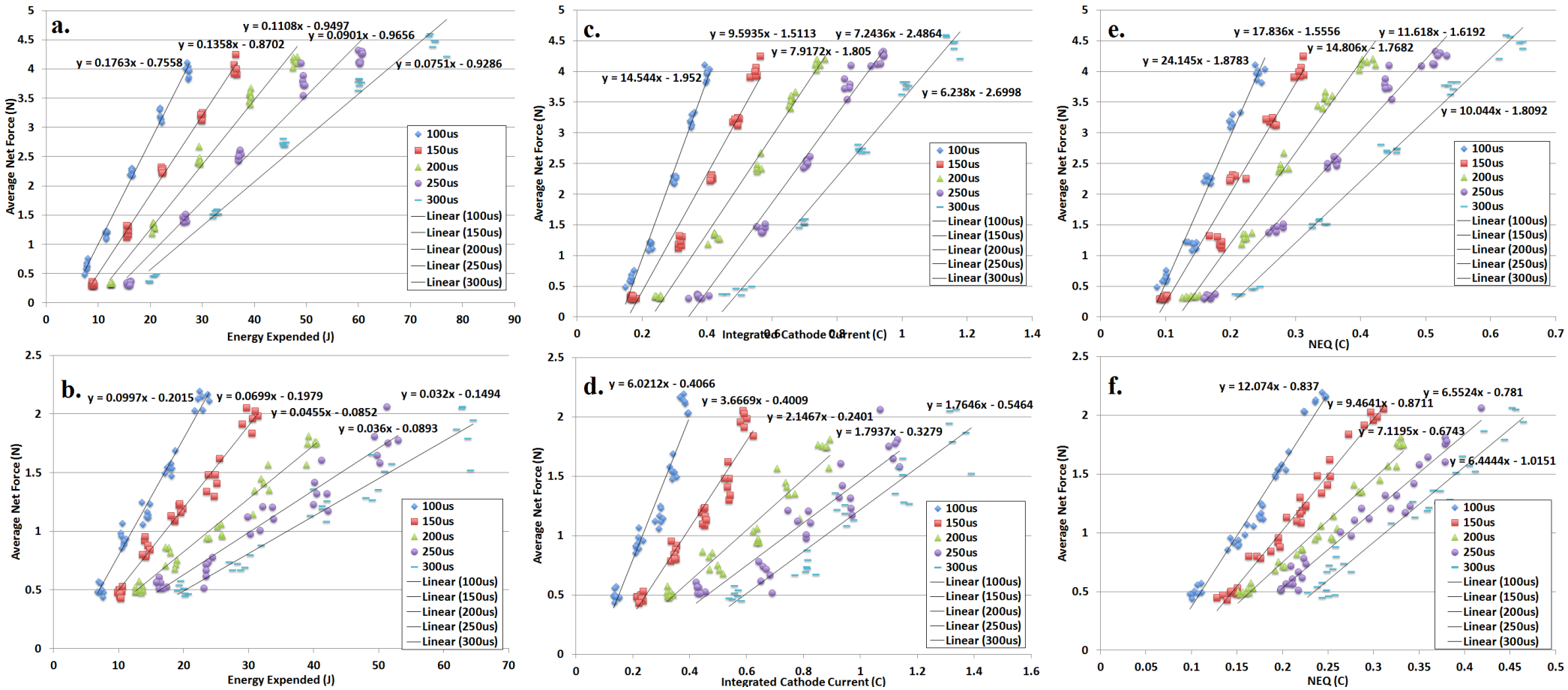

Figure 6.14: Ta thrust data.

Vertical axis in each plot is the average net force exerted on the pendulum by each pulse of plasma, while horizontal axes are (from left) the energy expended in the arc by that pulse, the integrated cathode current for that pulse and the net ejected charge (NEQ) for that pulse. Each trendline has R greater than 0.95. Top row of plots shows data for a non-eroded cathode, bottom row shows eroded cathode data.

6.2.6 Tungsten

Figures 6.15 and 6.16 show the data for W impulse measurements. Approximately 390,000 pulses were fired, which eroded approximately 7.7g of cathode material. Linear trendlines have been fitted, with regression coefficients greater than 0.9 in all cases. Tungsten was well-behaved and highly linear in its behaviour.

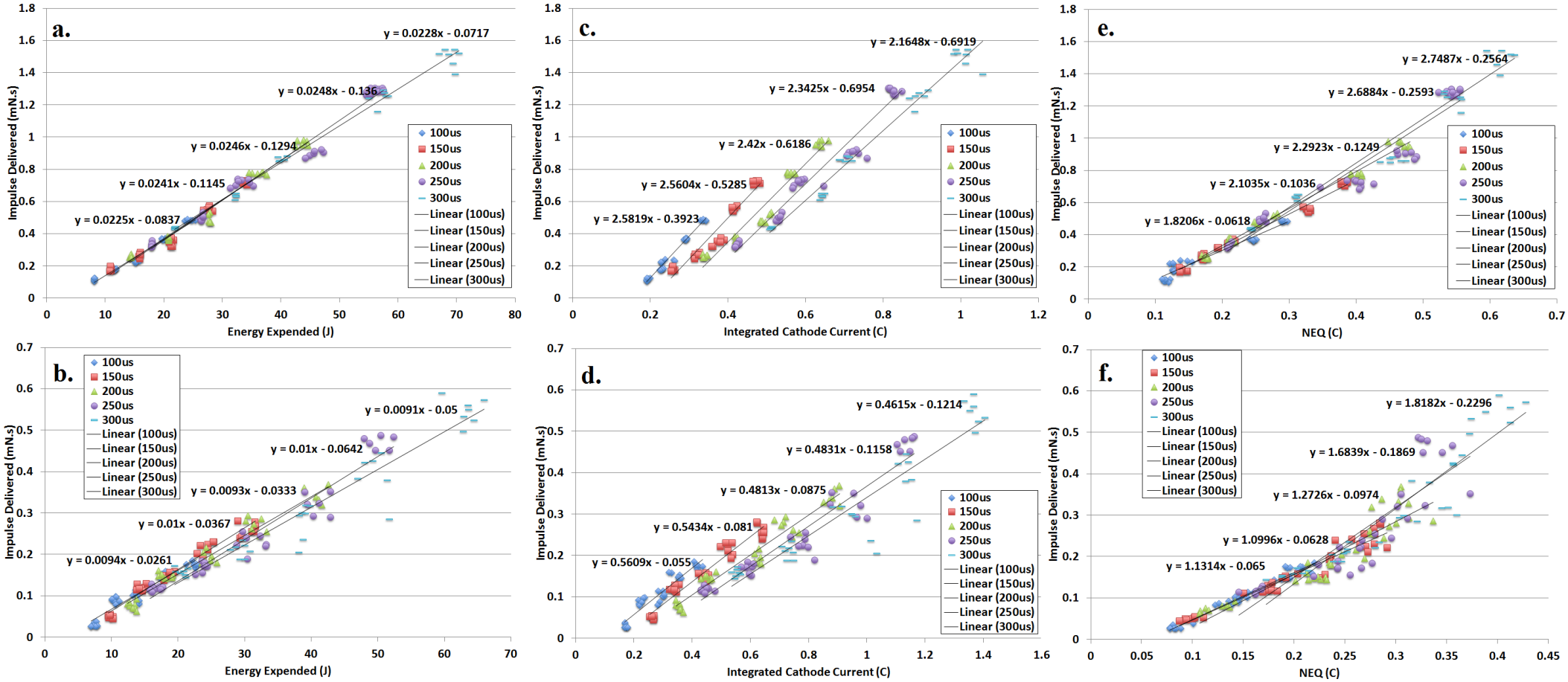

Figure 6.15: W impulse data.

Vertical axis in each plot is the measured impulse delivered to the pendulum by each pulse of plasma, while horizontal axes are (from left) the energy expended in the arc by that pulse, the integrated cathode current for that pulse and the net ejected charge (NEQ) for that pulse. Each trendline has R greater than 0.95. Top row of plots shows data for a non-eroded cathode, bottom row shows eroded cathode data.

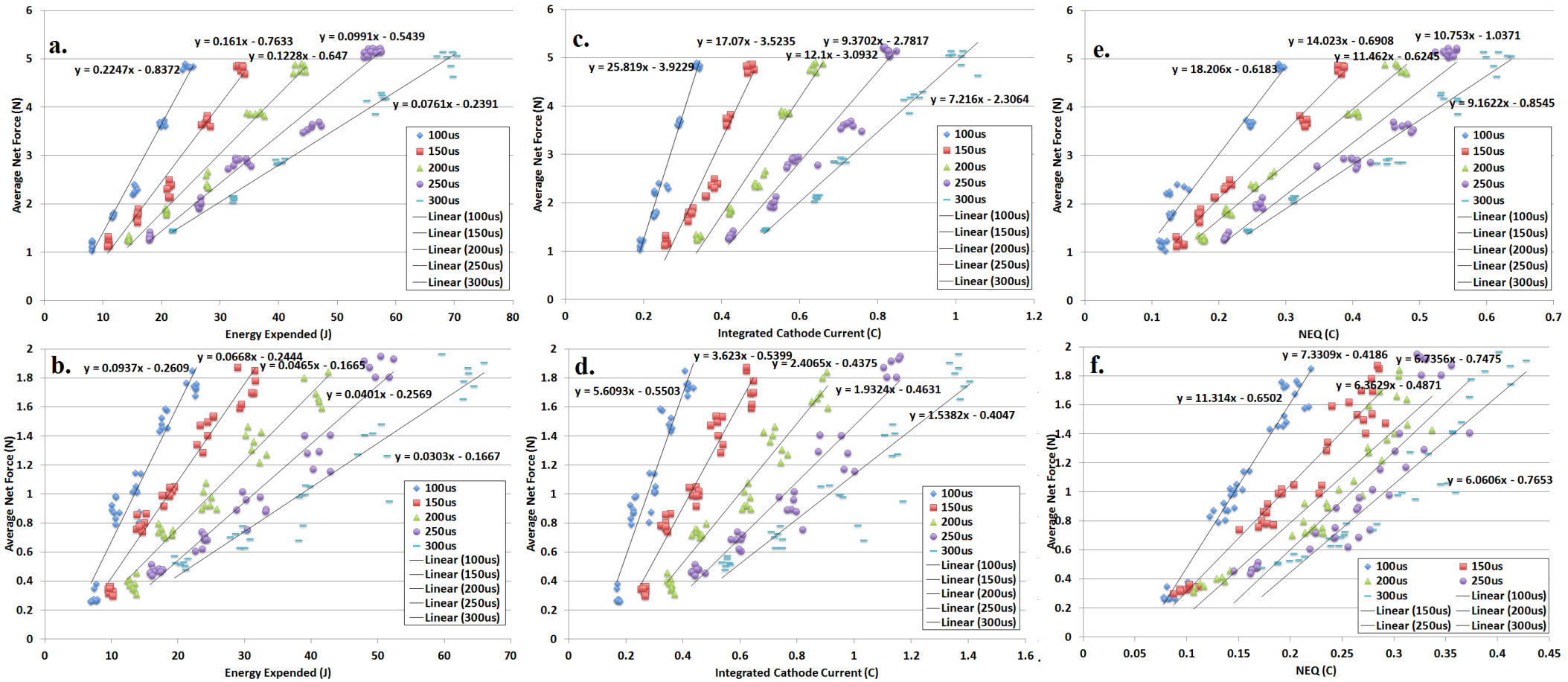

Figure 6.16: W thrust data.

Vertical axis in each plot is the average net force exerted on the pendulum by each pulse of plasma, while horizontal axes are (from left) the energy expended in the arc by that pulse, the integrated cathode current for that pulse and the net ejected charge (NEQ) for that pulse. Each trendline has R greater than 0.95. Top row of plots shows data for a non-eroded cathode, bottom row shows eroded cathode data.

6.3 Light Elements

Data for all light elements investigated, being C, Mg and Al, were taken in mid-2014 at the University of Sydney and have not been previously published.

6.3.1 Carbon

Performing erosion rate measurements on carbon cathodes seems to remove volatiles from the cathode, presumably via heating, with the result that an unused C cathode substantially underperforms one that has been used. The unused cathodes were typically a lighter grey than a used cathode, indicating the removal of impurities by use. In order to avoid the impact of impurities on the measurement, impulse measurements for a non-eroded C cathode surface were taken using a C cathode that had fired 3000 pulses at 4Hz. While not a completely non-eroded cathode surface, the 3000 "bake-out" pulses caused insignificant erosion compared to the 90,000 pulses fired prior to the collection of the eroded C data. Selected measurements for an unbaked C cathode are shown in figure 11.2 to illustrate the difference in performance between baked and unbaked C cathode performance.

Figures 6.17 and 6.18 show the data for C impulse measurements. Linear trendlines have been fitted, with regression coefficients greater than 0.9 in all cases. Carbon was well-behaved and highly linear in its behaviour, so long as the cathode was baked out prior to experiments.

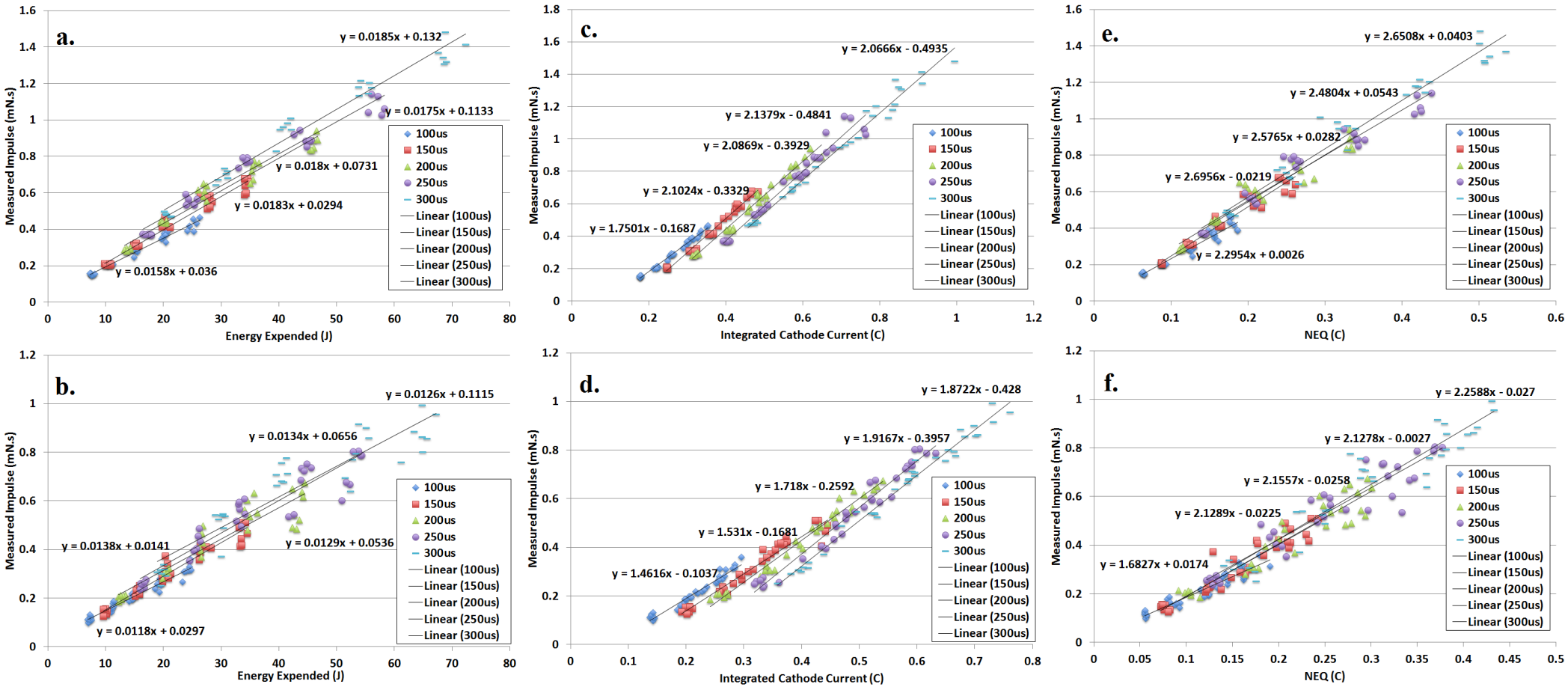

Figure 6.17: C impulse data.

Vertical axis in each plot is the measured impulse delivered to the pendulum by each pulse of plasma, while horizontal axes are (from left) the energy expended in the arc by that pulse, the integrated cathode current for that pulse and the net ejected charge (NEQ) for that pulse. Each trendline has R greater than 0.95. Top row of plots shows data for a non-eroded cathode, bottom row shows eroded cathode data.

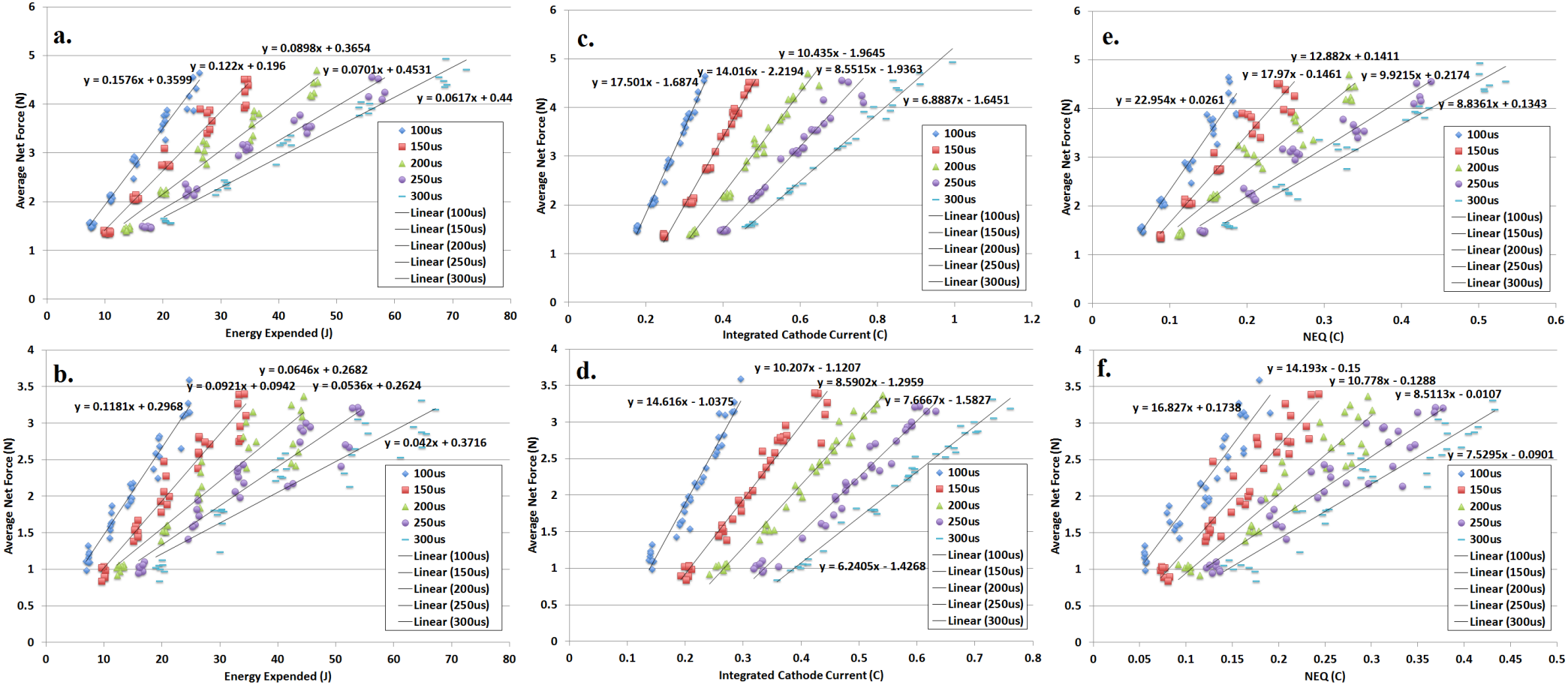

Figure 6.18: C thrust data.

Vertical axis in each plot is the average net force exerted on the pendulum by each pulse of plasma, while horizontal axes are (from left) the energy expended in the arc by that pulse, the integrated cathode current for that pulse and the net ejected charge (NEQ) for that pulse. Each trendline has R greater than 0.95. Top row of plots shows data for a non-eroded cathode, bottom row shows eroded cathode data.

6.3.2 Magnesium

Figures 6.19 and 6.20 show the data for Mg impulse measurements. Approximately 312,000 pulses were fired, which eroded approximately 2.4g of cathode material. Linear trendlines have been fitted, with regression coefficients greater than 0.9 in all cases. Magnesium was well-behaved and highly linear in its behaviour.

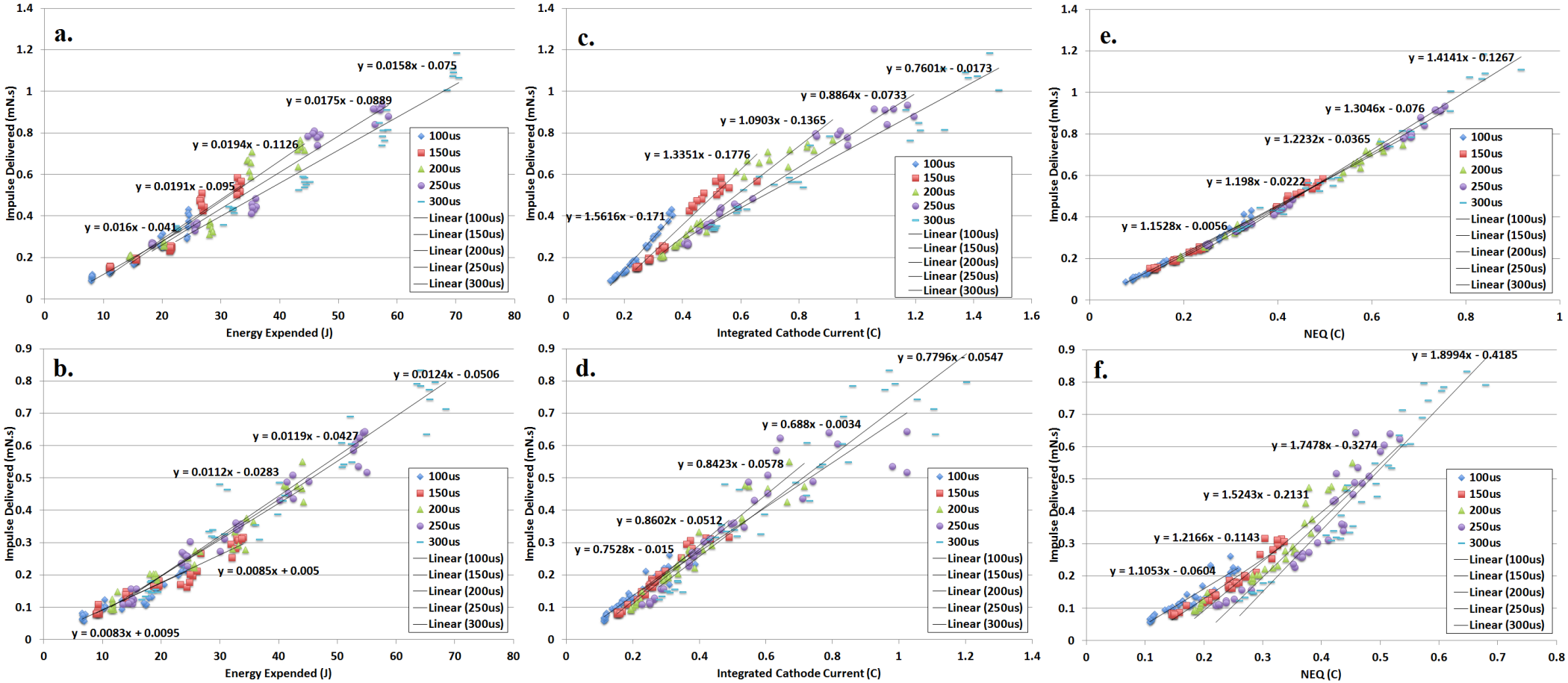

Figure 6.19: Mg impulse data.

Vertical axis in each plot is the measured impulse delivered to the pendulum by each pulse of plasma, while horizontal axes are (from left) the energy expended in the arc by that pulse, the integrated cathode current for that pulse and the net ejected charge (NEQ) for that pulse. Each trendline has R greater than 0.9. Top row of plots shows data for a non-eroded cathode, bottom row shows eroded cathode data.

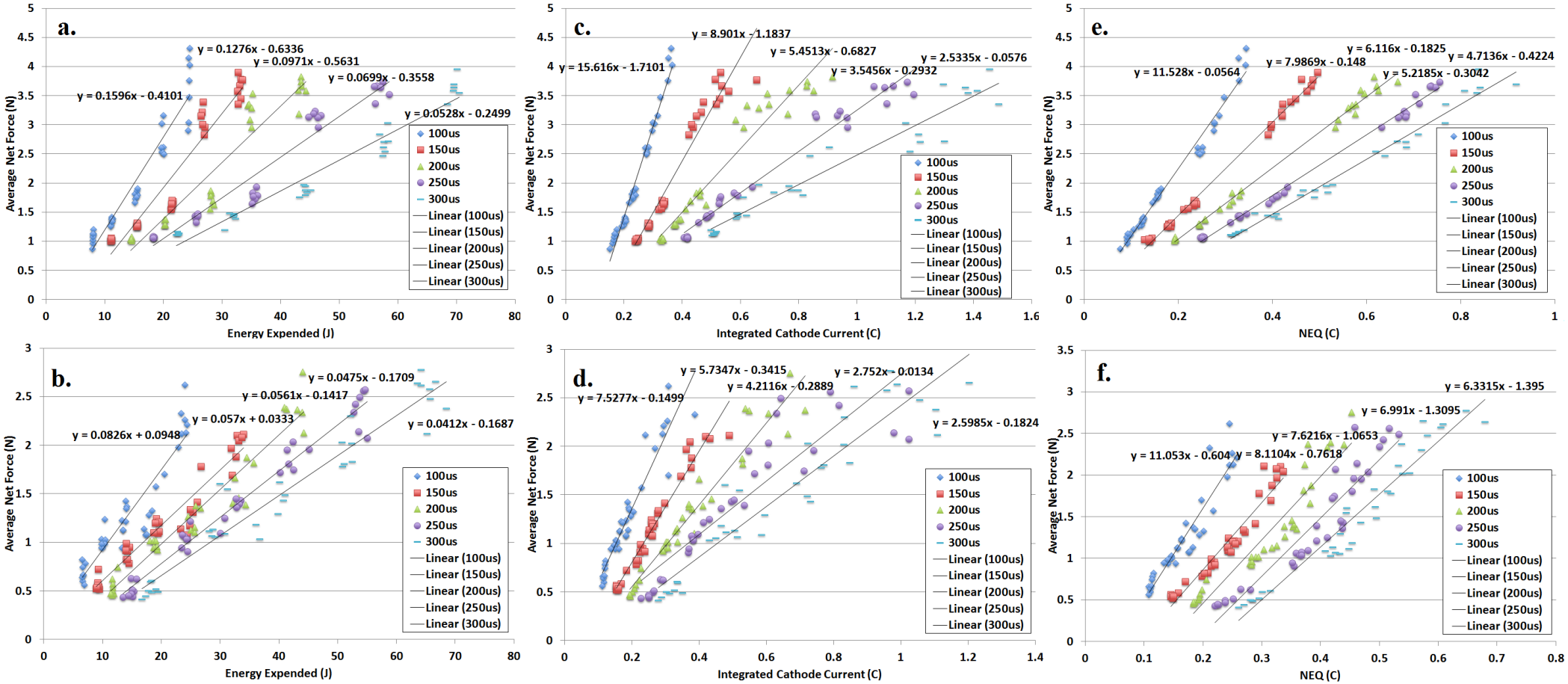

Figure 6.20: Mg thrust data.

Vertical axis in each plot is the average net force exerted on the pendulum by each pulse of plasma, while horizontal axes are (from left) the energy expended in the arc by that pulse, the integrated cathode current for that pulse and the net ejected charge (NEQ) for that pulse. Each trendline has R greater than 0.9. Top row of plots shows data for a non-eroded cathode, bottom row shows eroded cathode data.

6.3.3 Aluminium

Figures 6.21 and 6.22 show the data for Al impulse measurements. Approximately 228,000 pulses were fired, which eroded approximately 2.8g of cathode material. Linear trendlines have been fitted, with regression coefficients greater than 0.9 in all cases. Aluminium was well-behaved and highly linear in its behaviour except for pulses on eroded cathode surfaces, where more scatter was observed.

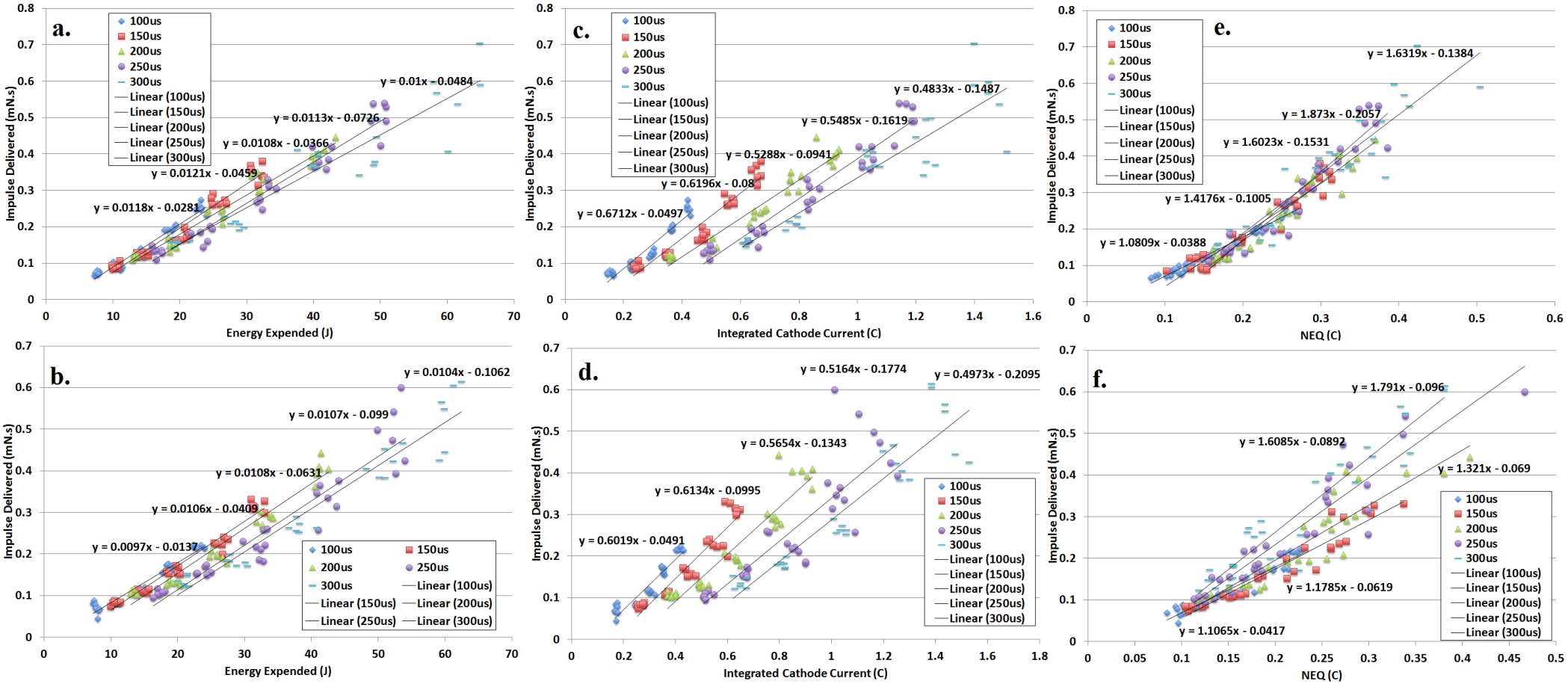

Figure 6.21: Al impulse data.

Vertical axis in each plot is the measured impulse delivered to the pendulum by each pulse of plasma, while horizontal axes are (from left) the energy expended in the arc by that pulse, the integrated cathode current for that pulse and the net ejected charge (NEQ) for that pulse. Each trendline has R greater than 0.9. Top row of plots shows data for a non-eroded cathode, bottom row shows eroded cathode data.

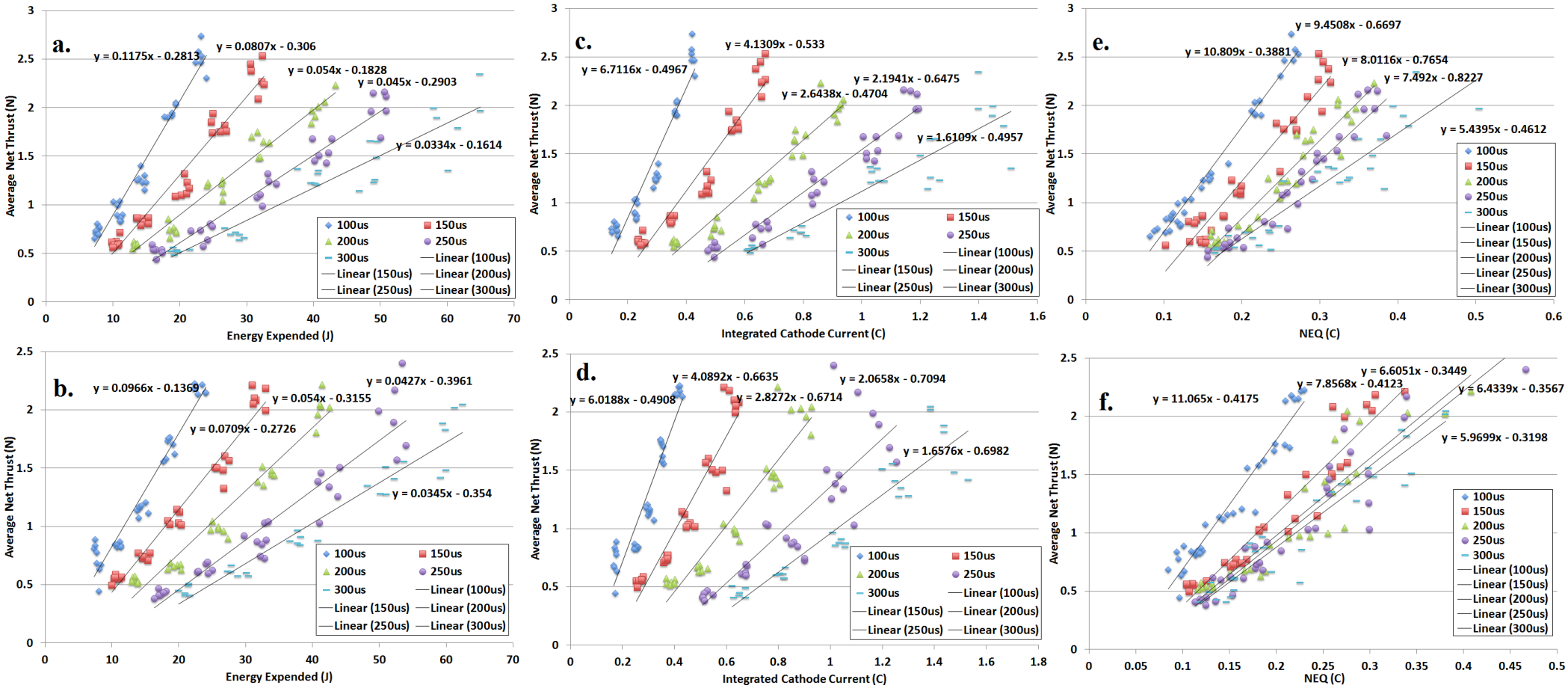

Figure 6.22: Al thrust data.

Vertical axis in each plot is the average net force exerted on the pendulum by each pulse of plasma, while horizontal axes are (from left) the energy expended in the arc by that pulse, the integrated cathode current for that pulse and the net ejected charge (NEQ) for that pulse. Each trendline has R greater than 0.9. Top row of plots shows data for a non-eroded cathode, bottom row shows eroded cathode data.

6.4 Summary of Impulse and thrust measurements

The data presented in this chapter was used to derive the standard efficiency metrics presented in chapter 7, together with the erosion rate measurements shown in chapter 5. The maximal values for impulse delivered and thrust exerted by plasma produced from each material examined is shown in table 6.2, where each measurement has 2% uncertainty as discussed in section 3.1.6. Analysis of the Standard Errors of the Mean for all impulse datasets were undertaken, with almost all having SEMs below 2%, as expected from the estimates in section 3.1.6. It should be noted that the pendulum always returned to its rest position after each pulse as determined by inspection of the photodiode trace. This indicates a lack of pendulum charging, as mentioned in the design criteria discussed in section 3.1.2.

Element	Maximum Thrust Non-eroded (N)	Maximum Thrust Eroded (N)	Maximum Impulse Non-eroded (mN.s)	Maximum Impulse Eroded (mN.s)
Sn	6.12	6.15	1.48	1.45
Bi	3.89	5.17	0.827	0.888
Ti	4.23	3.57	1.10	0.991
V	5.31	2.91	1.34	0.759
Cr	2.1f	1.95	0.548	0.508
Mo	4.45	4.12	1.33	1.24
Ta	4.56	2.20	1.38	0.62
W	5.22	1.96	1.54	0.589
C	4.93	3.59	1.48	0.992
Mg	4.32	2.77	1.19	0.832
Al	2.74	2.40	0.704	0.614

Table 6.2: Maximal thrust and impulse values for all elements examined, for both non-eroded and eroded cathode surfaces. All values are shown to three significant figures.

Trends common to all materials were the increase in impulse delivered with increasing pulse duration and cathode current. The thrust measurements for all materials also showed the same trends with respect to energy expenditure and integrated cathode current in that shorter pulses generated more thrust; this can be seen not only in the numerical values of thrust, but in the changing trendline slopes in the plots, for example in the Mg data in figure 6.20. This reduction in thrust is likely to be due to the production of neutral vapour by cathode heating as the pulse progresses, as this vapour would interfere with the motion of the ions in the plasma via collisional processes [24-27]. The production of neutral vapour is especially high in Bi and the mean ion charge state low, thus few ions are likely to escape and little charge transits the anode mouth [26]. This would lead to very low NEQ measurements and large amounts of noise in the NEQ signal, as shown in figures 6.3 and 6.4.

Another interesting result was the need for the C cathode to be baked out. Carbon cathodes are made from sintered carbon granules, and so would contain trapped volatiles from the manufacturing process as well as lubricants from any machining processes. These volatile species would lead to the production of neutral vapour during arc operation, reducing the plasma impulse as described previously. These volatiles can be removed by heating in vacuum, and this was done by using the heat produced during arc operation. After a 3000 pulse bake-out the C cathode was noticeably darker, implying a reduction in the impurity content.

7 Derived Quantities: Specific Impulse and Jet Power Efficiency

This chapter contains plots of the efficiency metrics derived from the results presented in chapters 5 and 6, using equations 1.2 and 1.7. Uncertainties in the derived quantities were determined by using standard errors of the means (SEMs), uncertainties in the trendline slopes used to derive the mass flow rate and the impulse measurement uncertainty derived in section 3.1.6 (2% for all thrust measurements). Integrated cathode current measurement SEMs were below 2% for all materials. The SEMs for measured energy expended were similar to those for the integrated cathode current measurements. Therefore 2% was considered a reasonable uncertainty bound for integrated cathode current and energy expenditure data. The cathode erosion rate trendline slopes (shown in table 5.2) had less than 10% uncertainty in fit. Since fuel specific impulse is calculated from the thrust, integrated cathode current and cathode erosion rate, the uncertainty for fuel specific impulse is therefore 14%. Similarly jet power efficiency is computed from the square of thrust, the integrated cathode current, cathode erosion rate and energy expended, meaning that the uncertainty in jet power efficiency is 18% of the derived quantity.

In all odd numbered figures in this chapter (ie 7.1, 7.3, 7.5 etc) the first row (subplots a, c and e) show the specific impulse data for a non-eroded cathode surface while the second row of plots (b, d and f) show the specific impulse measurements for an eroded cathode surface. Subplots a and b show the specific impulse plotted against energy expended in the arc per pulse; c and d against integrated cathode current; and e and f against NEQ, with linear trendlines fitted to allow comparison between plots

The even numbered figures in this chapter (ie 7.2, 7.4, 7.6 etc) plot jet power efficiency data. The first row of sub-plots (subplots a, c and e) plot the jet power efficiency of plasma from a non-eroded cathode surface while the second row of plots (b, d and f) show the jet power efficiency of plasma from eroded cathode surfaces. Subplots a and b show the jet power efficiency plotted against energy expended in the arc per pulse; c and d against integrated cathode current; and e and f against NEQ.

7.1 Non-Refractory metals

7.1.1 Tin

Figure 7.1 shows the specific impulse data for Sn. Approximately 20,000 pulses were fired, which eroded approximately 7.3g of cathode material. The plots in figure 7.2 show the jet power efficiency for Sn plasma pulses. Linear trendlines are fitted to allow comparison between plots, with more scatter apparent in pulses fired from eroded surfaces.

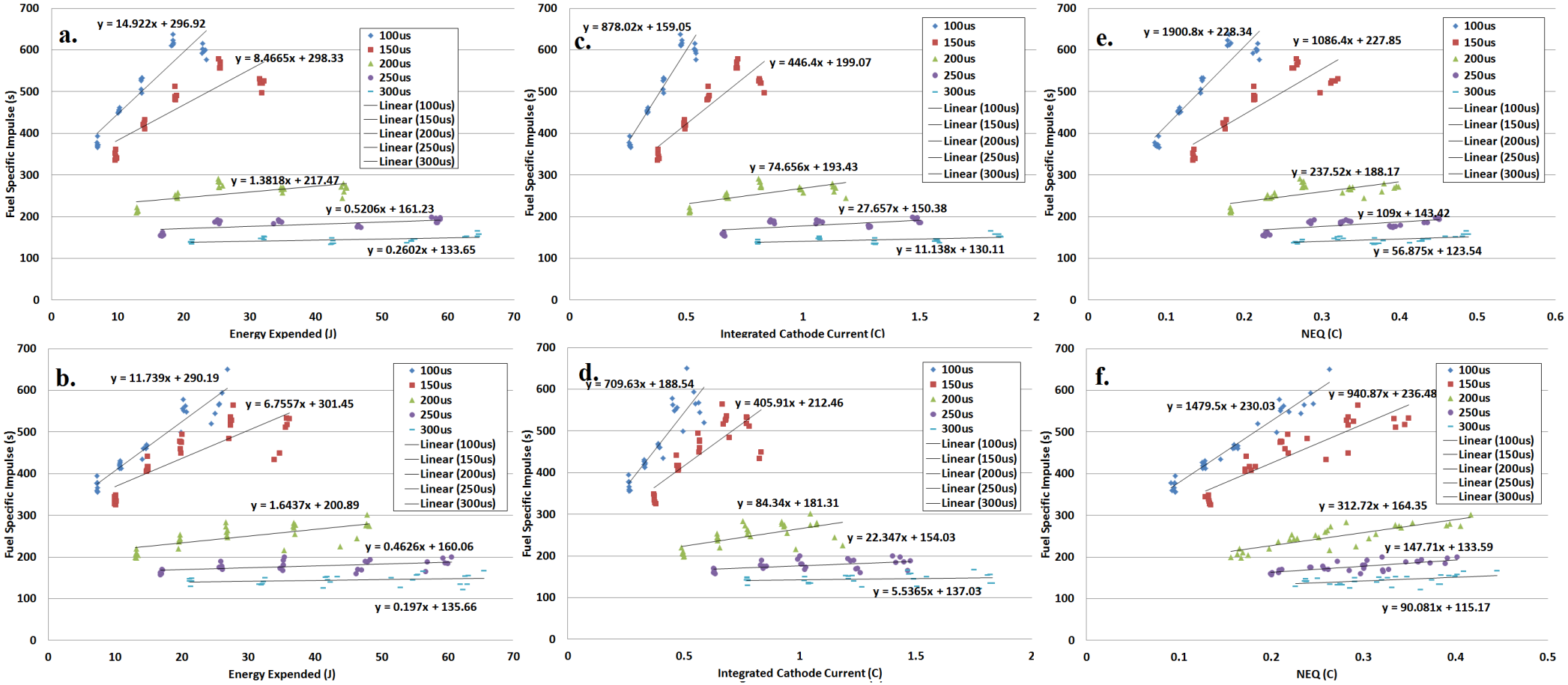

Figure 7.1: Sn specific impulse data.

Vertical axis in each plot is the fuel specific impulse of Sn, while horizontal axes are (from left) the energy expended in the arc by that pulse, the integrated cathode current for that pulse and the net ejected charge (NEQ) for that pulse. Top row of plots shows data for a non-eroded cathode, bottom row shows eroded cathode data.

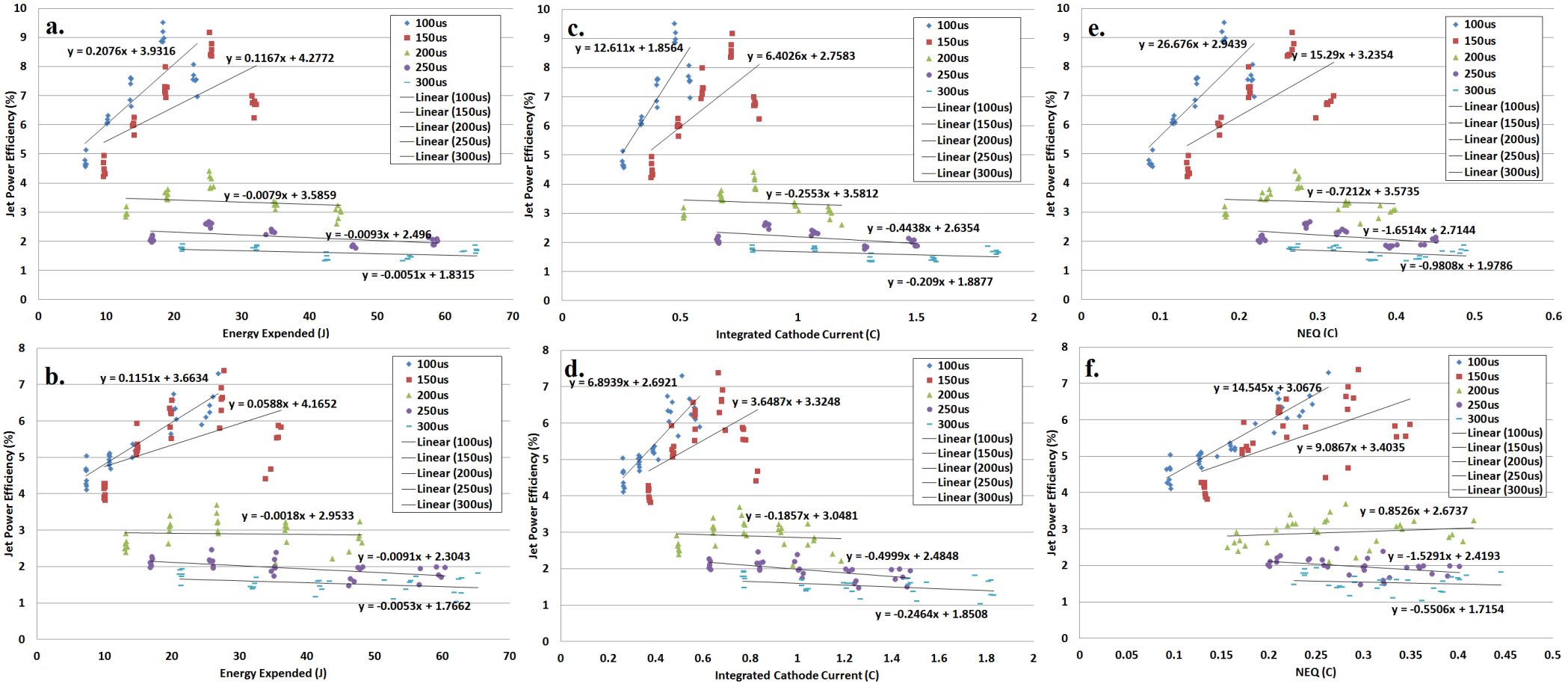

Figure 7.2: Sn Jet Power Efficiency data.

Vertical axis in each plot is the ratio of the kinetic energy in the exhaust to the input power, while horizontal axes are (from left) the energy expended in the arc by that pulse, the integrated cathode current for that pulse and the net ejected charge (NEQ) for that pulse. Top row of plots shows data for a non-eroded cathode, bottom row shows eroded cathode data.

7.1.2 Bismuth

Figure 7.3 shows the data for Bi specific impulse. Approximately 15,000 pulses were fired, which eroded approximately 14.9g of cathode material. The plots in figure 7.4 show the jet power efficiency for Bi plasma pulses. Linear trendlines are fitted to the data to all data sets to allow easy comparison, except for the data plotted against NEQ, for which no good fit could be found.

In both sets of plots the erosion rate used to compute the efficiency metrics for the 200μs long pulses is the slope of a linear fit to the whole Bi erosion data set. This rate is 1176.5 μg of Bi eroded per Coulomb of integrated cathode current, and is significantly higher than the measured rate of 722μg/C, which is anomalously low.

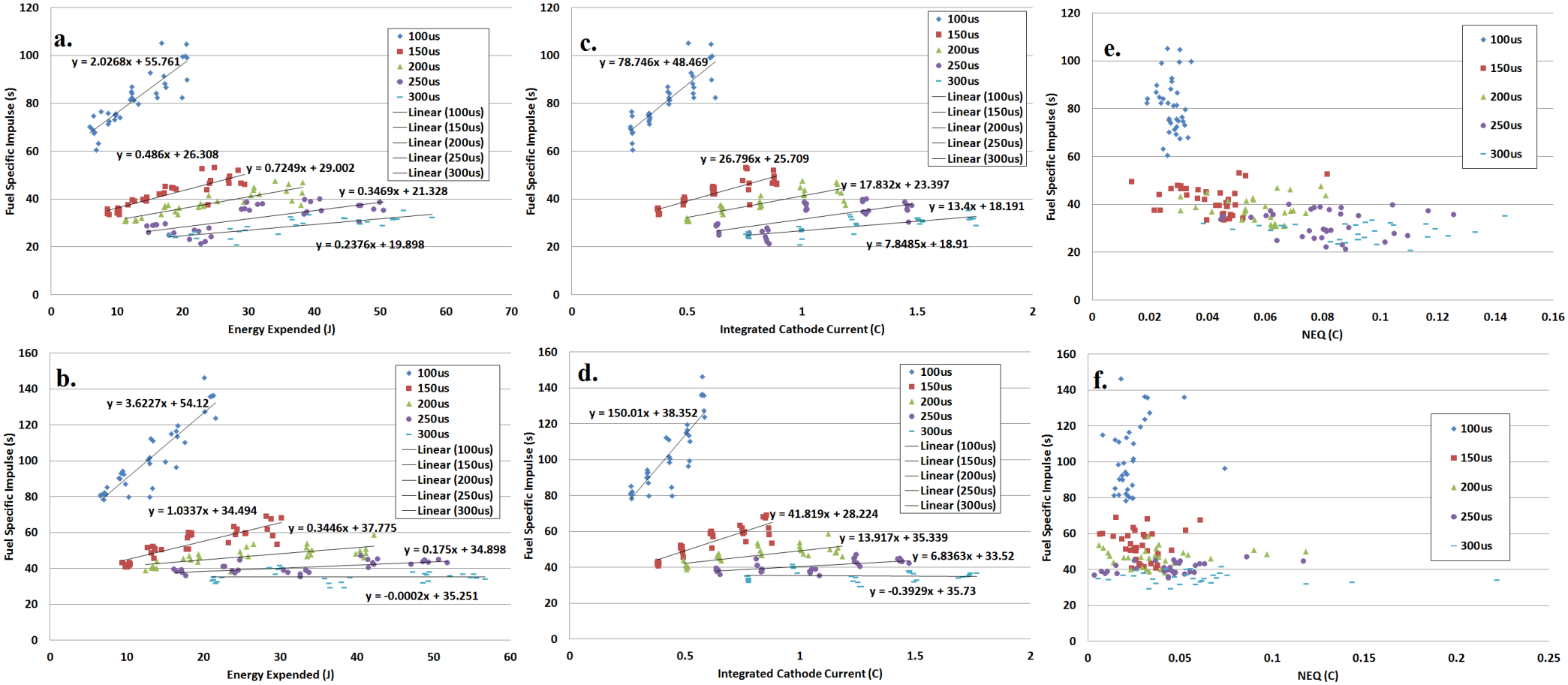

Figure 7.3: Bi fuel specific impulse data.

Vertical axis in each plot is the fuel specific impulse of Bi, while horizontal axes are (from left) the energy expended in the arc by that pulse, the integrated cathode current for that pulse and the net ejected charge (NEQ) for that pulse. Top row of plots shows data for a non-eroded cathode, bottom row shows eroded cathode data.

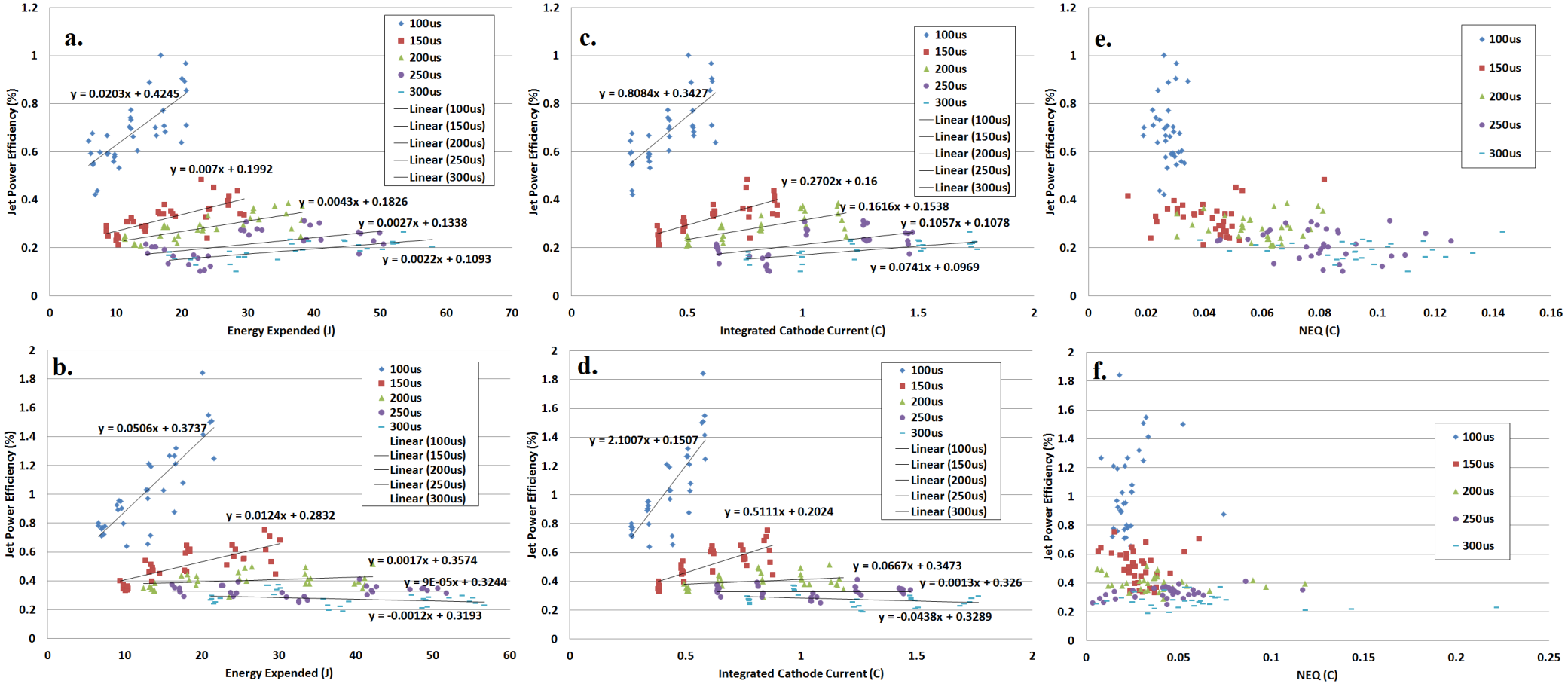

Figure 7.4: Bi Jet Power Efficiency data.

Vertical axis in each plot is the ratio of the kinetic energy in the exhaust to the input power, while horizontal axes are (from left) the energy expended in the arc by that pulse, the integrated cathode current for that pulse and the net ejected charge (NEQ) for that pulse. Top row of plots shows data for a non-eroded cathode, bottom row shows eroded cathode data.

7.2 Refractory Metals

Data for Ti, V, Cr, Mo, Ta, and W were taken in mid-2014 at the University of Sydney and have not been previously published. Ti, V and Cr are referred to as light refractory elements, Mo is the only medium refractory investigated (Zr and Nb were prohibitively expensive) and Ta and W are referred to as heavy refractory elements.

7.2.1 Titanium

Figure 7.5 shows the data for Ti specific impulse. Approximately 460,000 pulses were fired, which eroded approximately 3.8g of cathode material. The plots in figure 7.6 show the jet power efficiency for Ti plasma pulses. Linear trendlines are fitted, with regression coefficients greater than 0.95 in all cases, indicating that Ti is a reliable cathode material.

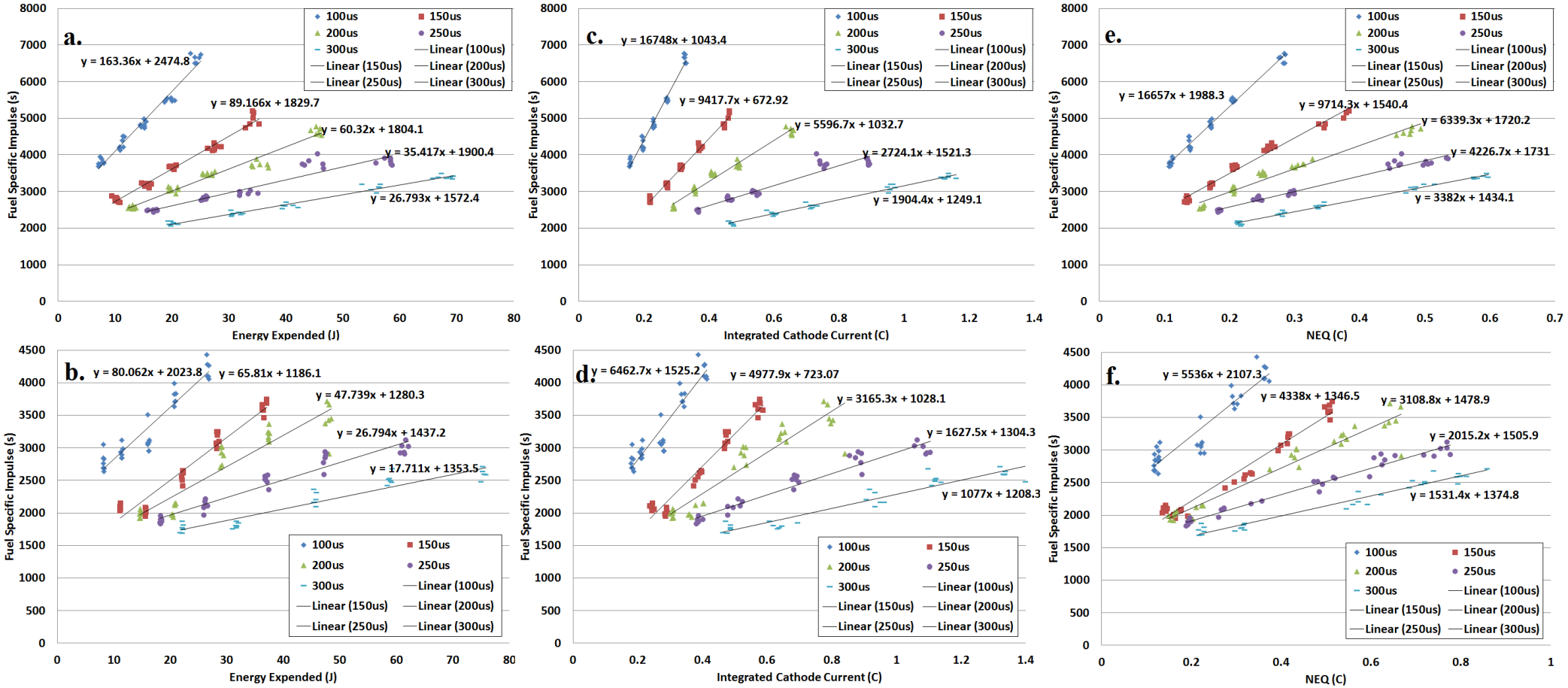

Figure 7.5: Ti fuel specific impulse data.

Vertical axis in each plot is the fuel specific impulse of Ti, while horizontal axes are (from left) the energy expended in the arc by that pulse, the integrated cathode current for that pulse and the net ejected charge (NEQ) for that pulse. Top row of plots shows data for a non-eroded cathode, bottom row shows eroded cathode data.

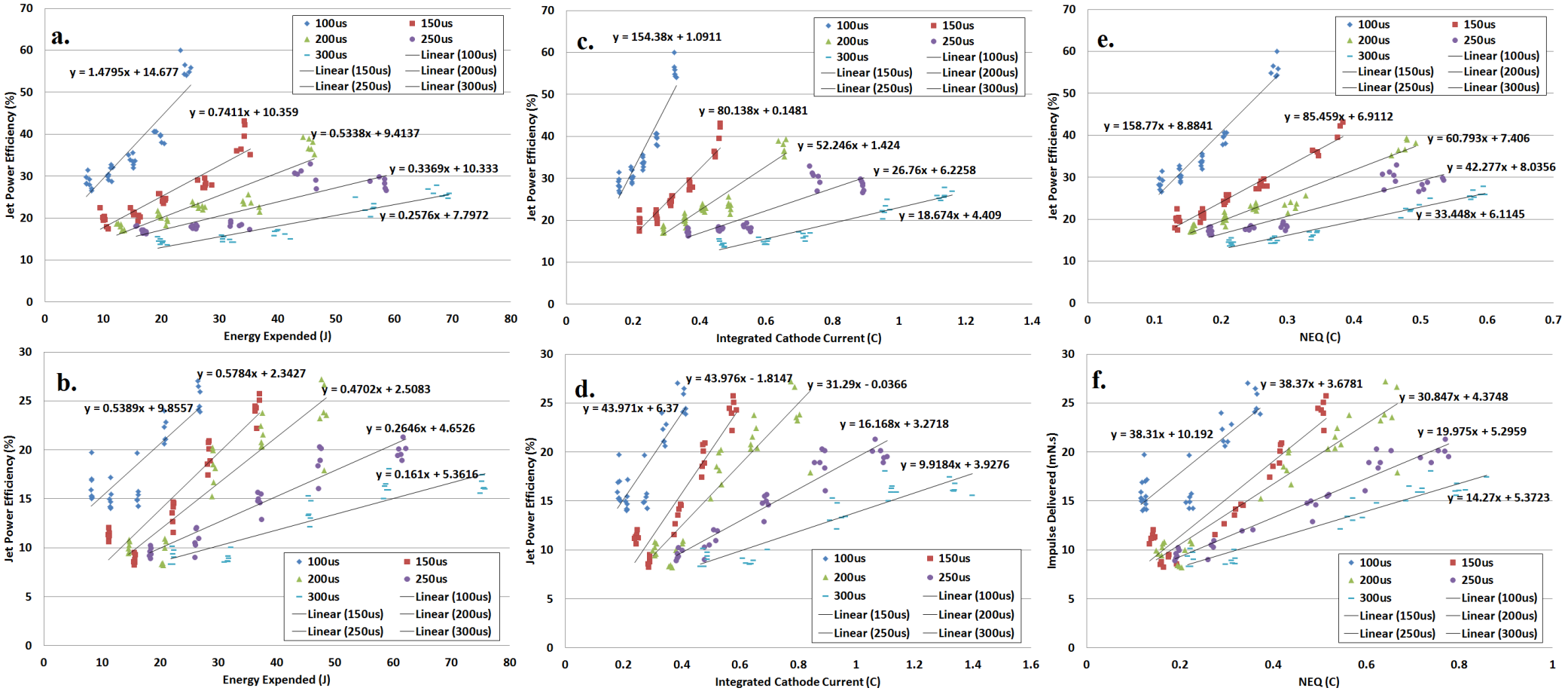

Figure 7.6: Ti Jet Power Efficiency data.

Vertical axis in each plot is the ratio of the kinetic energy in the exhaust to the input power, while horizontal axes are (from left) the energy expended in the arc by that pulse, the integrated cathode current for that pulse and the net ejected charge (NEQ) for that pulse. Top row of plots shows data for a non-eroded cathode, bottom row shows eroded cathode data.

7.2.2 Vanadium

Figure 7.7 shows the data for V specific impulse. Approximately 333,000 pulses were fired, which eroded approximately 3.0g of cathode material. The plots in figure 7.8 show the jet power efficiency for V plasma pulses. Linear trendlines are fitted, with regression coefficients greater than 0.95 in all cases, indicating that V is a reliable cathode material.

.

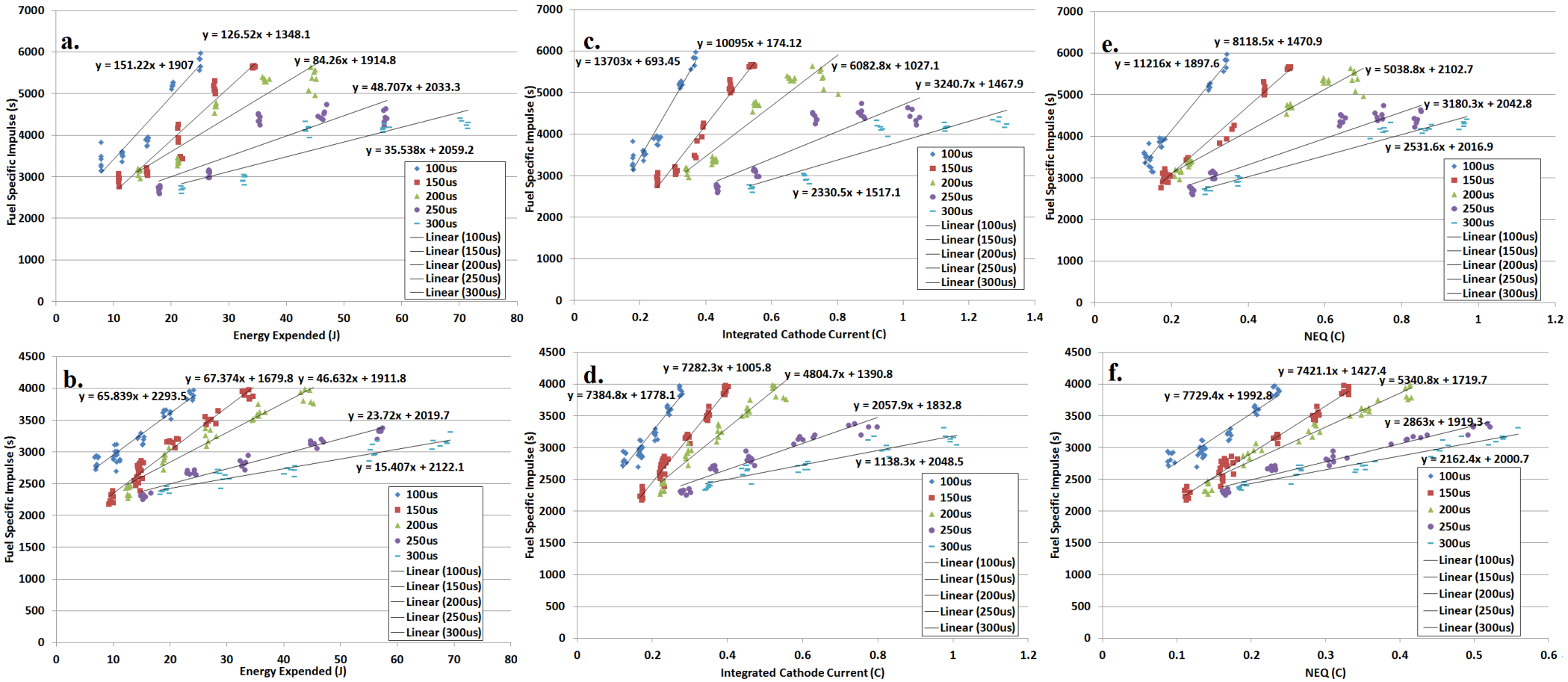

Figure 7.7: V fuel specific impulse data.

Vertical axis in each plot is the fuel specific impulse of V, while horizontal axes are (from left) the energy expended in the arc by that pulse, the integrated cathode current for that pulse and the net ejected charge (NEQ) for that pulse. Top row of plots shows data for a non-eroded cathode, bottom row shows eroded cathode data.

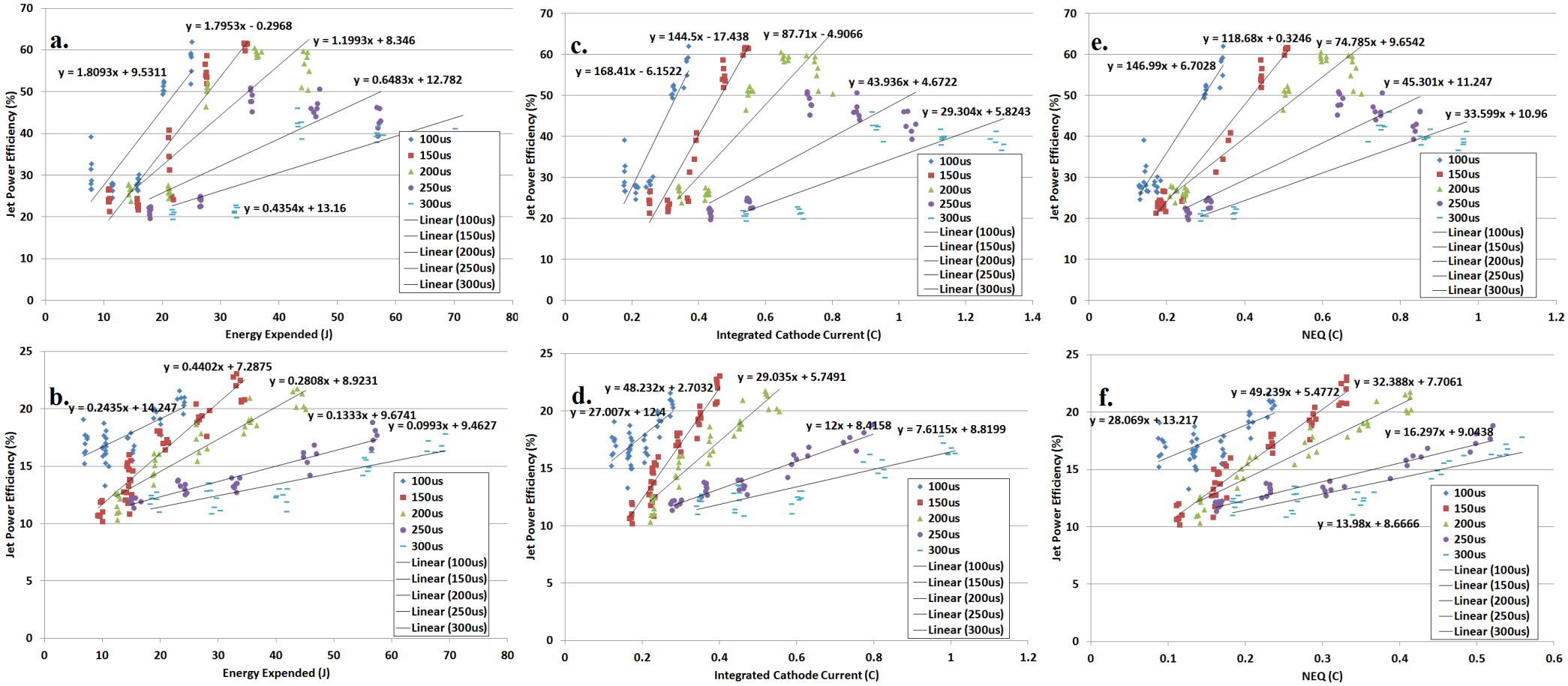

Figure 7.8: V Jet Power Efficiency data.

Vertical axis in each plot is the ratio of the kinetic energy in the exhaust to the input power, while horizontal axes are (from left) the energy expended in the arc by that pulse, the integrated cathode current for that pulse and the net ejected charge (NEQ) for that pulse. Top row of plots shows data for a non-eroded cathode, bottom row shows eroded cathode data.

7.2.3 Chromium

Figure 7.9 shows the data for Cr specific impulse. As discussed in chapter 5.2.3, due to anomalously low mass erosion measurement for the 150μs long, 180 V_{ch} pulses, the slope of the trendline for the other four points was used; this slope is 20.24μg/C, as opposed to the 17.01μg/C slope of the full data set; the amended slope is much closer to that of the rest of the dataset, at 23.25μg/C and is within the uncertainty bounds of the other trend slopes. Approximately 406,000 pulses were fired, which eroded approximately 3.1g of cathode material. The plots in figure 7.10 show the jet power efficiency for Cr plasma pulses. Linear trendlines are fitted, with regression coefficients greater than 0.9 in all cases, indicative of the greater scatter of the Cr datapoints.

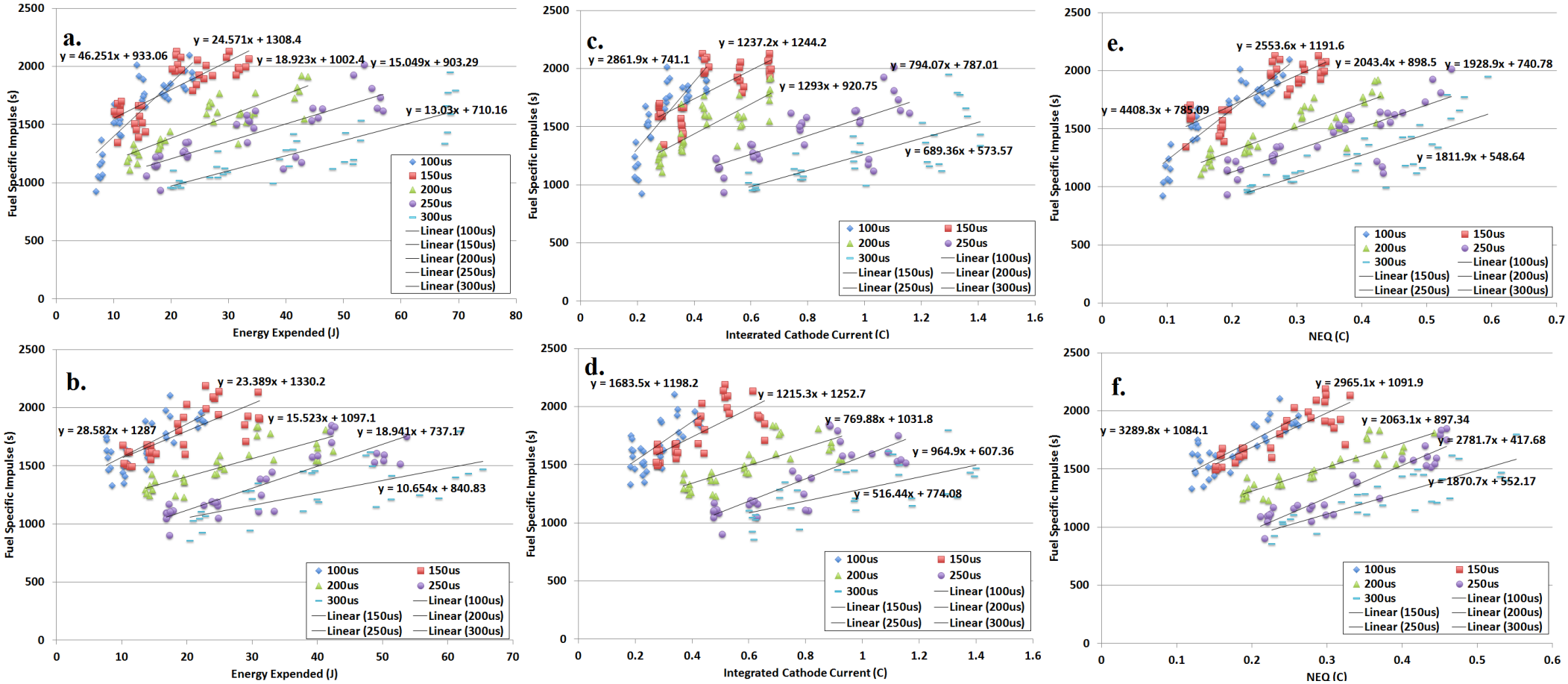

Figure 7.9: Cr fuel specific impulse data.

Vertical axis in each plot is the fuel specific impulse of Cr, while horizontal axes are (from left) the energy expended in the arc by that pulse, the integrated cathode current for that pulse and the net ejected charge (NEQ) for that pulse. Top row of plots shows data for a non-eroded cathode, bottom row shows eroded cathode data.

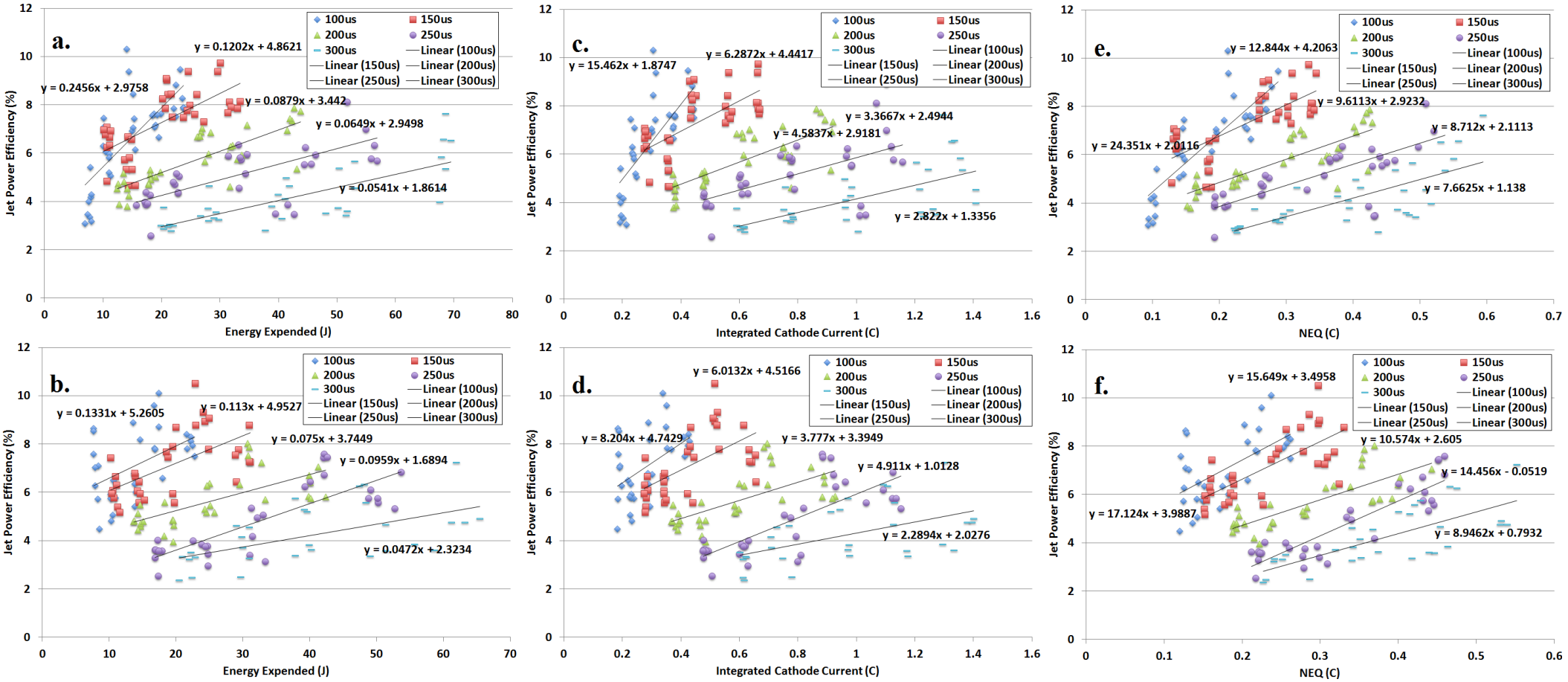

Figure 7.10: Cr Jet Power Efficiency data.

Vertical axis in each plot is the ratio of the kinetic energy in the exhaust to the input power, while horizontal axes are (from left) the energy expended in the arc by that pulse, the integrated cathode current for that pulse and the net ejected charge (NEQ) for that pulse. Top row of plots shows data for a non-eroded cathode, bottom row shows eroded cathode data.

7.2.4 Molybdenum

Figure 7.11 shows the data for Mo specific impulse. Approximately 333,000 pulses were fired, which eroded approximately 3.0g of cathode material. The plots in figure 7.12 show the jet power efficiency for Mo plasma pulses. Linear trendlines are fitted, with regression coefficients greater than 0.95 in most cases; the exceptions being the 250 and 300μs jet power efficiency data, with coefficients above 0.9. Molybdenum was well-behaved and highly linear in its behaviour.

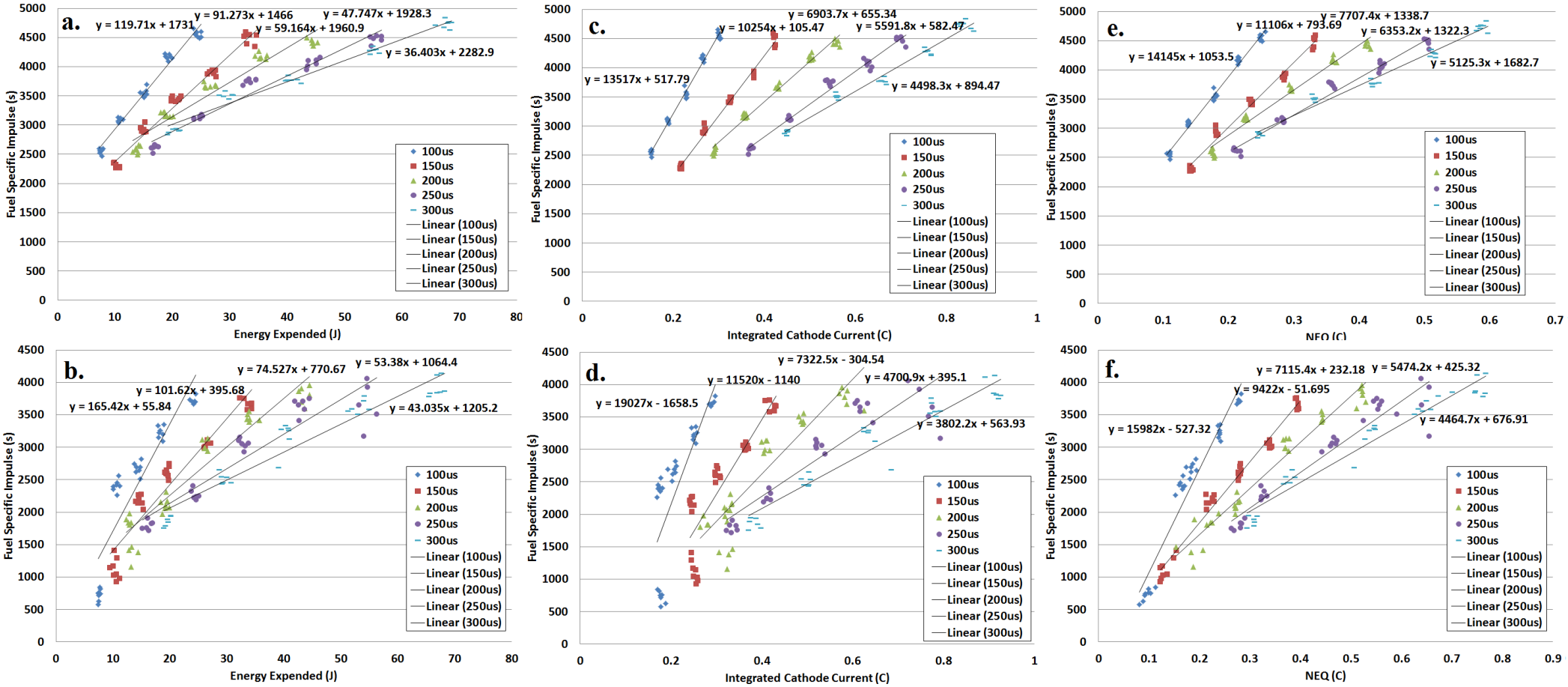

Figure 7.11: Mo fuel specific impulse data.

Vertical axis in each plot is the fuel specific impulse of Mo, while horizontal axes are (from left) the energy expended in the arc by that pulse, the integrated cathode current for that pulse and the net ejected charge (NEQ) for that pulse. Top row of plots shows data for a non-eroded cathode, bottom row shows eroded cathode data.

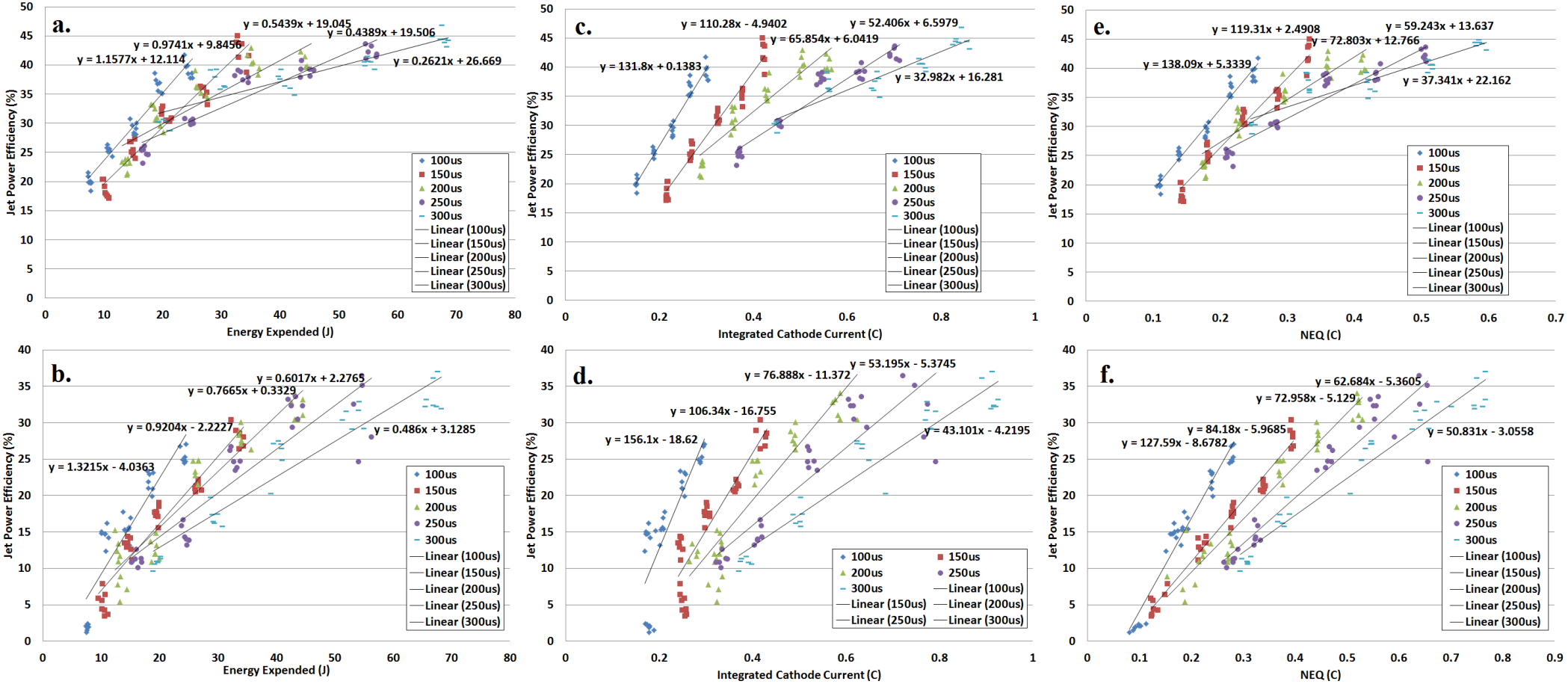

Figure 7.12: Mo Jet Power Efficiency data.

Vertical axis in each plot is the ratio of the kinetic energy in the exhaust to the input power, while horizontal axes are (from left) the energy expended in the arc by that pulse, the integrated cathode current for that pulse and the net ejected charge (NEQ) for that pulse. Top row of plots shows data for a non-eroded cathode, bottom row shows eroded cathode data.

7.2.5 Tantalum

Figure 7.13 shows the data for Ta specific impulse. Approximately 342,000 pulses were fired, which eroded approximately 8.6g of cathode material. The plots in figure 7.14 show the jet power efficiency for Ta plasma pulses. Linear trendlines are fitted, with regression coefficients greater than 0.9 in most cases; greater scatter in pulses fired from eroded surfaces lower the regression coefficients of some trendlines to ~0.85.

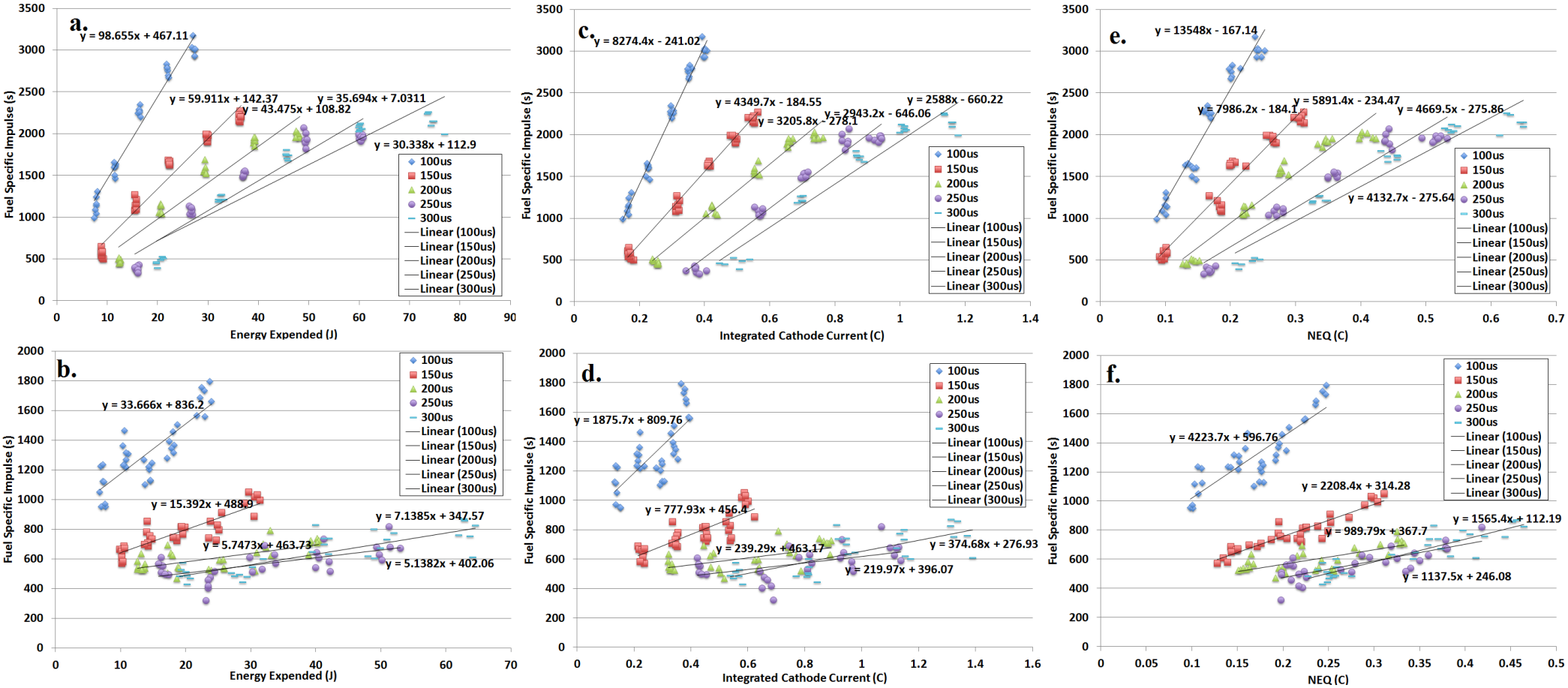

Figure 7.13: Ta fuel specific impulse data.

Vertical axis in each plot is the fuel specific impulse of Ta, while horizontal axes are (from left) the energy expended in the arc by that pulse, the integrated cathode current for that pulse and the net ejected charge (NEQ) for that pulse. Top row of plots shows data for a non-eroded cathode, bottom row shows eroded cathode data.

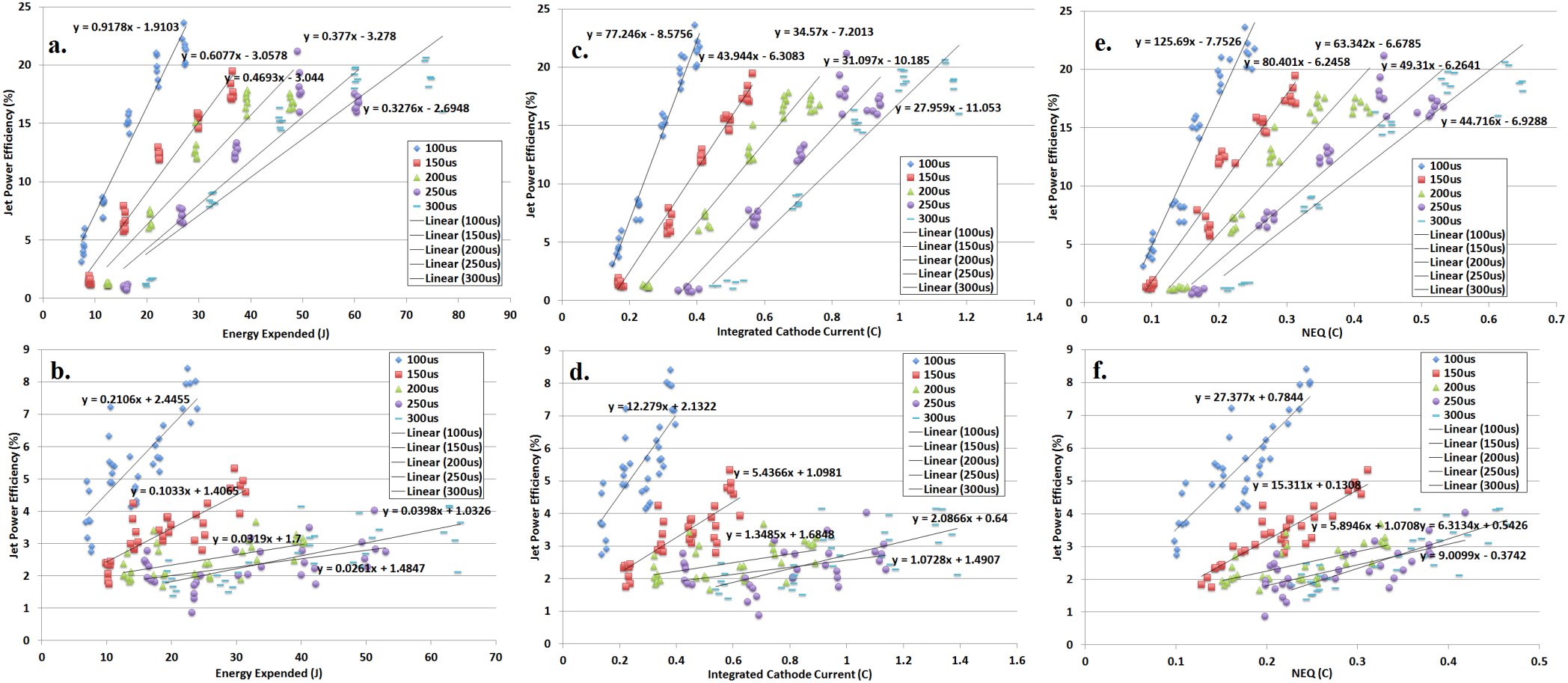

Figure 7.14: Ta Jet Power Efficiency data.

Vertical axis in each plot is the ratio of the kinetic energy in the exhaust to the input power, while horizontal axes are (from left) the energy expended in the arc by that pulse, the integrated cathode current for that pulse and the net ejected charge (NEQ) for that pulse. Top row of plots shows data for a non-eroded cathode, bottom row shows eroded cathode data.

7.2.6 Tungsten

Figure 7.15 shows the data for W specific impulse. Approximately 390,000 pulses were fired, which eroded approximately 7.7g of cathode material. Linear trendlines are fitted, with non-eroded surfaces producing highly linear (regression coefficients greater than 0.9) trends, while eroded surfaces behaving in a more scattered fashion.

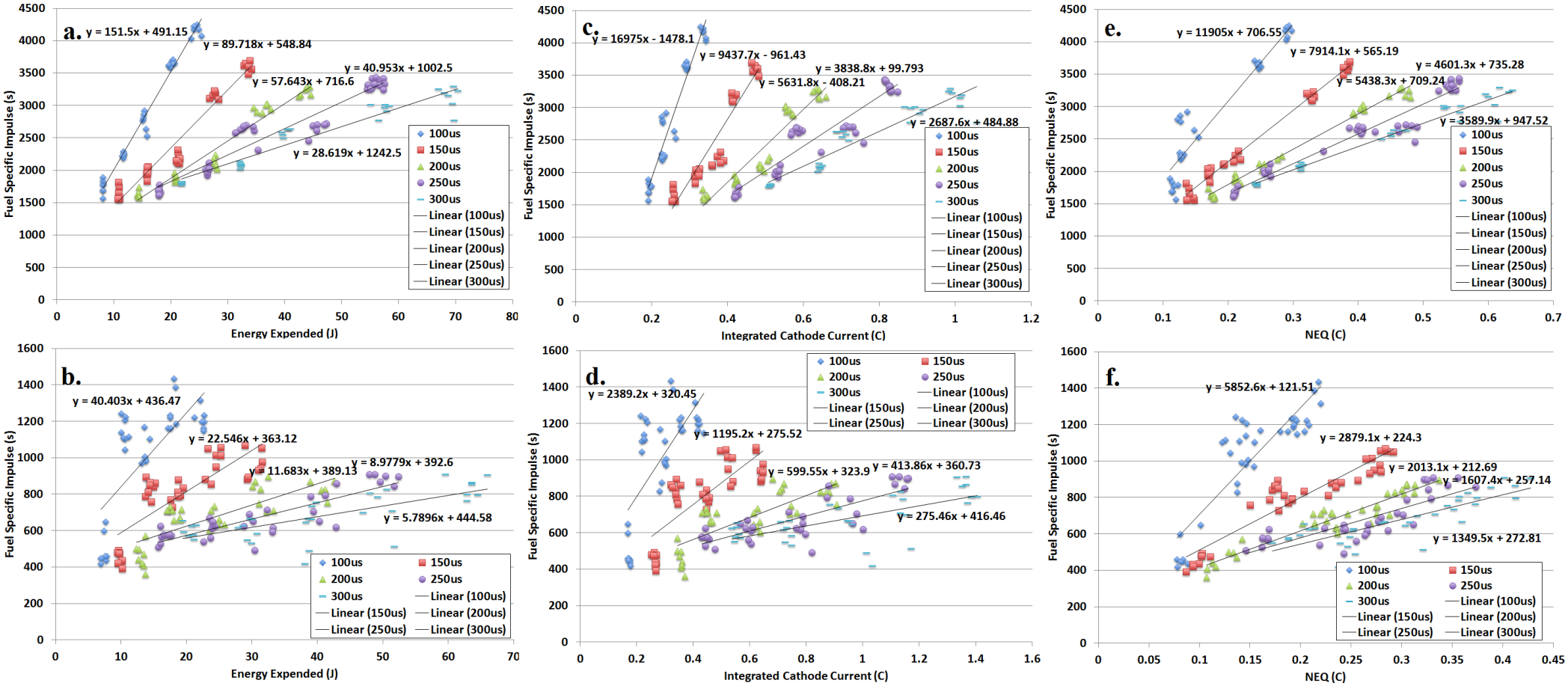

Figure 7.15: W fuel specific impulse data.

Vertical axis in each plot is the fuel specific impulse of W, while horizontal axes are (from left) the energy expended in the arc by that pulse, the integrated cathode current for that pulse and the net ejected charge (NEQ) for that pulse. Top row of plots shows data for a non-eroded cathode, bottom row shows eroded cathode data.

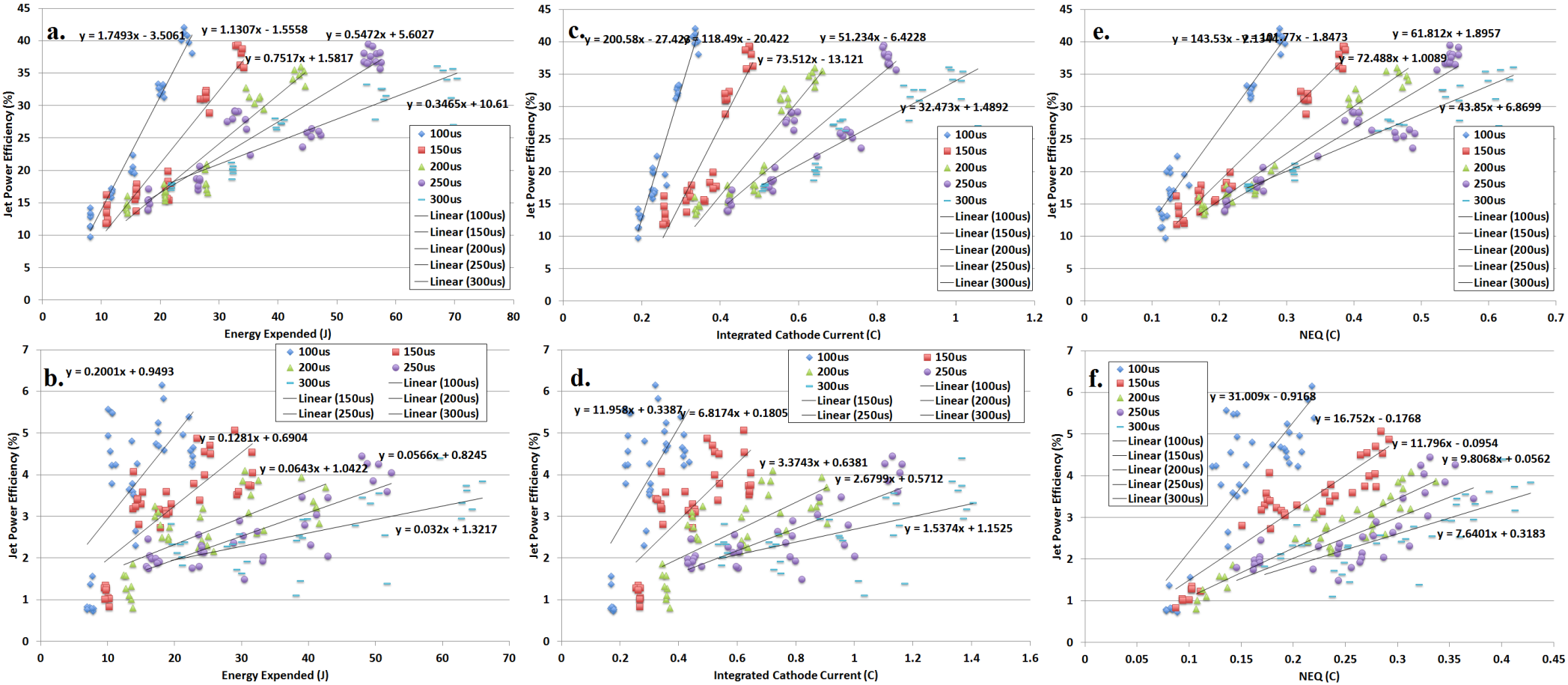

Figure 7.16: W Jet Power Efficiency data.

Vertical axis in each plot is the ratio of the kinetic energy in the exhaust to the input power, while horizontal axes are (from left) the energy expended in the arc by that pulse, the integrated cathode current for that pulse and the net ejected charge (NEQ) for that pulse. Top row of plots shows data for a non-eroded cathode, bottom row shows eroded cathode data.

7.3 Light Elements

Data for all light elements investigated, being C, Mg and Al, were taken in mid-2014 at the University of Sydney and has not been previously published.

7.3.1 Carbon

These figures use data that are derived from the combined carbon data erosion rate, being 33.46µg/C, as discussed in chapter 5.3.1. Figure 7.17 shows the data for C specific impulse while the plots in figure 7.18 show the jet power efficiency for C plasma pulses. Linear trendlines are fitted, with regression coefficients greater than 0.9 in all cases.

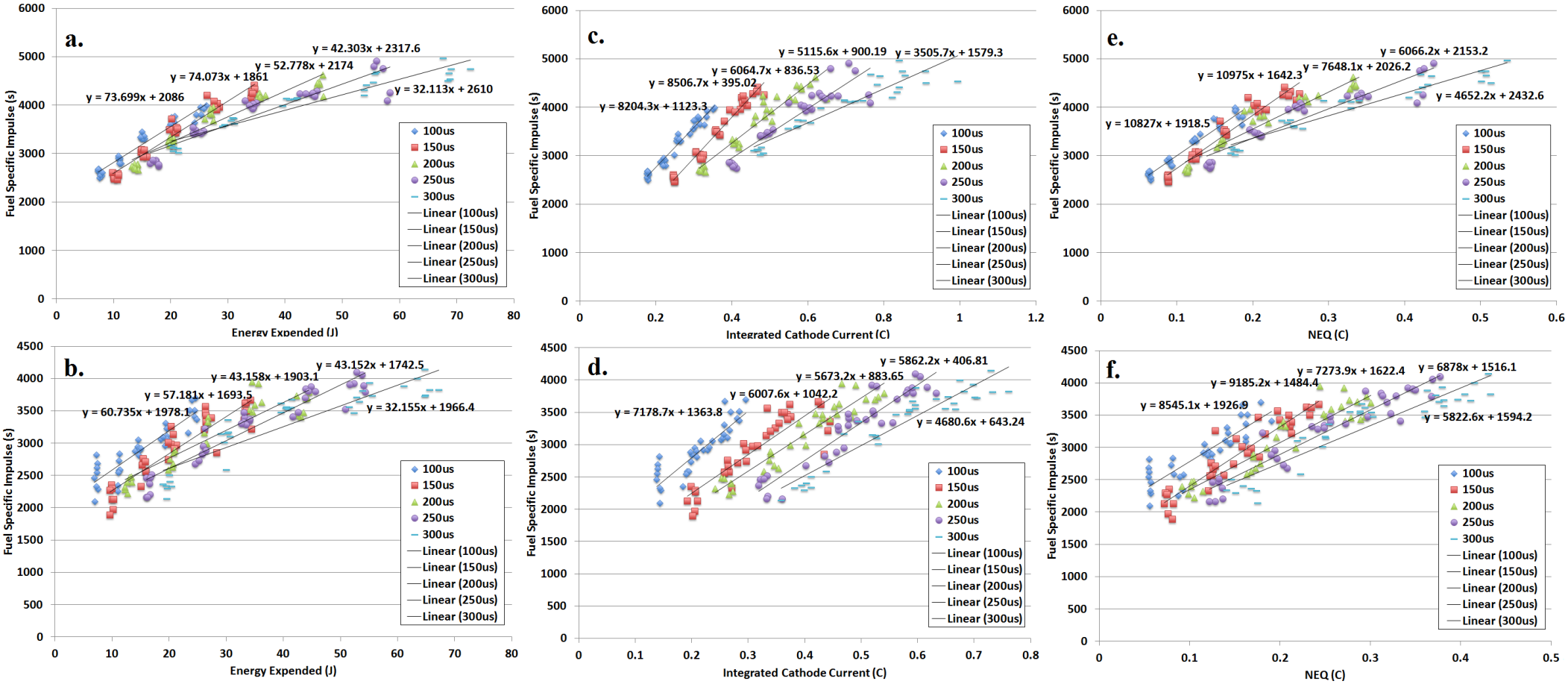

Figure 7.17: C fuel specific impulse data.

Vertical axis in each plot is the fuel specific impulse of C, while horizontal axes are (from left) the energy expended in the arc by that pulse, the integrated cathode current for that pulse and the net ejected charge (NEQ) for that pulse. Top row of plots shows data for a non-eroded cathode, bottom row shows eroded cathode data.

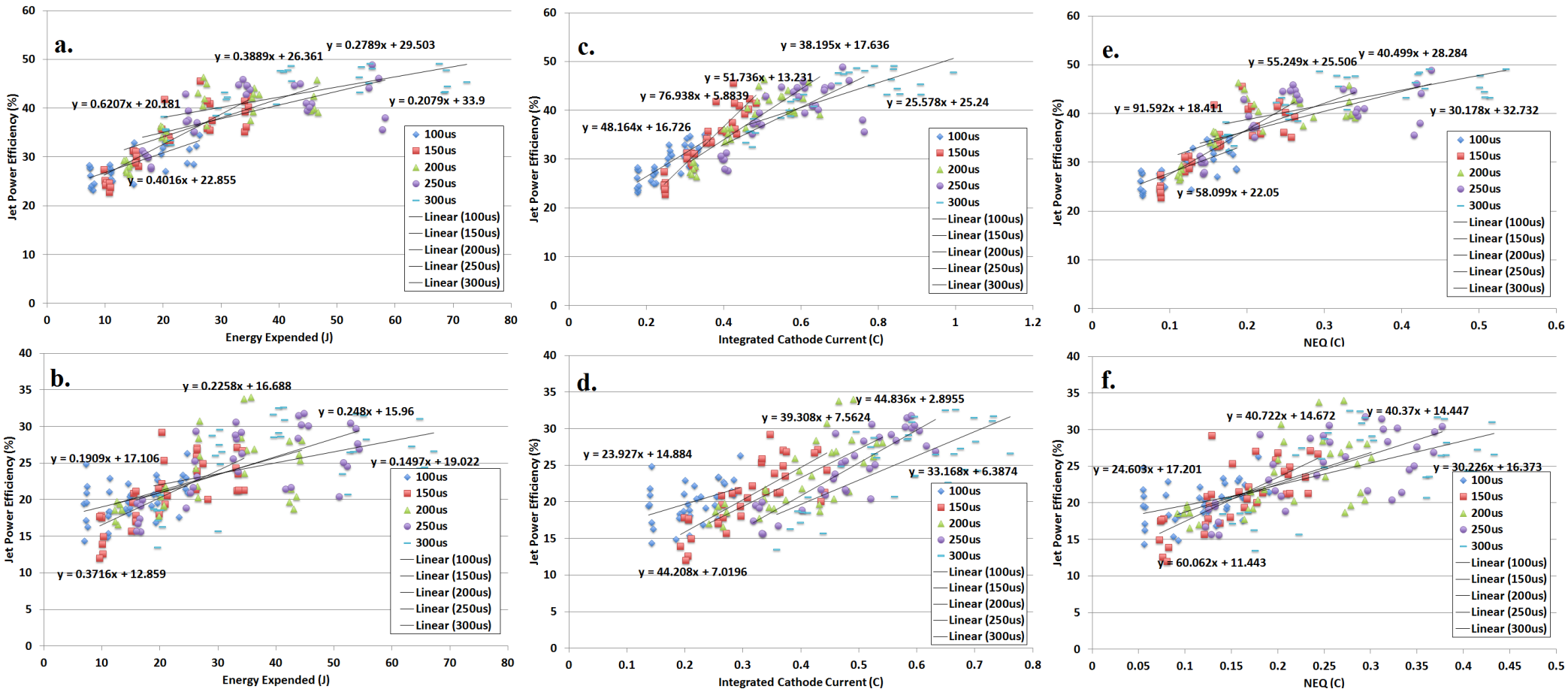

Figure 7.18: C Jet Power Efficiency data.

Vertical axis in each plot is the ratio of the kinetic energy in the exhaust to the input power, while horizontal axes are (from left) the energy expended in the arc by that pulse, the integrated cathode current for that pulse and the net ejected charge (NEQ) for that pulse. Top row of plots shows data for a non-eroded cathode, bottom row shows eroded cathode data.

7.3.2 Magnesium

Figure 7.19 shows the data for Mg specific impulse. Approximately 312,000 pulses were fired, which eroded approximately 2.4g of cathode material. The plots in figure 7.20 show the jet power efficiency for Mg plasma pulses. Linear trendlines are fitted, with regression coefficients greater than 0.9 in all cases, and it should be noted that Mg was the most efficient material tested by both metrics plotted. Further discussion of these results occurs in chapter 8, with special emphasis in chapters 8.4 and 8.5.

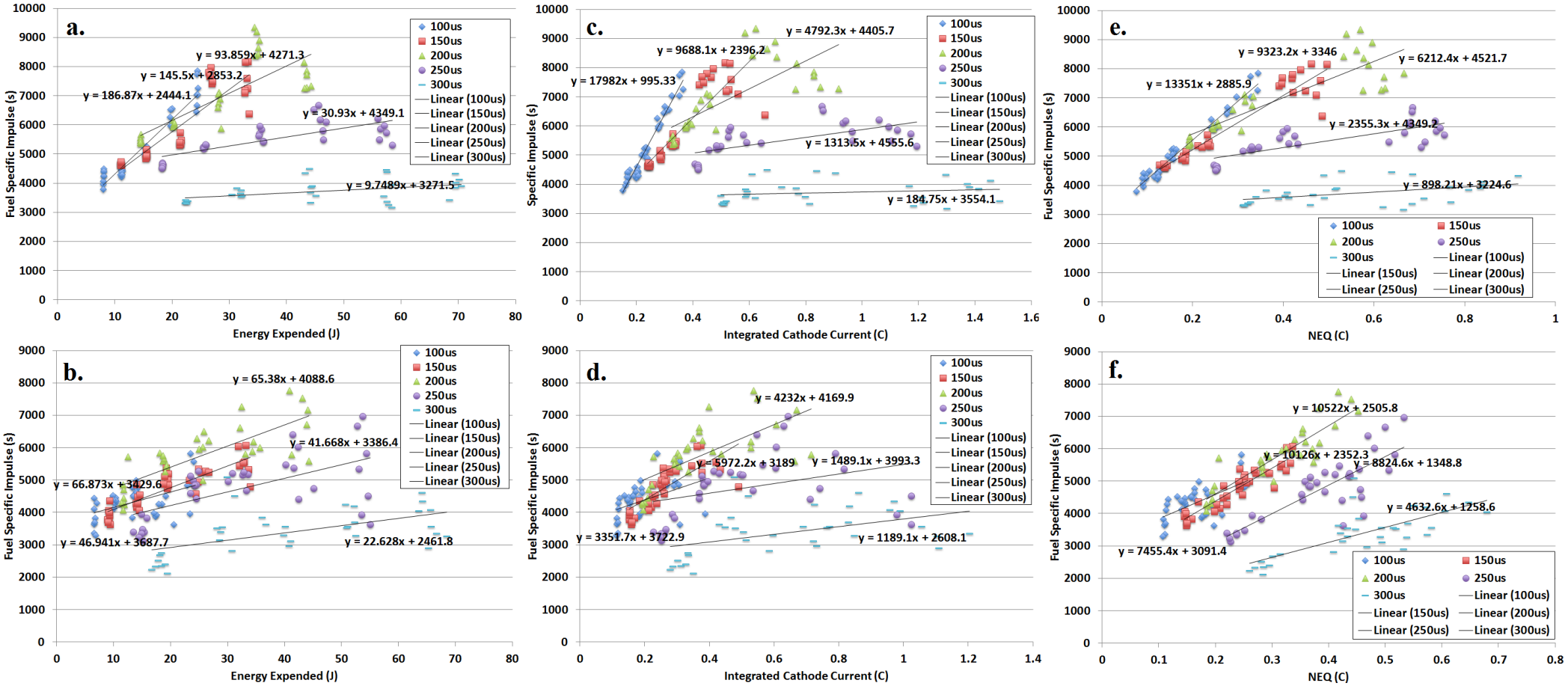

Figure 7.19: Mg fuel specific impulse data.

Vertical axis in each plot is the fuel specific impulse of Mg, while horizontal axes are (from left) the energy expended in the arc by that pulse, the integrated cathode current for that pulse and the net ejected charge (NEQ) for that pulse. Top row of plots shows data for a non-eroded cathode, bottom row shows eroded cathode data.

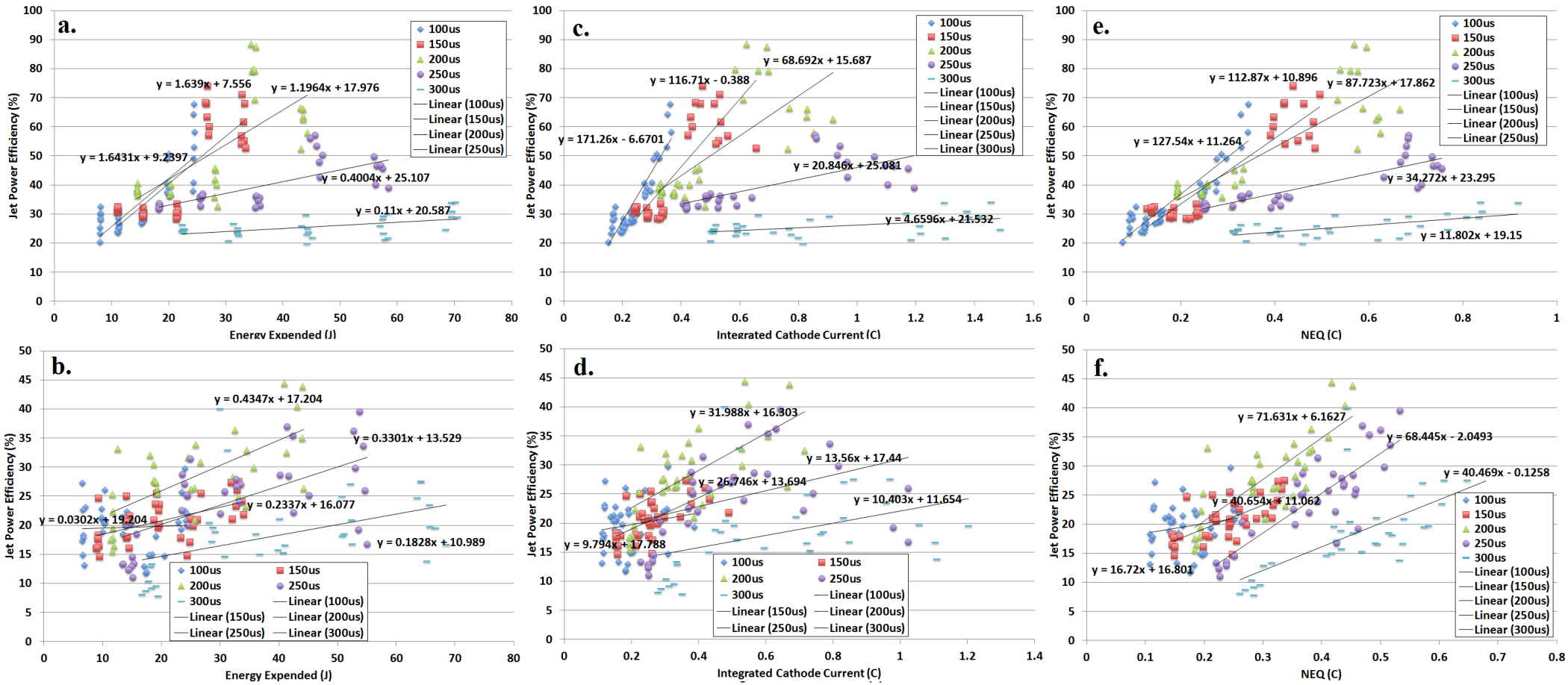

Figure 7.20: Mg Jet Power Efficiency data.

Vertical axis in each plot is the ratio of the kinetic energy in the exhaust to the input power, while horizontal axes are (from left) the energy expended in the arc by that pulse, the integrated cathode current for that pulse and the net ejected charge (NEQ) for that pulse. Top row of plots shows data for a non-eroded cathode, bottom row shows eroded cathode data.

7.3.3 Aluminium

Figure 7.21 shows the data for Al specific impulse. The plots in figure 7.22 show the jet power efficiency for Al plasma pulses. Approximately 228,000 pulses were fired, which eroded approximately 2.8g of cathode material. Aluminium was well-behaved though a degree of scatter is seen in these plots, especially when the eroded surface data is examined.

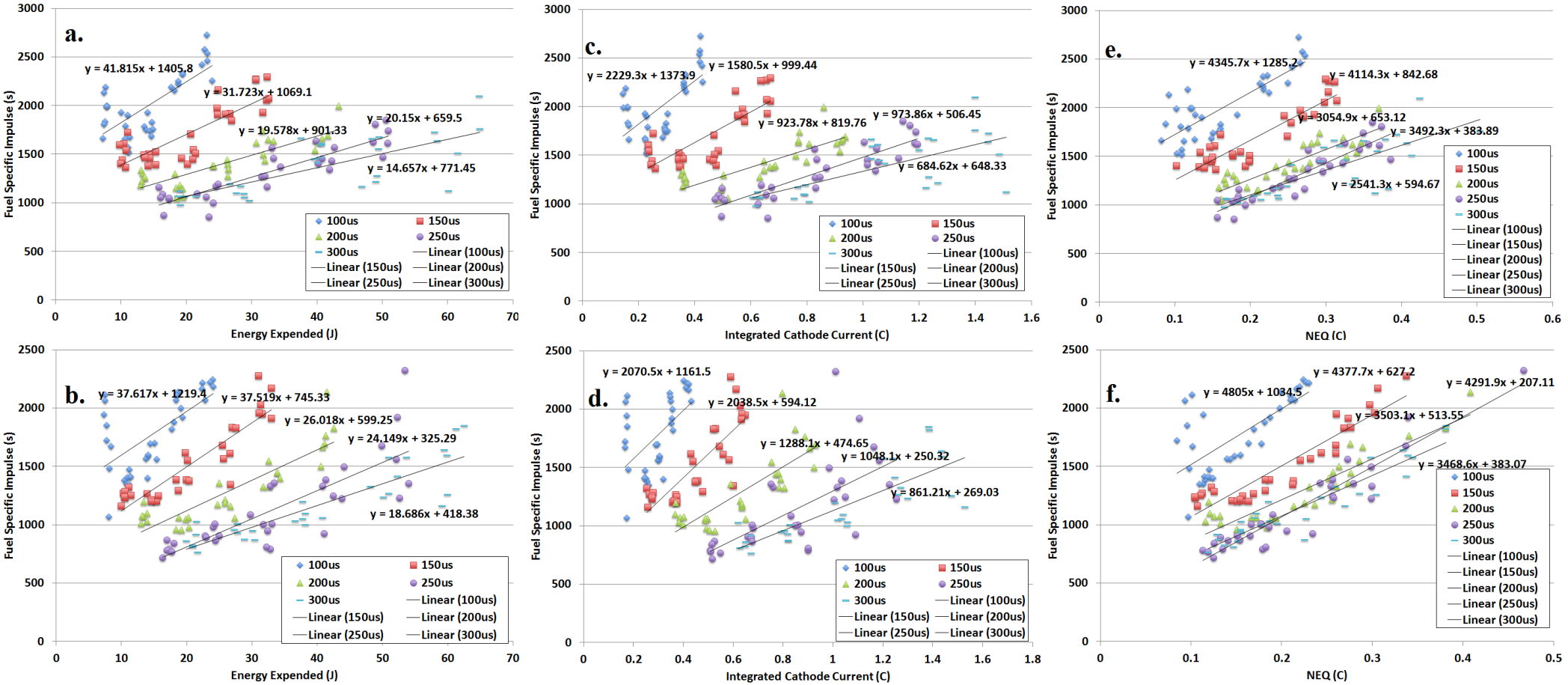

Figure 7.21: Al fuel specific impulse data.

Vertical axis in each plot is the fuel specific impulse of Al, while horizontal axes are (from left) the energy expended in the arc by that pulse, the integrated cathode current for that pulse and the net ejected charge (NEQ) for that pulse. Top row of plots shows data for a non-eroded cathode, bottom row shows eroded cathode data.

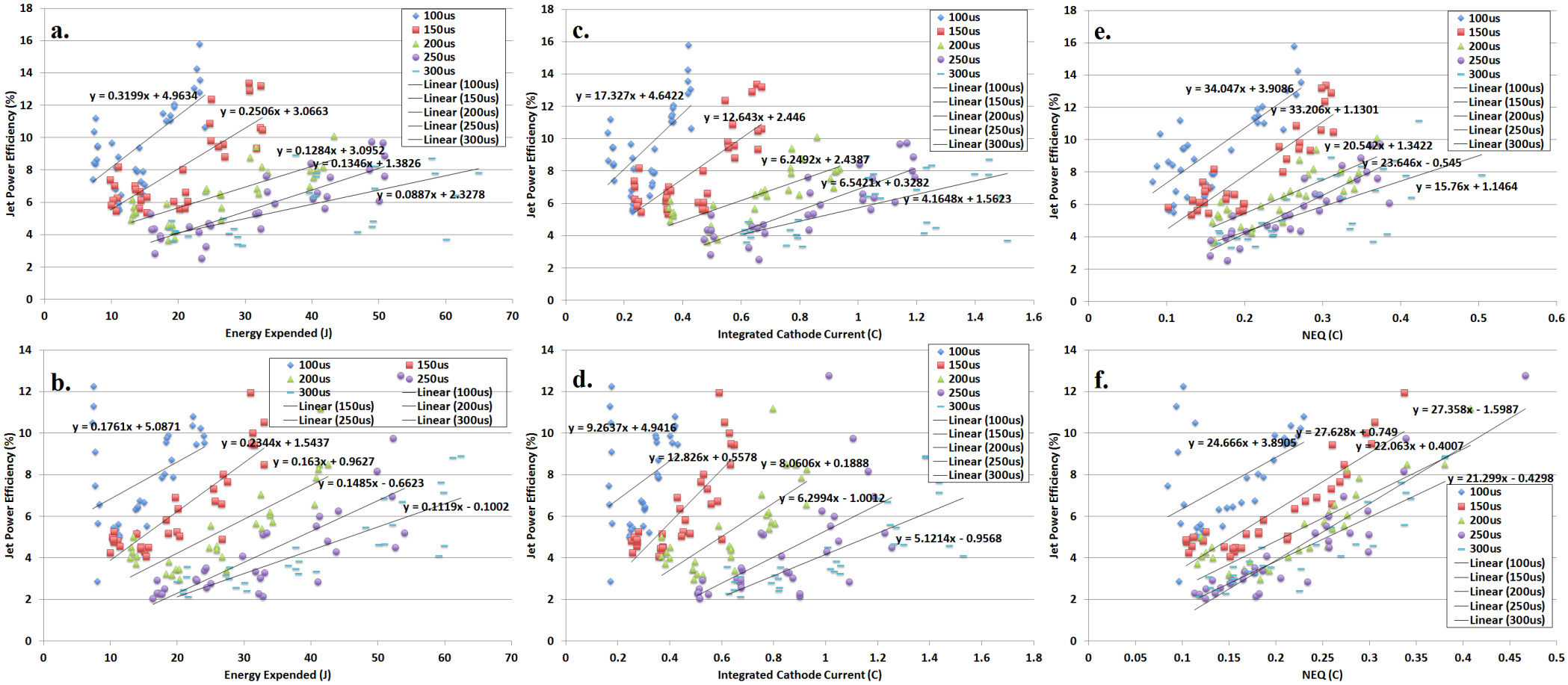

Figure 7.22: Al Jet Power Efficiency data.

Vertical axis in each plot is the ratio of the kinetic energy in the exhaust to the input power, while horizontal axes are (from left) the energy expended in the arc by that pulse, the integrated cathode current for that pulse and the net ejected charge (NEQ) for that pulse. Top row of plots shows data for a non-eroded cathode, bottom row shows eroded cathode data.

7.4 Summary of Derived Quantities

The data presented in chapter 7 is a result of combining the measurements presented in chapters 5 and 6 so that the efficiency metrics discussed in chapter 1 can be determined. Table 7.1 summarises these metrics for all elements studied, across the parameter space explored. Proper comparison between the efficiency metrics requires calculation of uncertainty bounds, which are included in table 7.1.

Element	Max Spec. Imp. Non-eroded (s)	Max Spec. Imp. Eroded (s)	Max Jet Eff. Non-eroded (%)	Max Jet Eff. Eroded (%)
Sn	637.8 ± 89.3	650.3 ± 91.0	9.520 ± 1.714	7.367 ± 1.326
Bi	105.1 ± 14.7	146.1 ± 20.5	1.001 ± 0.180	1.842 ± 0.332
Ti	6765 ±947	4431 ± 620	59.98 ±10.80	27.22 ± 4.90
V	5971 ± 836	3994 ± 559	61.93 ± 11.15	23.04 ± 4.14
Cr	2129 ± 298	2187 ± 306	10.50 ± 1.89	10.31 ± 1.86
Mo	4836 ± 677	4135 ± 579	46.80 ± 8.42	36.99 ± 6.66
Ta	3172 ± 444	1795 ± 251	23.63 ± 4.25	8.423 ± 1.516
W	4248 ± 595	1434 ± 201	42.08 ± 7.57	6.149 ± 1.107
C	4960 ± 694	4142 ± 580	49.15 ± 8.85	33.98 ± 6.12
Mg	9342 ± 1308	7755 ± 1086	88.53 ± 15.94	44.38 ± 7.99
Al	2728 ± 382	2323 ± 325	15.81 ± 2.85	12.77 ± 2.30

Table 7.1: Maximal fuel specific impulse and jet power efficiency values for all elements examined, for both non-eroded and eroded cathode surfaces.

All materials tested showed the same trends with respect to pulse duration in that short pulses tended to be more efficient than longer pulses. This is due to greater amounts of material eroded as vapour during longer pulses as well as the material eroded by side-arcing (see chapter 2.1), which is more prevalent in longer pulses. Both of these processes increase the cathode erosion rate without contributing to thrust as efficiently as forward-directed ion flow, and so lower the specific impulse and jet power efficiency. This is plainly illustrated in the Sn data plotted as figures 7.1 and 7.2, where the transition to side-arcing can be seen in the peaks in the data plotted for the 100, 150 and 200μs long pulses; longer pulses had side-arcing as standard, and so have flatter trendline slopes.. The very low performance of Bi is due to the very high mass flow rate measured in chapter five being primarily neutral vapour; this means that the majority of the thrust is produced by slow-moving neutral species that travel with approximately thermal velocity. This leads to very low specific impulse and jet power efficiency measurements.

8 Discussion of Results

Chapters 5 through 7 presented the results of experiments performed to determine the efficiencies for a range of potential fuels for a pulsed cathodic arc thruster. This chapter will discuss results common to all materials before discussing the performance of each material class. Comparison to current flight-rated thrusters will be made before avenues for future work are discussed.

8.1 Trends Common to All Materials Tested

All materials tested showed similar behaviour in their plots of cathode erosion rate against the energy expended in the arc during the pulse. The cathode erosion rate per unit energy expended in the arc is lower for short duration pulses and increases with increasing pulse length (see the "a" subplots in figures 5.1-11). This is shown by the trendlines fanning upwards from the horizontal as the pulses lengthen indicating a transition to a less efficient mode of operation. After a certain threshold is reached, the trendlines form parallel stacks on top of each other. That is to say, the short duration pulses tend to have shallow trendlines that intersect the vertical axis of each plot close to the origin. As pulse durations lengthen, the trendlines steepen and are also vertically off-set, resulting in intercepts that are further from the origin. Since this would imply non-zero erosion rates with zero energy expenditure, there must be another process eroding cathode material that expends little additional energy. It is proposed that this process is cathode heating. This would explain a gradual increase in cathode erosion rates in materials susceptible to evaporation, such as the heavy non-refractory metals. The Sn data plotted in figure 5.1a shows such a "fanning" of trendlines, where the slopes increase monotonically with energy expended in the arc. Side-arcing would result in more local heating as the cathode spots are less mobile, which would result in greater melting and evaporation of the surface. This would explain discontinuities in the erosion rate trends after the onset of side-arcing, such as in the Mg data plotted in figures 5.10 and 11.1.

All materials showed an increase in impulse delivered with increasing pulse duration and cathode current. All materials except Bi showed an increase in impulse delivered with increasing NEQ, while Bi impulse measurements showed no clear trends vs NEQ; this is thought to be due to the high erosion rate of Bi. Thrust measurements for all materials showed the same trends with respect to energy expenditure and integrated cathode current, but shorter pulses generated more thrust. This can be seen not only in the numerical values of thrust but in the changing trendline slopes in the plots, for example in the Mg data in figure 6.20. This reduction in thrust in longer pulses is due to the production of neutral vapour through cathode heating as the pulse progresses, as this vapour would interfere with the motion of the ions in the plasma via collisional processes [24-27].

While not a standard efficiency metric like fuel specific impulse or jet power efficiency, many sources cite the thrust-to-power ratio of electric propulsion systems as an important metric for comparison between various propulsion systems [2, 4, and 14]. The thrust-to-power ratio is identical to the impulse delivered per unit energy expended, which can be approximated from the gradients of the trendlines fitted to the plots of impulse delivered to the pendulum vs the energy expended in the arc per pulse. The approximations are good as the y-intercept values for each trendline are quite close to the origin, indicating that no thrust would be generated when no plasma is produced, which is as expected. The trendline gradients are shown in table 8.1, together with the uncertainties in each fit, to allow more robust comparisons with current flight rated propulsion technologies.

Data Set	100μs Thrust-to-Power Ratio (μN/W)	150μs Thrust-to-Power Ratio (μN/W)	200μs Thrust-to-Power Ratio (μN/W)	250μs Thrust-to-Power Ratio (μN/W)	300μs Thrust-to-Power Ratio (μN/W)
Sn Non-eroded	27.1±2.7	27.3±2.7	19.8±2.0	17.6±1.8	18.8±1.9
Sn Eroded	22.3±2.2	21.5±2.2	18.1±1.8	16.6±1.7	18.0±1.8
Bi Non-eroded	18.1±1.8	16.8±1.7	16.1±1.6	14.3±1.4	15.1±1.5
Bi Eroded	24.4±2.4	20.9±2.1	15.7±1.6	14.6±1.5	13.4±1.3
Ti Non-eroded	17.2±0.9	15.9±0.8	16.4±0.8	16.5±0.8	16.7±0.8
Ti Eroded	12.6±0.6	15.4±0.8	16.5±0.8	15.5±0.8	14.4±0.7
V Non-eroded	22.0±1.1	25.8±1.3	24.9±1.2	22.6±1.1	20.8±1.0
V Eroded	10.2±0.5	12.2±0.6	11.3±0.6	10.8±0.5	11.1±0.6
Cr Non-eroded	9.4±0.5	8.7±0.4	8.3±0.4	7.8±0.4	7.4±0.4
Cr Eroded	8.9±0.4	8.5±0.4	8.2±0.4	8.6±0.4	7.4±0.4
Mo Non-eroded	18.4±0.9	20.2±1.0	18.8±0.9	19.1±1.0	17.9±0.9
Mo Eroded	17.5±0.8	18.1±0.9	19.6±0. 9	20.3±1.0	20.1±1.0
Ta Non-eroded	17.6±0.8	20.4±1.0	22.2±1.1	22.5±1.1	22.5±1.1
Ta Eroded	10.0±0.5	10.5±0.5	9.1±0.5	9.0±0.5	9.6±0.5
W Non-eroded	22.5±1.1	24.1±1.2	24.6±1.2	24.8±1.2	22.8±1.1
W Eroded	9.4±0.5	10.0±0.5	9.3±0.5	10.0±0.5	9.1±0.5
C Non-eroded	15.8±0.8	18.3±0.9	18±0.9	17.5±0.9	18.5±0.9
C Eroded	11.8±0.6	13.8±0.7	12.9±0.6	13.4±0.7	12.6±0.6
Mg Non-eroded	16.0±0.8	19.1±0.9	19.4±0.9	17.5±0.9	15.8±0.8
Mg Eroded	8.3±0.4	8.5±0.4	11.2±0.6	11.9±0.6	12.4±0.6
Al Non-eroded	11.8±0.6	12.1±0.6	10.8±0.5	11.3±0.6	10.0±0.5
Al Eroded	9.7±0.5	10.6±0.5	10.8±0.5	10.7±0.5	10.4±0.5

Table 8.1: Thrust to Power ratios for all materials tested. Ratios are calculated from the gradients of the trendline fits for plots of impulse vs energy expended. All figures are to 1 decimal point, and units are μN/W.

Fuel specific impulse and jet power efficiency values for all materials showed the same trends with respect to pulse duration, with short-duration, high-current pulses tending to be more efficient than longer pulses. This is due to greater amounts of material eroded as vapour during longer pulses as well as the material eroded by side-arcing in longer pulses. Both of these processes increase the cathode erosion rate without contributing to thrust as efficiently as forward-directed ion flow, and so lower the specific impulse and jet power efficiency. This is illustrated in the Sn results plotted in figures 7.1 and 7.2.

8.2 Trends Specific to Non-Refractory Metals

Non-refractory metals had the highest erosion rates and thus lowest efficiencies, though they also had the highest thrust measured and the highest thrust-to-power ratio. Tin demonstrated the highest thrust of all the materials tested, though not the highest impulse. The similarity in trendline slopes for the 100 and 150μs long pulses in all the Sn plots indicates that the cathode spots are travelling on the front face of the cathode throughout the duration of these pulses, as opposed to the three longer pulse durations examined. This implies that somewhere between 150 and 200μs into the pulse the cathode spots on a Sn cathode reach the edge of a 25mm diameter cathode and begin side-arcing (this was confirmed by visual inspection during arc operation). Side-arcing results in much higher mass flow rates, due to higher local heating by less mobile cathode spots. The majority of this material is neutral vapour, which results in far higher cathode erosion rates when compared to shorter pulses.

The significantly lower lattice binding energy of Bi results in Bi erosion rates being the largest of all materials tested [59]. While Bi showed typical patterns in data in most plots, no trends were readily apparent in the Bi impulse and thrust data when plotted against NEQ. This is thought to be due to the high erosion rate of Bi. Since so much material is eroded from Bi cathodes during the pulse, and since most of this material is neutral vapour, there would be more collisions between ions and neutral species compared to other arc plasmas [26]. This increased rate of collisions reduces the ion charge state and would interfere with the free path of ions directed forwards, out of the anode. This phenomenon reduces the NEC substantially, and measured values are the lowest for all materials examined. These low NEQ measurements would therefore be dominated by random noise. The thrust from a Bi cathode is dominated by neutral vapour and macroparticles.

The comparatively large cathode erosion rates for Sn and Bi lead to them having low specific impulses and jet power efficiencies when compared to every other material tested. The dependence on eroded mass allows the onset of arcing to be very clear in the specific impulse plots for Sn. There

was little change for Sn between the non-eroded and eroded cathode surfaces, with most datapoints being within the uncertainty bounds of their counterparts, though Bi showed a slight performance increase after wear. This can also be seen in the thrust-to-power ratios shown in table 8.1. Photographs of the Sn and Bi cathodes are shown in figure 11.4; note the narrowing of the Bi cathode and its irregular surface. This is clear evidence of extensive erosion due to cathode heating causing melting, as well as side-arcing.

8.3 Trends Specific to Refractory Metals

The erosion data for the refractory metals was typical of the pattern described earlier in that shorter pulses eroded less material than longer pulses, with an increase in erosion with increased cathode heating over time. Several datasets show a transition towards side-arcing late in the pulse, such as the Ti and V 300 µs pulses; the increased slope of the trendline of eroded mass plotted against NEQ is plain evidence of this. The side-arcing transitions occur much later in the pulse for each of the refractory metals compared to non-refractory metals, which indicates lower spot velocities. The far lower erosion rates of all six refractories compared to both Sn and Bi is probably due to the higher lattice binding energies of the refractory metals. Erosion profiles for all refractory metals were typically concave, with V and Ta cathodes shown in figure 11.7.

A surprising result was that the light refractory metals (Ti, V, Cr) have lower cathode erosion rates than Mo, which in turn has lower erosion rates than the two heavy refractory metals tested (Ta and W). This is true for erosion rates with respect to energy expended as well as with respect to integrated cathode current and NEQ. This is different to what was predicted, as it would be expected that the heavier elements, with their higher lattice binding energies and boiling points, would produce less plasma for a given amount of energy put into the system due to the higher energy cost of removing ions from the lattice and evaporating neutral vapour. However, the erosion rates identified in chapter 5 are those related to eroded cathode mass, not the number of cathode atoms eroded; the molar erosion rates for all materials tested are shown in table 8.2.

Element	100 µs Molar Erosion Rate (nmol/J)	150 µs Molar Erosion Rate (nmol/J)	200 µs Molar Erosion Rate (nmol/J)	250 µs Molar Erosion Rate (nmol/J)	300 µs Molar Erosion Rate (nmol/J)	Lattice Binding Energy (eV/atom) [58]
Sn	36.48	38.92	75.31	95.19	116.25	3.14
Bi	88.53	162.22	103.36	175.61	293.81	2.18
Ti	3.55	4.97	5.39	6.23	8.17	4.85
V	3.59	3.85	4.46	4.24	4.99	5.31
Cr	3.48	2.35	3.62	3.46	2.96	4.10
Mo	2.64	3.23	3.42	3.48	3.27	6.82
Ta	1.30	2.54	3.54	3.72	3.58	8.10
W	1.60	2.15	3.25	2.83	3.08	8.90
C	32.00	26.75	37.08	32.33	26.50	7.37
Mg	5.31	5.43	6.46	8.60	11.77	1.51
Al	7.07	8.26	10.26	13.30	12.52	3.39

Table 8.2: Molar erosion rates for refractory cathodes; units are nanomoles of cathode material eroded per Joule of energy expended in the arc and all figures are to two decimal places

The molar erosion rate defines how many moles of cathode atoms are eroded per Joule of energy expended. Molar erosion rates with respect to energy were chosen because lattice binding energies are in units of energy per atom. It is clear that the heavy refractories erode far fewer atoms than the lighter refractories due to their higher lattice binding energies and lower vapour pressures. Furthermore, higher binding energies tend to result in lower erosion rates, with two exceptions; C and Mg. It is thought that the higher than trend erosion of C is due to ejection of carbon granules as macroparticles after the sintered bonds between granules have been eroded. The anomalously low Mg erosion rate is possibly due to the fast spot motion observed in arc operation leading to less cathode heating; the heating created by side-arcing would greatly increase the molar erosion rate in long pulses, which is shown in the data. The percentage uncertainties in the molar erosion rates are similar to those for the mass erosion rates given in chapter 5; most uncertainties are below 10%, and the data in table 8.2 are plotted in figure 8.1.

Refractory metal impulse and thrust data were also typical. The shallowing of the linear trendlines indicates that more energy is being expended with increases in pulse length without generating a comparable amount of thrust. Many of the impulse measurement plots have trendlines that are close to parallel, or even overlap; this would indicate that the arc is operating in the same mode of operation across all parts of the parameter space explored in that plot. Certain of the thrust measurements showed a major increase in thrust as V_{ch} was increased. This is particularly noticeable in the V thrust data for non-eroded cathodes plotted in figure 6.8, where each data set has a transitional jump in performance after the second or third value of cathode current (~3.25kA average cathode current in V)

explored. One explanation is that the higher cathode currents permitted the creation of higher charge state ions in the cathode spot, which would then be accelerated to a greater extent by the discharge [24-28]. This does not explain why this jump is so much less observable in the eroded thrust data and more work is needed to measure the ion charge state distribution in these materials during arc pulses at such high currents.

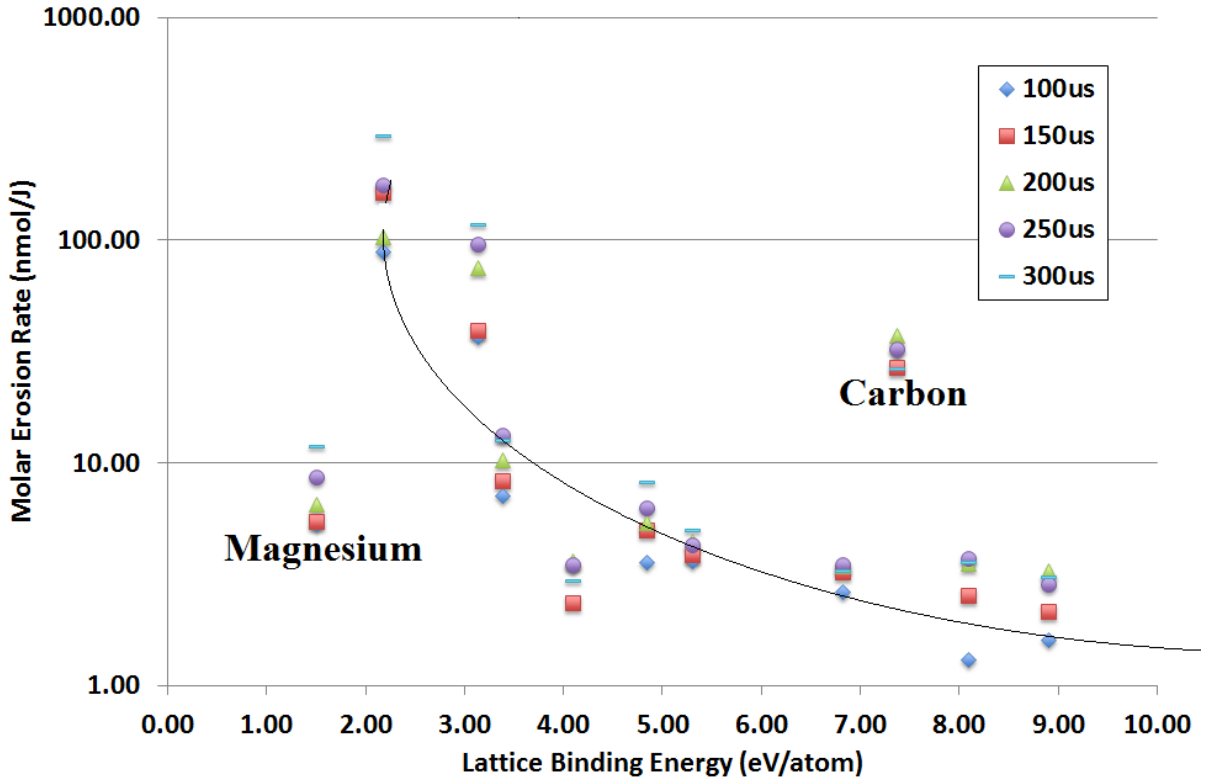

Figure 8.1: Molar erosion rates per unit energy expended in the arc. Vertical axis is logarithmic, showing erosion rate in units of nanomoles per Joule, horizontal axis is in units of electron-Volts per atom. Mg and C points are marked to showcase deviation from general trend, though the line plotted is not a trendline but merely present to guide the eye.

Fuel specific impulse and jet power efficiency data for refractory metals were also typical of the pattern described in section 8.1, with shorter pulses being more efficient. However, certain materials (e.g. V) showed a marked increase in performance when at higher currents (~3.25kA average cathode current) for the same pulse duration. This is a direct consequence of these two metrics being derived from the thrust measurements, which also showed this performance increase at the higher cathode currents.

The refractory metals all showed a drop in performance with cathode wear, though Cr and Mo had the lowest change. Many of the relevant data points have overlapping uncertainty bounds, indicating performance change too slight for the experimental apparatus to properly discern. The eroded cathode

surface performance of Ti and V was approximately one third to one half that of the comparable performance when non-eroded, and the changes for W and Ta were even greater.

8.4 Trends Specific to Light Elements

Aluminium data trends were similar to those described in section 8.1, in that short pulses were better, though those for C and Mg deviated slightly. Carbon showed a clear trend within each pulse duration data set, showing an increase in erosion with increasing current (and thus integrated cathode current, NEQ and energy expended). However, there was no clear trend with respect to pulse duration. Magnesium showed the expected trends with respect to cathode current and pulse duration, but was susceptible to side-arcing in long pulses as shown by the much higher cathode erosion rates for 250 and 300μs pulse durations.

Carbon cathodes behave differently to those made from metals due to their method of manufacture. Rather than being cast or drawn, C cathodes are sintered from smaller granules of carbon and then machined to the correct size. The lower adhesion between granules compared to the adhesion between metallic crystal domains would lead to more macroparticle emissions due to ejected granules. Combined with the collisional effects produced by any volatiles trapped inside the cathode, this is a likely cause for the high variability observed between data sets. The cathode was baked-out by firing 3000 pulses (see section 6.3.1) in order to reduce the variability due to volatiles, though nothing could be done to reduce macroparticle emissions from C. Cathode bake-out increased the performance and reliability of the C cathode, especially in longer and higher current pulses. A comparison between unbaked and baked carbon cathode performance is included as figure 11.2, while images of unbaked and baked C cathodes are shown in figure 11.3.

Aluminium and magnesium eroded more like the refractory metals; shorter pulses, and lower current pulses, erode less material than longer, higher current pulses. The erosion profile for Al was shallower than typically seen in the refractory metals, as shown in figure 11.5. The transition to arcing was seen in Mg when going from $160V_{ch}$ to $180V_{ch}$ during 200μs pulses, resulting in substantially higher cathode erosion. When included in the plot of erosion rate vs integrated cathode current, as in figure 11.1, the slope of the 200μs trendline increases from 11.7μg/C to 20.6μg/C, illustrating that transition to a different mode of operation is taking place. Also of note was the high volume eroded by side-arcing, and the deep channels cut into the cathode surface by the cathode spots. As such, the Mg cathode was flipped after shot number 33119, being the shots at $160V_{ch}$ and 250μs duration to measure erosion, so that the remaining erosion pulses could be done from a less

eroded surface. After flipping, the surface then eroded in the typical concave pattern; the erosion patterns on each Mg surface are shown in figure 11.6. One interesting result is that Mg had both the lowest lattice cohesive energy [58] and temperature at which the saturated vapour pressure is 1Pa (see table 4.1), which would imply that a lot of neutral vapour should be boiling off the cathode surface, leading to inefficient operation. This is not the case; Mg has the lowest cathode erosion rates of all the materials tested when measured against integrated cathode current and NEQ.

Impulse and thrust in carbon was close to typical. Cathode wear tended to result in more variability, due to the sharper and deeper erosion pits excavated in the surface of the C cathode during arc operation. Some of the eroded C cathode impulse measurement shots exhibited rapid oscillations in current and voltage during the pulse, termed "feathering"; traces from shot 35164 (C eroded cathode surface, 300μs duration, $180V_{ch}$) are shown as figure 8.2. Feathering was observed only in C data, and only for eroded cathode surfaces.

Feathering is in contrast to the smoother behaviour shown in figure 3.13 which was also an eroded C cathode impulse measurement at 300μs duration but at $120V_{ch}$. Feathered pulses tended to deliver less impulse to the pendulum, implying that the arc is less stable during this mode. Feathering is thought to be a product of cathode wear, as the deeper pits eroded into C cathodes would result in cathode spots being partially shielded from forming low impedance pathways to the anode during part of the arc. This would result in an increase in cathode voltage until a cathode spot can form in a more spatially favourable, but less energetically favourable, location. This new cathode spot would lower the voltage and increase the discharge current rapidly while it was operating. After cathode spot extinction, the process would repeat, resulting in the rapid oscillations observed in the plasma parameter traces seen in figure 8.2.

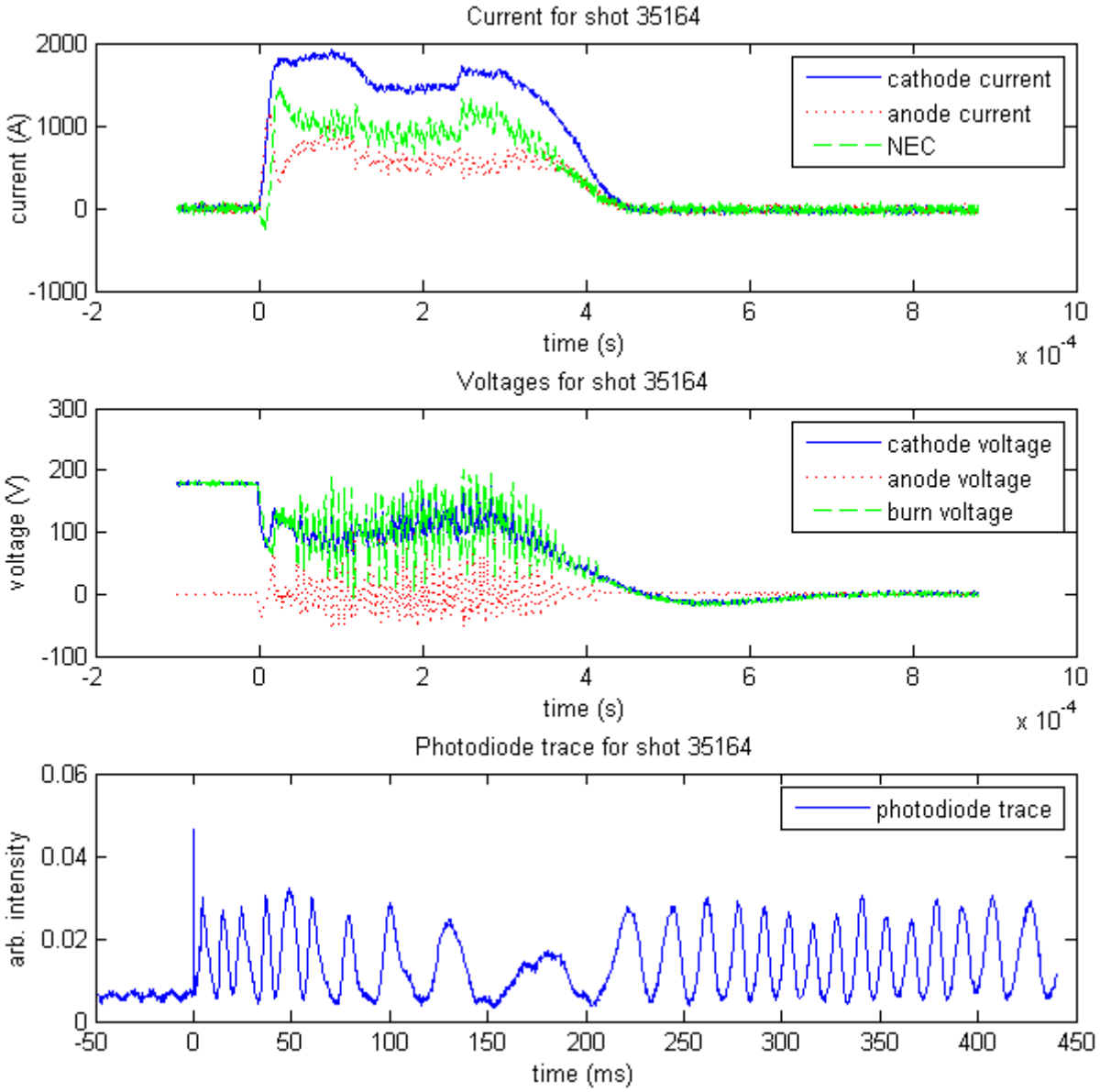

Figure 8.2: Data for shot 35164 showing evidence of "feathering."

The impulse and thrust data for Mg and Al were also typical in that best performance was observed in shorter pulses, though the non-eroded Mg thrust data showed the same performance jump at higher cathode currents (~3.25kA average cathode current) within the same pulse duration described in the previous section for V thrust.

Both C and Al showed a slight but measurable drop in performance with cathode erosion, with some differences being so small that the uncertainty bounds overlap. Mg showed a larger drop in performance, but due to it having the lowest measured erosion rate it had by far the best fuel specific impulse and jet power efficiency for both eroded and non-eroded cathode surfaces.

8.5 Comparison to Current Propulsion Technologies

Numerous electric propulsion systems have been deployed for orbital transfer and station-keeping applications in recent years, demonstrating the efficiency and reliability of the various technologies involved in their use. Examination of published literature on various flight-tested thrusters [2-9] shows that fuel specific impulses of 2500 to 3500s are routinely produced by these engines using xenon as fuel. Most materials tested in this work produced thrust with specific impulses greater than 3500s, with the exceptions being Sn, Bi and Cr. It is better to compare on the performance of eroded cathode faces, as electric thrusters must operate over long timescales to generate the total impulse change required. On this basis, Ti, V, Mo, C and Mg all outperform the cited flight-qualified ion thrusters and Hall Effect thrusters, with Mg being a standout performer. In fact, Mg performance is comparable to that of the HiPEP thruster developed by NASA, which is the current record holder for highest specific impulse of any well-characterised prototype thruster (7755 ± 1086s for Mg vs 9200s for HiPEP) [4].

Jet Power Efficiency, also called thrust efficiency [equation 17-12 in ref 1], is another key performance metric. The literature shows efficiencies for various thrusters of 50 to 80%, depending on the technology and the power levels used. Three materials tested had jet power efficiencies firmly within this range for non-eroded cathode surfaces, being Ti, V and Mg, with Mo and C being partially in this range. For the work done on eroded cathodes, only magnesium came close, with a max measured jet power efficiency of 44.4±8.0%. Thus Mg fuelled arc thrusters are at the low end of being competitive when measured against this metric.

Xenon-fuelled Hall effect thrusters have the best thrust-to-power ratio of the various flight-qualified electric propulsion technologies, with each one producing slightly less than 60µN/W [2, 3]. Xenon ion thrusters tend to produce 30 to 40µN/W [2, 4, 6], with lower efficiencies being found in small devices (such as the µ10 ECR thruster, 23.8µN/W) [table 9.6 in ref 2] and at high power consumptions (HiPEP, falling from 24.7µN/W at 9.7kW to 17.0 µN/W at 39.3kW) [4]. The best thrust-to-power ratio measured for eroded cathodes was that of Bi, followed by Sn; both of these were in the low 20s of microNewtons per Watt of power, which makes them competitive with HiPEP and the µ10 ECR thruster but none of the other thrusters. Of the materials with competitive specific impulses the best performer is Mo, which generates 20.3±1.0µN/W from an eroded cathode surface; easily better than Mg which can produce approx. 12µN/W from an eroded cathode surface under the best conditions tested. Thus, according to the thrust-to-power metric, cathodic arc thrusters are not

competitive with current flight rated propulsion systems for large thrust applications. However, flight-rated systems that perform well on the thrust-to-power ratio tend to have lower specific impulses, and the optimal published power ratings are only available for specific operation conditions. The data presented for PCA systems yields more consistent thrust-to-power ratios over the whole range of powers used for most cathode materials (exceptions being Sn, Bi and Mg).

In terms of comparing standout performers, we can compare the Mg results to those for HiPEP [4]. During the most efficient Mg pulses, energy expended in the arc per pulse was between 35 and 40J over 200μs of operation, or 175 to 200kW average power expended in the plasma while the arc is firing, while producing approximately 3N of force. This is approximately five times the force exerted by HiPEP for approximately five times the power exerted during the highest power setting (670mN from 39.3kW), which indicates that if Mg pulses were run "continuously" by staggering the firing pattern over a number of cathodes that they would be competitive with HiPEP at this early stage of development.

Miniaturisation of various thruster types results in lower efficiencies than is typical for that system; an example is the μ10 ECR ion thruster [2]. The PCA system described in this thesis is quite competitive with miniaturised existing thruster technologies, especially on the metric of specific impulse, but also with respect to the thrust-to-power ratio. Miniaturised systems typically have thrust-to-power ratios <10μN/W, whereas most cathodes tested had a thrust-to-power ratio >10μN/W [references 14-30 cited in reference 23]. The management of propellant is also much easier in a solid fuelled system when compared to a gaseous system, which is described by Keidar et al in their work on miniature PCA systems as "...the most important issue for microthrusters" [23].

The system described in this thesis outperforms miniature PCA thrusters developed for use in microsatellite manoeuvre applications based on the various efficiency metrics explored [17, 23, and 60]. This work by Keidar and others used Ti at much lower arc currents in an edge-triggered arc system rather than the centre-triggered arc used in this work. This work has demonstrated that high current centre-triggered arcs are more efficient than low current edge-triggered systems, delivering higher specific impulse (~4500s vs ~3000s), jet power efficiency (~27% vs ~15%) and a higher thrust to power ratio (~16μN/W vs ~5μN/W) when using Ti as fuel [23]. A large part of the inefficiency in Keidar's system would be due to the convex erosion profile created by the edge-triggering (see section 2.1). The concave erosion profile formed by a centre-triggered system directs more of the

plasma flow downstream without the use of focussing magnetic fields, as used by Keidar et al (300mT at anode mouth) [23, 30]. The higher charge states found in higher current arcs would also increase efficiency [27, 36]. Choosing Mg as the fuel would increase the system efficiencies further, giving a specific impulse of ~8000s, jet power efficiency ~45% and a thrust-to-power ration of ~12μN/W. While Keidar's device is suited for microsatellite applications it is apparent that the device tested herein could also be a replacement for larger thrusters used for orbital transfer manoeuvres as well as station-keeping.

8.6 Avenues for Future Work and Optimisation

There are three areas that present themselves for consideration in future work in order to develop this technology into a practical thruster and further improve the performance of the system: magnetic field focussing for thrust enhancement; cathode advancement; and cathode spot steering to enhance cathode consumption efficiency.

It has been known for some time that a magnetic nozzle can increase the efficiency of arc discharges, or electric thrusters in general, via the end-Hall effect and thermodynamic processes [11, 40]. The use of magnetic fields can increase plasma drift velocity by a factor of 2 to 3 in Ti plasma by applying up to 60mT magnetic fields, and it would be reasonable to assume that such effects would be seen in other metal plasmas [40]. Magnetic fields would also tend to focus the plasma plume into a narrower cone centred along the thrust axis, which would also be beneficial for increasing the thrust [23]. Similar magnetic nozzles are used in HDLT and other cathodic arc thruster applications with similar degrees of success [11, 23]. If the nozzle were to use permanent magnets or the discharge current itself (by running either the cathode or anode currents through field coils downstream of the cathode face) then this increase in performance would come with minimal power consumption increases and only a small increment in mass. Doubling drift velocity without appreciably affecting the input power or erosion rate would lead to a doubling of the momentum carried by the plasma; this would therefore double the thrust of the engine, its fuel specific impulse and thrust-to-power ratio. Since jet power efficiency scales to the square of thrust, the jet power efficiency would quadruple, theoretically leading to better than unity efficiencies for many materials, assuming the same conditions hold. Testing the effect of magnetic field geometry would be a fruitful area for future work to optimise the operation of the arc thruster.

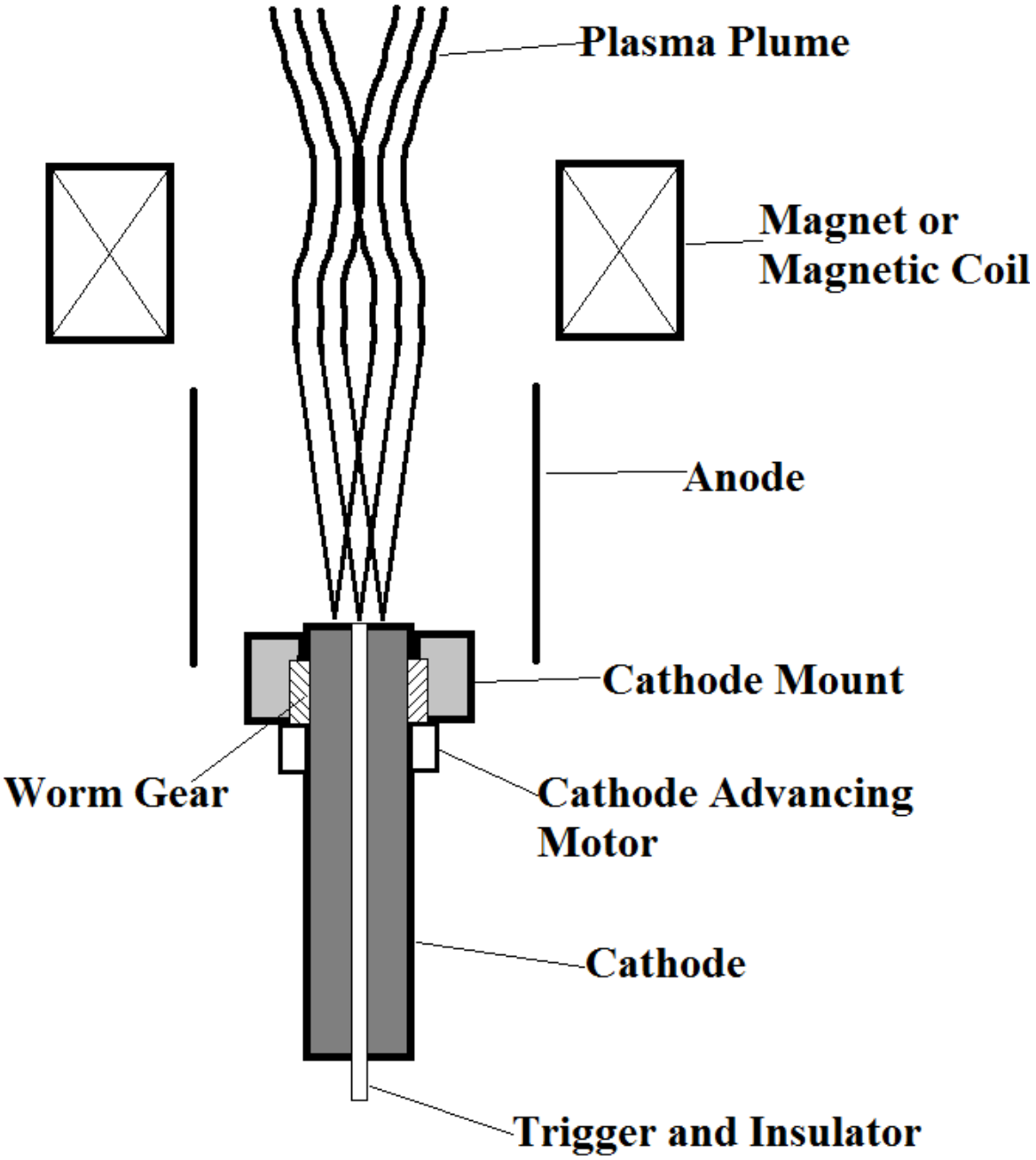

Figure 8.3: Sketch of apparatus for prototyping and future work, showing the proposed advancing motors and magnetic field sources.

As the arc fires it erodes material from the surface of the cathode, gradually wearing it away and leading to difficulty in triggering the arc if there is too much distance from the trigger pin to the cathode. One way of solving this would be to periodically advance the cathode by a fraction of a millimetre after enough material has been eroded to warrant this. Edge-triggered systems such as those used by Fu et al [41, 42] have found success using a threaded rod to push the cathode forwards. A centre-triggered system can adapt this idea, as shown by the design in figure 8.3. In order to maintain comparability with the design tested for this thesis, let us propose a 25mm rod of test material, around 100mm long. To hold the cathode in place inside the cathode mount, one cuts

M24x2 thread into the outside of the cathode rod and the same thread on the inside of the cathode mount. On the face of the cathode mount away from the arc discharge one would mount some stepper motors attached to worm gears that extend forward, into hollows cut into the cathode mount. After the experimentally determined correct number of pulses are fired, the stepper motors are engaged to turn the cathode rod by a small amount; a quarter of a turn would advance an M24x2 bolt by 0.5mm. Holding the trigger pin and insulator in place would mean that they are not carried forwards by any deposition present, and so help to ensure continued operation of the arc over long durations. Testing the system with a 100mm long rod ought to be an effective prototyping compromise, as rods of over a metre long may need to be used in any practical application.

Other effects of magnetic field application that would merit investigation include steering the cathode spots across the surface of the cathode so that the use of the cathode is optimised. In conjunction with tuning the shape of the current pulses, by switching more capacitors into the discharge at the correct times, this would increase the cathode usage efficiency and minimise the deposition of eroded material onto the ridges left on the cathode surface by the erosive processes of arc operation [36]. Modern capacitor technology is developing rapidly, leading to lower mass per Farad and higher discharge efficiencies, which lower the mass of any thruster technology dependant on capacitive energy storage methods.

8.7 Chapter Summary

From analysis of the data presented in earlier chapters, and comparing it to the published data on various flight rated electric thrusters, we can see that the pulsed arc thruster is a promising technology for orbital transfer and station-keeping applications due to its high specific impulse and jet power efficiency as well as the predictability with which several materials can be relied upon to produce scalable impulse bits. Table 8.3 summarises the results of this work, showing a direct comparison between current technologies and the materials tested in this thesis on the basis of their performance against the standard efficiency metrics.

Efficiency metric	Best current technology or thruster	Competitor's value	Best material tested in this thesis	Best results from this thesis (eroded at bottom)	Are these competitive?
Specific Impulse (s)	NASA HiPEP	9200 [4]	Magnesium	9342 ± 1308 7755 ± 1086	Yes, when not eroded.
Jet Power Efficiency (%)	Xe Gridded Ion	80 [2]	Magnesium	88.53 ± 15.94 44.38 ± 7.99	Yes, when not eroded
Thrust-to-Power Ratio (μN/W)	Xe Hall Effect	55-60 [2, 3]	Tin	27.3±2.7 22.3±2.2	No.

Table 8.3: Summary of performance metrics

Tin and bismuth are not to be suggested for use in future work due to their high erosion rates leading them to have low specific impulses and jet power efficiencies. While these two materials had the greatest thrust-to-power ratios of the materials tested, their ratios are far lower than those cited for current generation technologies. Magnesium is by far the most promising material tested, while molybdenum, vanadium, titanium and carbon each earn honourable mentions.

9 Summary

Pulsed arcs have been widely used in industry for decades for materials science applications, and while some work has been done to determine their potential as a spacecraft thruster, this is the first work that has been done to investigate fuels and test a centre-triggered arc thruster in a rigorous fashion. The results clearly show that magnesium is by far the most promising material tested to date, with molybdenum, vanadium, titanium and carbon each receiving honourable mentions. The high specific impulses measured for Mg imply such a high exhaust velocity that high cargo fraction missions from LEO to the outer planets could be readily achievable.

Indeed, assuming that half of the mass of any mission is Mg fuel, one has a delta-V budget from LEO of approximately 55km.s^{-1}. A low-thrust transfer to Mars would require 15km.s^{-1} of delta-V, and the main belt asteroids not much more, indicating that such a system could be used for investigation and exploitation of off-world resources. Magnesium is one of the most common elements in the universe, and is thought to be a major constituent of many asteroidal surfaces; reflectance spectroscopy has shown that several bodies covered by the SMASS II survey have Mg-rich olivine minerals over most of their surface. Additionally, Mg, Al and Ti are materials used in the construction of spacecraft, suggesting that the recycling of defunct satellites could be used as a fuel source for this system.

That there are flaws to the design as it stands is easy to see; these experiments have been done on cathodes 25mm in diameter and 12.5mm tall. In order to provide sufficient total momentum change for orbital transfer manoeuvres or station-keeping, there will need to be much more reaction mass available to the thruster; this would require much larger cathodes that would need to be moved to ensure reliable operation over many hours of use. The threaded rod design advanced in figure 8.3 would be an option, and one that deserves investigation. The system sketched would also allow exploration of the effects of magnetic fields on thrust optimisation and cathode erosion profiles. We have shown that such work is important, as it would allow more mission profiles to be achieved with higher deliverable mass and/or lower launch costs. Given these results and the correct development, a centre-triggered pulsed cathodic arc thruster could well be the key to exploiting the inner solar system from low Earth orbit.

10 Acknowledgements

I would like to thank all those who supported me along the way as I wrestled with my thesis over these past five and a half years. Firstly, my supervisors Marcela, David and Paul, for providing me with support, ideas and challenging me to become more than I thought I could be. My housemates Tina and Dan I thank for ensuring that I took care of myself and had a roof over my head. The technical staff at both the University of Sydney and the City University of Hong Kong, especially Phil, Chula, Mick, David, Mr Wong, Mr Poon and Rob, for building large parts of the system I worked on and helping me to diagnose the issues that inevitably arose; sorry about the transformer, Phil and Chula! To the many friends who helped by listening to me rant about setbacks and crow about success, particularly those Ursulans who listened to me rambling about potential applications, like Anton, Cian, Murasaki and others. To fellow postgrads with whom I could discuss the mysteries and vagaries of administration and being a student, particularly Alice, Jane, Gemma, Adam, Scott, Stephen, Gerry, Danya, Dave, Perry, Gav (thanks for the proof-read, mate!), Tallulah and Pip. To the admin staff who helped me to organise my exchange as well as work things out back in Sydney, like Alexis, Cynthia, Sang, Tricia and the group of helpful people at the AP General Office. To my friends in Hong Kong who made me welcome, in particular Tobi, Jack, Chesney, Ariel, Hannah, Laurie, Ricky, Weihong, Penghui and everyone else in the Plasma Lab. To Lara, who helped give me the strength to get over the line. Lastly, to my family who, though they were often several thousand kilometres away from me, were always there to offer encouragement.

-Patrick Reinhard Christian Neumann, at Camperdown in New South Wales, this twenty-fourth day of February in the two-thousand and fifteenth year of the common era, with final amendments finished on the twenty-seventh day of August in that same year.

11 References

1. *Space Mission Analysis and Design*, Wiley and Larson (ed.), 3rd Edition, Microcosm Press, 2004, El Segundo California USA
2. "Fundamentals of Electric Propulsion: Ion and Hall Thrusters", Goebel and Katz, 2008, available online via NASA JPL at http://descanso.jpl.nasa.gov/SciTechBook/st_series1_chapter.html
3. Snecma Moteurs product datasheet for Snecma PPS1350, http://www.snecma.com/IMG/pdf/PPS1350_Anglais.pdf
4. Foster et al, "The High Power Electric Propulsion (HiPEP) Ion Thruster," Nasa Publication 2004-213194
5. L-3 Electron Communications Technologies data sheet on the Boeing Xenon Ion Propulsion System (XIPS) http://www2.l-3com.com/eti/downloads/8cm_xips.pdf
6. http://sci.esa.int/smart-1/34201-electric-spacecraft-propulsion/ European Space Agency website, detailing fundamentals of rocketry and describing electric propulsion systems, accessed 06/01/2015
7. http://sci2.esa.int/Conferences/LowCostMissions03/smart1.pdf Conference presentation discussing future missions for the European Space Agency. Accessed 06/01/2015
8. http://www.tipmagazine.com/tip/INPHFA/vol-6/iss-5/p16.pdf Article by E J Lerner on the state of electric propulsion systems, published in "The Industrial Physicist" magazine, accessed 30/1/09.
9. Johnson, N. L., Handbook of soviet lunar and planetary exploration - volume 47 science and technology series, Amer. Astronau. Soc. Publ., 1979.
10. http://pepl.engin.umich.edu/ University of Michigan Plasma and Electric Propulsion Laboratory, with links to current research projects and past publications, accessed 06/01/2015.
11. Takahashi K et al, Plasma Sources Sci Technol Vol 23 (2014) 044004
12. Blackhall and Khachan, *J. Phys. D: Appl. Phys.* Vol.**40 (2007)** 2491
13. Marcuccio et al, Journal of Propulsion and Power, Vol 14, No. 5, 1998
14. Ahedo E, Plas. Physics Cont. Fusion, Vol 53 (2011), 124037
15. http://www.nasa.gov/centers/glenn/about/fs23grc.html NASA Glenn Research Centre page on PPTs, showing specifications for the EO-1 thruster, accessed 19th January 2015.
16. Longmier B W et al, Proceedings of the 32nd International Electric Propulsion Conference, IEPC-2011-156, Sept. 2011, Wiesbaden, Germany.
17. Keidar M et al, Plasma Sources Sci. Technol. 14 (2005) 661-9
18. J. Schein, A. Anders et al, Rev Sci Instr, Vol 73, No 2, Feb 2002, 925-7
19. Polk et al, IEEE Tran. on Plas. Sci., Vol. 36, No. 5, pp 2167-79 Oct 2008
20. Neumann PRC et al, Proceedings of the 12th Asia Pacific Physics Conference, JPS Conf. Proc. 1, 015059 (2014)
21. Neumann PRC et al, AIAA Journal of Propulsion and Power, Vol: 28,Iss: 1, pp: 218-21, 2012
22. Neumann P R C et al, Plasma Sources Sci. Technol. 18 (2009) 045005
23. Keidar et al, Plasma Phys. Control. Fusion, Vol 57 (2015), 014005
24. Anders, Oks and Yushkov, J. of App. Physics **102**, 043303, 2007
25. Yushkov and Anders, App. Physics Letters **92**, 041502, 2008
26. Anders and Yushkov, App. Physics Letters **91**, 091502, 2007
27. Sanginés R *et al*, 2009 *Plasma Sources Sci. Technol.* 18 045007
28. Hantzsche, E "Mysteries of the Arc Cathode Spot: A Retrospective Glance," IEEE Transaction on Plasma Science, Vol. 31, No. 5, Oct 2003.

29. E Hantzsche, B Juttner, F Puchkarovt, W Rohrbeck and H Wolff; “Erosion of metal cathodes by arcs and breakdowns in vacuum;” J. Phys. D: Appl. Phys., Vol. 9, 1976.
30. Gan BK, Bilek MMM, McKenzie DR, Swift PD, McCredie G; Plasma Sources Sci. Technol., **12** (2003) 508-512
31. Oates THW, Pigott J, McKenzie DR, Bilek MMM, Rev Sci Instr, Vol 74, No 11, Nov 2003, pp 4750-4
32. Yushkov, Anders, Oks, and Brown, J. Appl. Phys., Vol. 88, No. 10, pp 5618-5622, Nov. 2000
33. Gilmour and Lockwood, Proc. of the IEEE, Vol. 60 (1972), No. 8, 977-991
34. Hantzsche, E; “Theory of Cathode Spot Phenomena;” Physica 104C (1981) 3-16
35. Anders, A; “The Fractal Nature of Vacuum Arc Cathode Spots” IEEE Transaction on Plasma Science, Vol. 33, No. 5, Oct 2005
36. Ryves L, McKenzie D R and BilekMMM, 2009 *IEEE Trans.Plasma Sci.* **37** 365–8
37. Hantzsche, E; “Two-Dimensional Models of Expanding Vacuum Arc Plasmas,” IEEE Transaction on Plasma Science, Vol23, No. 6, Dec 1995
38. Hantzsche, E; “A Hydrodynamic Model of Vacuum Arc Plasmas,” IEEE Transaction on Plasma Science, Vol. 20, No. 1, Feb 1992
39. Hantzsche, E; “Consequences of Balance Equations Applied to the Diffuse Plasma of Vacuum Arcs;” IEEE Transaction on Plasma Science, Vol. 17, No. 5, Oct. 1989
40. Hohenbild et al, J. Phys. D: Appl. Phys. 41 (2008) 205210
41. R. K. Y. Fu et al., Diamond and Related Materials, vol. 14, no. 9, pp. 1489 -1493 (2005).
42. R. K. Y. Fu et al., Surface and Coatings Technology, vol. 196, no. 1 - 3, pp. 150 - 154 (2005).
43. Ferguson et al., IEEE Trans. On Plasma Sci., Vol. 34, No.5, 1948-58
44. Tajmar, M, Journal of Spacecraft and Rockets, Vol. 39, No.6, 886-893
45. Cubbin EA, Ziemer JK, Choueiri EY, Jahn RG; Rev. Sci Instr. 68 (6), June 1997, 2339-44
46. Neumann, P R C; “Pulsed Cathodic Arc Plasma Thruster,” thesis created for eligibility for the degree of Honours in Engineering, University of Sydney, compiled Oct. 2006.
47. Pelletier, J, Anders, A; Plasma-Based Ion Implantation and Deposition: A Review of Physics, Technology, and Applications, IEEE Transaction on Plasma Science, Vol. 33, No. 6, Dec 2005
48. Tan IH et al, Surface & Coatings Technology, Vol. 186 (2004) pp.234– 238
49. Zaporojtchenko et al, Applied Surface Science, Vol 144-5 (April 1999), pp355-9
50. P. Sigmund, “Sputtering by particle bombardment I,” in Topics inApplied Physics, vol. 47, Berlin: Springer Verlag, 1981, ch. 2, p. 9.
51. Sigmund P, Physical Review, Vol 184, No 2, 10 Aug 1969, pp 383-416
52. Chapman G et al, Radiation Effects, Vol 13 (1972), pp121-9
53. Wehner G and Rosenberg D, Journal of Applied Physics, Vol 31 No 1 (Jan 1960, pp177-9
54. Brown I and Shiraishi H, IEEE Tran. on Plas. Sci., Vol. 18, No. 1, Feb 1990, pp170-171
55. Kimblin C, J Appl. Phys., Vol 44, No 7, July 1973, pp3074-81
56. Plyutto A, Ryzhkov V, Kapin A, Soviet Physics JETP, Vol 20, No 2, Feb 1965, pp. 328-337
57. Anders, A, Binder, R, Yotsombat, B; “Correlation between cathode properties, burning voltage, and plasma parameters of vacuum arcs” Journal of Applied Physics Vol 89, No 12, 15 Jun 2001
58. *CRC Handbook of Chemistry and Physics*; 56th ed.; 1976; CRC Press; Cleveland, Ohio
59. Kittel C, Introduction to Solid State Physics, Sixth Ed., John Wiley and Sons Inc. New York, 1986
60. Lun J et al, Experimental Techniques, Volume 38, Issue 3, May/June 2014
61. *University Physics With Modern Physics*, Young and Freedman, 10th edition, 1999, Pearson Education.

62. Kodys A and Choueiri E 2005 A critical review of the state-of-the-art in the performance of appliedfield magnetoplasmadynamic thrusters *41st AIAA Joint Propulsion Conf. (Tucson, AZ)* (Washington, DC: American Institute of Aeronautics and Astronautics) AIAA 2005-4247

12 Appendices

12.1 Appendix A – Modelling Code

```
%Simple pendulum modelling code
%Written for matlab 7.0.4
%P Neumann

clear all       %setup workspace
close all

vi=20000;       %ion velocity
dt=300*10^-6;   %time duration of pulse
r=0.025/2;      %radius of flow cylinder
mi=47.86*1.67*10^-27;   %mass of ion
ni=10^20;       %number density of ions

hh=vi*dt;       %height of flow cylinder
V=hh*pi*r*r;    %volume of flow cylinder
Ni=V*ni;        %total number of ions
Mi=mi*Ni;       %total ion mass
p1=Mi*vi;       %ion momentum

m=(linspace(2.5,20))*10^-3;       %Pendulum masses

v=p1./m;        %velocity imparted by impulse

plot (1000*m,v), xlabel ('Pendulum Mass (g)'), ylabel('Maximum Velocity
(m/s)')  %plot final vel's
 grid on
h=0.5.*v.^2/9.81;       %height of swung pendulum , mv^2=mgh
figure (2)  % new figure

plot (1000*m,1000*h), xlabel ('Pendulum Mass (g)'), ylabel('Maximum Height
(mm)')    %plot heights
 grid on
l=0.15;     %length of pendulum string

x=sqrt(2*h*l-h.*h);     %use similar traingles to determine horizontal
displacement

figure (3)      %new figure

plot (1000*m,1000*x), xlabel ('Pendulum Mass (g)'), ylabel('Maximum
Horizontal Displacement (mm)')     %plot sideways displacements
grid on
```

12.2 Appendix B – Processing Code

```
%Code to turn .txt files into .mat files
%written for MatLab 7.04
% P Neumann


clear    %clear workspace
close
astart2=input('which dataset to begin with?');    %first dataset of range
afini2=input('which dataset to end with?');       %last dataset of range
ashot2=astart2;    %step variable for for loop
r=1;       %step variable for figures

display('*****************************************************')
display('*******DATA STARTS HERE**********')
display('*****************************************************')



for ashot2=astart2:afini2;   %for loop stepping thru datasets
   ahh2=int2str(ashot2);  %transform step variable into string

   afile2=[ahh2,'.txt'];
   jub=load(afile2);                          %load dataset
   [hite,width]=size (jub);
      t_step=(jub(2,1)-jub(1,1))*10^-6;
      Iabase=mean (jub(1:50,2));
      Icbase=mean (jub(1:50,4));                %find base values
      Vabase=mean (jub(1:50,8));
      Vcbase=mean (jub(hite-50:hite,10));         %as it should be nil when t->large

      Ia=1000*(jub(:,2)-Iabase);
      Ic=1000*(jub(:,4)-Icbase);        %correct for dc bias/noise/scale
      Va=(jub(:,8)-Vabase);
      Vc=(jub(:,10)-Vcbase);
      Vburn=Vc-Va;
      inst_pow2 = Ic.*Vburn;    %find instantaneous power
      NEC=Ic-Ia;                %find Net Ejected Current
      Ph = jub(:,14);
      t_Ph = 1e-3*jub(:,13);


   for i=2:hite,      %charge integ loop
   if i==2     %initial charge value
      Q=(Ic(i)+Ic(i-1))/2*t_step;   %integrate dQ/dt via Riemannian Average Method

      WD=(inst_pow2(i)+inst_pow2(i-1))/2*t_step;   %integrate dpower/dt via Riemannian Average
Method

      NEQ=(NEC(i)+NEC(i-1))/2*t_step;   %integrate dQ/dt via Riemannian Average Method

   elseif NEC(i)>0
      Q=Q+(Ic(i)+Ic(i-1))/2*t_step; %integrate dQ/dt via Riemannian Average Method
```

```
    WD=WD+(inst_pow2(i)+inst_pow2(i-1))/2*t_step; %integrate dpower/dt via Riemannian
Average Method

    NEQ=NEQ+(NEC(i)+NEC(i-1))/2*t_step;   %integrate dQ/dt via Riemannian Average Method
if NEQ flow is positive

  else
    Q=Q+(Ic(i)+Ic(i-1))/2*t_step; %integrate dQ/dt via Riemannian Average Method

    WD=WD+(inst_pow2(i)+inst_pow2(i-1))/2*t_step; %integrate dpower/dt via Riemannian
Average Method

  end %end if

   i=i+1;    %increment
end %end charge loop


all=['dat_',ahh2,'.mat'];   %make into datafile name
save (all);       %save datafile

QQQ(r,1)=Q;
WWW(r,1)=WD;        %collate all data
NEQQQ(r,1)=NEQ;
NUMM(r,1)=ashot2;
Vch(r,1)=mean (Vc(1:50));
MaxIc(r,1)=max (Ic);
r=r+1;
end
QQQ;
WWW;
NEQQQ;
NUMM;
Vch;
```

12.3 Appendix C – Plotting Code

```
%Code to plot .mat files for inspection of photodiode traces
%written for MatLab 7.04
% P Neumann

%Note: most subplots suppressed to conserve memory, though option to plot is open to allow
inspection of traces.



clear    %clear workspace
close
start=input('which dataset to begin with?');    %first dataset of range
fini=input('which dataset to end with?');       %last dataset of range
shot=start;    %step variable for for loop
q=1;        %step variable for figures

display('*****************************************************')
display('*******DATA STARTS HERE**********')
display('*****************************************************')



for shot=start:fini,   %for loop stepping thru datasets
   hh=int2str(shot);  %transform step variable into string

   file=['dat_',hh,'.mat'];
   load(file);                %load datafile

hh;
Q;        %data to confirm files are loading, left over from debugging stage
WD;


figure(q)       %open new figure window
% subplot (3,2,1) %subplot matrix selection
% plot(t_Ic(1:2500,:),Ic,'b-')%,t_Ia(1:2500,:),Ia,'r:',t_Ia(1:2500,:),NAC,'g--')   %plot Ic,Ia, NAC vs
time
% xlabel('time (s)'), ylabel('current (A)'), legend('cathode current')%,'anode current','NAC')    %labels
% titl=['Current for shot ',hh];
% title (titl)    %title

% subplot (3,2,2) %subplot matrix selection
% plot(t_Vc(1:2500,:),Vc,'b-',t_Va(1:2500,:),Va,'r:',t_Va(1:2500,:),burn,'g--')   %plot Vc,Va, burn
voltage vs time
% xlabel('time (s)'), ylabel('voltage (V)'), legend('cathode voltage','anode voltage','burn voltage')
%labels
% titl=['Voltages for shot ',hh];
% title (titl)    %title
%
%
% subplot (3,2,3) %subplot matrix selection
plot(t_Ph.*1000,Ph), xlabel('time (ms)'), ylabel ('arb. intensity')    %plot photodiode trace+label
legend('photodiode trace')
```

```
titl=['Photodiode trace for shot ',hh];
title (titl)    %title
%
% subplot (3,2,4) %subplot matrix selection
% plot(t_Va(1:2500,:),inst_pow), xlabel('time (s)'), ylabel ('power (W)')    %plot photodiode
trace+label
% legend('instantaneous plasma power')
% titl=['Instantaneous Plasma Power for trace ',hh];
% title (titl)    %title
%
% subplot (3,2,5) %subplot matrix selection
% plot(t_Ia(1:2500,:),inst_res), xlabel('time (s)'), ylabel ('Resistance (ohms)')    %plot photodiode
trace+label
% legend('instantaneous plasma resistance')
% titl=['Instantaneous Plasma Resistance for shot ',hh];
% title (titl)    %title

q=q+1;              %increment loop

end                 %end loop
```

12.4 Supplementary Figures

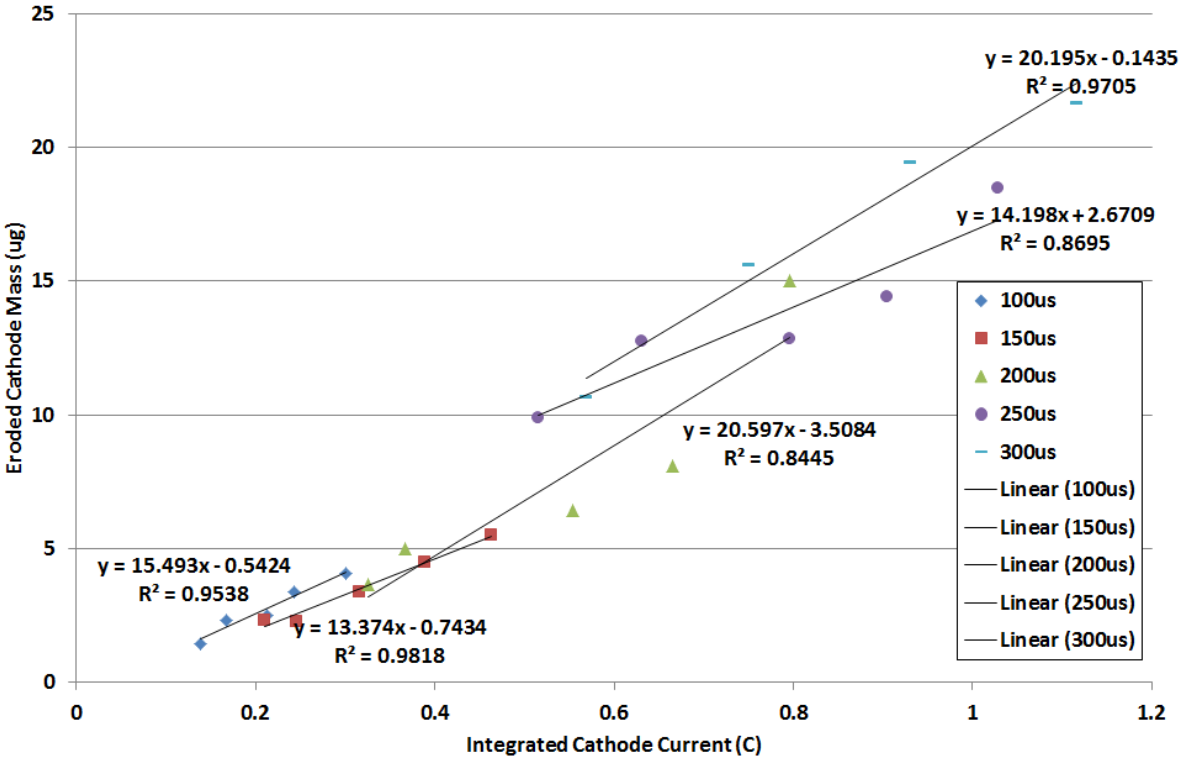

Figure 12.1 Mg average mass eroded per pulse vs integrated cathode current, including the 180V_{ch}, 200µs pulses showing transition to arcing.

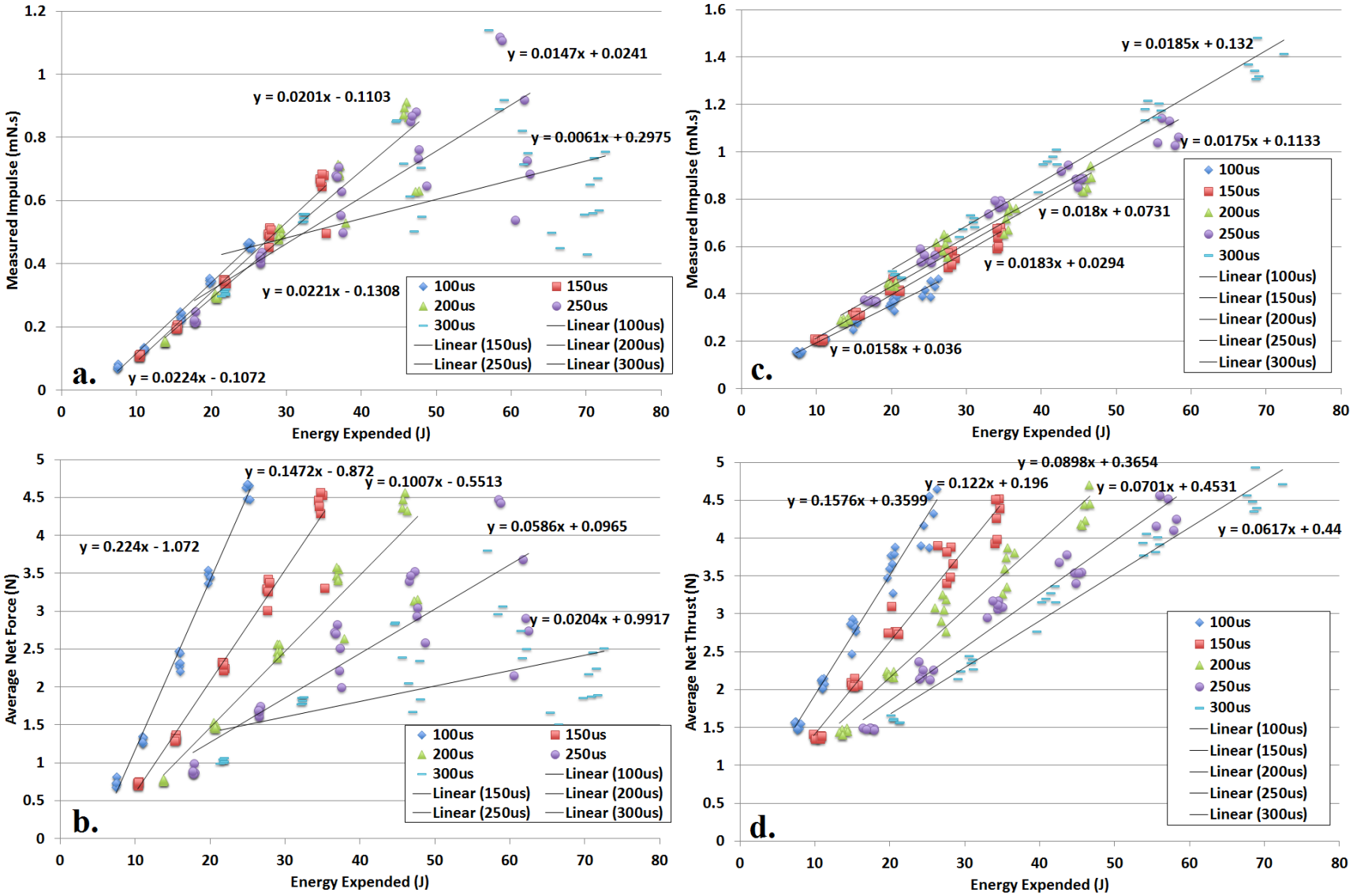

Figure 12.2: Unbaked vs Baked (via 3000 pulses, 4Hz, 180Vch, 310 us duration) Carbon results. Subplots a and b show impulse and thrust produced by plasma from an unbaked non-eroded cathode surface, while subplots c and d show data for a "non-eroded" C surface, measured after the bake-out pulses.

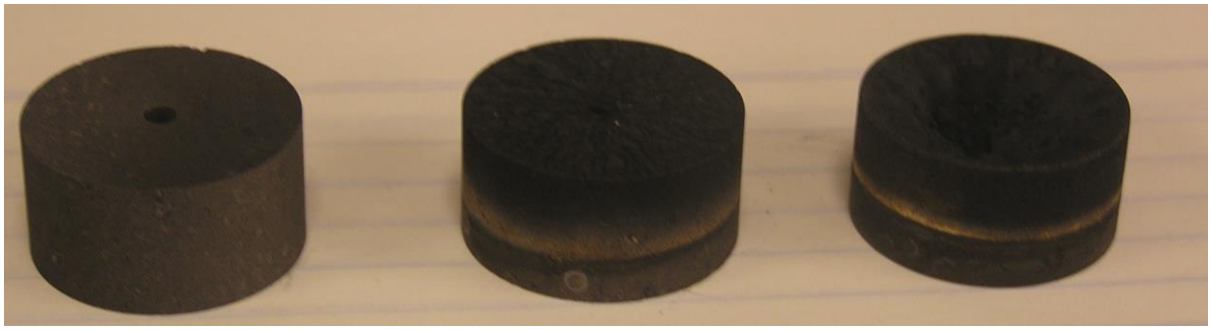

Figure 12.3: Three carbon cathodes; from left to right unused, post bake-out and after significant erosion. Note the colour change from unused to bake-out, indicating compositional change

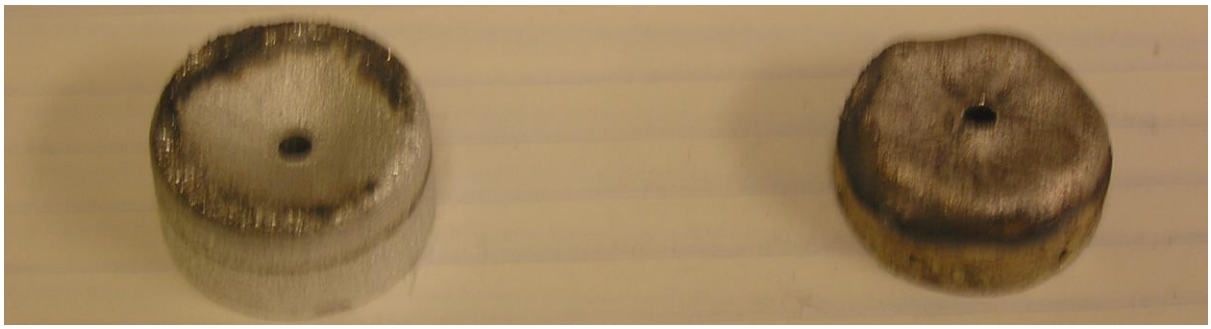

Figure 12.4: The non-refractory cathodes used, being tin (left) and bismuth (right)

Figure 12.5: Aluminium cathode used in this work

Figure 12.6: Magnesium cathode used in this work, with anomalous erosion trenches shown at left and typical erosion profile at right.

Figure 12.7: Two of the refractory cathodes used in this work, vanadium (left) and tantalum (right), showing typical erosion profile.